Piezoelectrically Generated Bistable Composites for Morphing, Energy Harvesting, and Vibration Control

by

Andrew J. Lee

A dissertation submitted in partial fulfillment
of the requirements for the degree of
Doctor of Philosophy
(Aerospace Engineering)
in the University of Michigan
2019

Doctoral Committee:

Professor Daniel J. Inman, Chair
Professor Henry A. Sodano
Associate Professor Veera Sundararaghavan
Professor Kon-Well Wang

Andrew J. Lee
ajle@umich.edu
ORCID iD: 0000-0001-9355-7024

ACKNOWLEDGEMENTS

I would like to sincerely thank my advisor, Dr. Daniel J. Inman, for being such a supportive mentor throughout my graduate studies. His positive attitude and can do spirit have always been a source of encouragement during challenging times. It made such a difference to have an advisor who provided me with the creative freedom, independence, and resources necessary to complete the work in this dissertation. He gave me my first research opportunity as a master's student and the entire journey since then has been a pleasure. I am grateful for the lessons and advice I've received for my career path and professional development, but also for the moments of levity that we shared. I would also like to thank Dr. Kon-Well Wang, Dr. Henry A. Sodano, and Dr. Veera Sundararaghavan for offering their expertise and insight while serving as members of my Ph.D. committee. I appreciate the time and effort they have given on improving the contents of this dissertation. I want to thank all of the professors at the University of Michigan responsible for continuously challenging me to grow academically throughout my undergraduate and graduate education.

This dissertation would not have been possible without the help and encouragement from my friends. I am blessed to have supportive labmates and would like to thank both current and past members of the Adaptive Intelligent Multifunctional Structures (AIMS) Lab. Specifically, I want to thank Dr. Katie Reichl, Dr. Lawren Gamble, Brittany Essink, Krystal Acosta, Lori Groo, Kevin Haughn, Christina Harvey, Piper Sigrest, Dr. Alex Pankonien, and Dr. Eun Jung Chae. I also want to thank Dr. Jared Hobeck, Dr. Ya Wang, and Dr. Amin Moosavian for much of the early technical guidance that was needed to get my research started. A special thanks to Dr. Antai Xie for the assistance on the active control work in this dissertation.

I am thankful to my girlfriend Jianan Zhang for being by my side for the majority of my Ph.D. She has become a huge part of my life and I feel that I am a better person with her in it. She provided me with an immeasurable amount of support during periods of self-doubt and stress and has allowed for my current state of well-being. I am grateful that I can share myself with her and look forward to our experiences ahead.

I would like to specially recognize my parents Dr. Young Jai Lee and Bonghee Lee for being my biggest source of inspiration for pursuing a doctorate. I would not have been able to get as far in life without their constant love and support through my ups and downs. I want to thank my dad for all of the advice and care he provided which gave me confidence and helped me to persevere. He is my role model and somebody I strive to emulate. My mom has been equally impactful in shaping me to who I am today and I am lucky to be her son. I would also like to thank my sister Christine Lee for being the special somebody that I can personally relate to and confide in.

This work is supported in part by the US Air Force Office of Scientific Research under a grant number FA9550-16-1-0087, titled "Avian-Inspired Multifunctional Morphing Vehicles" monitored by Dr. BL Lee and in part by the Rackham Merit Fellowship from the University of Michigan.

TABLE OF CONTENTS

LIST OF FIGURES

FIGURE

LIST OF TABLES

TABLE

LIST OF APPENDICES

APPENDIX

LIST OF ABBREVIATIONS

CFRP Carbon Fiber Reinforced Plastic

CLT Classical Lamination Theory

CTE Coefficient of Thermal Expansion

FEA Finite Element Analysis

FFT Fast Fourier Transform

FRF Frequency Response Function

GFRP Glass Fiber Reinforced Plastic

IDE Interdigitated Electrode

MDOF Multiple Degrees of Freedom

MFC Macro Fiber Composite

PPF Positive Position Feedback

PZT Lead Zirconate Titanate

RMS Root Mean Square

SDOF Single Degree of Freedom

SMA Shape Memory Alloy

UAV Unmanned Aerial Vehicle

VEH Vibration Energy Harvester

ABSTRACT

Elastic instabilities associated with buckling in multistable structures have been harnessed toward energy-based and control-based applications, with significant research toward energy harvesting and morphing. Often combined with smart materials such as piezoelectric or shape memory alloy actuators, bistable composite plates are popular host structures due to maintaining two geometrically distinct stable shapes without any external influence. A second potential well is traditionally generated from anisotropic thermal residual stresses in fiber-reinforced composite laminates during cure cycle cooldown. In this work, a novel method of inducing bistability is investigated by bonding two piezoelectrically actuated Macro Fiber Composites (MFC) in a cross-ply layup and releasing the voltage post cure to yield two cylindrically stable configurations. Since the MFCs are simultaneously the transducer and host structure, the resulting efficiencies and increase in actuation authority enable multifunctionality while exceeding the limits of conventional bistable prototypes that are designed with a single application in mind. Through MFC actuation, quasi-static snap through morphing is achieved with no external assistance while unwanted cross-well instabilities resulting from nonlinear vibrations are suppressed with active control strategies. The same cross-well dynamics are also exploited in various broadband energy harvesting applications. Voltage perturbations from low to high amplitude solutions are demonstrated for the purpose of enhancing energy harvesting performance through the extension of cross-well bandwidths.

CHAPTER 1

Introduction

The development of adaptive structures has been an active research area due to their ability to conform to various operating environments and concurrently fulfill multiple roles. They are generally composed of reconfigurable elements, sensors, and actuators, and have had notable aerospace applications in aircraft morphing. The potential of such aircraft structures to adapt to variable loading and design requirements lead to aerodynamic and structural efficiencies when compared to conventionally discrete systems. The ongoing development of smart materials and technologies have enabled researchers to integrate these components into smooth and continuous control surfaces that allow traditionally unachievable shape changes. However, there is an inherent conflict in designing a structure stiff enough to withstand external loading and maintain stability while simultaneously being compliant enough to allow for full range of actuated motion.

Multistable structures are capable of having two or more statically stable equilibrium states and they have been proposed as a solution to the conflicting stiffness requirements. Each stable state is a separate geometric configuration corresponding to a potential energy minimum, where no energy input is required to maintain any of these states. The simplest case of multistability is bistability, or the existence of two distinct potential energy minima. This is illustrated for a symmetric and Single Degree of Freedom (SDOF) system in Figure 1.1(a), which shows the relationship between

the total potential energy and the displacement with the latter being chosen as the representative geometric parameter. The transition between shapes occurs through a dynamic jump phenomenon known as a snap-through event and it is highly nonlinear in nature. This is made possible when the structure's total potential energy is increased enough to overcome the unstable peak between the two wells through either external loading or actuation. As shown in Figure 1.1(b), the structure will dynamically jump from the first to second stable branch when the applied load exceeds the limit load. Subsequently removing the load will place it in the second potential energy well. This behavior is reversible if the direction of the load is flipped, and the bistable structure can be returned to its original state.

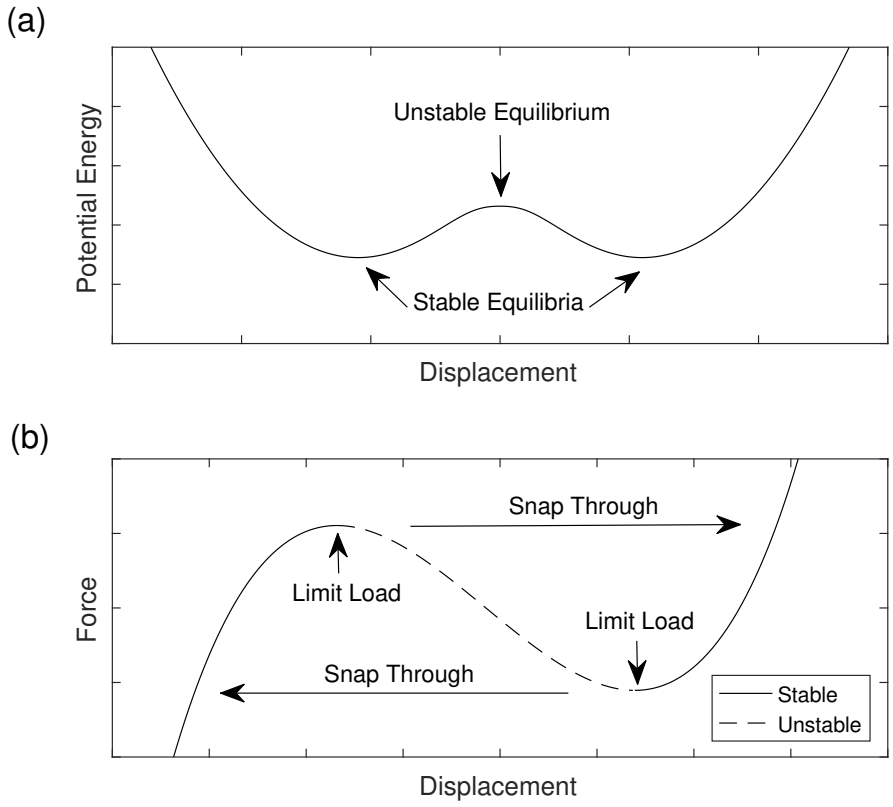

Figure 1.1: Representative (a) potential energy profile vs. displacement and (b) force vs. displacement behavior for a bistable structure.

1.1 Background

Multistable structures have drawn significant attention in control surface designs for their potential morphing applications, with recent review articles by Hu and Burgueno [1] and Emam and Inman [2] outlining recent advances. The attraction derives from their capability to achieve multiple configurations with large displacements using relatively low energy input while being lightweight, mechanically simple, and stiff enough to be part of the load bearing structure. Smart materials such as piezoelectric actuators are often paired with multistable plates to trigger snap-through motion. Aside from morphing, there has been a recent emergence of research into leveraging the elastic instabilities of multistable structures under dynamic environments. This has shifted the notion of buckling being associated with unwanted structural failure to a phenomenon that is desirable for many adaptive and smart applications. The nonlinear dynamical behavior exhibited by bistable structures with two potential energy wells include large amplitude motion associated with the sudden energy release of snap-through events. This type of response has attracted significant attention from researchers as an efficient and robust mechanism to convert nonlinear vibrations into electrical energy through piezoelectric or electromagnetic transduction [3, 4]. The same snap-through dynamics has also been investigated as a mechanism for energy dissipation and vibration absorption [5, 6]. The following sections present the literature review of the research and development into multistable structures and their applications.

1.1.1 Bistable Composite Laminates

The classical method for achieving structural bistability is with thin unsymmetric composite laminates, which has been the subject of study for the last four decades ever since Hyer [7, 8] found

that their cured shapes are not predicted by Classical Lamination Theory (CLT) [9]. These composite laminates exhibit geometric nonlinearity and an anisotropic response to elevated temperatures experienced during cure cycles while they are in a flat configuration under vacuum. This leads to residual thermal stresses during cooldown to room temperature that results in a pitchfork bifurcation into two cylindrically curved shapes. The stresses arise from the mismatch of the Coefficient of Thermal Expansion (CTE) between orthotropic lamina plies consisting of constituent fibers and matrix materials, inducing internal strains under thermal loading. For a cross-ply bistable composite laminate as shown in Figure 1.2, the major curvatures of each stable shape far exceed the minor curvatures in the perpendicular direction, which results in large out-of-plane deflections in opposing directions between the states.

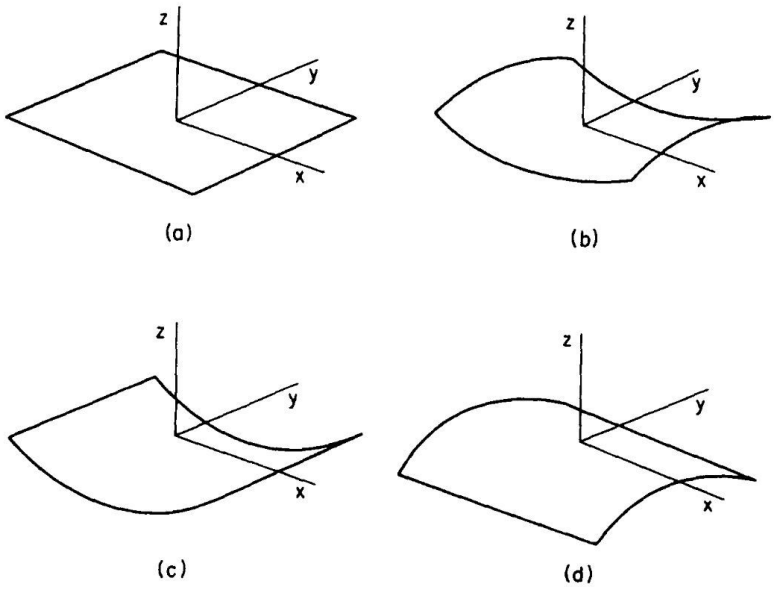

Figure 1.2: Basic shapes of a cross-ply bistable composite laminate: (a) flat at cure temperature, (b) unstable saddle state, and the two (c)-(d) stable cylindrical states [10].

To model the stable shapes of bistable composite laminates, nonlinear terms were added to the strain-displacement kinematic relationships in CLT to capture the out-of-plane displacements ob-

served to be many laminate thicknesses in magnitude [7, 8]. This extension to CLT was combined with a simple quadratic Rayleigh-Ritz approximation of the displacement and strain fields in the minimization of total potential energy. With just four unknown coefficients to approximate the resulting shapes, an closed-form analytical solution captured the bifurcation behavior of $[0_2/90_2]_T$ graphite-epoxy laminates and revealed the transition between the monostable saddle shape to the two cylindrical shapes for various geometric parameters. This model was used by Hamamoto and Hyer [10] to show that bistable laminates at room temperature will revert back to a monostable saddle shape as ambient temperature increases, until settling to a flat shape at cure temperature. All combinations of unsymmetric four-ply layups consisting of 0° and 90° orientations were modelled with the two additional shape coefficients for better accuracy [11]. With the increased complexity, a Newton-Raphson numerical method was used to obtain the six unknown coefficients and a limit point was observed to replace the ideal bifurcation behavior for $[0/0/0/90]_T$ and $[0/0/90/0]_T$ laminates. Jun and Hong [12] extended Hyer's model by including in-plane shear strain and found that although it is negligible at low and high length-to-thickness ratios, this effect cannot be neglected when the ratio is in the intermediate range or when the laminate is close to the bifurcation point.

To predict the bistable behavior of unsymmetric composite laminates with arbitrary layups, Dang and Tang [13] modified Hyer's model in [11] to be in terms of the principal curvature coordinate system, where transformation was used to obtain shapes in the structural coordinate system. This was based on the assumption that unsymmetric laminates will always have two perpendicular principal curvatures in a certain coordinate system. Jun and Hong [14] modified the displacement shape functions of this model so that unknown coefficients can be independently solved, which was not possible in [13]. Peeters et al. [15] further simplified but also restricted the scope the theory by using third order polynomials to approximate the displacement field, assuming that the

principal curvature angle was fixed to 45° relative to the edge for all laminates, and assuming that the in-plane strains in the principal curvature coordinate system were independent of orientation.

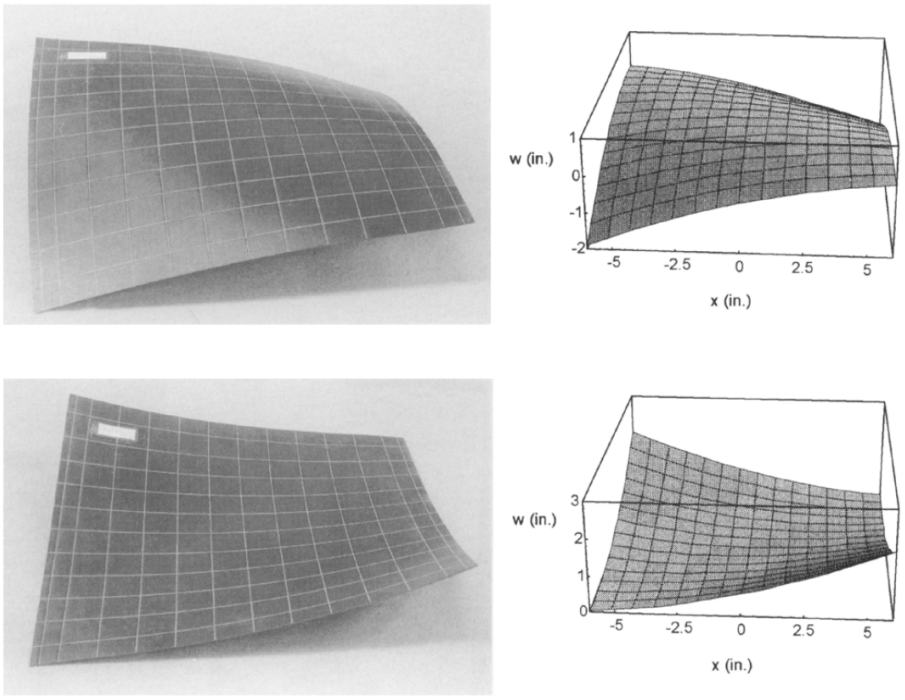

Figure 1.3: Model and experimental shapes of a bistable [-30_4/30_4]$_T$ graphite-epoxy laminate [16].

All theories up to this point used the same technique of approximating displacements with various polynomial shape functions. Dano and Hyer [16] observed that through nonlinear kinematic relations, this approach leads to unnecessarily complex strain fields, which are used to compute the total potential energy. Thus, direct approximations of the strain field were proposed with 14 unknown coefficients and the predicted stable shapes were well correlated with experimental data, as shown for one of the cases in Figure 1.3. The model curvatures had better agreement with Finite Element Analysis (FEA) compared to those of Jun and Hong [14], particularly around the bifurcation point. However, errors in the out-of-plane displacement grew towards the laminate edges and corners, which were attributed to the constant curvature approximation made in the shape functions

which failed to capture free edge effects. The directions of principal curvatures were also analyzed to show that the assumption made by Peeters et al. [15] was incorrect. Dano and Hyer's model in [16] is considered the state of the art for bistable composite laminates with arbitrary layups, and it has been the starting point for many variations, extensions, and applications for this type of structure.

1.1.2 Methods for Inducing Multistability

More recently, alternative methods to produce multistable shells and plates have been developed to mitigate known shortcomings, extend performance capabilities, or overcome design restrictions of traditional bistable composites. These techniques include utilizing elastic prestress [17–19], isotropic metal layers [20, 21], curvature effects [22–24], viscoelastic effects [25, 26], plastic deformation [27], discrete connections [28,29], and continuous connections [30–35]. Some of the cited works are shown in Figure 1.4. Daynes et al. [17,18] mechanically prestressed selected ply fibers with a clamp tool during the cure cycle of symmetric $[0/90/90/0]_T$ Carbon Fiber Reinforced Plastic (CFRP) and Glass Fiber Reinforced Plastic (GFRP) laminates, which resulted in two stable configurations once the prestress was released after cure. Advantages to this method over the traditional technique include the laminate being insensitive to hygro-thermal effects and the ability to tailor its stiffness for specific applications. For example, the two stable shapes retained the same major curvature direction as opposed to being orthogonal to each other, which is the case for unsymmetric cross-ply bistable composites. Chillara and Dapino [19] found that the curvatures of a bistable plate can be tuned by varying the level of mechanical prestress in elastomeric matrix composites and bonding them to a stress-free isotropic mid-layer.

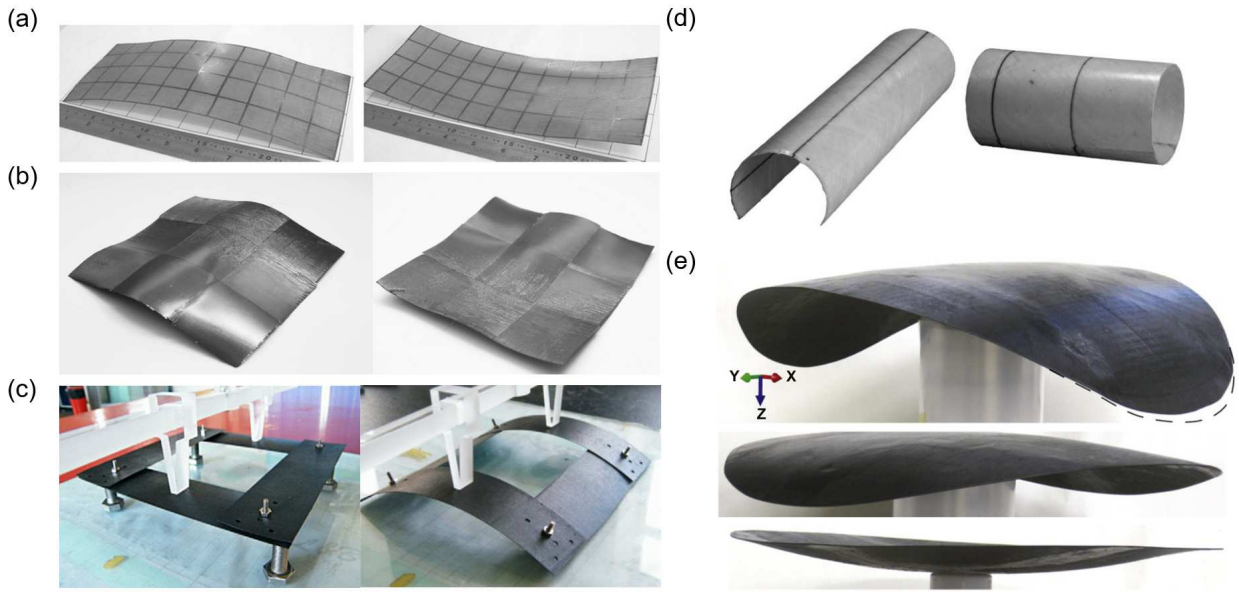

Figure 1.4: Generating multistable composite structures with (a) elastic prestress [17], (b) continuous connections [35], (c) discrete connections [28], and (d)-(e) initial curvature [22, 23].

Although mechanical prestress is a popular mechanism for yielding stiffness properties that are not possible with thermal residual stresses, many other approaches to inducing multistability have been investigated by varying passive materials, geometries, loads, or boundary conditions. Daynes and Weaver [20] included a metallic isotropic layer between CFRP plies to increase snap-through moments and out-of-plane displacements while Li et al. [21] set aluminum plies in a piecewise configuration within a symmetric composite laminate to generate stable major curvatures in the same direction as done in [18]. Coburn et al. [23] tailored the material properties and Gaussian curvatures of doubly curved orthotropic shells to achieve tristability while Eckstein et al. [24] showed that cross-ply laminates with initial curvature exhibit multistability under thermal loading. Guest and Pellegrino demonstrated that thin cylindrically curved shells with high aspect ratios are inherently bistable when made from fiber-reinforced composites in antisymmetric layups [22]. These structures have a strain-free extended configuration with a curved cross-section and

exhibit a second stable coiled configuration that is highly strained but energy minimized. Pseudo-bistability was shown by Brinkmeyer et al. [25] with a viscoelastic spherical dome that, once actuated, automatically reverts to its original state, while Wang and Fancey [26] produced a bistable structure by bonding viscoelastically prestressed composite strips to the edges of a fiberglass sheet. Kebadze et al. [27] plastically deformed isotropic cylindrical shells similar to a steel tape measure to generate residual stresses required for bistability.

With the cited literature only focusing on a single bistable element, researchers have also explored combining two or more composite laminates to either create more complex geometries or increase the number of stable configurations for morphing applications. Mattioni et al. [30,31] connected a symmetric monostable laminate to a unsymmetric bistable laminate and extended Dano and Hyer's model [36] by incorporating matching conditions and utilizing higher order displacement functions for accurate shape predictions. Arrieta et al. [32] and Kuder et al. [33] were able to retain bistability when connecting two monostable composite laminates to the opposing edges of a bistable plate by embedding variable stiffness elements with shared plies between different regions. To generate more than two stable states, Dai et al. [28, 29] fabricated tristable composite lattices which possess a plane, concave, and convex shape by discretely joining four rectangular bistable laminates with bolts at each corner. Lachenal et al. [37] joined two pre-stressed composite flanges with multiple spokes to yield a stable extended state and a twisted state. With the objective of forming a continuously connected structure, Cui and Santer [34] developed a quadstable plate by linking two unsymmetric bistable laminates with $[0/0]_T$ composite strips. They then extended this concept by connecting nine square composite elements to form a highly multistable tessellated laminate [35].

1.1.3 Morphing Applications

The out-of-plane deformations in composite laminates are generally unintentional and countered with the addition of extra plies to achieve symmetric layups, which reduce the global effect of residual stresses. More recently these characteristics have been tailored for a range of adaptive structures, particularly for morphing aerospace structures. There have been a wide variety of techniques to generate multistable composites and researchers have employed some of them for conceptual designs or applied analysis and testing, as shown in Figure 1.5. Some works have even characterized structural response while operating in different configurations under dynamic loading environments.

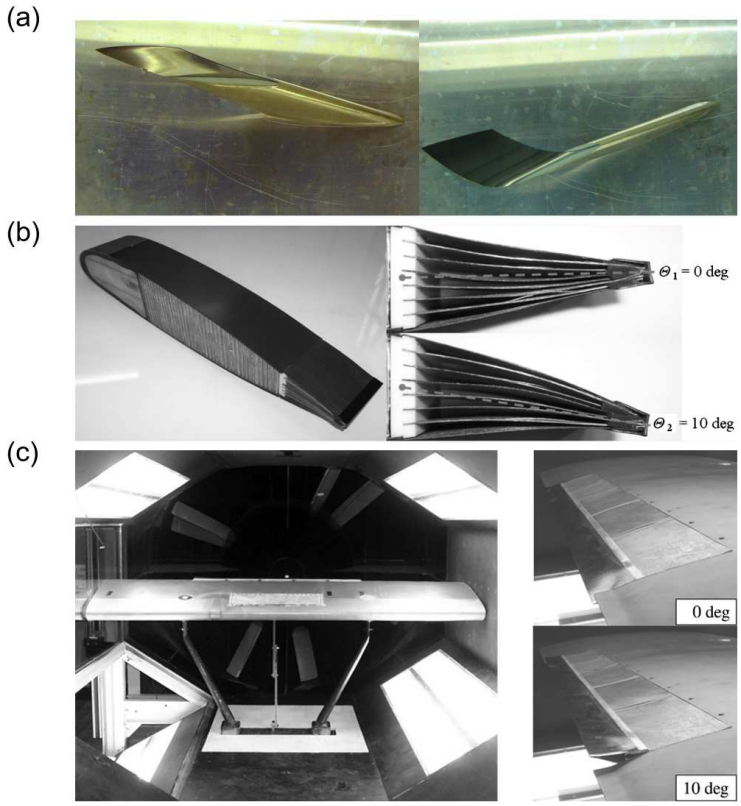

Figure 1.5: Bistable composites integrated as morphing (a) winglet [38] (b) trailing edge section [39], and (c) rotor blade flap in wind tunnel testing [40].

Early examples involved prototypes of bistable composites incorporated into a variable swept wing as spars in a hinge mechanism, a winglet structure, and a variable camber trailing edge [38]. Most subsequent applications have focused on the trailing edge of airfoil sections. Diaconu et al. [41] conducted a theoretical investigation into the necessary geometries and layups of bistable composites to be utilized for trailing edge morphing. Daynes et al. [39] directly integrated multiple prestressed bistable composite laminates from [18] in a stacked arrangement to form a bistable flap of a helicopter rotor blade section. In a following work, they demonstrated that the bistable flap was operational and able to withstand aerodynamic loading when paired with an electromechanical actuator under wind tunnel testing [40]. Apart from wing designs, prestressed bistable composites have also been used as a morphing air inlet, which can be in an open or closed state without any additional energy input [42]. In contrast to most multistable morphing applications where the composites directly cause shape change, Kuder et. al [43] internally placed multiple bistable elements in an airfoil section to allow multiple stiffness configurations for adapting to various flight conditions. Structural and aeroelastic responses to external loading were numerically and experimentally evaluated to demonstrate feasibility of the concept [44].

1.1.4 Snap-through Actuation

To be effective as adaptive structures, multistable composites require a mechanism for actuation to achieve snap-through between their stable states. This capability to quickly and efficiently transition between shapes is critical in morphing applications where full configuration control is required. There have been numerous theoretical and experimental works in this area that can be classified as either mechanical or smart actuation. Early works with the former method investigated

how external static forces can be applied in various in-plane and off-axis directions to initiate snap-through [36, 45, 46]. However, there are practical limitations to implementing them in morphing structures because of external equipment being required to provide the necessary mechanical force.

Smart materials can be actuators capable of delivering strain or displacement to the host structure and alter its mechanical state [47]. Actuation with these materials is the preferred method due to their commercial availability, ease of integration into composite laminates, exploitation of electromechanical or thermomechanical coupling, and high performance with low size and weight penalties. The most commonly used smart material for the actuation effect is piezoelectric, where an applied electric field will strain the material. For example, Lead Zirconate Titanate (PZT) is a ceramic material widely used as monolithic patch actuators, but new piezoelectric technologies have been developed to extend the actuation performance such as THUNDER [48], RAINBOW [49], and Active Fiber Composites [50]. For bistable composites however, an orthotropic piezocomposite actuator called the Macro Fiber Composite (MFC) has been the most popular candidate to provide the necessary shape control and it was first developed by NASA Langley Research Center [51]. As shown in Figure 1.6, MFCs consist of unidirectional piezoceramic fibers embedded in an epoxy matrix and placed between two polyimide films with an Interdigitated Electrode (IDE) pattern that are used for poling, sensing, and actuation. The poling direction is aligned with the fiber direction and the electric field is applied parallel to the poling direction to generate maximum strain per unit electric field. The actuation strain is then generated via the d_{11} piezoelectric coefficient associated with elongation, which is typically twice the magnitude of the transverse d_{12} coefficient. Their higher energy density, actuation authority, and flexibility allow them to be the most appropriately designed for morphing purposes, especially when compared to monolithic piezoelectric actuators.

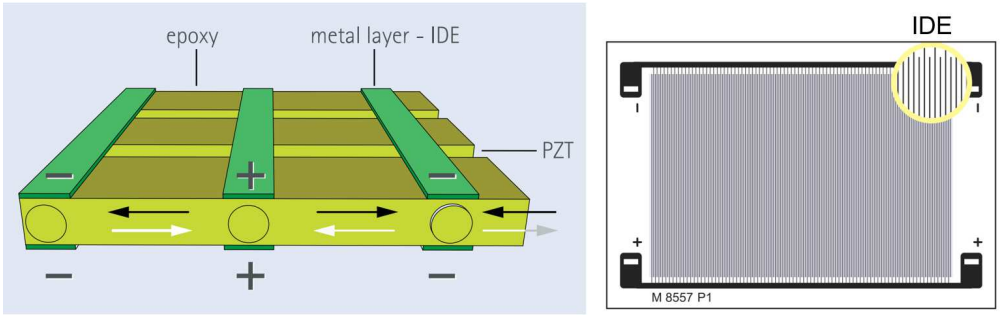

Figure 1.6: P1 type Macro Fiber Composite actuator utilizing the d_{11} piezoelectric effect [52].

Giddings et al. [53] experimentally characterized the blocking force, free displacement, and load-displacement characteristics of a bistable composite laminate with a MFC bonded to its upper surface, and demonstrated snap-through from its initial to final stable states. With similar setups, Bowen et al. [54] experimentally showed that reverse snap-through back to the initial stable state could only be achieved with the aid of mechanical loads. Portela et al. [55] noted the difficulty of initiating reversible actuation with a single MFC due to improper alignment of the piezoceramic fibers relative to the major curvature direction of the second stable state, which negates the MFC's actuation authority. Analytical modelling of actuating cross-ply bistable laminates with MFCs was first done by Schultz and Hyer [56], where strain energy contributions were modelled as separate steps between the host structure, actuator, and its application of an electric field. Ren [57] then extended the modelling approach of Dano and Hyer [16] to include the effect of piezoelectric loads on composite laminates with arbitrary layups. Gude et al. [58], Bowen et al. [59], and Giddings et al. [60] demonstrated close correlation between analytical, FEA, and experimental results when inducing snap-through of a cross-ply bistable laminate with a single MFC.

To achieve reversible snap-through actuation, a variety of techniques have been proposed to mitigate the lack of actuation authority required for overcoming the laminate stiffness when it is

in either stable states. Schultz et al. [61] was the first to consider attaching two MFCs in orthogonal directions on opposite surfaces of a bistable composite laminate. This layup enabled quasi-static reversible snap-through actuation to be possible for a cross-ply laminate, but the voltages required to induce the state change were much greater than what was analytically predicted, and far beyond the operating limitations of the MFCs. By combining piezoelectric and Shape Memory Alloy (SMA) wire actuators, Kim et al. [62] experimentally showed that reversible state changes are possible for a $[0/0/90/90]_T$ cantilevered bistable composite laminate. SMA wires are a popular class of smart actuators which are able to induce much higher strains than piezoelectric materials through a temperature-induced phase change from martensite to austenite with joule heating. However, they are limited by slow response times and low bandwidths, where maximum operating frequencies are lower than 10 Hz compared to the order of 10 kHz for piezoelectric materials [63]. These create time constraints between snap-through events and prevent near-instantaneous configuration control made possible with piezoelectric actuation. Combined with the lack of fine control and difficulty of integration into existing models, SMA actuators have received considerably less interest for multistable structures.

Arrieta et al. [65] proposed a method of dynamically inducing snap-through with sinusoidal bursts of two MFCs at the resonant frequency of the bistable laminate. The laminate was cantilevered to create asymmetry between the stable shapes and their potential wells, which also separated the location of their first harmonic modes. This meant that snap-through back to the initial state was possible through harmonic excitation at the second state's resonant frequency while lowering the chance of divergence into snap-through oscillations. Bilgen et al. [64] utilized this actuation technique to demonstrate configuration control of a cantilevered bistable wing structure while under aerodynamic loading in a wind tunnel. Simsek and Bilgen [66] refined the method

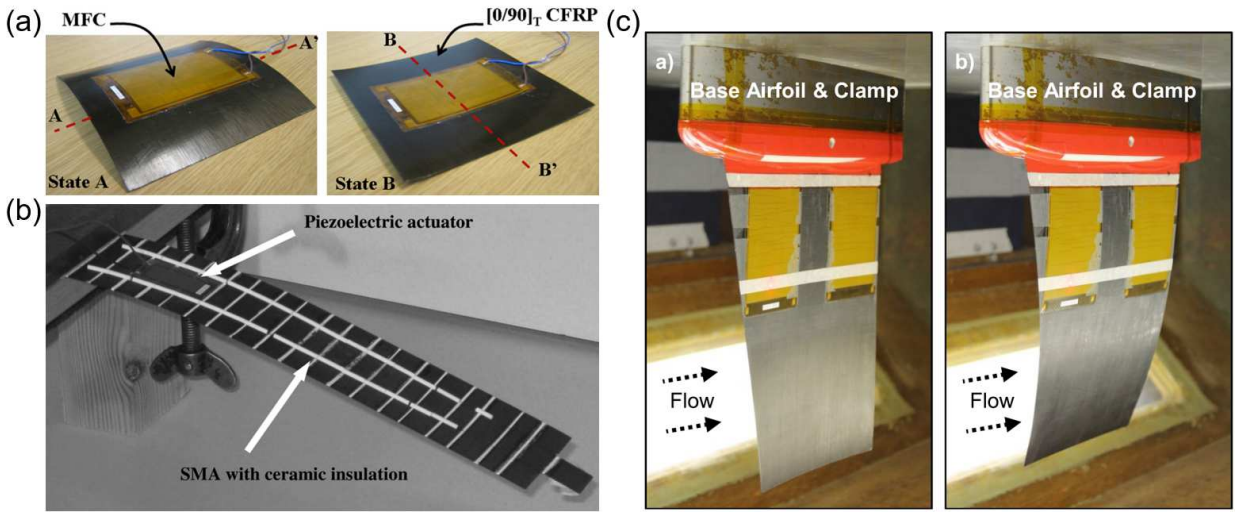

Figure 1.7: Initiating snap-through of bistable composites with (a) quasi-static actuation of a MFC [60], (b) combined actuation of SMA wires and a MFC [62], and (c) harmonic excitation of MFCs [64].

by utilizing a Positive Position Feedback (PPF) controller with a negative gain to destabilize the initial state to cause snap-through, then attenuate the resulting oscillations by switching the gain to a positive value. The purpose was to eliminate the possibility of triggering snap-through oscillations all together. However, dynamically induced snap-through requires asymmetric potential wells, and cannot be effectively used for bistable composites whose stable states have identical resonant frequencies.

1.1.5 Broadband Energy Harvesting

While the snap-through event between the stable shapes of bistable composite laminates has been a favored mechanism for morphing, this nonlinear phenomenon has also been exploited for high performance energy harvesting applications. These structures are able to retain efficiency when ambient vibrational energy is distributed over a wide spectrum, and where the spectral density is variable over time and dominant at low frequencies [4]. In contrast, linear harvesters are

suited only for stationary and narrowband excitation at their fundamental resonant frequencies which limit their usefulness in more realistic environments. Depending on the excitation frequency and amplitude, bistable structures exhibit multiple dynamic regimes that are distinct. This includes single-well vibrations around either of the stable configurations, or cross-well vibrations causing either periodic or aperiodic snap-through between both stable equilibria. In certain cases, multiple solutions may coexist under the same input, but only one is physically realizable depending on the initial conditions. Cross-well regimes such as high amplitude limit cycle oscillations have shown to significantly improve power generation over linear resonance as the harvesters displace between states under high velocities [67]. The appeal to bistable harvesters derive from being able to trigger cross-well vibrations associated with large deformations across a wide range of excitation conditions, which alleviate the performance limitations experienced by their linear counterparts.

Various mechanisms to induce bistability for the purpose of broadband energy harvesting have been explored in past investigations. As shown in Figure 1.8, popular concepts include obtaining bistability in a cantilevered ferromagnetic beam with magnetic attraction [68, 69], destabilizing a cantilevered beam with a magnetic tip mass from its neutral position with a facing magnet of the same polarity through repulsion [70, 71], buckling a clamped-clamped beam with an axial load to obtain a mechanically induced bistable structure [72, 73], and generating internal thermal stresses within a unsymmetric composite laminate during cure cycle cooldown which result in two stable configurations. As for the energy harvesting method, piezoelectric materials are attached to bistable structures to convert vibration induced strains to electrical energy due to their large power densities, ease of fabrication and application over other methods such as electrostatic, electromagnetic, and magnetostrictive transduction. Bistable composite laminates bonded with piezoelectric transducers are particularly attractive due to retaining two stable equilibrium states without any

external influence from clamps or magnets as required by isotropic beams.

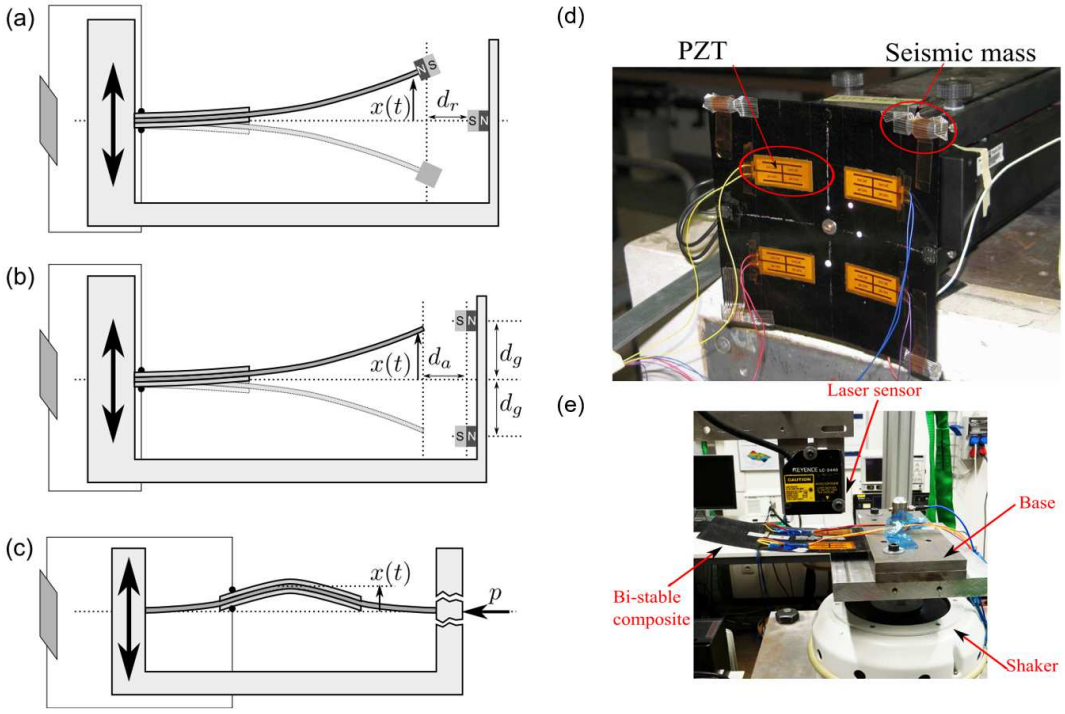

Figure 1.8: Piezoelectric energy harvesters as bistable beams [4] induced by (a) magnetic repulsion, (b) magnetic attraction, (c) axial loading, and bistable composite laminates with (d) fixed center [74], and (e) cantilevered boundary conditions [75].

Although there have been an extensive number of works investigating vibrational energy harvesting with bistable composite laminates, the majority of these efforts are experimental. Arrieta et. al [74] was the first to characterize the electromechanical response under cross-well oscillations and demonstrate the broadband energy harvesting capability of a center fixed bistable laminate plate made from CFRP with an asymmetric cross-ply layup attached to four piezoelectric elements. A subsequent work studied a rectangular cantilevered configuration of the bistable harvester, which increased its effectiveness in generating power due to the larger strains near the clamped end where the piezoelectric transducers were bonded [75]. These have been followed by other experimental studies utilizing the nonlinear response of bistable composite laminates under

various implementations for piezoelectric energy harvesting [76–85].

Modelling efforts have mostly focused on the uncoupled mechanical portion to the nonlinear dynamics associated with bistable composite plates. Diaconu et. al [86] derived a simple analytical model utilizing Hamilton's principle with the Rayleigh-Ritz method to predict the time dependent response of bistable plates during snap-through, though the snap-through load was overpredicted when compared to the FEA. This model was a dynamic extension of the popular static model proposed by Dano and Hyer [16], which used second and third order polynomials for the assumed shape functions and accounted for twist relevant in non-cross-ply layups. Arrieta et. al [87] experimentally characterized the nonlinear single-well dynamics of a bistable plate, and a modal approach based on the test data yielded a model predicting the experimental subharmonic behavior at two points on the plate. The model was then extended by including higher order piecewise restoring forces in the modal equations to account for cross-well dynamics, and provided the overall nonlinear responses of the plate [88]. A reduced order model was derived to predict the nonlinear response about a stable state with the Galerkin approach by projecting the nonlinear solutions onto the linearized mode shapes, then retaining only the nonlinear terms in the modal equations [89]. As with the previous two studies, the values of the nonlinear terms had to first be experimentally found. Vogl and Hyer [90] utilized Hamilton's principle with the Rayleigh Ritz approach to derive a linearized dynamic model and was able to predict the first vibration modes about each equilibrium point when compared to finite element analysis. Firouzian-Nejad et. al [91] used fourth and fifth order shape functions to more accurately predict the natural frequencies and dynamic response to ramp and harmonic forces applied on the corners of a bistable plate. Most recently, Wu et. al [92] proposed the use of a sixth order polynomial for the out-of-plane displacement function with Hamilton's principle to derive a nonlinear model describing the response over the entire range

of cross-ply bistable plates. A range of different cross-well behavior observed in the finite element analysis and experimental data were predicted by the model.

While modelling the nonlinear dynamics of bistable composite laminates has been the focus of many researchers, the number focused on predicting the electromechanically coupled response of bistable plates with piezoelectric transducers is limited, and especially more so when compared to the number of experimental works. Betts et. al [93] optimized the geometry of a bistable plate and layout of piezoelectric patches to maximize the power output during snap-through based on a simple static model. Arrieta et. al [94, 95] derived an electromechanically coupled model using Lagrange's equations of a cantilevered bistable plate with piezoelectric actuators and found fairly accurate closed and open circuit natural frequencies for each stable state against experimental data. Taki et. al [96] derived a nonlinear model with higher order shape functions to obtain the time dependent response of a cross-ply bistable plate when excited by piezoelectric layers and found good correlation with finite element analysis. However, there are limitations in the available literature implementing models to accurately yield voltage and power outputs from cross-well oscillations in broadband energy harvesting. With many experimental studies having no modelling basis for their harvester designs, a validated model can serve as a valuable design tool that maximizes the performance of these harvesters.

1.1.6 Control of Dynamic Response

The rich assortment of nonlinear behaviors that bistable composite laminates exhibit to vibrational excitation have almost entirely been applied towards broadband energy harvesting. Recently however, there has been a shift from simply characterizing the input to output efficiency and per-

formance of a nonlinear Vibration Energy Harvester (VEH) to actively manipulating its dynamic response [97]. Various implementations of nonlinear VEHs have included single-well [98, 99], double-well [69, 100], and triple-well [101, 102] systems associated with their potential energy functions. These were modelled with Duffing type equations which describe the behaviors of monostable, bistable, and tristable oscillators, respectively. The high amplitude cross-well oscillations of multistable VEHs enable greater power generation over monostable structures confined within a single potential well [72, 103]. Due to nonlinear dynamical phenomena such as multistability and hysteresis, frequency responses can branch into any of the co-existing stable steady state solutions which may include both low and high energy outputs. Which steady state solution a nonlinear VEH selects is driven by the excitation parameters and initial conditions. In such systems exhibiting the co-existence of multiple stable attractors, attaining the desired steady state is critical for maintaining high energy transduction. Simultaneously, these same attractors' sensitivity to perturbations vary considerably and forces control to be difficult. With varying excitation frequencies and amplitudes under real-world environments, efficient and reliable control mechanisms are necessary for maintaining high energy orbits to facilitate maximum energy conversion.

Different strategies for perturbing nonlinear VEHs from low energy to co-existing high energy orbits have been proposed to address this challenge. Zhou et al. [104] imparted external mechanical shocks to magnetically induced bistable and tristable VEHs to achieve cross-well orbits. Piezoelectric actuators or electrical circuits were coupled with oscillators to apply harmonic bursts [99, 105] and voltage impulses [106] to induce jumps into high energy solutions, but the success of these methods were shown to be probabilistic and dependent on the electrical signal's phase and amplitude. Udani et al. [107] proposed a perturbation method that characterizes and then selects co-existing high energy attractors by introducing a phase shift in the forcing signal

through a piezoelectric actuation of a bistable composite laminate. Masuda et al. [108] utilized self-excited vibrations induced by a load resistance switching circuit to destabilize low energy oscillations and drive the electromagnetic VEH to jump into high energy orbits. While these methods were considered for isolated frequencies or narrow bandwidths, how these external perturbations can be applied to extend nominal cross-well bandwidths of bistable VEHs have been sparsely investigated. Under frequency sweeps with no external influence, cross-well bandwidths narrow with decreasing forcing amplitudes until disappearing at a critical excitation level. Disturbances are required for bistable VEHs to maintain their desirable broadband cross-well response in low amplitude conditions since they will likely remain in single-well orbits according to their basins of attraction. If stable high energy orbits can be accessed and maintained in multi-solution regions, nonlinear VEHs have been shown to exhibit wider corresponding bandwidths [109]. Huguet et. al [110] recently demonstrated this with an electromagnetic VEH in the form of a bistable buckled beam by placing it into co-existing subharmonic orbits through pulse disturbances.

Apart from extending the range of input parameters that cause cross-well oscillations, suppressing these same vibrations becomes important when snap-through instabilities are undesirable. Energy harvesting and morphing have conflicting requirements regarding how nonlinear dynamics are exploited. For efficient conversion to electrical energy, bistable VEHs seek to maximize cross-well amplitudes under low external forcing levels and large bandwidths which trigger these responses. These same excitations are undesirable for bistable morphing structures since complete control over their stable configurations is required. To ensure this condition, vibration control is needed to suppress cross-well oscillations that arise from a wide array of dynamic environments. Passive approaches have been implemented by incorporating dampers parallel to bistable elements in a structural system [5] or negative stiffness inclusions within a host material matrix [111] to

achieve large dissipation of energy upon activation of cross-well dynamics. These dynamics have also served as mechanisms for vibration absorption through bistable attachments supplying an opposing force to cause destructive interference onto the host structure under harmonic excitation [6]. However, to escape the high energy orbits of cross-well oscillations, active approaches comprised of feedback or feedforward controllers are needed as they can destabilize these orbits and place the structure into the desired state, while being able to adapt to environmental variations and uncertainties. The only implementation of active control in bistable structures have been for dynamically initiating snap-through between stable states and controlling the resulting transient vibrations with a position or velocity feedback controller [66, 112]. As outlined before, techniques for switching between co-existent steady state solutions could be applied to jump into single-well oscillations. However, they are limited to hysteretic regions and do not utilize active control laws required for vibration attenuation where solutions do not co-exist.

1.2 Motivation and Scope

As outlined in Sections 1.1.3 - 1.1.6, research into leveraging bistable composites as adaptive structures can be categorized into three general applications with complementary areas of focus. These are shape changes with quasi-static snap-through morphing, broadband energy harvesting from nonlinear vibrations, and the control of dynamic responses through the suppression or extension of cross-well oscillations. All three applications are most commonly enabled by piezoelectric transducers due to their effectiveness under dynamic environments and these smart materials are often externally paired with host bistable structures. The snap-through phenomenon serves as the basis for morphing and energy harvesting while configuration control is the shared objective

between morphing and vibration suppression. The nonlinear dynamical behaviors of bistable structures dictate the strategies used for effective energy harvesting and control of vibrational responses.

Outstanding challenges still remain for each research application of bistable composite structures. For quasi-static morphing, piezoelectric actuators lack the authority to trigger reversible snap-through from either stable states because of not being able to overcome the host laminate stiffness. A variety of techniques have been implemented to overcome this problem which have included bimorph configurations exceeding actuator limits [61], mechanical assistance with external loads [54], dynamic assistance with induced resonance [65], and supplementation with SMA actuators [62]. However, each of these techniques have operational restrictions, performance limitations, or requirements for complex setups, and achieving reversible snap-through while mitigating such factors is still an open research problem. For bistable composite VEHs, a design conflict exists where larger piezoelectric patches could generate more energy, but reduce the curvature of host structures. This effect limits their response amplitudes and strains along the transducer's polarization direction. In addition, the increased stiffness from larger piezoelectric layers raise the vibrational energy requirement for cross-well dynamics. To mitigate this issue, Betts et al. [93] determined optimal layups, aspect ratios, and piezoelectric areas for a bistable composite VEH, but resolving the conflict remains as a design objective. Another open challenge in broadband energy harvesting is to accurately predict the electromechanical response of bistable composite VEHs due to a gap in the available literature for experimentally validated models. With nearly all works being experimental, a validated model has the potential to yield numerically optimized VEH designs. In dynamic response control, no approaches have yet been proposed for suppressing cross-well oscillations or extending the cross-well bandwidths of bistable composite laminates.

The dissertation aims to develop an active bistable composite structure capable of addressing

the design and performance challenges outlined above. As discussed in Section 1.1.2, there have been numerous techniques for generating multistability, but these have all utilized passive materials which are incapable of providing structural control post fabrication. With the division of roles between the primary host structure and the smart transducer restricting performance in multistable applications, the current work's objective is to investigate how these roles can be combined through a novel method for inducing bistability with piezoelectric materials. Prototypes of bistable structures have always been catered to be effective at a single application which is functionally inflexible and costly. This is due to the difficulty of combining capabilities because of conflicting load environments and stability requirements. However, incorporating the active element in piezoelectric bistable composites as the mechanism for inducing bistability yields design efficiencies which allow for multiple functions. The capability to actively alter geometry and stability characteristics allow both static and dynamic responses to be manipulated for the purpose of adapting to various operating environments.

1.3 Proposed Concept

When two actuated MFCs are bonded together in an unsymmetric layup, releasing the voltage post cure will produce in-plane residual stresses that result in two stable configurations that are geometrically distinct [113]. This is due to the MFC's anisotropic strain response to an applied electric field from the mismatch of its effective piezoelectric constants. The mechanics are analogous to how bistable composite laminates are conventionally manufactured through the mismatch of CTEs between plies. By letting the MFCs be both the actuator and primary structure, the challenges of initiating reversible snap-through in an unassisted manner between both stable states can

be alleviated [114]. The energy input requirement for snap-through is much lower than previously explored designs and complex setups are not required. Due to retaining sufficient actuation authority, the MFCs has the capability to either impart large perturbations or be effective at active control implementations for the purpose of controlling the nonlinear dynamic response. As an entirely piezoelectric VEH, the design conflict between the smart transducer and the host composite is avoided since it lacks the stiffness of the latter component while retaining the curvatures generated by the MFCs. Its lower stiffness implies that the vibrational energies required for maintaining high energy orbits and broadening cross-well bandwidths are lower than those of conventional bistable composites, and does not require proof masses utilized by many of these harvesters to inertially aid snap-through [115].

1.4 Dissertation Outline

The dissertation consists of six chapters. The first chapter provides an introduction to the concept of multistability and how this nonlinear phenomenon is leveraged in adaptive structures. The background and literature review of multistable composites outline how they are manufactured, integrated into morphing structures, actuated with smart materials, and used in energy harvesting and vibration control. Open research problems are identified from the literature review and the dissertation objectives are then formulated through the proposed piezoelectrically generated bistable laminate. Chapter 2 presents its static and dynamic electromechanical model, where the generalized nonlinear equilibrium equations and coupled equations of motion are derived. The bistable laminate's parametric design analysis, manufacturing procedure, static profiles, bifurcation behavior, and snap-through morphing capability are covered in Chapter 3. Chapter 4 experimentally

correlates the model simulations of the electromechanical response to nonlinear vibrations and the broadband energy harvesting performance of the bistable laminate is then evaluated. Chapter 5 proposes a strategy to suppress cross-well oscillations by combining active control with static actuation, and numerically and experimentally demonstrates it. It then extends the cross-well frequency bandwidth of the bistable laminate with voltage perturbations to enlarge the range of excitation parameters where energy harvesting effectiveness can be maintained. Finally, Chapter 6 summarizes the dissertation results and their main research contributions. It is closed out with recommendations for future work and a list of relevant publications.

CHAPTER 2

Electromechanically Coupled Model

During the cure cycle, a rectangular composite laminate with an unsymmetric stacking sequence experiences thermal residual stresses between its plies that results in curved deformation. With a sufficiently high enough edge length to thickness ratio, the thermal warping can lead to a two stable states where each configuration holds its shape with no external influence. Decades of research have yielded variations of the Rayleigh-Ritz approximation approach to predict the room temperature geometries, stability properties, and the dynamics of these composite laminates. With the more recent development of piezocomposite actuators, these analytical models have been expanded to account for the quasi-static shape changes made possible when the actuators are bonded to the bistable composites. In this chapter, past works are extended to derive the electromechanically coupled equilibrium equations and equations of motion which describe the stable shapes and nonlinear dynamical behaviors of a bistable laminate generated with piezoelectric actuation, where the entire structure is composed of active material. The aim is to accurately predict its snap-through actuation, broadband energy harvesting, and active control capabilities through numerical simulations of the governing equations.

Since the mismatch of CTEs in conventional bistable composites operates under the same principle as the mismatch of piezoelectric coefficients between MFCs, the kinematic relationships and

the assumed shape functions for the former can be applied to the latter. This is given that each MFC is modelled as an individual orthotropic ply through CLT. The static model for rectangular bistable composites with arbitrary layups and free edge boundary conditions is based on the work by Dano and Hyer [36]. The derivation begins with the nonlinear kinematic extension of CLT with Rayleigh-Ritz approximations of the mid-plane strain functions and non-zero in-plane shear strain associated with spatially constant curvatures. Higher order displacement functions are also considered to allow for variable curvatures which result in lower geometrical errors. The minimization of total potential energy is implemented to obtain the equilibrium equations which are then numerically solved to compute the strain field, displacement field, and curvatures. The thermal strains generated by temperature change in the cure cycle of conventional composite plates are replaced with the piezoelectric strains caused by MFC voltage actuation in the potential energy. During the cure cycle for the adhesive, the laminate remains flat while the MFCs are kept at a specified bonding voltage. Voltage is removed post cure and the laminate then generates curvature and out-of-plane deflection. The static analytical model is also extended to include inertial and damping forces under dynamic excitation and electromechanical coupling for time dependent control. Using Lagrange's equations from an energy formulation, the nonlinear equations of motion are obtained.

2.1 Nonlinear Extension of Classical Lamination Theory

The origin of the laminate coordinate system is at its geometric center with x and y denoting the in-plane directions and z being the out-of-plane direction, as shown in Figure 2.1. L_x and L_y are the side lengths, h is the total thickness, and n is the total number of plies, with the ply order starting at the bottom layer. In this dissertation, variables enclosed in braces and square brackets

are vectors and matrices, respectively.

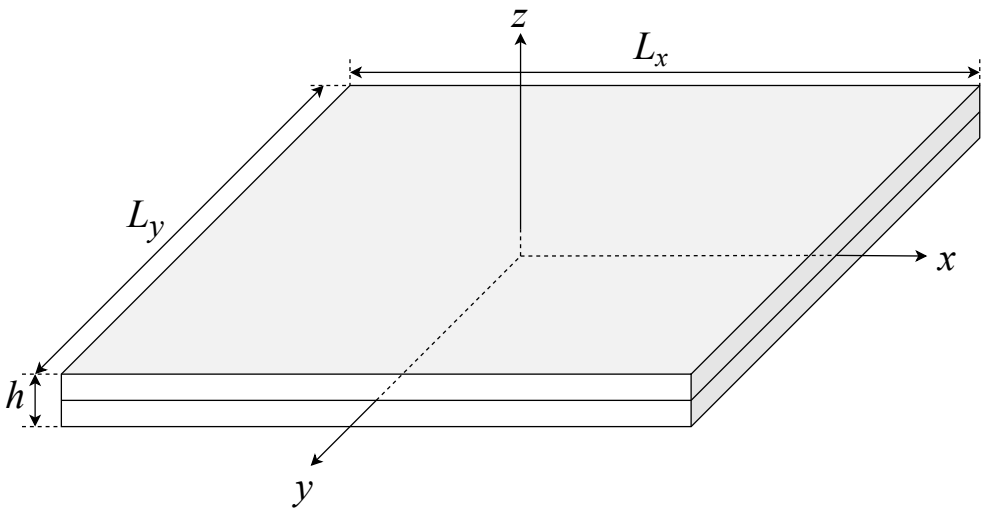

Figure 2.1: Definition of geometric parameters and laminate coordinate system.

2.1.1 Kinematic Equations

The general assumptions of CLT [9] are modified to include the nonlinear strain-displacement relationships from the von Karman plate theory [116], and these are listed below. u and v are defined as the in-plane displacements corresponding to the x and y axes, respectively, and w is the out-of-plane displacement.

1. The plate consists of orthotropic laminae with principal material axes arbitrarily oriented with respect to the $x - y$ plane.

2. The plate thickness is constant and much smaller than the lengths along the plate edges: $L_x \gg h$, $L_y \gg h$.

3. The von Karman nonlinearity is adopted in the strain-displacement relationships to include moderate rotations of the middle surface.

4. The out-of-plane displacement w is of a similar order as the thickness h.

5. The in-plane strains are small: $\epsilon_x \ll 1$, $\epsilon_y \ll 1$, $\gamma_{xy} \ll 1$.

6. Transverse shear strains γ_{xz} and γ_{yz} are negligible.

7. Transverse shear stresses τ_{xz} and τ_{yz} vanish on the plate surfaces.

8. In-plane displacements u and v are linear functions of the z coordinate.

9. Transverse normal strain ϵ_z and normal stress σ_z are negligible.

10. Each ply is linearly elastic.

Assumptions 6 and 9 are the result of assuming that each orthotropic ply is under a state of plane stress and assumptions 6 and 8 define the Kirchhoff hypothesis which states that normals to the middle surface remain straight and normal during deformation. The nonlinear effects that arise from the large out-of-plane displacement experienced by the laminate's mid-plane as it undergoes stretching are accounted for in assumptions 3 and 4. Under assumptions 8 and 9, the in-plane displacements vary linearly through the plate thickness, whereas the out-of-plane displacement remains constant as shown below.

$$u(x, y, z) = u^o(x, y) - z\frac{\partial w^o}{\partial x} \tag{2.1a}$$

$$v(x, y, z) = v^o(x, y) - z\frac{\partial w^o}{\partial y} \tag{2.1b}$$

$$w(x, y, z) = w^o(x, y) \tag{2.1c}$$

u^o, v^o, and w^o are the mid-plane displacements in the x, y, and z directions, respectively. The

general strain-displacement relationships with von Karman nonlinearity are given below.

$$\epsilon_x = \frac{\partial u}{\partial x} + \frac{1}{2}\left(\frac{\partial w}{\partial x}\right)^2 \tag{2.2a}$$

$$\epsilon_y = \frac{\partial v}{\partial y} + \frac{1}{2}\left(\frac{\partial w}{\partial y}\right)^2 \tag{2.2b}$$

$$\gamma_{xy} = \frac{\partial u}{\partial y} + \frac{\partial v}{\partial x} + \frac{\partial w}{\partial x}\frac{\partial w}{\partial y} \tag{2.2c}$$

Higher order theories keep more terms in the strain definitions which covers a broader range of nonlinear interactions, such as curvature and rotatory effects. However, more terms equate to more complex analysis and their effects are negligible for obtaining accurate shape predictions. Substituting Equations 2.1a-2.1c into Equations 2.2a-2.2c yields

$$\epsilon_x = \frac{\partial u^o}{\partial x} - z\frac{\partial w^o}{\partial x} + \frac{1}{2}\left(\frac{\partial w^o}{\partial x}\right)^2 \tag{2.3a}$$

$$\epsilon_y = \frac{\partial v^o}{\partial y} - z\frac{\partial w^o}{\partial y} + \frac{1}{2}\left(\frac{\partial w^o}{\partial y}\right)^2 \tag{2.3b}$$

$$\gamma_{xy} = \frac{\partial u^o}{\partial y} - z\frac{\partial w^o}{\partial x} + \frac{\partial v^o}{\partial x} - z\frac{\partial w^o}{\partial y} + \frac{\partial w^o}{\partial x}\frac{\partial w^o}{\partial y} \tag{2.3c}$$

By rewriting the above equations in terms of mid-plane strains ϵ^o and curvatures κ^o, the total strains can be expressed as

$$\epsilon_x = \epsilon_x^o + z\kappa_x^o \tag{2.4a}$$

$$\epsilon_y = \epsilon_y^o + z\kappa_y^o \tag{2.4b}$$

$$\gamma_{xy} = \gamma_{xy}^o + z\kappa_{xy}^o \tag{2.4c}$$

Therefore, the mid-plane strain and curvatures can be defined as below. Note that κ_x^o and κ_y^o are bending curvatures associated with the bending of the middle surface in the $x-z$ and $y-z$ planes, respectively. κ_{xy}^o is the twist curvature associated with the out-of-plane twisting of the middle surface, which lies in the $x-y$ plane before deformation.

$$\epsilon_x^o = \frac{\partial u^o}{\partial x} + \frac{1}{2}\left(\frac{\partial w^o}{\partial x}\right)^2 \tag{2.5a}$$

$$\epsilon_y^o = \frac{\partial v^o}{\partial y} + \frac{1}{2}\left(\frac{\partial w^o}{\partial y}\right)^2 \tag{2.5b}$$

$$\gamma_{xy}^o = \frac{\partial u^o}{\partial y} + \frac{\partial v^o}{\partial x} + \frac{\partial w^o}{\partial x}\frac{\partial w^o}{\partial y} \tag{2.5c}$$

$$\kappa_x^o = -\frac{\partial^2 w^o}{\partial x^2} \tag{2.5d}$$

$$\kappa_y^o = -\frac{\partial^2 w^o}{\partial y^2} \tag{2.5e}$$

$$\kappa_{xy}^o = -2\frac{\partial^2 w^o}{\partial x \partial y} \tag{2.5f}$$

2.1.2 Constitutive Relations

For a specially orthotropic lamina under the state of plane stress, the stress-strain relationships with respect to the material axes (1,2) are shown below

$$\begin{Bmatrix} \sigma_1 \\ \sigma_2 \\ \tau_{12} \end{Bmatrix} = \begin{bmatrix} Q_{11} & Q_{12} & 0 \\ Q_{12} & Q_{22} & 0 \\ 0 & 0 & Q_{66} \end{bmatrix} \begin{Bmatrix} \epsilon_1 \\ \epsilon_2 \\ \gamma_{12} \end{Bmatrix} \tag{2.6}$$

where 1 and 2 are the longitudinal and transverse directions. The elements in the reduced stiffness matrix $[Q]$ are functions of the lamina's longitudinal E_1 and transverse E_2 modulus of elasticity,

shear modulus G_{12}, and major ν_{12} and minor ν_{21} Poisson's ratio. The corresponding definitions are given as

$$Q_{11} = \frac{E_1}{1 - \nu_{12}\nu_{21}} \tag{2.7a}$$

$$Q_{22} = \frac{E_2}{1 - \nu_{12}\nu_{21}} \tag{2.7b}$$

$$Q_{12} = \frac{\nu_{12}E_2}{1 - \nu_{12}\nu_{21}} \tag{2.7c}$$

$$Q_{66} = G_{12} \tag{2.7d}$$

The transformation matrix $[T]$ is given as

$$[T] = \begin{bmatrix} \cos^2\theta & \sin^2\theta & -2\cos\theta\sin\theta \\ \sin^2\theta & \cos^2\theta & 2\cos\theta\sin\theta \\ \cos\theta\sin\theta & -\cos\theta\sin\theta & \cos^2\theta - \sin^2\theta \end{bmatrix} \tag{2.8}$$

where applying it to Equation 2.6 results in the generally orthotropic stress-strain relationships of the kth lamina in the global laminate coordinate system as shown below.

$$\begin{Bmatrix} \sigma_x \\ \sigma_y \\ \tau_{xy} \end{Bmatrix}_k = \begin{bmatrix} \bar{Q}_{11} & \bar{Q}_{12} & \bar{Q}_{16} \\ \bar{Q}_{12} & \bar{Q}_{22} & \bar{Q}_{26} \\ \bar{Q}_{16} & \bar{Q}_{26} & \bar{Q}_{66} \end{bmatrix}_k \begin{Bmatrix} \epsilon_x \\ \epsilon_y \\ \gamma_{xy} \end{Bmatrix}_k \tag{2.9}$$

In Equation 2.9, $\left[\bar{Q}\right] = [T]\,[Q]\,[T]^T$ is the transformed reduced stiffness matrix and θ is the arbitrary angle relative to the lamina coordinate system.

For bistability to be induced by piezoelectric actuation through an applied voltage ΔV during

bonding, its effects are modelled as strains caused by an electric field in Equation 2.9 and the resulting constitutive relations are given below.

$$\begin{Bmatrix} \sigma_x \\ \sigma_y \\ \tau_{xy} \end{Bmatrix}_k = \begin{bmatrix} \bar{Q}_{11} & \bar{Q}_{12} & \bar{Q}_{16} \\ \bar{Q}_{12} & \bar{Q}_{22} & \bar{Q}_{26} \\ \bar{Q}_{16} & \bar{Q}_{26} & \bar{Q}_{66} \end{bmatrix}_k \begin{Bmatrix} \epsilon_x - d_x \frac{\Delta V}{\Delta x} \\ \epsilon_y - d_y \frac{\Delta V}{\Delta x} \\ \gamma_{xy} - d_{xy} \frac{\Delta V}{\Delta x} \end{Bmatrix}_k \tag{2.10}$$

Δx is the IDE spacing in each MFC and d_x, d_y, and d_{xy} are the in-plane effective piezoelectric constants defined in the laminate coordinate system, which are computed from the MFC's piezoelectric constants d_{11} and d_{12} through the relationship below.

$$\{d\}_k = \begin{Bmatrix} d_x \\ d_y \\ d_{xy} \end{Bmatrix}_k = \begin{Bmatrix} d_{11}\cos^2\theta + d_{12}\sin^2\theta \\ d_{11}\sin^2\theta + d_{12}\cos^2\theta \\ 2\cos\theta\sin\theta(d_{11} - d_{12}) \end{Bmatrix}_k \tag{2.11}$$

The 1, 2, and 3 directions correspond to the piezoceramic fiber, electrode, and out-of-plane directions in the lamina coordinate system of each P1 type MFC ply. Since the mechanics of how each MFC strains under actuation is analogous to how a passive fiber-reinforced lamina strains under thermal loading, the resultant stresses will be similar in form. This similarity is also described as the thermal analogy.

Equation 2.10 allows the stress at each ply to be calculated for any given fiber orientation and integrating it with respect to z yields the stress resultants, or the total forces $\{N\}$ and moments

$\{M\}$ per unit length as given below.

$$\begin{Bmatrix} N_x \\ N_y \\ N_{xy} \end{Bmatrix} = \int_{\frac{-h}{2}}^{\frac{h}{2}} \begin{Bmatrix} \sigma_x \\ \sigma_y \\ \tau_{xy} \end{Bmatrix} dz = \sum_{k=1}^{n} \int_{z_{k-1}}^{z_k} \left[\bar{Q}\right]_k \left(\{\epsilon\}_k - \frac{\Delta V}{\Delta x} \{d\}_k \right) dz \tag{2.12}$$

$$\begin{Bmatrix} M_x \\ M_y \\ M_{xy} \end{Bmatrix} = \int_{\frac{-h}{2}}^{\frac{h}{2}} \begin{Bmatrix} \sigma_x \\ \sigma_y \\ \tau_{xy} \end{Bmatrix} z dz = \sum_{k=1}^{n} \int_{z_{k-1}}^{z_k} \left[\bar{Q}\right]_k \left(\{\epsilon\}_k - \frac{\Delta V}{\Delta x} \{d\}_k \right) z dz \tag{2.13}$$

Assuming that the thickness and material properties of each lamina is constant through the ply, the integration over z can be reduced to a summation over the number of plies n. With Equation 2.10 substituted in, this simplification is also shown in Equations 2.12 and 2.13, where z_k and z_{k-1} are the distances from the middle surface to the outer and inner surfaces of the kth lamina, respectively.

In the analysis of composite laminate plates, the mid-plane strains and curvatures are related to the applied forces and moments per unit length by static equilibrium for convenience. This means Equations 2.4a-2.4c are inserted into Equations 2.12 and 2.13 and the stiffness and loading terms

are re-arranged such that the following constitutive equations can be defined.

$$\begin{Bmatrix} N_x \\ N_y \\ N_{xy} \\ M_x \\ M_y \\ M_{xy} \end{Bmatrix} = \begin{bmatrix} A_{11} & A_{12} & A_{16} & B_{11} & B_{12} & B_{16} \\ A_{12} & A_{22} & A_{26} & B_{12} & B_{22} & B_{26} \\ A_{16} & A_{26} & A_{66} & B_{16} & B_{26} & B_{66} \\ B_{11} & B_{12} & B_{16} & D_{11} & D_{12} & D_{16} \\ B_{12} & B_{22} & B_{26} & D_{12} & D_{22} & D_{26} \\ B_{16} & B_{26} & B_{66} & D_{16} & D_{26} & D_{66} \end{bmatrix} \begin{Bmatrix} \epsilon_x^o \\ \epsilon_y^o \\ \gamma_{xy}^o \\ \kappa_x^o \\ \kappa_y^o \\ \kappa_{xy}^o \end{Bmatrix} - \begin{Bmatrix} N_x^P \\ N_y^P \\ N_{xy}^P \\ M_x^P \\ M_y^P \\ M_{xy}^P \end{Bmatrix} \tag{2.14}$$

$[A]$, $[B]$, and $[D]$ are the extensional, coupling, and bending stiffness matrices, respectively, and are given as

$$[A] = \sum_{k=1}^{n} \left[\bar{Q}\right]_k (z_k - z_{k-1}) \tag{2.15a}$$

$$[B] = \frac{1}{2} \sum_{k=1}^{n} \left[\bar{Q}\right]_k \left(z_k^2 - z_{k-1}^2\right) \tag{2.15b}$$

$$[C] = \frac{1}{3} \sum_{k=1}^{n} \left[\bar{Q}\right]_k \left(z_k^3 - z_{k-1}^3\right) \tag{2.15c}$$

$\left\{N^P\right\}$ are the piezoelectric forces per unit length and $\left\{M^P\right\}$ are the piezoelectric moments per unit length due to MFC actuation as shown below.

$$\left\{N^P\right\} = \frac{1}{\Delta x} \sum_{k=1}^{n} \Delta V_k \left[\bar{Q}\right]_k \{d\}_k (z_k - z_{k-1}) \tag{2.16}$$

$$\left\{M^P\right\} = \frac{1}{2\Delta x} \sum_{k=1}^{n} \Delta V_k \left[\bar{Q}\right]_k \{d\}_k \left(z_k^2 - z_{k-1}^2\right) \tag{2.17}$$

2.2 Rayleigh-Ritz Approximations

With the kinematic and constitutive relations derived, admissible shape functions for the mid-plane strains and displacements are required to capture the equilibrium shapes of unsymmetric bistable laminates. This is due to the non-existence of closed-form solutions, and so approximations are obtained by numerically solving for unknown coefficients placed in each term by minimizing the total potential energy. In accordance with this requirement, polynomial shape functions for the displacement and strain fields are found to give good results relating to the multistable characteristics of the composite laminate. Hyer [7] originally found that the cylindrical out-of-plane deflections of thin unsymmetric composite laminates can be fitted into a polynomial through the least squares method. Due to the free edge boundary conditions, sinusoidal functions such as the classical double Fourier sine and cosine series cannot be utilized [9, 117]. The Rayleigh-Ritz method only requires satisfaction of the geometric boundary conditions, which is the fixed origin, and the natural boundary conditions at the free edges do not need to be satisfied. The original lower order polynomial functions by Dano and Hyer [36] are first presented, and then the order of the shape functions that model the mid-plane displacements are raised to allow spatial variation of curvatures within the domain for better accuracy.

2.2.1 Lower Order Functions

The extensional mid-plane strains are assumed to be the following set of second order polynomials.

$$\epsilon_x^o = c_1 + c_2 x^2 + c_3 y^2 + c_4 xy \tag{2.18}$$

$$\epsilon_y^o = c_5 + c_6 x^2 + c_7 y^2 + c_8 xy \tag{2.19}$$

To predict the stable cylindrical geometries after bonding, a second order polynomial is chosen which satisfies the fixed center geometric boundary conditions of the composite laminate as shown below.

$$w^o(x, y) = \frac{1}{2}\left(c_9 x^2 + c_{10} y^2 + c_{11} xy\right) \tag{2.20}$$

The c_i variables are coefficients to be determined. According to Equations 2.5d-2.5f, c_9, c_{10}, and c_{11} are the negative curvatures in the x and y directions, and the negative twist curvature, respectively. As seen below, the curvatures are predicted to be constant through the laminate and can be thought of as average values.

$$\kappa_x^o = -c_9 \tag{2.21a}$$

$$\kappa_y^o = -c_{10} \tag{2.21b}$$

$$\kappa_{xy}^o = -c_{11} \tag{2.21c}$$

Since the in-plane shear strain needs to be consistent with the extensional mid-plane strains, it needs to be determined using the strain-displacement relationships in Equations 2.5a-2.5c. The mid-plane displacement functions are derived by solving for $\frac{\partial u^o}{\partial x}$ and $\frac{\partial v^o}{\partial y}$ and integrating them with respect to x and y as shown below.

$$u^o(x,y) = \int \epsilon_x^o - \frac{1}{2}\left(\frac{\partial w^o}{\partial x}\right)^2 dx \tag{2.22}$$

$$v^o(x,y) = \int \epsilon_y^o - \frac{1}{2}\left(\frac{\partial w^o}{\partial y}\right)^2 dy \tag{2.23}$$

Inserting Equations 2.18-2.20 into 2.22-2.23 and evaluating them leads to

$$u^o(x,y) = c_1 x + \frac{1}{3}c_2 x^3 + c_3 xy^2 + \frac{1}{2}c_4 x^2 y - \frac{1}{6}c_9^2 x^3 - \frac{1}{4}c_9 c_{11} x^2 y - \frac{1}{8}c_{11}^2 xy^2 + h(y) \tag{2.24}$$

$$v^o(x,y) = c_5 y + \frac{1}{3}c_7 y^3 + c_6 x^2 y + \frac{1}{2}c_8 xy^2 - \frac{1}{6}c_{10}^2 y^3 - \frac{1}{4}c_{10} c_{11} xy^2 - \frac{1}{8}c_{11}^2 x^2 y + g(x) \tag{2.25}$$

where $h(y)$ and $g(x)$ arise from the partial integration step. These two functions are chosen to be the following equations based on the trend of maintaining odd powers of x and y in Equations 2.24 and 2.25.

$$h(y) = c_{12} y + \frac{1}{3}c_{13} y^3 \tag{2.26}$$

$$g(x) = c_{15} x + \frac{1}{3}c_{14} x^3 \tag{2.27}$$

To prevent rigid body rotation in the $x-y$ plane from being in the assumed displacement functions, c_{15} must equal c_{12} and the resulting functions after inserting in $h(y)$ and $g(x)$ become

$$u^o(x,y) = c_1 x + c_{12} y + \frac{1}{2}\left(c_4 - \frac{1}{2}c_9 c_{11}\right) x^2 y + \left(c_3 - \frac{1}{8}c_{11}^2\right) x y^2 + \frac{1}{3}\left(c_2 - \frac{1}{2}c_9^2\right) x^3 + \frac{1}{3}c_{13} y^3 \tag{2.28}$$

$$v^o(x,y) = c_{12} x + c_5 y + \frac{1}{2}\left(c_8 - \frac{1}{2}c_{10} c_{11}\right) x y^2 + \left(c_6 - \frac{1}{8}c_{11}^2\right) x^2 y + \frac{1}{3}\left(c_7 - \frac{1}{2}c_{10}^2\right) y^3 + \frac{1}{3}c_{14} x^3 \tag{2.29}$$

The in-plane shear strain can now be solved by substituting Equations 2.20, 2.28, and 2.29 into Equation 2.5c and results in

$$\gamma_{xy}^o = 2c_{12} + \left(c_9 c_{10} - \frac{1}{4}c_{11}^2 + 2c_3 + 2c_6\right) x y + \left(\frac{1}{2}\left(\frac{c_9 c_{11}}{2} + c_4\right) + c_{14}\right) x^2 + \left(\frac{1}{2}\left(\frac{c_{10} c_{11}}{2} + c_8\right) + c_{13}\right) y^2 \tag{2.30}$$

The mid-plane strains, curvatures, and displacements are approximations consisting of 14 unknown coefficients ($c_i; i = 1, 2, ..., 14$). The lower order shape functions allow minimal computation times for numerically solving for c_i at the cost of accuracy, especially when under dynamic analysis. Although static profiles contain controllable errors, time dependent simulations require higher order functions to maintain these errors since they are amplified when inertial and damping forces are introduced into the system. Spatially constant curvatures artificially stiffen bistable composites and higher forcing levels are required to initiate the nonlinear dynamical behavior observed in experiments when under lower forcing levels. However, the order cannot be excessively raised with

no restraints since the number of unknown coefficients is directly proportional to this value, which will lead to prohibitive computation times. Therefore, determining an appropriate order number for the shape functions is critical for both an accurate and timely analysis.

2.2.2 Higher Order Functions

The Rayleigh-Ritz method relies on good approximations to accurately predict the stable shapes and stability properties of the composite laminate. With higher order functions, this method is used to approximate the mid-plane strains, curvatures, and displacements with 17 unknown coefficients c_i where $i = 1, 2, ..., 17$. The mid-plane displacements are modelled as admissible fourth and fifth order polynomial shape functions satisfying the fixed center geometric boundary conditions and given below.

$$u^o(x,y) = c_1x + c_2xy^2 + c_3x^3 + c_4xy^4 + c_5x^3y^2 + c_6x^5 \tag{2.31}$$

$$v^o(x,y) = c_7y + c_8x^2y + c_9y^3 + c_{10}x^4y + c_{11}x^2y^3 + c_{12}y^5 \tag{2.32}$$

$$w^o(x,y) = \frac{1}{2}\left(c_{13}x^2 + c_{14}y^2 + c_{15}x^2y^2 + c_{16}x^4 + c_{17}y^4\right) \tag{2.33}$$

It should be noted that the choice of out-of-plane displacement function w^o is more important than the in-plane displacement functions since the former is associated with a larger order of magnitude than the latter. Due to the large bending of bistable laminates, the in-plane displacements have a negligible effect on their static characteristics [11]. Overall, these higher ordered shape functions more accurately capture the stable geometries and dynamics of the bistable laminate when compared to the second and third order polynomials of the lower order functions. This is due to allowing spatially variable curvatures which prevents the over prediction of laminate stiffness caused

by the constant curvature assumption [91, 96]. Shape functions beyond the fifth order are not considered since it significantly increases computation times without any proportional improvement in the accuracy of the solution [118].

One of the advantages of starting with assumed mid-plane displacement functions is that computing the mid-plane strain and curvature functions with Equations 2.5a-2.5f is much more direct. This is due to not requiring the integration step. Substituting Equations 2.31-2.33 into these kinematic relationships result in

$$\epsilon_x^o = c_1 + 3c_3x^2 + 5c_6x^4 + c_2y^2 + 3c_5x^2y^2 + c_4y^4 + \frac{1}{2}x^2\left(c_{13} + 2c_{16}x^2 + c_{15}y^2\right)^2 \tag{2.34}$$

$$\epsilon_y^o = c_7 + c_8x^2 + c_{10}x^4 + 3c_9y^2 + 3c_{11}x^2y^2 + 5c_{12}y^4 + \frac{1}{2}y^2\left(c_{14} + c_{15}x^2 + 2c_{17}y^2\right)^2 \tag{2.35}$$

$$\gamma_{xy}^o = xy\left(2c_2 + 2c_8 + 4c_{10}x^2 + 2c_5x^2 + 2c_{11}y^2 + 4c_4y^2 + \left(c_{13} + 2c_{16}x^2 + c_{15}y^2\right)\left(c_{14} + c_{15}x^2 + 2c_{17}y^2\right)\right) \tag{2.36}$$

$$\kappa_x^o = -c_{13} - 6c_{16}x^2 - c_{15}y^2 \tag{2.37}$$

$$\kappa_y^o = -c_{14} - c_{15}x^2 - 6c_{17}y^2 \tag{2.38}$$

$$\kappa_{xy}^o = -4c_{15}xy \tag{2.39}$$

2.3 Minimization of Total Potential Energy

Under the state of plane stress with no external work, the total elastic potential energy U_{el} of a composite laminate with arbitrary layup can be expressed as

$$U_{el} = \frac{1}{2}\sum_{k=1}^{n}\int_{\mathcal{V}_k}\left(\sigma_x\epsilon_x + \sigma_y\epsilon_y + \sigma_{xy}\epsilon_{xy}\right)_k d\mathcal{V}_k \tag{2.40}$$

where $\mathcal{V}_k$ is the total volume of the kth ply. Substituting the stress-strain relationships in Equation 2.10 into Equation 2.40 yields

$$\begin{aligned} U_{el} = \frac{1}{2}\sum_{k=1}^{n}\int_{\mathcal{V}_k}\Bigg(\epsilon_x\left(2\epsilon_y\bar{Q}_{12}+2\gamma_{xy}\bar{Q}_{16}-\left(d_x\bar{Q}_{11}+d_y\bar{Q}_{12}+d_{xy}\bar{Q}_{16}\right)\frac{\Delta V}{\Delta x}\right) \\ +\epsilon_y\left(2\gamma_{xy}\bar{Q}_{26}-\left(d_x\bar{Q}_{12}+d_y\bar{Q}_{22}+d_{xy}\bar{Q}_{26}\right)\frac{\Delta V}{\Delta x}\right)+\epsilon_x^2\bar{Q}_{11}+\epsilon_y^2\bar{Q}_{22} \\ +\gamma_{xy}\left(\gamma_{xy}\bar{Q}_{66}-\left(d_x\bar{Q}_{16}+d_y\bar{Q}_{26}+d_{xy}\bar{Q}_{66}\right)\frac{\Delta V}{\Delta x}\right)\Bigg)_k d\mathcal{V}_k \end{aligned} \tag{2.41}$$

Similar to what was implemented in Section 2.1.2, the elastic potential energy is re-arranged in terms of its extensional $[A]$, coupling $[B]$, and bending $[D]$ stiffness matrices and piezoelectric forces $\left\{N^P\right\}$ and moments $\left\{M^P\right\}$ per unit length from Equation 2.14. This is given below.

$$U_{el} = \int_{\frac{-L_x}{2}}^{\frac{L_x}{2}}\int_{\frac{-L_y}{2}}^{\frac{L_y}{2}}\left(\frac{1}{2}\begin{bmatrix}\{\epsilon^o\}\\ \{\kappa^o\}\end{bmatrix}^T\begin{bmatrix}[A] & [B]\\ [B] & [D]\end{bmatrix}\begin{bmatrix}\{\epsilon^o\}\\ \{\kappa^o\}\end{bmatrix}-\begin{bmatrix}\{\epsilon^o\}\\ \{\kappa^o\}\end{bmatrix}^T\begin{bmatrix}\{N^P\}\\ \{M^P\}\end{bmatrix}\right)dxdy \tag{2.42}$$

where $\{\epsilon^o\} = \left\{\epsilon_x^o, \epsilon_y^o, \gamma_{xy}^o\right\}^T$ and $\{\kappa^o\} = \left\{\kappa_x^o, \kappa_y^o, \kappa_{xy}^o\right\}^T$ are the vectors of mid-plane strains and curvatures, respectively. Their definitions from Section 2.2 are inserted into Equation 2.42 and the spatial integration is carried out. The resulting equations depend on 14 or 17 unknown variables c_i from either the lower or higher order shape functions, respectively, such that $U_{el} = U_{el}(c_i)$. The minimization of total potential energy principle states that the first variation of $U_{el}(c_i)$ must be zero for the laminate to be in equilibrium, that is,

$$\delta U_{el} = \sum_{i=1}^{n_u}\frac{\partial U_{el}}{\partial c_i}\delta c_i = 0 \tag{2.43}$$

where n_u is the total number of unknown coefficients. To satisfy Equation 2.43, it is necessary to impose the following condition for $i = 1, 2, ..., n_u$:

$$f_i = \frac{\partial U_{el}}{\partial c_i} = 0 \tag{2.44}$$

where f_i are the n_u nonlinear equilibrium equations that are solved for the n_u unknown coefficients c_i to find the laminate shapes as defined by the assumed mid-plane strain and displacement functions. The predicted equilibrium state is stable if its corresponding Jacobian matrix $[J]$ shown below is positive definite.

$$[J] = \begin{bmatrix} \frac{\partial f_1}{\partial c_1} & \frac{\partial f_1}{\partial c_2} & \cdots & \frac{\partial f_1}{\partial c_{n_u}} \\ \frac{\partial f_2}{\partial c_1} & \frac{\partial f_2}{\partial c_2} & \cdots & \frac{\partial f_2}{\partial c_{n_u}} \\ \vdots & \vdots & \ddots & \vdots \\ \frac{\partial f_{n_u}}{\partial c_1} & \frac{\partial f_{n_u}}{\partial c_2} & \cdots & \frac{\partial f_{n_u}}{\partial c_{n_u}} \end{bmatrix} \tag{2.45}$$

Symbolic computing in MATLAB is used to generate the equilibrium equations and the *fsolve* function is then implemented to solve them for c_i. The solutions are inserted back into the assumed shape functions to obtain the static profiles of the laminate. This procedure can repeated for each applied voltage or geometric increment to capture the laminate's stability characteristics such the static bifurcation behavior. The numerical solver requires specific initial solutions to be able to converge to the desired equilibrium state and so multiple trials are necessary to identify all stable and unstable configurations.

2.4 Derivation of a Dynamic Model

The potential energy contains geometrically nonlinear terms to yield the large out-of-plane deformations and stable states of the bistable system. With the addition of the composite plate's kinetic energy, the equations of motion can be derived through Lagrange's equations. This derivation method is appropriate since the geometric boundary conditions are implicitly satisfied through the selection of shape functions while their unknown coefficients can conveniently serve as the discrete set of generalized coordinates, which become a function of time t. While the lower order shape functions from Section 2.2.1 may give adequate results under static analysis, the higher order shape functions in Section 2.2.2 are required if predictive accuracy is to be maintained under dynamic analysis. Specifically, the critical forcing levels to induce cross-well oscillations are much better correlated with experimental results. Therefore, all dynamic analysis in this dissertation will utilize the higher order shape functions. The out-of-plane displacement function w^o in Equation 2.33 is redefined as

$$w^o(x,y,t) = \frac{1}{2}\left(q_1(t)\,x^2 + q_2(t)\,y^2 + q_3(t)\,x^2y^2 + q_4(t)\,x^4 + q_5(t)\,y^4\right) + f(t) \tag{2.46}$$

where the unknown coefficients c_{13} to c_{17} are replaced by five generalized curvature coordinates $q_j(t)$ for $j = 1, ..., 5$. The out-of-plane displacement is also superposed with the base excitation function $f(t)$ applied at the center of the laminate. Since $f(t)$ only has temporal dependence, it will appear through the kinetic energy and disappear in the potential energy due to the required differentiation to obtain the mid-plane strains and curvatures. The in-plane displacements u^o and v^o in Equations 2.31 and 2.32 remain unchanged in form, but the unknown coefficients become

time dependent through $c_i(t)$ where $i = 1, 2, ..., 12$. These unknowns are carried through the mid-plane strains and curvatures in the total potential energy.

2.4.1 Electromechanical Coupling

The electromechanical coupling terms from the MFCs must first be included in the total potential energy if dynamic voltage response or control of the bistable laminate with piezoelectric actuators is to be made possible. They are derived from the piezoelectric constitutive equations of the kth ply in the laminate coordinate system, which represents each P1 type MFC [119]. For a Kirchhoff plate under the state of plane stress, the compliance form is given by

$$\begin{Bmatrix} \epsilon_x \\ \epsilon_y \\ \gamma_{xy} \\ \mathcal{D}_x \end{Bmatrix}_k = \begin{bmatrix} \bar{S}_{11} & \bar{S}_{12} & \bar{S}_{16} & d_x \\ \bar{S}_{12} & \bar{S}_{22} & \bar{S}_{26} & d_y \\ \bar{S}_{16} & \bar{S}_{26} & \bar{S}_{66} & d_{xy} \\ d_x & d_y & d_{xy} & \epsilon_x^T \end{bmatrix}_k \begin{Bmatrix} \sigma_x \\ \sigma_y \\ \tau_{xy} \\ \mathcal{E}_x \end{Bmatrix}_k \tag{2.47}$$

For the kth ply, $\{\sigma\}_k$ is the total stress, $[\bar{S}]$ is the transformed reduced compliance matrix, $\mathcal{D}_{x_k}$ is the effective electric displacement, $\mathcal{E}_{x_k}$ is the effective electric field, and ϵ_x^T is the effective dielectric permittivity constant in the compliance form. Note that $[\bar{S}]$ is obtained with the transformation matrix in Equation 2.8 through $[\bar{S}] = [T][S][T]^{-1}$, where $[S]$ is the reduced compliance matrix, or the inverse of the reduced stiffness matrix $[Q]$ in Equation 2.6. The piezoelectric constitutive

equations in Equation 2.47 are rearranged into the stiffness form as seen below.

$$\begin{Bmatrix} \sigma_x \\ \sigma_y \\ \tau_{xy} \\ \mathcal{D}_x \end{Bmatrix}_k = \begin{bmatrix} \bar{Q}_{11} & \bar{Q}_{12} & \bar{Q}_{16} & -e_x \\ \bar{Q}_{12} & \bar{Q}_{22} & \bar{Q}_{26} & -e_y \\ \bar{Q}_{16} & \bar{Q}_{26} & \bar{Q}_{66} & -e_{xy} \\ e_x & e_y & e_{xy} & \epsilon_x^S \end{bmatrix}_k \begin{Bmatrix} \epsilon_x \\ \epsilon_y \\ \gamma_{xy} \\ \mathcal{E}_x \end{Bmatrix}_k \tag{2.48}$$

Where again for the kth ply, $\{e\}_k$ are the effective piezoelectric constants and ϵ_x^S is the effective dielectric permittivity constant in the stiffness form. With the constitutive equations now including the piezoelectric effect, the initial form of the elastic potential energy in Equation 2.40 becomes the piezoelectric potential energy U_p. The internal electrical energy W_{ie} is given below.

$$W_{ie} = \frac{1}{2} \sum_{k=1}^{n} \int_{\mathcal{V}_k} (\mathcal{E}_x \mathcal{D}_x)_k \, d\mathcal{V}_k \tag{2.49}$$

The coupled stress-strain definitions in Equation 2.48 are substituted into Equation 2.40 and Equation 2.49, but since the stiffness terms of the potential energy are already accounted for in Equation 2.41, only the electromechanical coupling terms are retained and this results in

$$U_p = -\frac{1}{2} \sum_{k=1}^{n} \int_{\mathcal{V}_k} \left(\mathcal{E}_x \left(\epsilon_x e_x + \epsilon_y e_y + \gamma_{xy} e_{xy}\right)\right)_k d\mathcal{V}_k \tag{2.50}$$

$$W_{ie} = \frac{1}{2} \sum_{k=1}^{n} \int_{\mathcal{V}_k} \left(\mathcal{E}_x \left(\epsilon_x^S \mathcal{E}_x + \epsilon_x e_x + \epsilon_y e_y + \gamma_{xy} e_{xy}\right)\right)_k d\mathcal{V}_k \tag{2.51}$$

where the effective electric field for the kth MFC ply is given by the following equation.

$$\mathcal{E}_{x_k} = \frac{v_k(t)}{\Delta x} \tag{2.52}$$

$v_k(t)$ is the time dependent generalized voltage coordinate, where one electrical degree of freedom models the electrical response of each MFC. This variable is different than ΔV_k given in the piezoelectric forces and moments per unit length in Equation 2.16 and Equation 2.17, which represents the delta from the bonding voltage during manufacturing. Inserting the total strain definitions in Equations 2.4a-2.4c into Equations 2.50 and 2.51 yields U_p and W_{ie} in terms of the mid-plane strains and curvatures, as given below.

$$U_p = -\frac{1}{2}\sum_{k=1}^{n}\int_{\mathcal{V}_k}\left(\mathcal{E}_x\left(e_x\left(\epsilon_x^o + z\kappa_x^o\right) + e_y\left(\epsilon_y^o + z\kappa_y^o\right) + e_{xy}\left(\gamma_{xy}^o + z\kappa_{xy}^o\right)\right)\right)_k d\mathcal{V}_k \tag{2.53}$$

$$W_{ie} = \frac{1}{2}\sum_{k=1}^{n}\int_{\mathcal{V}_k}\left(\mathcal{E}_x\left(\epsilon_x^S\mathcal{E}_x + e_x\left(\epsilon_x^o + z\kappa_x^o\right) + e_y\left(\epsilon_y^o + z\kappa_y^o\right) + e_{xy}\left(\gamma_{xy}^o + z\kappa_{xy}^o\right)\right)\right)_k d\mathcal{V}_k \tag{2.54}$$

For both Equation 2.53 and Equation 2.54, the strains are assumed to be at the mid-surface of each MFC ply. The total potential energy of the laminate can now be written as the expression below

$$\Pi = U_{el} + U_p - W_{ie} \tag{2.55}$$

where it becomes a function of the unknowns $c_i(t)$, $q_j(t)$, and $v_k(t)$. Note that U_{el} is Equation 2.42.

2.4.2 Energy Formulation

To determine the inertial forces under dynamic excitation, the total kinetic energy of the composite plate is given in the equation below

$$T = \frac{1}{2}\rho \int_{\frac{-h}{2}}^{\frac{h}{2}} \int_{\frac{-L_x}{2}}^{\frac{L_x}{2}} \int_{\frac{-L_y}{2}}^{\frac{L_y}{2}} \left(\frac{\partial w^o}{\partial t}\right)^2 + \left(\frac{\partial u^o}{\partial t} - z\frac{\partial^2 w^o}{\partial x \partial t}\right)^2 + \left(\frac{\partial v^o}{\partial t} - z\frac{\partial^2 w^o}{\partial y \partial t}\right)^2 dydxdz \tag{2.56}$$

where ρ is the overall density of the laminate. By neglecting the in-plane inertial terms due to the fixed center boundary condition and integrating through the thickness h, the kinetic energy becomes

$$T = \frac{1}{2}\rho h \int_{\frac{-L_x}{2}}^{\frac{L_x}{2}} \int_{\frac{-L_y}{2}}^{\frac{L_y}{2}} \frac{h^2}{12}\left(\left(\frac{\partial^2 w^o}{\partial x \partial t}\right)^2 + \left(\frac{\partial^2 w^o}{\partial y \partial t}\right)^2\right) + \left(\frac{\partial w^o}{\partial t}\right)^2 dydx \tag{2.57}$$

Inserting the out-of-plane displacement w^o in Equation 2.46 into Equation 2.57 results in the kinetic energy being purely a function of the generalized curvature coordinates $q_j(t)$.

Before Lagrange's equations can be used to derive the equations of motion, the number of generalized coordinates or the degrees of freedom of the system must be truncated if computational efficiency is to be maintained. This is done by rearranging the system so that it is solely a function of the generalized coordinates $q_j(t)$ and $v_k(t)$. The unknown coefficients $c_i(t)$ in the total potential energy Π in Equation 2.55 are linearly independent throughout the functional. Minimizing the total potential energy Π by taking the first variation in terms of the twelve $c_i(t)$ coefficients yields

the twelve equilibrium equations shown below.

$$\frac{\partial \Pi}{\partial c_i} = 0 \tag{2.58}$$

With Equation 2.58, $c_i(t)$ can be found as functions of $q_j(t)$ and $v_k(t)$ such that

$$c_i(t) = f(q_j(t), v_k(t)) \tag{2.59}$$

Inserting Equation 2.59 into Equation 2.55 yields the functional of the total potential energy as shown below.

$$\Pi = f(q_j(t), v_k(t)) \tag{2.60}$$

Now the system no longer has any dependence on the coefficients $c_i(t)$. However, $c_i(t)$'s contribution to the static equilibrium states and their stability is still retained in the total potential energy in Equation 2.60 through Equation 2.59. This is how the information on the stable states are retained in dynamic equilibrium when Equation 2.60 is carried through the equations of motion, where it becomes the nonlinear restoring forces yielding the bistable dynamics.

2.4.3 Equations of Motion

Given the Lagrangian definition $\mathcal{L} = T - \Pi$, the electromechanically coupled equations of motion for the bistable laminate are obtained using Lagrange's equations as shown below.

$$\frac{d}{dt}\left(\frac{\partial \mathcal{L}}{\partial \dot{q}_j}\right) - \frac{\partial \mathcal{L}}{\partial q_j} = 0 \tag{2.61}$$

$$\frac{d}{dt}\left(\frac{\partial \mathcal{L}}{\partial \dot{v}_k}\right) - \frac{\partial \mathcal{L}}{\partial v_k} = \varphi \tag{2.62}$$

where φ is the electrical charge output resulting from the non-conservative electrical work, $\dot{q}_j = \frac{\partial q_j}{\partial t}$, and $\dot{v}_k = \frac{\partial v_k}{\partial t}$. Substituting Equations 2.57 and 2.60 into Equations 2.61 and 2.62 yields the Multiple Degrees of Freedom (MDOF) Duffing type equations of motion:

$$[M]\{\ddot{q}\} + [D(\dot{q})] + [K(q)] + [\Theta]\{v\} = \{F\} \tag{2.63}$$

$$[\Theta]^T\{q\} + [C_p]\{v\} = \{\varphi\} \tag{2.64}$$

$[M]$ is the mass matrix, $[D(\dot{q})]$ is the nonlinear damping matrix, $[K(q)]$ is the nonlinear stiffness matrix, $[\Theta]$ is the electromechanical coupling matrix, $[C_p]$ is the capacitive matrix, $\{\varphi\}$ is the electrical charge output vector, and $\{F\}$ is the forcing vector derived from the base excitation. Note that the number of MFCs in the laminate equates to the number of generalized voltage coordinates, which is a different value than the five generalized curvature coordinates. For example, if the bistable laminate consists of two MFCs, then $\{v\} = \{v_1, v_2, 0, 0, 0\}^T$. All terms in the equations of motion are linear with the exception of $[K(q)]$ and $[D(\dot{q})]$, which contain linear, quadratic, and cubic terms. These higher ordered curvature terms in $[K(q)]$ are the source of geometric and dynamic nonlinearity needed to predict the wide variety of nonlinear behavior seen in bistable

systems. They represent the restoring force as seen in the popular double well Duffing equation, which is used to model single degree of freedom bistable oscillators in numerous past works [4]. To incorporate energy dissipation into the system, Rayleigh damping is assumed in Equation 2.63, where the nonlinear damping matrix is given by

$$[D(\dot{q})] = \alpha[M]\{\dot{q}\} + \beta[K(\dot{q})] \tag{2.65}$$

and α and β are the mass and stiffness damping coefficients, respectively. Equation 2.65 assumes that the damping matrix is proportional to the mass and stiffness matrices, and must satisfy the condition below to avoid modal coupling.

$$2\omega_{ni}\zeta_i = \alpha + \beta\omega_{ni}^2 \tag{2.66}$$

ω_{ni} and ζ_i are the ith natural frequency and corresponding damping ratio. It can be seen that the damping matrix is nonlinear due to being partially proportional to the stiffness matrix.

To assess the power dissipation across a resistive load for each MFC while the laminate is under dynamic excitation, the electrical work done by the system where each MFC is connected to a resistor in parallel is modelled. This is implemented by differentiating Equation 2.64 with respect to time which converts $\{\varphi\}$ to the electrical current and through Ohm's law yields the coupled equation below.

$$[\Theta]^T\{\dot{q}\} + [C_p]\{\dot{v}\} = \frac{1}{R}\{v\} \tag{2.67}$$

Note that R is the load resistance which is assumed to be identical for both MFCs.

2.5 Chapter Summary

The electromechanically coupled analytical model of a piezoelectrically generated bistable laminate is derived for both static and dynamic analysis. By bonding two actuated MFCs in an unsymmetric layup and releasing the voltage post cure, piezoelectric strain anisotropy and the resulting in-plane residual stresses yield two statically stable states that are cylindrically shaped. To capture the large out-of-plane deformations associated with bistable composite laminates, CLT is extended to included nonlinear terms in the kinematic strain-displacement relationships according to the von Karman plate theory, which allows for moderate rotations of the middle surface and large out-of-plane displacements. Within the CLT constitutive equations, the thermal analogy is used to replace thermal strains induced by temperature change to piezoelectric strains caused by an applied electric field due to MFC voltage actuation. The resulting piezoelectric forces and moments per unit length are responsible for generating the residual stresses necessary for bistability through the elastic potential energy.

To predict the cylindrical geometries, Rayleigh-Ritz approximations are made for the mid-plane strain and displacement functions which satisfy geometric boundary conditions. Second and third order polynomials proposed by Dano and Hyer [36] provide adequate accuracy for static profiles, but higher order shape functions are necessary to retain low errors for dynamic analysis. By allowing spatially variable curvatures through fourth and fifth order polynomials, the laminate stiffness is not artificially raised which allows for accurate forcing level input to laminate response output trends. The elastic potential energy carrying the laminate stiffness and the bonding voltage loading terms is minimized relative to the number of unknown coefficients associated with the Rayleigh-Ritz shape functions. The resulting nonlinear equilibrium equations can be numerically

solved to obtain the static laminate shapes under a variety of specified geometrical parameters and piezoelectric loading. The stability of the solution is determined by evaluating if the Jacobian matrix of the equilibrium equations is positive definite.

The nonlinear electromechanical MDOF equations of motion are derived using Lagrange's equations, where the degrees of freedom are the generalized curvature and voltage coordinates. To allow for dynamic voltage control and response with the MFCs, the electromechanical coupling terms are separately obtained using the piezoelectric constitutive equations, internal electric energy, and piezoelectric potential energy, and they are combined with the elastic potential energy. The total potential energy is then reformulated to be a function of just the generalized curvature and voltage coordinates to reduce computation times. The kinetic energy is also obtained to account for the inertial forces and base excitation at the laminate center. Once the equations of motion are found, Rayleigh damping is assumed to incorporate energy dissipation in the system.

CHAPTER 3

Laminate Design and Snap-through Morphing

Given the proposed concept of utilizing the piezoelectric actuation of MFCs to generate bistability in composite laminates, the presented chapter's objectives are as follows. They are to explore the design space with parametric studies, characterize the geometry, stability properties, and snap-through morphing capability of the yielded design, and experimentally validate the static analysis. The stable shapes of conventionally rectangular bistable composite laminates generated with thermal residual stresses are a deeply analyzed phenomenon, and the previous research outlined in Chapter 1 agrees on the following findings for the equilibrium configurations and dependency on geometric parameters. These are that the amount of generated curvature is inversely proportional to the laminate thickness and that bistability is lost when the side length to thickness ratio drops below a critical value. However, the mechanism for inducing bistability is voltage application with MFCs instead of temperature loading on passive materials and how this affects the curvature and the existence of stable states are investigated here. In addition, the MFCs simultaneously being the actuator and primary structure gives rise to a design efficiency and how this addresses the research challenge of initiating reversible quasi-static snap-through is presented. The electromechanically coupled model derived in Chapter 2 and finite element analysis are implemented for static analysis, and a specimen of the bistable laminate is manufactured and experimentally characterized to

provide model validation.

3.1 Design Considerations and Parameter Effects

Since the objective is to develop a smart bistable laminate useful for morphing applications, its design must be catered towards the most favorable conditions for inducing bistability and maximizing the range of motion between the stable configurations. Under broadband energy harvesting applications, the latter condition will also enable larger strains to be imparted on the laminate during cross-well vibrations, which will raise the subsequent power output. A $[0^{MFC}/90^{MFC}]_T$ layup is chosen to minimize the laminate thickness and allow outside access to the electrode leads of each MFC. In addition, the cross-ply configuration will maximize the out-of-plane displacements of each stable state, since moving the ply angles closer together will lower displacements and push the laminate towards monostability [120]. This is analytically demonstrated in Appendix A. The laminate will be square because shifting its aspect ratio away from one will cause an imperfect static bifurcation behavior that is not accurately predicted by the analytical model [121]. The P1 type MFC that utilizes the d_{11} effect is chosen for its actuation capabilities required for control applications, which strains in the piezoceramic fiber direction under an operating voltage of -500 V to 1500 V. The MFCs will be bonded together in a flat configuration while both are actuated at 1500 V so that the post cure delta voltage and the resulting piezoelectric strains will be the maximum possible under the operating limits. This will provide the most margin for static bifurcation, that is, it will move the bifurcation voltage furthest away from the unactuated state where there is no applied voltage.

Given the laminate design choices, the only remaining parameters are the laminate side length

and the adhesive used to bond the two MFCs. The following sections will present an analytical examination of how these parameters affect the resulting laminate shape, bifurcation voltage, stability characteristics, and a design will be finalized thereafter. Table 3.1 presents the relevant material properties of the P1 type MFC and the two candidate adhesives, which are the 3M DP-460 epoxy and the Cytec FM300-2M film adhesives [122–124].

Table 3.1: Material properties of P1 MFC, DP-460, and FM300-2M adhesives.

Properties	MFC	DP-460	FM300-2M
E_1 (GPa)	29.4	2.7	2.44
E_2 (GPa)	15.2	2.7	2.44
ν_{12}	0.312	0.4	0.38
G_{12} (GPa)	6.06	0.96	0.88
Thickness h (mm)	0.3	0.0875	0.13
d_{11} (10^{-9} mm/V)	380	–	–
d_{12} (10^{-9} mm/V)	-170	–	–
Electrode Spacing Δx (mm)	0.5	–	–
Dielectric Constant ϵ_x^S (10^{-11} F/mm)	1.5	–	–
α_1 (10^{-6}/°C)	7.5 (60°C), 10 (120°C)	59	58
α_2 (10^{-6}/°C)	18 (60°C), 38 (120°C)	59	58

It should be noted that the piezoelectric constants in Table 3.1 are for high electric field values (>1 kV/mm), or greater than 500 V for the P1 type MFC due to the chosen 1500 V bonding voltage. Also, the thickness of the DP-460 epoxy adhesive is an averaged experimental measurement due to it being variable across the bond line. The average laminate density of $\rho = 4281 kg/m^3$ is found by measuring its volume and mass. Although the MFC consists of a mix of active and passive materials, it is modelled as a single orthotropic ply since accounting for its constituent layers through CLT has a negligible effect on the resulting laminate profiles. This is demonstrated in Appendix A. Finally, Williams [122] found that the MFC CTEs α_1 and α_2 are temperature dependent, and so their values at the cure temperatures of both adhesives are presented.

3.1.1 Side Length and Geometry

Utilizing the static analytical model with lower order shape functions, the curvature vs. voltage behaviors for multiple laminate side lengths are shown in Figure 3.1. The lower order functions are chosen due to their constant curvatures across the domain, which allows the laminate shapes to be conveniently represented as a scalar value in parametric analysis. It should be noted that the model accounts for the adhesive layer between the two MFCs by including it as an inactive isotropic ply. The DP-460 epoxy is chosen for this section because it can be cured at room temperature, and so the cure cycle thermal effects do not have to be considered.

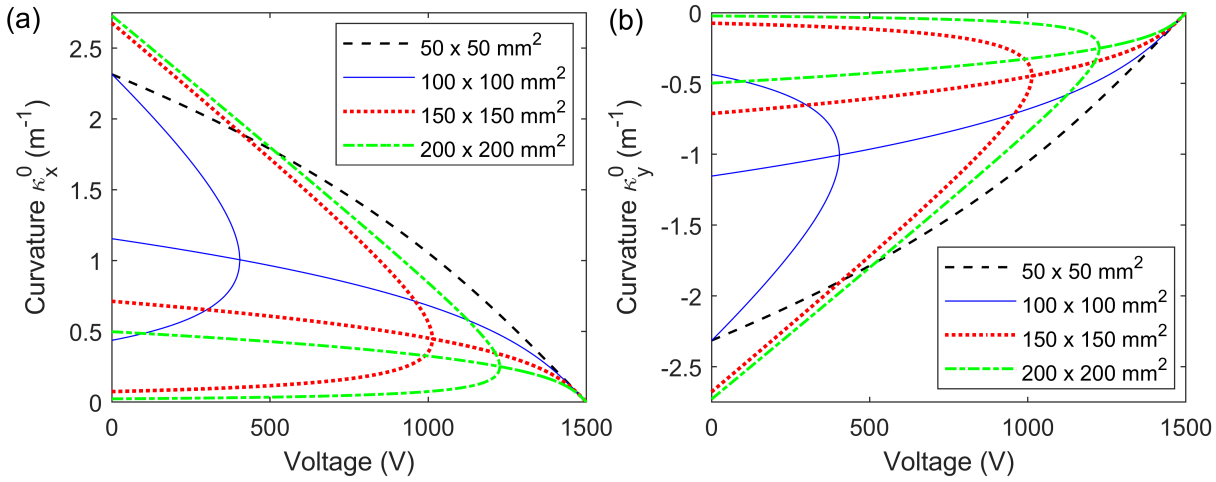

Figure 3.1: $[0^{MFC}/90^{MFC}]_T$ curvatures (a) κ_x^0 and (b) κ_y^0 vs. voltage for 50 x 50 mm^2, 100 x 100 mm^2, 150 x 150 mm^2, and 200 x 200 mm^2 laminates.

At the bonding voltage of 1500 V, the laminate is in a flat configuration with zero curvature and displacement. Once the power is shut off post cure, the resulting delta voltage generates curvature due to residual stresses generated by the mismatch in the effective piezoelectric constants. Initially, laminates of all side lengths exhibit a monostable saddle shape and the curvatures associated with this configuration increases as the delta voltage magnitude increases. Bifurcation for

the 100 x 100 mm^2, 150 x 150 mm^2, and 200 x 200 mm^2 laminates occur respectively at the delta voltages of -1095 V, -486 V, and -273 V from the bonding voltage. At bifurcation, the stable saddle shaped path splits into two cylindrically stable paths and a single unstable path with a saddle shape, corresponding to the middle path. After the pitchfork bifurcation and in terms of magnitude, the stable path with the larger curvatures in the κ_x^0 plots corresponds to the path with lower curvatures in the κ_y^0 plots, and vice versa. For the 50 x 50 mm^2 laminate, bifurcation is not observed in the examined voltage range, and the laminate remains in a monostable saddle shape. The major curvatures and the resulting out-of-plane displacements increase with larger laminate side lengths. These plots show that bistability can be piezoelectrically generated for a square $[0^{MFC}/90^{MFC}]_T$ laminate with sufficient side length.

According to the unactuated $[0^{MFC}/90^{MFC}]_T$ curvatures vs. side length plotted in Figure 3.2(a) and (b), the exact minimum side length required to induce bistability is 85 mm. The laminate retains similar stability trends and characteristics between the applied voltage and side length. As observed in Figure 3.1, the curvatures κ_x^0 and κ_y^0 have equal magnitude in opposite out-of-plane directions and have a monostable saddle shape until the pitchfork bifurcation into the two cylindrically stable branches is observed at the 85 mm side length. Post bifurcation, the amount of generated curvature exponentially decays with increasing side length. This means that increasing the side length indefinitely has diminishing returns for the out-of-plane deformation and the range of motion between stable configurations. Figure 3.2(c) shows the voltage where bifurcation occurs from a bonding voltage of 1500 V when the side length is varied. Since the plot indicates the voltage where the laminate becomes bistable for each side length, the area above the plot represents a monostable configuration while the area below corresponds to the bistable configuration. Similar to the generated curvatures, the exponential trend indicates that increasing the laminate side length

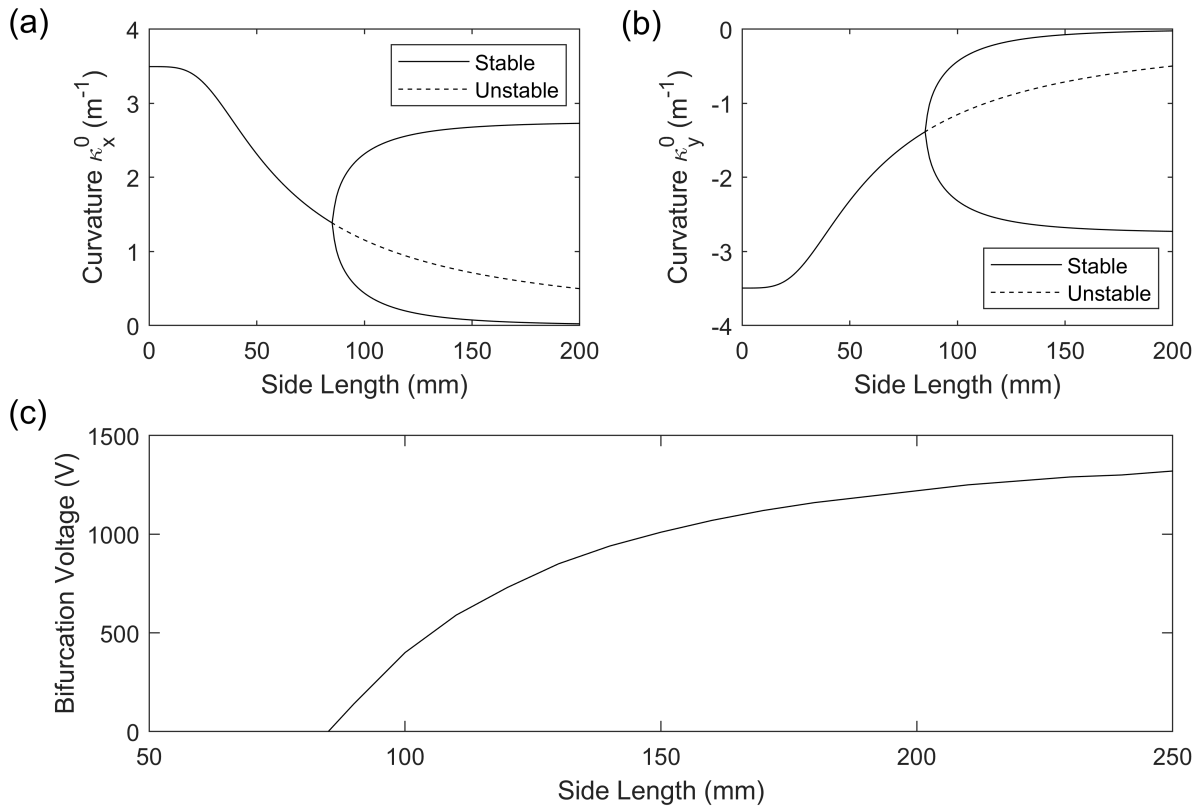

Figure 3.2: $[0^{MFC}/90^{MFC}]_T$ curvatures (a) κ_x^0, (b) κ_y^0, and (c) bifurcation voltage vs. side length at 0 V from 1500 V bonding voltage.

has diminishing returns for the applied delta voltage required to induce bistability.

There are limitations to how large MFCs can be manufactured, and so the side length must be judiciously chosen. Simultaneously, a design goal is to minimize the voltage difference between bifurcation and bonding to compensate for potential manufacturing imperfections. Therefore, a side length of 200 mm is chosen to ensure sufficiently large out-of-plane displacements and adequate margin for generating bistability. Figure 3.3 shows both the stable and unstable analytical shape predictions of a 200 x 200 mm^2 $[0^{MFC}/90^{MFC}]_T$ laminate bonded at 1500 V.

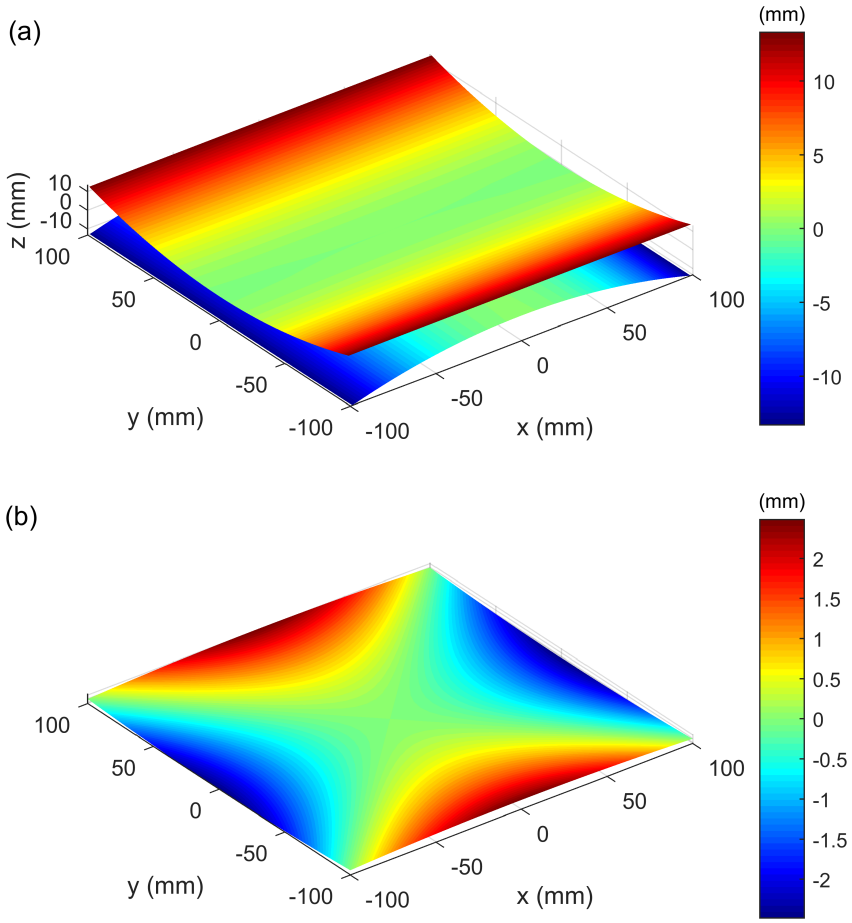

Figure 3.3: Out-of-plane displacements of a 200 x 200 mm^2 $[0^{MFC}/90^{MFC}]_T$ laminate in (a) stable cylindrical states and (b) unstable saddle state at 0 V.

3.1.2 Adhesive and Cure Cycle

The two adhesives being considered for bonding the MFCs are the DP-460 epoxy and the FM300-2M film adhesive. The primary motivation for this section is to determine the effects of each adhesive's cure cycle on the laminate's stability characteristics and stable shapes, and then select the appropriate adhesive. To be accurate, the predictive models must take the adhesive into account because as its thickness increases, the resulting laminate's out-of-plane displacements decrease and its bifurcation is further delayed as will be shown in this section. The cure cycles occur at elevated temperatures that impart thermal strains on the actuated MFCs during cooldown

to room temperature and alter their piezoelectric strains and the residual stresses. This interaction between the anisotropic CTEs and piezoelectric constants must be characterized before an actual laminate can be bonded.

The DP-460 adhesive is a manually applied two part epoxy where the resulting bond line will be non-uniform due to the lack of thickness control and thus contribute to the manufacturing error. However, it allows a range of temperature dependent cure durations, with the longest being 24 hours at room temperature and the shortest being 2 hours at 60 °C, and are both considered here. The FM300-2M is a film adhesive that has a uniform thickness known beforehand, and more accurately reflects the perfect bond line assumption made in the models. Despite the advantage, it requires a 2 hour cure at 120 °C, which will have a larger impact on the piezoelectric strains. Since the MFC's maximum operating temperature is 130 °C, the film adhesive's cure cycle is a feasible option. In general, shorter cure durations are preferred due to the reduced time under actuation at the operating limit, thus raising the probability of survival.

To account for the thermal strains from the adhesive cure cycles, Equation 2.42 in Section 2.3 is modified to include the effects of thermal loading in the total potential energy, as shown by

$$U_{el} = \int_{\frac{-L_x}{2}}^{\frac{L_x}{2}} \int_{\frac{-L_y}{2}}^{\frac{L_y}{2}} \left(\frac{1}{2} \begin{bmatrix} \{\epsilon^o\} \\ \{\kappa^o\} \end{bmatrix}^T \begin{bmatrix} [A] & [B] \\ [B] & [D] \end{bmatrix} \begin{bmatrix} \{\epsilon^o\} \\ \{\kappa^o\} \end{bmatrix} - \begin{bmatrix} \{\epsilon^o\} \\ \{\kappa^o\} \end{bmatrix}^T \begin{bmatrix} \{N^P\} + \{N^T\} \\ \{M^P\} + \{M^T\} \end{bmatrix} \right) dxdy \tag{3.1}$$

where the thermal forces $\{N^T\}$ and moments $\{M^T\}$ per unit length due to an applied delta tem-

perature ΔT from the cure cycle are given as

$$\left\{N^T\right\} = \Delta T \sum_{k=1}^{n} \left[\bar{Q}\right]_k \left\{\alpha\right\}_k \left(z_k - z_{k-1}\right) \tag{3.2}$$

$$\left\{M^T\right\} = \frac{\Delta T}{2} \sum_{k=1}^{n} \left[\bar{Q}\right]_k \left\{\alpha\right\}_k \left(z_k^2 - z_{k-1}^2\right) \tag{3.3}$$

The effective CTEs in the laminate coordinate system is given as $\{\alpha\}_k$ where they are a function of the CTEs α_1 and α_2 in the lamina coordinate system, and this relationship is shown below.

$$\{\alpha\}_k = \begin{Bmatrix} \alpha_x \\ \alpha_y \\ \alpha_{xy} \end{Bmatrix}_k = \begin{Bmatrix} \alpha_1 \cos^2\theta + \alpha_2 \sin^2\theta \\ \alpha_1 \sin^2\theta + \alpha_2 \cos^2\theta \\ 2\cos\theta \sin\theta(\alpha_1 - \alpha_2) \end{Bmatrix}_k \tag{3.4}$$

Using the modified analytical model, the curvature vs. voltage relationships for a 200 x 200 mm^2 $[0^{MFC}/90^{MFC}]_T$ laminate bonded at 1500 V with the three proposed adhesive cure cycles are presented in Figure 3.4. The bifurcation voltage, stability, and the resulting curvatures remain consistent for the laminate under the DP-460 room temperature cure as the behavior outlined in the 200 x 200 mm^2 case of Figure 3.1. Once the cure temperature is raised to 60 °C, bifurcation occurs further away from the bonding voltage at -688 V delta voltage from 1500 V. This indicates that the margin of available voltage to induce bistability is reduced when the laminate is cured at elevated temperatures. The major curvatures of each stable state are also significantly reduced, which means the resulting out-of-plane displacements are lower for both stable states after the applied thermal loading. For the laminate under the FM300-2M cure at 120 °C, there is no bifurcation under piezoelectric actuation and so it remains monostable over the entire voltage range. This elimination

of bistability means that the FM300-2M is not a viable option for bonding the MFCs, even if it provides the advantage of a uniform bond line.

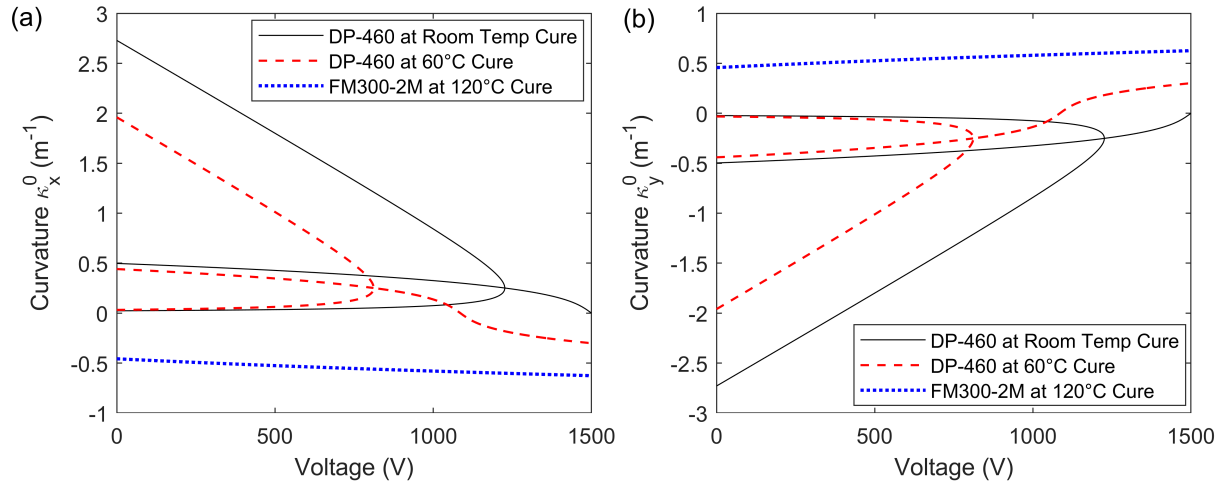

Figure 3.4: 200 x 200 mm^2 $[0^{MFC}/90^{MFC}]_T$ curvatures (a) κ_x^0 and (b) κ_y^0 vs. voltage bonded with DP-460 at room temperature, 60 °C, and with FM300-2M at 120 °C.

Thermal loading from cure cycles with elevated temperatures have debilitating effects on piezoelectrically generated bistability due to the conflicting MFC CTEs and piezoelectric constants. Under voltage actuation, the MFC strains are dominant in the piezoceramic fiber 1 direction over the transverse electrode 2 direction. Under thermal loading, the opposite is true due to the CTEs being greater in the transverse 2 direction. With higher cure temperatures, the thermal strains become large enough to reduce the piezoelectric strains like the DP-460 60 °C case, or completely overtake them like the FM300-2M 120 °C case. Since the design objectives are to minimize the laminate bifurcation delta voltage and maximize its out-of-plane displacements, the DP-460 room temperature cure cycle is chosen for bonding the MFCs.

The thickness of the DP-460 epoxy can vary for each application or within the laminate domain. To determine the sensitivity of the stability margins and generated deformations due to the

adhesive thickness, the $[0^{MFC}/90^{MFC}]_T$ laminate's bifurcation voltage and maximum out-of-plane displacement versus the epoxy thickness are presented in Figure 3.5. With increasing thickness, both metrics are significantly reduced and these are proportional to the thickness squared. The relationships show that the laminate's shape and margin for bistability are adversely affected by thicker adhesives, and an effort must be made to minimize the bond line thickness during fabrication. Although the adhesive is passive and does not contribute to inducing bistability through actuation, its effects on the laminate are non-trivial and will be included in all subsequent analysis.

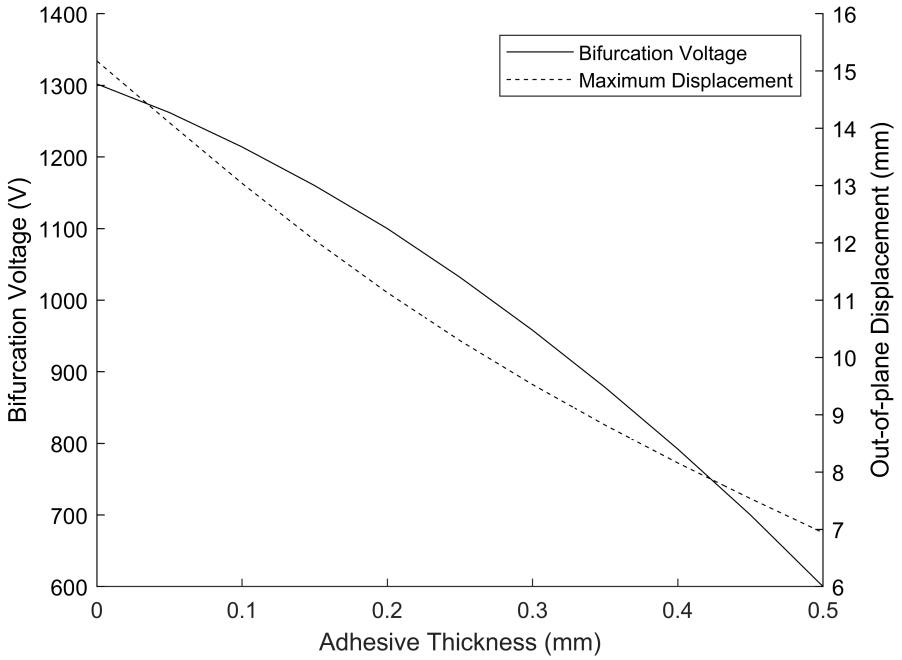

Figure 3.5: 200 x 200 mm^2 $[0^{MFC}/90^{MFC}]_T$ bifurcation voltage and maximum out-of-plane displacement vs. DP-460 adhesive thickness with no thermal loading.

3.2 Finite Element Analysis

This section presents the finite element modelling approach with the motivation of it being validation to the analytical model in conjunction with the experimental data. It also acts as an

alternative predictive tool of the laminate's shapes by accounting for effects that are not captured by the analytical model. With the $[0^{MFC}/90^{MFC}]_T$ laminate design finalized in the previous section, it is implemented in MSC Nastran with Altair HyperMesh and HyperView serving as the pre and post processors. Although the 200 x 200 mm^2 represents the active area where the piezoceramic fibers are housed, the total MFC dimensions are 207 x 218 mm^2 due to the peripheral area housing the electrode rails and leads between the polyimide films. When two of these MFCs are bonded in a cross-ply layup, the total bonded area becomes 207 x 207 mm^2 which leaves an inactive outer area containing only the Kapton and acrylic materials. This is modelled to account for its influence on the resulting laminate shape and is shown in Figure 3.6.

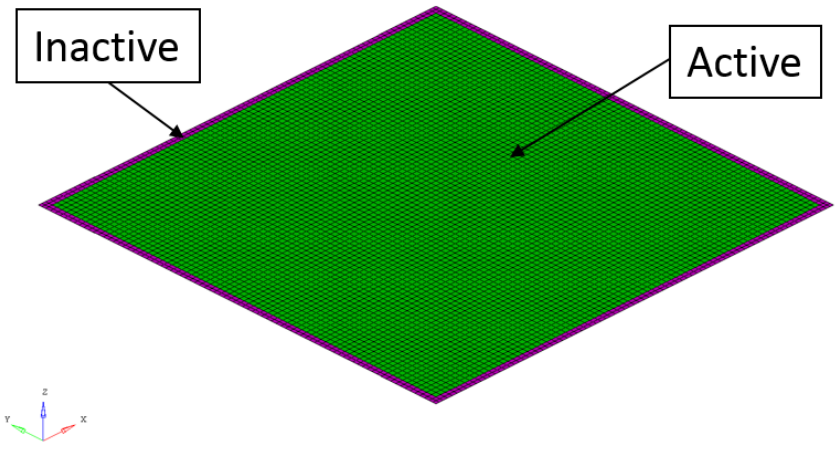

Figure 3.6: Finite element mesh of 207 x 207 mm^2 $[0^{MFC}/90^{MFC}]_T$ laminate containing both active piezoelectric and inactive peripheral areas.

The FEA model consists of 7056 CQUAD4 (4 node quadrilateral shell) elements with 43350 degrees of freedom and 9 center nodes fixed at the center of the laminate to prevent near-singularities in the stiffness matrix. The inner active area is characterized with the MFC and DP-460 material properties from Table 3.1, but the outer inactive area is characterized as isotropic with the average of the Kapton and acrylic stiffness properties [122]. The thickness of both materials was experi-

mentally measured to be 0.12 mm. The orthotropic MAT8 and isotropic MAT1 cards are used to input the constituent properties, and then the laminate is assembled with the PCOMP card which defines its layup over the shell elements.

To simulate voltage actuation of the MFCs, the piezoelectric-thermal analogy approach is utilized. Cote et al. [125] numerically and experimentally validated this approach, which was implemented in MSC Nastran. The linearized in-plane piezoelectric to thermal strain relationship is given by

$$\begin{Bmatrix} \epsilon_1 \\ \epsilon_2 \\ \gamma_{12} \end{Bmatrix} = \frac{\Delta V}{\Delta x} \begin{Bmatrix} d_{11} \\ d_{12} \\ 0 \end{Bmatrix} = \Delta T \begin{Bmatrix} \alpha_1 \\ \alpha_2 \\ 0 \end{Bmatrix} \tag{3.5}$$

which shows that the piezoelectric strains imparted by voltage actuation are described by the thermal strains from temperature change through equations with same form. In the model, the CTEs of the active MFC plies are replaced with the piezoelectric constants divided by the electrode spacing so that any thermal loading on the laminate is equivalent to an applied delta voltage. The CTEs of the adhesive layer and the inactive outer area are set to zero so that a delta temperature representing voltage change is only applied on the MFCs. The models are run using the SOL 106 non-linear solver, where a delta temperature, or ΔV of -1500 V is applied with TEMP cards to simulate the bonding of actuated MFCs. The step size is 0.15 V from 0 to -300 V and 1.5 V from -300 to -1500 V. The initial lower step size is chosen to let the solver converge at bifurcation earlier and more accurately capture the voltage at which it occurs. Minimal geometric imperfections (206 x 207 or 207 x 206 mm^2) are used to force the solver into either stable branch after bifurcation.

3.3 Experimental Methodology

3.3.1 Manufacturing Procedure

The 200 x 200 mm^2 $[0^{MFC}/90^{MFC}]_T$ laminate was manufactured under vacuum by bonding two P1 type MFCs while actuated at 1500 V. The MFCs were custom made by Smart Material Corp. As mentioned in the previous section, each MFC has an active area of 200 x 200 mm^2 housing the piezoceramic fibers and electrodes, but its total dimensions are 207 x 218 mm^2. Therefore, the resulting laminate's total bonded area is 207 x 207 mm^2 with 5.5 mm of overhang on each edge.

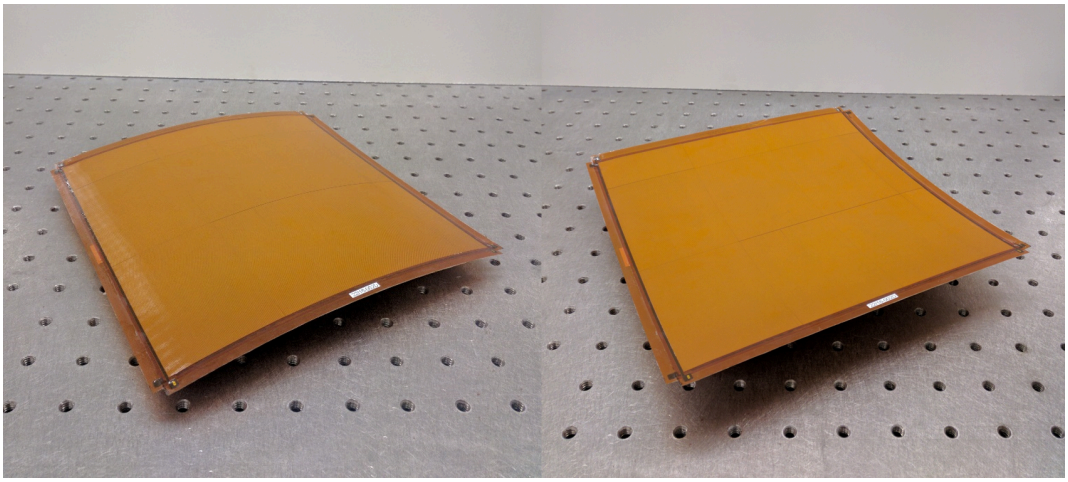

Figure 3.7: Stable configurations of a manufactured 200 x 200 mm^2 $[0^{MFC}/90^{MFC}]_T$ laminate at 0 V from a bonding voltage of 1500 V.

The two MFCs were simultaneously actuated in parallel at 1500 V with a BK Precision 9130 DC power supply connected to a Trek 2220 high voltage amplifier. Both MFCs were then bonded together on a flat tool under vacuum with the DP-460 epoxy. The adhesive cure cycle was 24 hours at room temperature and a standard vacuum bag bonding procedure was implemented. The flat tool had to be partially drilled where the bottom MFC leads and soldered wires sit to allow adequate

space. This enabled both MFCs to stay flat against the tool, let the vacuum apply even pressure across the laminate, and reduced the chance of the wires disconnecting while the epoxy was curing. After the cure cycle, the laminate was taken out of vacuum and power to both MFCs were shut off. The flat laminate immediately took a cylindrical shape and was qualitatively confirmed to be bistable through a snap-through test. Figure 3.7 shows both stable states of the manufactured $[0^{MFC}/90^{MFC}]_T$ laminate. All experimental measurements were taken once the MFCs discharged completely to allow the laminate to reach its full profile.

3.3.2 Measurement of Laminate Shapes

To characterize the $[0^{MFC}/90^{MFC}]_T$ laminate's geometry, bifurcation, and snap-through behaviors, full 3D profiles and out-of-plane displacement trends under voltage actuation were captured. As shown in Figure 3.8, this was achieved with two separate experimental setups.

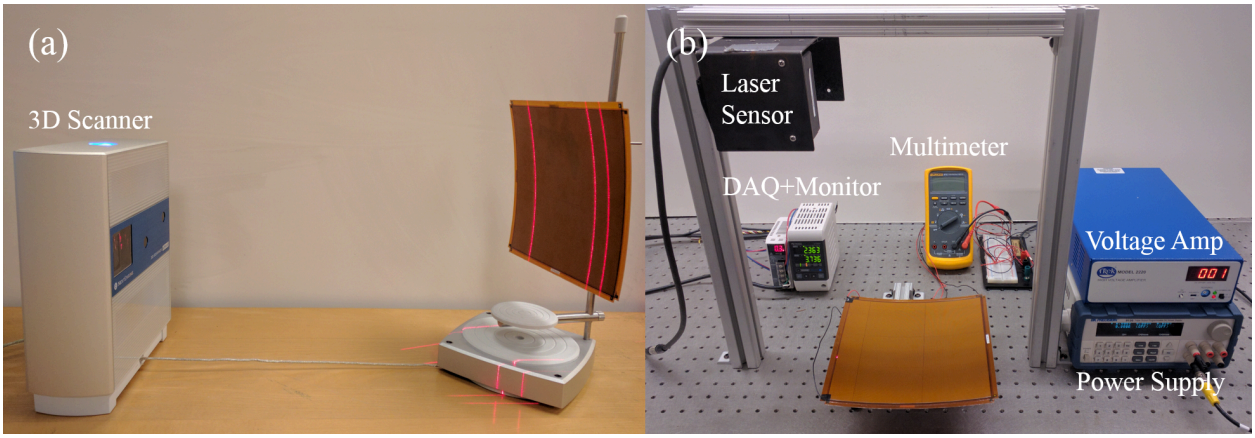

Figure 3.8: Experimental setup with (a) a 3D scanner measuring laminate profiles at 0 V and (b) a 1D laser sensor measuring laminate displacements under voltage actuation.

The shape profiles of both stable configurations at 0 V were measured with a NextEngine Desktop 3D Scanner, which utilizes multi-stripe laser triangulation to obtain the 3D coordinates

of every assigned grid point across the laminate. The scan resolution was 1.32 points/mm^2 with a depth accuracy of 0.127 mm. The laminate was attached to a controlled fixture which allowed an aligned bracket scan to be assembled from 3 separate scans that are rotated 30 ° apart from each other. In the Scan Studio software, the laminate profiles were trimmed, aligned with the coordinate system established in Figure 2.1, then exported into MATLAB for evaluation against the model predictions. This particular setup was not implemented for capturing actuated laminate profiles due to the long scanning and post processing durations which limit the number of measurements that can be taken.

For a more efficient setup required by the large number of measurements collected under voltage actuation, a Keyence LK-G402 laser displacement sensor was used to obtain the out-of-plane displacements of a single point on the laminate edge. The edge locations are defined to be that of the piezoceramic fiber layer area. The sensor was mounted overhead on a sliding test rig and hung over the laminate which was attached to a sliding support. Both MFCs remained connected to the DC power supply and high voltage amplifier for actuation. During data collection, the MFC voltages were increased from 0 to 1500 V in 10 V increments every 120 seconds to account for charging duration and creep. The out-of-plane displacements were measured at the end of every voltage step. Between each set of measurements, the MFCs were allowed to discharge completely so that the laminate could return to its original profile.

3.4 Experimental Validation of Static Model

3.4.1 Unactuated Geometry

The lower and higher order analytical, finite element, and experimental stable shapes of a 200 x 200 mm^2 $[0^{MFC}/90^{MFC}]_T$ laminate are presented in Figure 3.9 where the left column is state I and the right column is state II. The 3D scanned profiles are overlaid with their least squares polynomial fits so that displacement and curvature comparisons can be made against the models. A 4th order polynomial is the lowest ordered equation that managed to accurately capture the experimental localized edge deflections which are accentuated at the corners. All residual rigid body displacements and rotations from the scanned profiles are eliminated in the fits so that they are perfectly aligned with the laminate coordinate system. To more easily evaluate the shape differences, the absolute errors of the lower and higher order analytical and finite element models against the experimental fits are presented in Figure 3.10. The error values represent the out-of-plane displacement difference $w^o_{model} - w^o_{experiment}$. Percent errors are not presented in this format due to the displacements becoming small towards the laminate center relative to the measurement accuracy of 0.127 mm, which lead to artificially high errors.

The shape differences between all models and the experimental measurements are small over the majority of the laminate and greater errors are found towards the edges with the corners containing the largest errors. This free edge effect is well documented for bistable composites in [16, 126, 127], and is due to the rapid increase of interlaminar stresses towards the laminate edges which locally alter their deflections [128]. The in-plane residual stresses that arise from the mismatch of effective piezoelectric constants need to be zero at the free edges to satisfy their boundary conditions. Thus, interlaminar stresses are generated instead and the superposition of

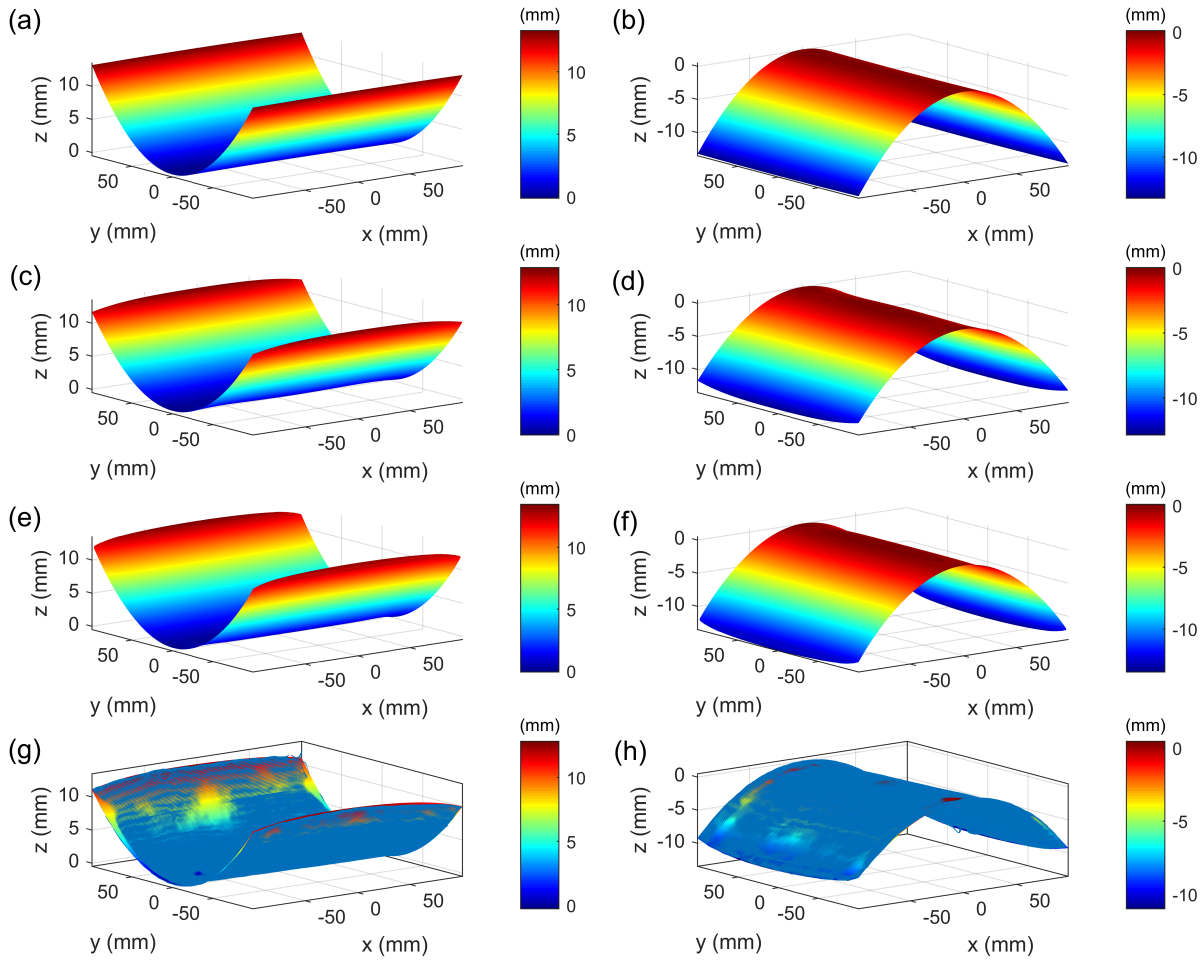

Figure 3.9: 200 x 200 mm^2 $[0^{MFC}/90^{MFC}]_T$ out-of-plane displacements at 0 V from lower order model in (a) state I, (b) state II, from higher order model in (c) state I, (d) state II, from finite element analysis in (e) state I, (f) state II, and from experimental measurements in (g) state I and (h) state II.

two adjacent free edges further deflects the corner displacement [129]. However, the effect is localized and does not significantly alter the overall cylindrical shape or the stability properties of the laminate. Both analytical models and the FEA fail to capture the free edge effects due to their plane stress assumption preventing the interlaminar stresses to be accounted for. Complex analytical models accounting for the through thickness effects have been developed to capture this behavior by Nosier and Maleki [130], but the approach is computationally expensive and requires

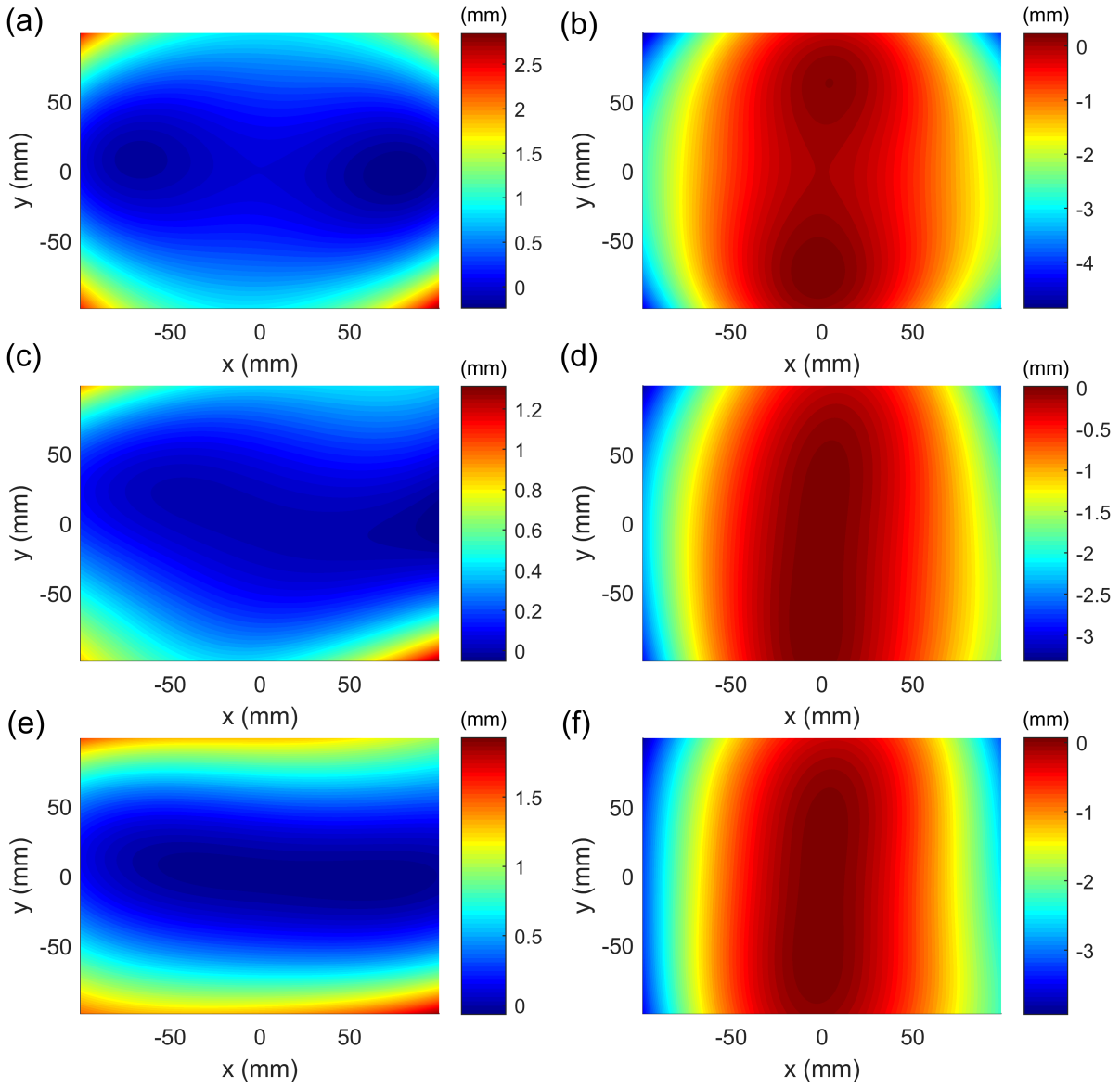

Figure 3.10: 200 x 200 mm^2 $[0^{MFC}/90^{MFC}]_T$ out-of-plane displacement absolute errors against experimental measurements for lower order model in (a) state I, (b) state II, for higher order model in (c) state I, (d) state II, and from finite element analysis in (e) state I and (f) state II.

a prior knowledge of the solution. Therefore, it is not fit for parametric design studies or modelling voltage actuated shapes as done in this chapter. Between the predictions, the higher order model exhibits the lowest and most even distribution of absolute errors for both stable configurations while the lower order model shows the highest shape errors. Table 3.2 shows the experimental, analytical, and finite element corner displacements and their corresponding percent errors, which are the largest when compared to any other locations. Again, the higher order model retains the lowest percent errors at all four corner locations.

Table 3.2: Corner out-of-plane displacements and percent errors.

State	Corner Location	Experimental (mm)	Lower Order (mm)	Lower Order Error (%)	Higher Order (mm)	Higher Order Error (%)	FEA (mm)	FEA Error (%)
I	(x, y)	11.31	13.19	14.2	11.69	3.3	12.29	8.0
	(-x, y)	10.76	13.19	18.4	11.69	8.0	12.29	12.5
	(x, -y)	10.42	13.19	21.0	11.69	10.9	12.29	15.2
	(-x, -y)	10.85	13.19	17.7	11.69	7.2	12.30	11.8
II	(x, y)	-9.16	-13.19	30.6	-11.69	21.6	-12.29	25.5
	(-x, y)	-8.44	-13.19	36.0	-11.69	27.8	-12.29	31.3
	(x, -y)	-10.07	-13.19	23.7	-11.69	13.9	-12.29	18.1
	(-x, -y)	-8.80	-13.19	33.3	-11.69	24.7	-12.30	28.5

All models over-predict the laminate's out-of-plane displacements with better agreement found in state I when compared to state II. The experimental displacements are inconsistent from corner to corner due to the non-uniform distribution of residual stresses. These discrepancies are likely due to manufacturing errors involving an imperfect layup alignment, a non-uniform epoxy bond line, MFC performance degradation from long actuated bonding times at their operating limit, and the variation of piezoelectric constants and elastic properties between the two MFCs. The imperfections cannot be controlled during the bonding procedure, and require specialized equipment to be measured and characterized. Long electrical loading times during bonding and localized laminar

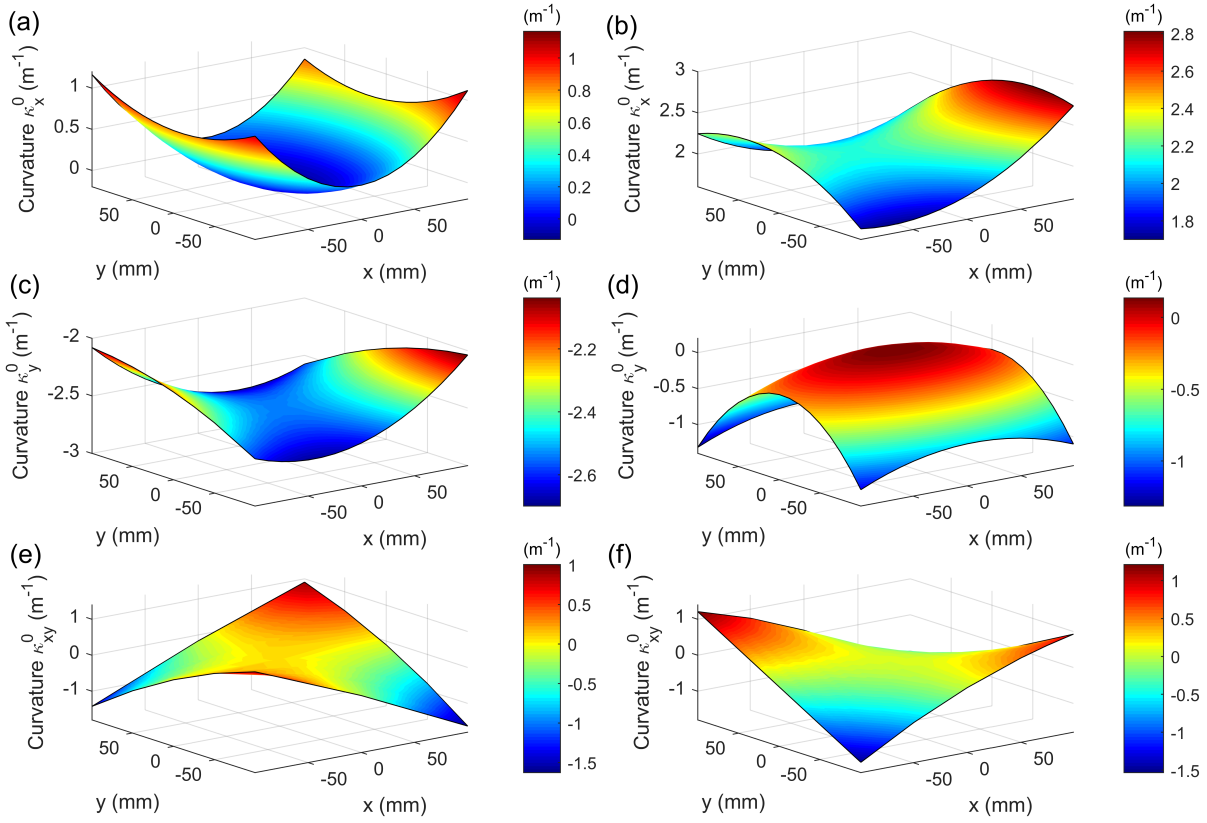

Figure 3.11: 200 x 200 mm^2 $[0^{MFC}/90^{MFC}]_T$ experimental curvatures κ_x^o in (a) state I, (b) state II, κ_y^o in (c) state I, (d) state II, and κ_{xy}^o in (e) state I and (f) state II.

compression from the residual stresses of either states may have caused minor depolarization of the piezoceramic material. This would result in the degradation of the MFCs' piezoelectric constants which accounts for the lower experimental out-of-plane displacements. Another reason for the differences are the curvature assumptions made in each model. The lower order model's quadratic polynomial shape functions assume constant curvatures that represent the averages across the laminate. In reality, the curvatures vary across the domain and this is shown in the experimental data in Figure 3.11. They are obtained with Equations 2.5d-2.5f where the out-of-plane displacement functions $w^o(x, y)$ are the 4th order least squares fit of the experimental profile for each stable state.

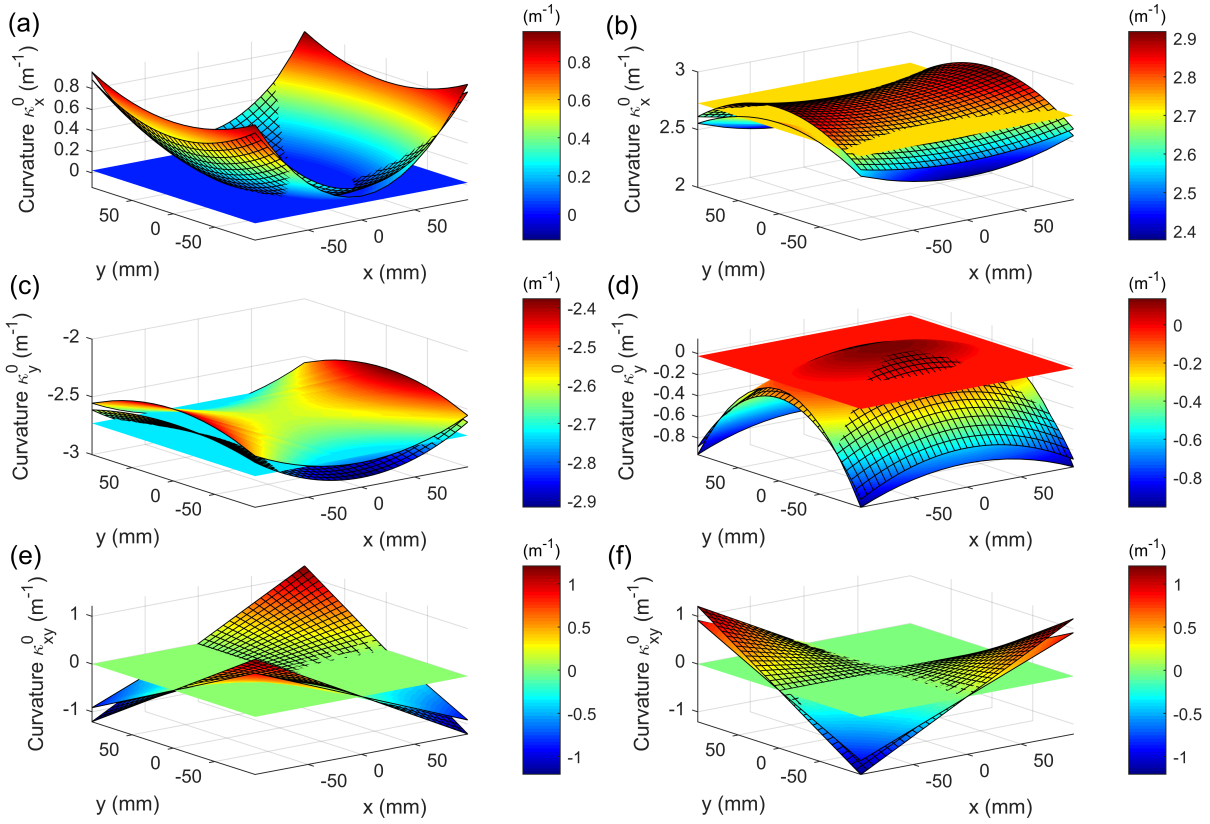

Figure 3.12: 200 x 200 mm^2 $[0^{MFC}/90^{MFC}]_T$ curvatures κ_x^o in (a) state I, (b) state II, κ_y^o in (c) state I, (d) state II, and κ_{xy}^o in (e) state I and (f) state II. Unmeshed flat surfaces are from the lower order model, meshed surfaces are from finite element analysis, and unmeshed curved surfaces are from the higher order model.

For comparison, the corresponding curvatures predicted by the lower and higher analytical models and the FEA are shown in Figure 3.12. The absolute curvature errors of the models against the experimental results are given in Appendix A. Similar to the out-of-plane displacement comparisons, all models over-predict the major curvature magnitudes with lower accuracy at the edges. However, the higher order model and FEA more closely resemble the curvature distributions found in the experimental profiles due to not being restricted by spatially constant curvatures. Unlike the lower order model, their allowance of curvature variation enables the geometric errors towards the free edges to be mitigated, which are characterized by sharp changes in curvatures and displace-

ments near the laminate edges and corners. Raising the shape function's order in the analytical model is effective in obtaining more accurate stable shape predictions because the reduction of the imposed artificial stiffness allows better convergence to the experimental profiles. In the case of the $[0^{MFC}/90^{MFC}]_T$ laminate, the higher order shape functions are even able to retain lower errors than the FEA.

3.4.2 Bifurcation Behavior

With the objective of characterizing the bifurcation behavior of the $[0^{MFC}/90^{MFC}]_T$ laminate, its corner displacements are measured with the setup shown in Figure 3.8(b) while voltage is simultaneously applied to both MFCs. The data is obtained with the laminate in states I and II over two separate runs. The corner locations with the lowest out-of-plane displacements are measured to ensure the most conservative analysis. Figure 3.13 presents the experimental results compared against the lower and higher order analytical and finite element model predictions. The corner displacement is chosen as the metric of comparison since it allows the laminate geometry under actuation to be represented as a scalar value. For a cross-ply layup, only the corners have significant out-of-plane displacements in both stable configurations, so they alone are suitable locations for evaluating both bifurcation and snap-through behavior. In addition, the experimental setup and procedure for obtaining test data are greatly simplified with this metric. Curvatures under a large number of different voltages cannot be easily compared since they are non-constant in the higher order model, FEA, and experimental profiles.

In the lower and higher order analytical and finite element models, the laminate is predicted to bifurcate respectively at delta voltages of -273 V, -251 V, and -247 V from the 1500 V bonding

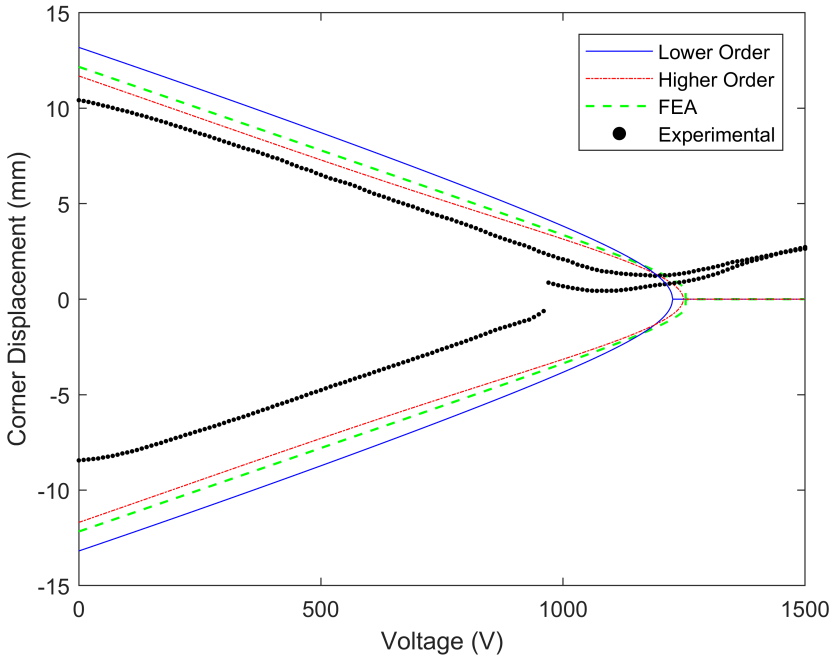

Figure 3.13: 200 x 200 mm^2 $[0^{MFC}/90^{MFC}]_T$ corner displacement vs. voltage from lower and higher order analytical model, finite element analysis, and experimental measurements.

voltage. However, the perfect bifurcation behavior is not observed in the measured displacement data. When actuated from state I starting at 0 V, the laminate remains in the same stable branch throughout the entire voltage range. It starts off in a cylindrical shape at 0 V and smoothly transitions into a saddle shape as the voltage is increased to 1500 V. When actuated from state II starting at 0 V, the laminate jumps to the first stable branch at 970 V. This is seen in the discontinuity between the experimental corner displacements at 970 V in Figure 3.13. Once the jump occurs, the corner displacements converge with those measured from state I and the laminate returns to this configuration when the power is shut off after being actuated to 1500 V. In terms of the displacements, the higher order model has better agreement with the test data than the lower order and finite element models which follows the trends of the previous section. The experimental data shows unequal displacement magnitudes between states I and II and an offset at high voltages

when compared to the models. The offset may be caused by non-uniform residual stresses within the laminate that do not disappear with increasing voltage. This would result in non-zero corner deflections while the laminate is in a saddle shape at high voltages.

The lack of a bifurcation point and unequal displacements between states I and II are attributed to imperfections that arise from manufacturing errors, which are discussed in Section 3.4.1. The factors that cause the imperfect behavior cannot be easily controlled or quantified. Instead, their qualitative effects on the laminate's stability and geometry are evaluated to better understand the experimental data. All models are idealized and assume a perfect layup, uniform ply thicknesses, and identical material properties between the two MFCs. If some of these assumptions are relaxed, the imperfect behavior from the test data can be qualitatively predicted. From the lower order analytical model, Figure 3.14 shows the effects of varying the ply thicknesses and piezoelectric constants by 5% on the laminate corner displacements under voltage actuation.

Introducing imperfections within the laminate has several effects that are seen in the experimental data. The bifurcation point disappears and a discontinuity is introduced between the two stable branches. If already in state I, the laminate will remain in the first stable branch throughout the entire voltage range. It exhibits a cylindrical shape for the majority of branch and smoothly transitions into a saddle shape as the voltage is increased to 1500 V. If starting from state II at 0 V, increasing the voltage input will cause the corner displacement magnitude to decrease until it reaches the limit voltage at which the second branch becomes unstable. At this voltage the laminate will jump to the first stable branch and remain there. Also, the corner displacement magnitudes in state I are increased while those in state II are decreased which results in them being unequal. These effects are all exhibited by the experimental data in Figure 3.13. Although the exact causes are unknown, it is reasonable to conclude that the manufactured $[0^{MFC}/90^{MFC}]_T$ laminate con-

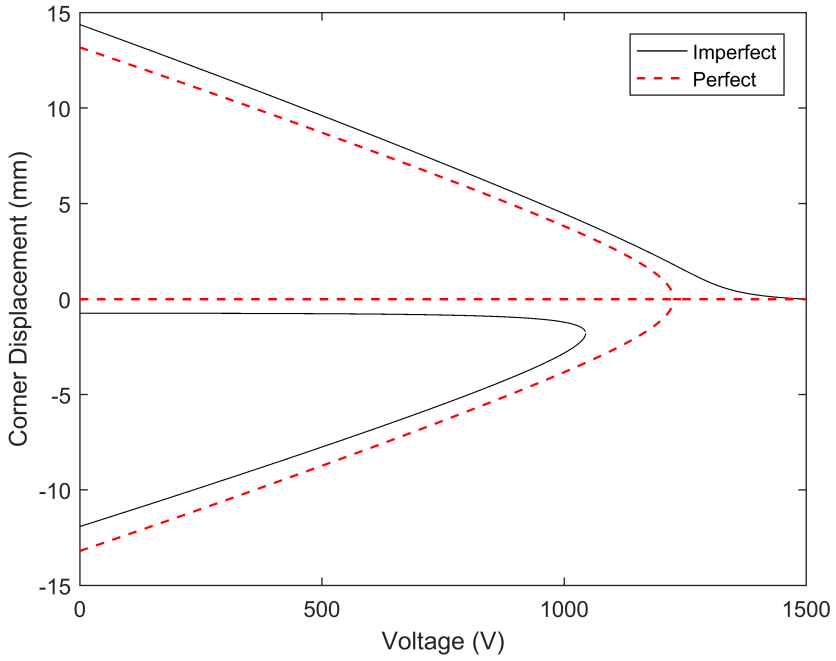

Figure 3.14: Effect of 5% thickness and piezoelectric constant imperfections on 200 x 200 mm^2 $[0^{MFC}/90^{MFC}]_T$ corner displacement vs. voltage relationship from lower order analytical model.

tains some forms of geometric or material imperfection causing the state I over II bias.

3.4.3 Quasi-Static Snap-Through

To initiate snap-through between the two stable states, only one MFC needs to be actuated at a time. In state I, actuating the top 90° MFC ply will cause snap-through to state II due to its piezoceramic fibers being positively strained in the y direction. This reduces the magnitudes of κ_y^o and the positive out-of-plane displacements until the limit voltage is reached where the laminate becomes unstable. Due to the instability, limit point behavior is exhibited and the laminate will snap-through to the second stable branch. It will then fully transition into state II once the voltage is removed. To snap the laminate back, the bottom 0° MFC ply is actuated to let it be positively strained in the x direction. The magnitudes of κ_x^o and the negative out-of-plane displacements are

reduced until the laminate snaps through to the first stable branch at the same limit voltage. The voltage is then removed to let the laminate fully transition back into state I.

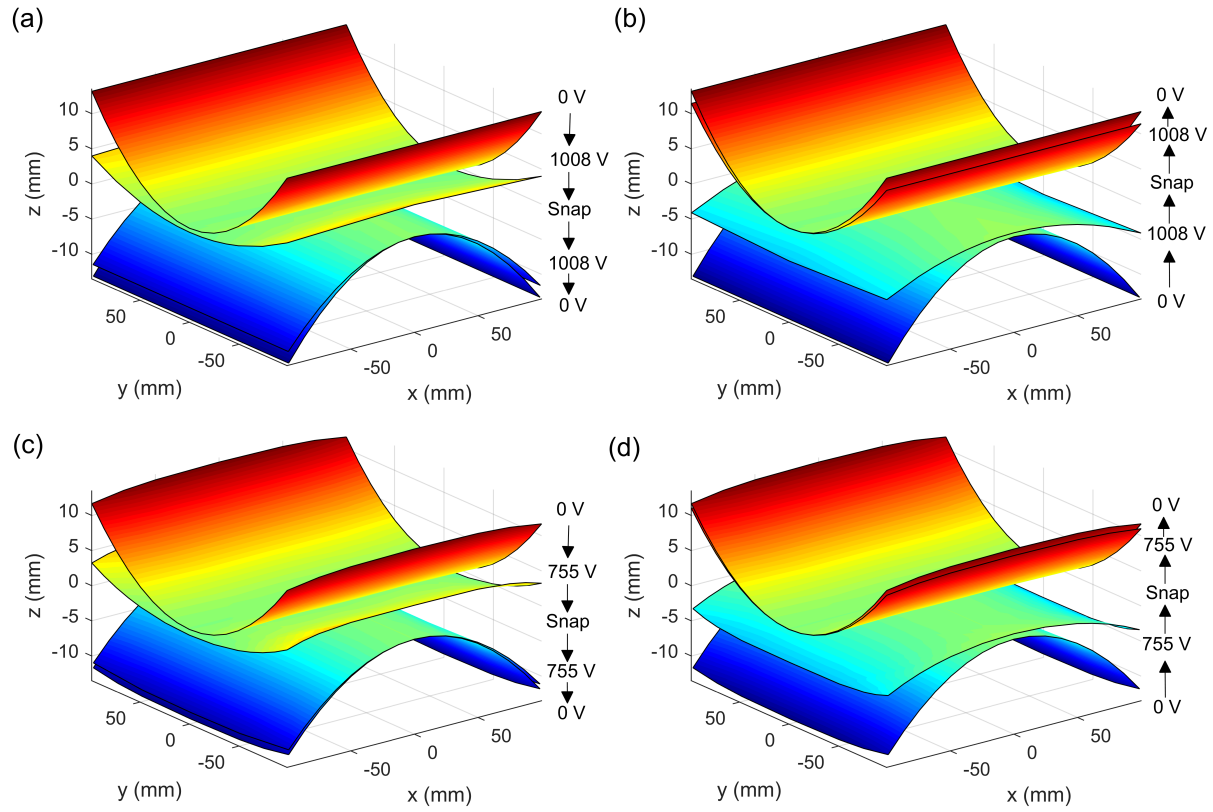

Figure 3.15: Analytical snap-through predictions of 200 x 200 mm^2 $[0^{MFC}/90^{MFC}]_T$ for lower order model from (a) state I to II, (b) state II to I, and for higher order model from (c) state I to II and (d) state II to I.

For analytically predicting the $[0^{MFC}/90^{MFC}]_T$ snap-through behavior, the applied bonding voltage ΔV_k is varied away from 1500 V to simulate MFC actuation. ΔV_k in the piezoelectric forces $\{N^P\}$ and moments $\{M^P\}$ per unit length in Equations 2.16 and 2.16 cannot remain identical for each MFC as was done in all previous analysis in this chapter. Only the voltage applied to the actuated MFC is varied while the unactuated MFC is held at the constant bonding voltage. Figure 3.15 shows the lower and higher order shape predictions during snap-through from state I to II and back. Figure 3.16 presents the corresponding lower and higher order analytical

and experimental corner displacement vs. voltage plots during snap-through between either stable configurations. In Figure 3.15(a) and (c) for the lower and higher order models, the laminate starts in state I at 0 V and the limit voltages at which snap-through occurs are predicted to be 1008 V and 755 V, respectively. The limit voltages are also shown in Figure 15 3.16(a), where the first stable branch turns unstable at 1008 V and 755 V for the lower and higher order models, respectively. After snap-through, the laminate joins the second branch and enters state II when the voltage returns to 0 V. As shown in Figure 3.15(b) and Figure 3.16(b), this process is reversed for the laminate to snap back to state I while the limit voltages remain the same.

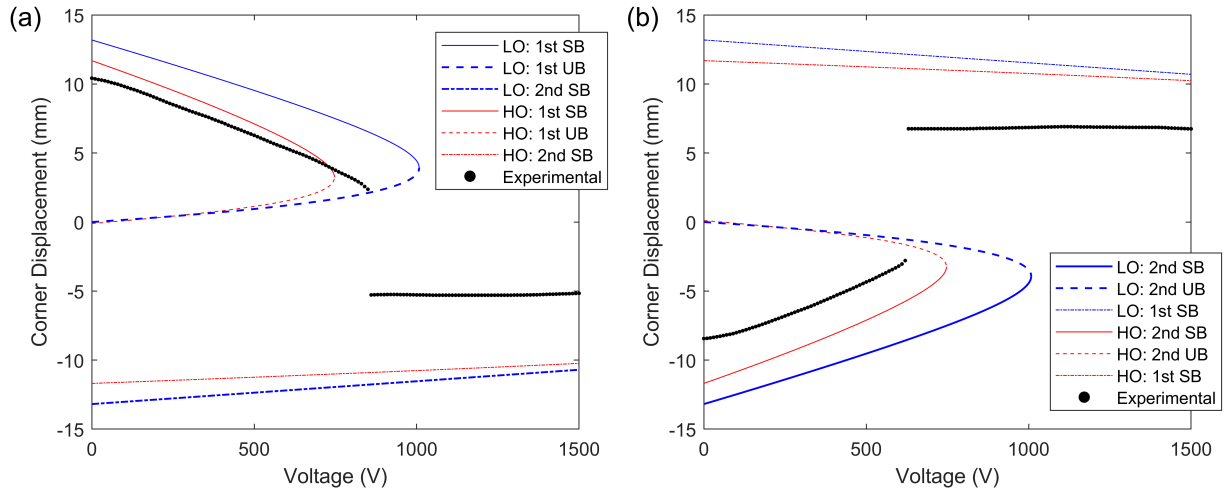

Figure 3.16: Lower order (LO) and higher order (HO) analytical and experimental comparison of 200 x 200 mm^2 $[0^{MFC}/90^{MFC}]_T$ corner displacement vs. voltage during snap-through from (a) state I to II and (b) state II to I. SB and UB are stable branch and unstable branch, respectively.

The experimental results show that the limit voltages are measured to be 860 V for state I to II and 630 V for state II to I, which results in percent errors of 14.7% and 37.5% for the lower order model and 13.9% and 16.6% for the higher order model, respectively. Snap-through is experimentally confirmed by shutting off the power after actuation to 1500 V and observing if the laminate transitioned to the other stable state. The lower limit voltage for state II to I is due to

the laminate's bias of state I over II as explained in Sections 3.4.1 and 3.4.2. The discrepancies in the corner displacement magnitudes are also explained in those sections. The lower order analytical model over-predicts the limit voltages and this is attributed to its constant curvature assumption where the degrees of freedom corresponding to the shape functions are restricted, which artificially increases the stiffness of the model. The model also fails to capture the free edge effects and so the resulting anticlastic curvatures along its minor axis are lower than those of the manufactured laminate. Both factors raise the voltage actuation requirement to induce snap-through. In contrast, the higher order model yields more accurate limit voltage predictions due to allowing spatially variable curvatures. Despite the overall differences, the voltages required to quasi-statically snap-through between either states are well within the operating limits of the MFCs. Therefore, the piezoelectrically generated bistable laminate is a viable morphing structure with full configuration control. In addition, no mechanical, geometric, or dynamic assistance is needed to initiate forward and reverse snap-through.

3.5 Chapter Summary

Utilizing the static analytical model of the $[0^{MFC}/90^{MFC}]_T$ bistable laminate from Chapter 2, the effects of the laminate side length, adhesives, and their cure cycles on the resulting shapes and their stability are characterized in order to design a viable morphing structure. For square laminates bonded at 1500 V with P1 type MFCs, the minimum side length to induce perfectly symmetric bistability is predicted to be 85 mm and lengths greater than this value yield stable geometries with greater out-of-plane deformations post bifurcation. To ensure enough margin for modelling and manufacturing errors, a 200 mm side length is chosen for fabrication. Adhesive

thickness and high cure cycle temperatures are found to have an adverse effect on bistability, and so the room temperature cure of the DP-460 epoxy is chosen to avoid thermal loading on the MFCs while maintaining a thin bond line.

The $[0^{MFC}/90^{MFC}]_T$ laminate is then manufactured and its unactuated geometry, bifurcation behavior, and snap-through actuation are experimentally measured and compared against model predictions. FEA is also conducted to provide an additional modelling tool for static analysis. Overall, good agreement is found in the stable shapes with errors growing towards the edges and corners due to free edge effects and manufacturing errors. The higher order analytical model retains the greatest accuracy when compared to the FEA and the lower order model. When both MFCs are simultaneously actuated, the laminate's bifurcation point disappears due to material and geometric imperfections. By actuating one MFC at a time within its operating limits, the laminate can snap-through unassisted between either stable states. This is analytically and experimentally demonstrated and the capability is critical for morphing where full configuration control is required.

Limitations may exist for structural applications due to the active laminate's lower stiffness when compared to conventional fiber-reinforced composites. However, it is envisioned that the concept of piezoelectrically induced bistability will be extended into more complex structures. Piezoelectric strain could be additive to thermal or elastic strain within bistable composites to generate larger motion, alleviate snap-through requirements, and minimize design restrictions. This has the potential of producing a fully load bearing bistable structure that maintains complete snap-through capability without any external assistance. Overall, this chapter has demonstrated the validity of the static model for the piezoelectrically generated bistable laminate by capturing complex nonlinear phenomena associated with its stable shapes, stability, and the snap-through behavior.

CHAPTER 4

Broadband Energy Harvesting from Nonlinear Vibrations

The wide array of nonlinear responses that bistable structures exhibit to vibrational excitation are leveraged in numerous energy harvesting applications [1, 2]. Bistable composite laminates bonded with piezoelectric transducers are particularly popular due to retaining two stable equilibrium states without any external influence from clamps or magnets, which are required for inducing bistability in isotropic beams [3]. The two potential wells are owed to a purely elastic phenomenon resulting from residual thermal stresses that are internally generated within thin unsymmetric composites during the cooldown phase of their cure cycle. Under harmonic excitation at low frequencies, these plate structures undergo snap-through motion, or jump instabilities between their two distinct configurations which can be periodic, aperiodic, or a mix of both. These are called cross-well oscillations, as opposed to single-well oscillations which describe vibrations about either stable state. The highly energetic cross-well responses impart large strains on the laminate, which are converted to substantial amounts of electrical energy by the paired piezoelectric materials when compared to linear resonant harvesters [4]. An additional advantage is that cross-well dynamics can be triggered over wide ranges of excitation frequencies and amplitudes, which

allow for effective broadband energy harvesting performance.

The piezoelectrically generated bistable laminate offers design advantages over conventional bistable composites paired with piezoelectric transducers. Having an entirely active laminate where the MFCs are directly responsible for the two stable configurations means that the design conflict between the passive composite and the piezoelectric elements becomes irrelevant. By combining their roles of generating curvature and harvesting power onto the MFCs, a bistable laminate with large out-of-plane displacements and low stiffness properties can be obtained. Although this design choice has enabled unassisted and reversible quasi-static snap-through actuation as shown in Chapter 3, the lowered stiffness is also a disadvantage in morphing applications where the laminate must be a load bearing structure. However in broadband energy harvesting applications, this characteristic is attractive as the vibrational energy input required to initiate the favorable cross-well oscillations does not need to be excessively large. The proposed laminate consists of two P1 type MFCs which have a d_{11} poling direction along the piezoceramic fibers with IDE electrodes. The P1 type MFC is not the ideal choice for energy harvesting applications due to its low capacitance which limits the current output [131, 132]. In all studies utilizing MFCs as the harvesting unit, the P2 type is chosen which has a d_{12} poling direction through its thickness in a parallel plate configuration, which results in higher capacitance and lower impedance characteristics [76,78,82]. Despite this, only the P1 type MFCs operate with a large enough piezoelectric coefficient and voltage range necessary for generating bistability, as explained in Chapter 3.

The purpose of this chapter is to analytically and experimentally characterize the dynamics of the $[0^{MFC}/90^{MFC}]_T$ bistable laminate by evaluating its mechanical and electrical responses to harmonic excitation. Through time and frequency domain analysis, a range of forcing amplitudes are applied to the laminate at its origin with unconstrained edges to identify both linear single-well

and nonlinear cross-well behaviors. This is done as the precursor to demonstrating the broadband energy harvesting capability of the laminate. With most past works being experimental, there are limitations in the available literature for validated model predictions of the electromechanical response resulting from cross-well oscillations for bistable composite harvesters. This chapter aims to experimentally validate the analytical model derived in Chapter 2 with corresponding test data by correlating the excitation parameters required to initiate certain dynamic regimes and their response magnitudes. To maintain consistency, the laminate's major curvature axis of state I is defined to be along the piezoceramic fiber direction of MFC 1 and that of state II corresponds to MFC 2 in the same manner. Additionally, the chapter experimentally characterizes the bistable laminate's broadband energy harvesting performance and investigates how this can be utilized to initiate snap-through morphing. The power output of the identified dynamic responses are measured with a simple resistive circuit for energy conversion across the observed vibration modes. A rectifying energy harvesting module consisting of onboard capacitors is then charged and provides the input voltage signal required for inducing snap-through. The combined morphing and energy harvesting capabilities enable the laminate to retain multiple roles, unlike other bistable structures which are designed for a single application.

4.1 Experimental Setup

Characterizing the $[0^{MFC}/90^{MFC}]_T$ laminate's dynamic regimes and electromechanical output under vibrational excitation is achieved with the experimental setup shown in Figure 4.1. The harmonic input to the laminate is provided by the APS 113 seismic shaker and powered by the APS 125 amplifier. The laminate is fixed at the center to a stinger, which is a 130 mm hex bolt,

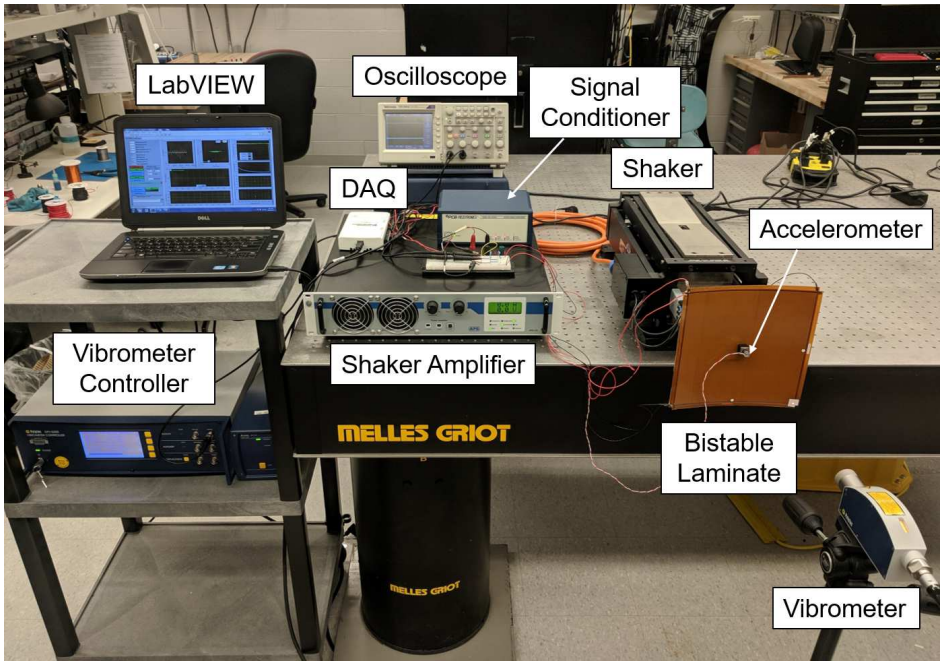

Figure 4.1: Experimental setup for measuring electromechanical response of a 200 x 200 mm^2 $[0^{MFC}/90^{MFC}]_T$ laminate.

that is attached at one end of the shaker with washers and nuts. To avoid invasive attachment methods such as drilling a hole and damaging the MFCs, the laminate is mounted at its center between two 12.7 x 12.7 x 12.7 mm^3 neodymium magnets, where the inner magnet is bonded to the free end of the stinger with epoxy. The acceleration at the laminate center is measured by a PCB Piezoelectronics 352C67 accelerometer and the velocity response is measured at a single point by a Polytec OFV-534 laser vibrometer with the Polytec OFV-5000 controller. Reflective tape is adhered to the laminate to improve the signal return of the laser vibrometer. The acceleration, voltage, and velocity responses are recorded with the NI USB-6211 DAQ connected to LabVIEW at a sample rate of 2500 Hz while this combination simultaneously provides the shaker signal based on the acceleration measurements. The voltage responses of each MFC are measured separately and voltage divider circuits are used to reduce the signals to adhere to the DAQ input limit of ± 10 V during frequency sweeps. All signals are low-pass filtered and processed in MATLAB. When

measuring the harvested power with resistor sweeps, a Tektronix TDS2004C oscilloscope is used to record the Root Mean Square (RMS) voltage output of each MFC without the voltage divider circuits to allow for simple variation of resistive loads, which is quickly implemented with an IET ohmSOURCE resistance box.

4.2 Linear Vibration Modes

Before the nonlinear dynamic response can be evaluated, the dominant linear vibration modes of the laminate for both stable states are experimentally identified with low amplitude forward frequency sweeps. Each resulting Frequency Response Function (FRF) is compared against its analytical counterpart. Determining the resonant frequencies allow subsequent sweep ranges and locations to be appropriately chosen for characterizing nonlinear dynamic regimes at high excitation amplitudes, since they appear around these modes. The model predictions, corresponding experimental results, and damping parameters obtained from test data are presented and discussed in this section.

4.2.1 Frequency Response Functions

The electromechanically coupled equations of motion in Equations 2.63 and 2.67 from Chapter 2 are linearized to yield the low amplitude FRFs by assuming simple harmonic motion about either stable state. Assume that the five generalized curvature coordinates has the form

$$q_j(t) = q_j^e + \Delta q_j(t) \tag{4.1}$$

where q_j^e is a static equilibrium solution and $\Delta q_j(t)$ is a small perturbation about q_j^e. The static equilibria are computed by minimizing the uncoupled elastic portion of Equation 2.63 to obtain five equilibrium equations, which are then numerically solved. The stability of each solution is determined by evaluating the positive definiteness of the Jacobian matrix found from the equilibrium equations, as outlined in Section 2.3. Substituting Equation 4.1 into Equations 2.63 and 2.67 yields their linearized form about a particular q_j^e as shown below.

$$[M]\{\Delta\ddot{q}\} + [D]^e\{\Delta\dot{q}\} + [K]^e\{\Delta q\} + [\Theta]\{v\} = \{F\} \tag{4.2}$$

$$[\Theta]^T\{\Delta\dot{q}\} + [C_p]\{\dot{v}\} = \frac{1}{R}\{v\} \tag{4.3}$$

Since $\Delta q_j(t)$ is assumed to be small, its higher ordered terms in the nonlinear stiffness matrix $[K(q)]$ and damping matrix $[D(\dot{q}]$ can be neglected and what remains are only linear terms. Harmonic excitation is assumed for $f(t)$ in the forcing vector $\{F\} = \ddot{f}\{F_b\}$, which results in harmonic response for $\{\Delta q\}$ and $\{v\}$, where ω is the frequency, i is the imaginary number, a_b is the base acceleration, and $\{Q\}$, $\{V\}$, and $\{F_b\}$ are the corresponding amplitude vectors. These are shown below.

$$\{F\} = \{F_b\}\, a_b e^{i\omega t} \tag{4.4a}$$

$$\{\Delta q\} = \{Q\}\, e^{i\omega t} \tag{4.4b}$$

$$\{v\} = \{V\}\, e^{i\omega t} \tag{4.4c}$$

Substituting the assumed solutions into Equations 4.2 and 4.3 yields their steady state forms as

$$\left(-\omega^2[M] + i\omega[D] + [K]^e\right)\{Q\} + [\Theta]\{V\} = a_b\{F_b\} \tag{4.5}$$

$$i\omega[\Theta]^T\{Q\} + \left(i\omega[C_p] - \frac{1}{R}[I]\right)\{V\} = 0 \tag{4.6}$$

where $[I]$ is the identity matrix. The output voltage can now be found from Equation 4.6 as

$$\{V\} = \frac{-i\omega[\Theta]^T\{Q\}}{i\omega[C_p] - \frac{1}{R}[I]} \tag{4.7}$$

Substituting Equation 4.7 into Equation 4.5 yields

$$\left(-\omega^2[M] + i\omega[D] + [K]^e - \frac{i\omega[\Theta][\Theta]^T}{i\omega[C_p] - \frac{1}{R}[I]}\right)\{Q\} = a_b\{F_b\} \tag{4.8}$$

Both sides of Equation 4.8 are then multiplied by $e^{i\omega t}$ and rearranged to obtain the electromechanically coupled curvature to base acceleration FRF as shown below.

$$\Delta q_j^{FRF}(\omega) = \frac{\{\Delta q\}}{a_b e^{i\omega t}} = \left(-\omega^2[M] + i\omega[D] + [K]^e - \frac{i\omega[\Theta][\Theta]^T}{i\omega[C_p] - \frac{1}{R}[I]}\right)^{-1}\{F_b\} \tag{4.9}$$

The short and open circuit curvature to base acceleration FRFs can be obtained by letting the load resistance $R \to 0$ and $R \to \infty$, respectively. The relative out-of-plane displacement to base acceleration FRF is obtained by inserting Equation 4.9 into Equation 2.46 without $f(t)$ as seen below.

$$w^{FRF}(x, y, \omega) = \frac{1}{2}(\Delta q_1^{FRF}x^2 + \Delta q_2^{FRF}y^2 + \Delta q_3^{FRF}x^2y^2 + \Delta q_4^{FRF}x^4 + \Delta q_5^{FRF}y^4) \tag{4.10}$$

The velocity to base acceleration FRF can then be found from Equation 4.10 with the following equation [119].

$$\dot{w}^{FRF}(x,y,\omega) = \frac{1}{i\omega} + i\omega w^{FRF}(x,y,\omega) \tag{4.11}$$

Alternatively, the voltage to base acceleration FRF can be obtained by first solving Equation 4.8 for $\{Q\}$ as given below.

$$\{Q\} = \left(-\omega^2[M] + i\omega[D] + [K]^e - \frac{i\omega[\Theta][\Theta]^T}{i\omega[C_p] - \frac{1}{R}[I]}\right)^{-1} a_b \{F_b\} \tag{4.12}$$

Equation 4.12 is then substituted into the output voltage in Equation 4.7 and multiplying both sides by $e^{i\omega t}$ and rearranging results in the voltage to base acceleration FRF such that

$$v_k^{FRF}(\omega) = \frac{\{v\}}{a_b e^{i\omega t}} = \frac{-i\omega[\Theta]^T}{i\omega[C_p] - \frac{1}{R}[I]} \left(-\omega^2[M] + i\omega[D] + [K]^e - \frac{i\omega[\Theta][\Theta]^T}{i\omega[C_p] - \frac{1}{R}[I]}\right)^{-1} \{F_b\} \tag{4.13}$$

The undamped vibration modes are obtained by solving the homogeneous form of Equation 4.8 where there is no external forcing. This combined with the short and open circuit electrical boundary conditions imposed on the MFCs respectively result in the lowest and highest stiffness forms as shown below.

$$\left(-\omega_{sc}^2[M] + [K]^e\right)\{Q\}_{sc} = 0 \tag{4.14}$$

$$\left(-\omega_{oc}^2[M] + [K]^e - \frac{[\Theta][\Theta]^T}{[C_p]}\right)\{Q\}_{oc} = 0 \tag{4.15}$$

Equations 4.14 and 4.15 are solved for the eigenvalues, or the short and open circuit natural frequencies ω_{sc} and ω_{oc} and the corresponding eigenvectors $\{Q\}_{sc}$ and $\{Q\}_{oc}$, which lead to the mode shapes through Equation 4.10. For a lightly damped system, the modal damping ratios have a negligible effect on the damped natural frequencies, and are nearly identical to the undamped frequencies.

4.2.2 Mode Shapes

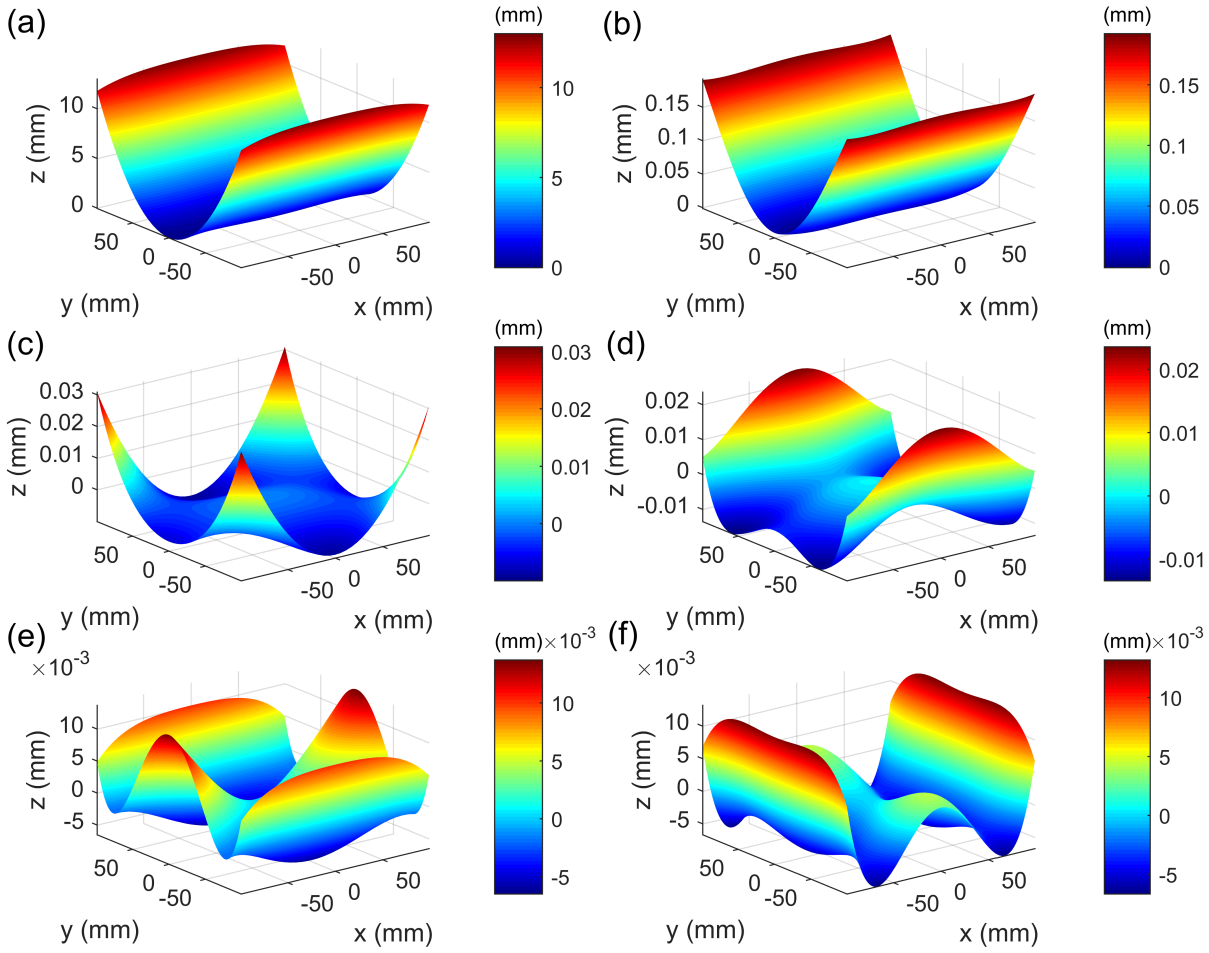

Figure 4.2: (a) Static cylindrical configuration of stable state I and the normalized open circuit out-of-plane mode shapes of $[0^{MFC}/90^{MFC}]_T$ laminate about state I at (b) 25.12 Hz, (c) 216.78 Hz, (d) 311.95 Hz, (e) 446.25 Hz, and (f) 866.04 Hz.

The out-of-plane normalized mode shapes found from Equation 4.15 is presented in Figure 4.2 with the open circuit boundary condition for both MFCs. With Figure 4.2(a) showing the static shape for state I, the first 5 elastic modes relative to to this state are at 25.12 Hz, 216.78 Hz, 311.95 Hz, 446.25 Hz, and 866.04 Hz. At the fundamental frequency of 25.12 Hz, the laminate exhibits a plate bending mode with a cylindrical shape similar to that of the static configuration. The second to fifth mode shapes still retain symmetry and show the influence of the higher ordered terms in the out-of-plane displacement shape function in Equation 4.10. Due to decreasing deflection magnitudes as the modal frequencies increase, the high amplitude motion that cross-well oscillations require occur around the first bending mode and so this is where frequency sweep ranges are set. The modal frequencies for state II are identical to state I and their mode shapes are orthogonal to those of state I.

4.2.3 Damping Parameters

To incorporate damping forces into the equations of motion, the ith natural frequency ω_{ni} and corresponding damping ratio ζ_i must first be found according to Equation 2.66. The quadrature peak picking method [133] is used to obtain these parameters from experimental corner velocity to base acceleration FRFs of the $[0^{MFC}/90^{MFC}]_T$ laminate for both stable states as shown in Figure 4.3. These low amplitude FRFs are measured during forward frequency sweeps from 10 Hz to 45 Hz at 0.05 g to minimize nonlinear effects while both MFCs are in open circuit. The damping ratio for the ith mode is given below.

$$\zeta_i = \frac{\omega_{bi} - \omega_{ai}}{2\omega_{ni}} \tag{4.16}$$

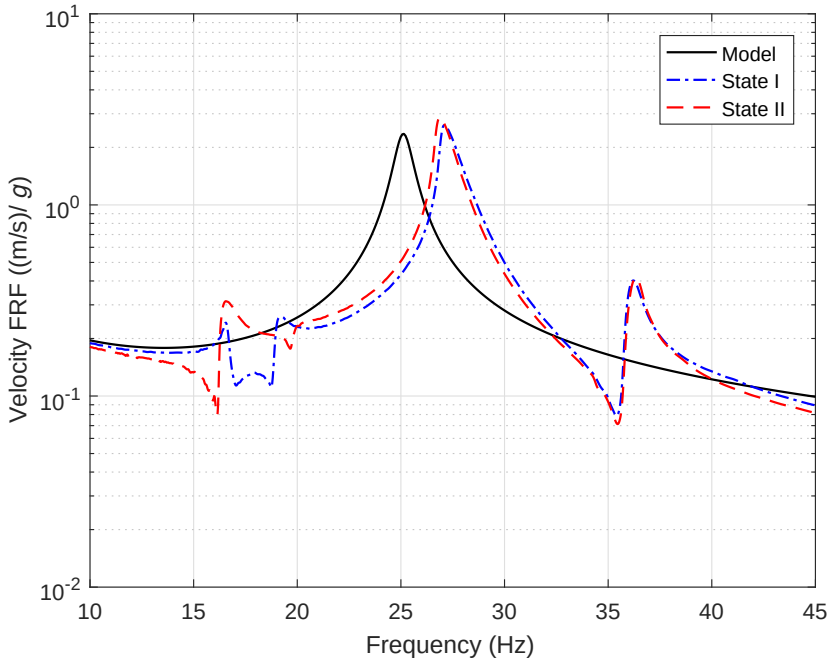

Figure 4.3: Open circuit corner velocity to base acceleration frequency response functions of $[0^{MFC}/90^{MFC}]_T$ laminate for both stable states.

The frequencies ω_{ai}, ω_{bi}, and ω_{ni} satisfy the following condition where $|H(\omega_{ni})|$ is FRF magnitude at resonance as shown below.

$$|H(\omega_{ai})| = |H(\omega_{bi})| = \frac{|H(\omega_{ni})|}{\sqrt{2}} \tag{4.17}$$

For states I and II, the first bending mode is at 27.09 Hz and 26.88 Hz and the second twisting mode is at 36.22 Hz and 36.34 Hz, respectively. Although stiffness softening still exists in the first bending mode, this effect is minimal and the experimental FRFs provide reasonable estimates of the modal frequencies. With higher forcing amplitudes however, ω_{ni} shifts further from increased softening and causes the mass and stiffness damping coefficients α and β in Equation 2.66 to become variable, which forces the damping matrix in Equation 2.65 to be amplitude dependent. In

practice, the damping coefficients found from Figure 4.2 are applied for all forcing levels in subsequent simulations by assuming that they are simple approximations for higher forcing amplitudes. Due to the shaker setup providing an elastic support at the center of the laminate, an rigid body rotation mode is also seen at 16.58 Hz for both states.

With the natural frequencies for the bending and twisting modes, the corresponding damping ratios, mass, and stiffness damping coefficients for both states are found and shown in Table 4.1. α and β are computed according to the first two elastic modes in Equation 2.66. Although the damping matrix is heavily proportional to the mass matrix as observed with Rayleigh damping at low frequencies [134], the bistable system is found to be sensitive to the stiffness proportional damping, and thus cannot be neglected even if the stiffness damping coefficient is near zero. In the presented work, the damping parameters for state I are used for all simulations.

Table 4.1: Damping ratios and coefficients of the $[0^{MFC}/90^{MFC}]_T$ laminate.

State	Damping Ratio ζ_1	Damping Ratio ζ_2	Mass Damping Coefficient α	Stiffness Damping Coefficient β
I	0.0166	0.0125	5.667	$1.346{\cdot}10^{-9}$
II	0.0159	0.0114	5.221	$7.138{\cdot}10^{-6}$

With identical excitation inputs, the analytical corner velocity to base acceleration FRF from Equation 4.11 for state I is also presented in Figure 4.3. The load resistance for both MFCs are set to the DAQ input impedance of 10 GΩ, which represents the experimental open circuit condition. Only a single FRF curve from the model is shown due to state II yielding identical results as state I. The analytical first bending mode at 25.12 Hz is in good agreement with the experimental results where the percent errors are 7.8% and 7.0% for states I and II, respectively. The slight under-prediction can be attributed to the variable curvatures in the higher ordered shape functions which mitigate the artificial plate stiffness causing models to over-predict the fundamental frequency

[94, 95]. Since the rigid body rotation mode at 16.58 Hz is due to the joint flexibility of the stinger to magnet interface holding the laminate, this experimental imperfection is not predicted by the model. The twisting mode is also absent due to the choice of generalized curvature coordinates made in Equation 2.46, where the higher ordered terms yield modes with higher frequencies after the first bending mode. However, only the first bending mode is of interest since the subsequent modes are outside the frequency range where cross-well oscillations occur. The FRF amplitude of the first mode is under-predicted due to the experimental damping parameters. Although theses values could be empirically tuned to match the experimental FRF amplitude, the ratio between the mass and stiffness damping coefficients cannot be obtained without the second twisting mode.

4.3 High Amplitude Frequency Sweeps

Based on where the linear vibration modes are, forward and backward frequency sweeps at higher amplitudes are both experimentally conducted and numerically simulated to characterize the nonlinear dynamic regimes of the $[0^{MFC}/90^{MFC}]_T$ bistable laminate. Their electromechanical responses are examined for the purpose of providing model validation. The sweeps range from 10 Hz to 34 Hz, which encompass the first plate bending mode of each state. During testing, the time histories of the base acceleration, corner velocity, MFC 1 and MFC 2 open circuit voltages are recorded every 0.5 Hz. This procedure is done for input accelerations of 0.5 g to 4 g in steps of 0.5 g for both initial states. The corner location is chosen for velocity measurements because it is the only point on the laminate to have significant out-of-plane amplitudes for both stable configurations, which makes it appropriate for measuring cross-well vibrations from a single location.

4.3.1 State Space Form

To match the experimental data with model predictions, the time histories of the corner velocity, MFC 1, and MFC 2 open circuit voltages during sweeps are obtained from the state space form of the equations of motion in Equations 2.63 and 2.67. Note that harmonic forcing in Equation 2.63 is modelled with the following base excitation function

$$f(t) = A_f sin(\omega_f t) \tag{4.18}$$

where ω_f and A_f are the forcing frequency and amplitude, respectively. The state space form is given below

$$\{\dot{p}_1\} = \{p_2\} \tag{4.19a}$$

$$\{\dot{p}_2\} = [M]^{-1} \left(\{F\} - [\Theta]\{p_3\} - [D(p_2)] - [K(p_1)]\right) \tag{4.19b}$$

$$\{\dot{p}_3\} = [C_p]^{-1} \left(\frac{1}{R}\{p_3\} - [\Theta]^T \{p_2\}\right) \tag{4.19c}$$

where the state variables are defined as $\{p_1\} = \{q\}$, $\{p_2\} = \{\dot{q}\}$, and $\{p_3\} = \{v\}$. Equations 4.19a-4.19c are assembled in MATLAB and numerically evaluated with the *ode15s* ordinary differential equation solver. Before the frequency sweeps are performed, the initial conditions for $\{q\}$ are set to be the curvatures corresponding to either potential well, and $\{\dot{q}\} = \{v\} = 0$. During the sweeps for each frequency, the $\{q\}$, $\{\dot{q}\}$, and $\{v\}$ states corresponding to the final time step are used as the initial conditions for the next excitation frequency. This procedure accurately replicates the experimental sweep conditions and the resulting direction dependent hysteresis seen in the data. Corner velocity time histories are found by numerically differentiating corner out-of-

plane displacement data obtained from the curvatures $\{q\}$.

4.3.2 Peak to Peak Amplitudes with Stroboscopic Sampling

Peak to peak amplitudes of the recorded and simulated time histories are obtained with stroboscopic sampling at excitation frequencies over multiple forcing periods. The results from both initial states under 1 g, 2 g, and 3 g forcing inputs are respectively shown in Figures 4.4, 4.5, and 4.6 for analysis in this section. The remaining results for 0.5 g, 1.5 g, 2.5 g, 3.5 g, and 4 g are given in Appendix B. These plots are a combination of an FRF and a bifurcation diagram with the excitation frequency being the bifurcation parameter under constant acceleration amplitude [74]. For linear regimes, the sampled amplitude for a given excitation frequency appears as a single point while nonlinear responses are given by multiple points indicating the variation of amplitudes over several consecutive periods. 3 g is the lowest excitation level where all dynamic regimes are present for both states, and so the results for higher accelerations are not shown here. At 1 g in Figure 4.4, the majority of frequency responses are single-well oscillations as indicated by single points. The cluster of points per frequency at 2 g in Figure 4.5 suggest cross-well motion and their bandwidth grows with increased forcing levels, as seen for 3 g in Figure 4.6.

Note that Figures 4.4-4.6 do not include all coexisting solutions per sweep, but the ones shown are due to the nonlinearities inherent to the bistable laminate and their dependency on the initial conditions. These arise from the softening stiffness effect causing the reduction of resonant frequencies, sweep direction dependent hysteresis forcing the boundaries between single and cross-well regimes to shift, and the asymmetry of the bistable laminate's potential wells causing static state dependent responses and bandwidths [135]. As expected, the strength of these nonlinear ef-

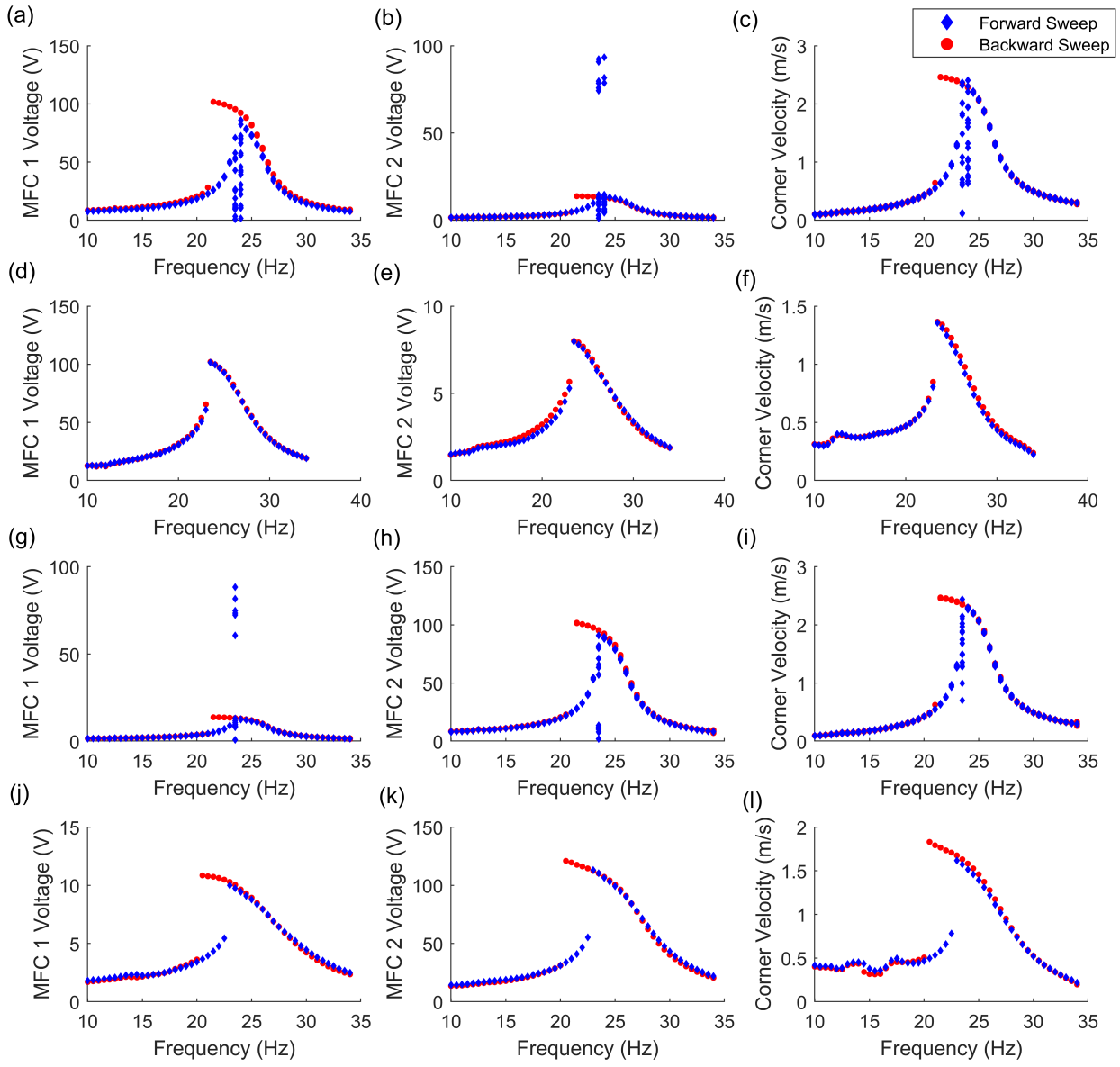

Figure 4.4: Peak to peak amplitudes from forward and backward frequency sweeps at 1 g. From initial state I, model predictions of (a) MFC 1 open circuit voltage, (b) MFC 2 open circuit voltage, (c) corner velocity, and experimental results for (d) MFC 1 open circuit voltage, (e) MFC 2 open circuit voltage, (f) corner velocity. From initial state II, model predictions of (g) MFC 1 open circuit voltage, (h) MFC 2 open circuit voltage, (i) corner velocity, and experimental results for (j) MFC 1 open circuit voltage, (k) MFC 2 open circuit voltage, (l) corner velocity.

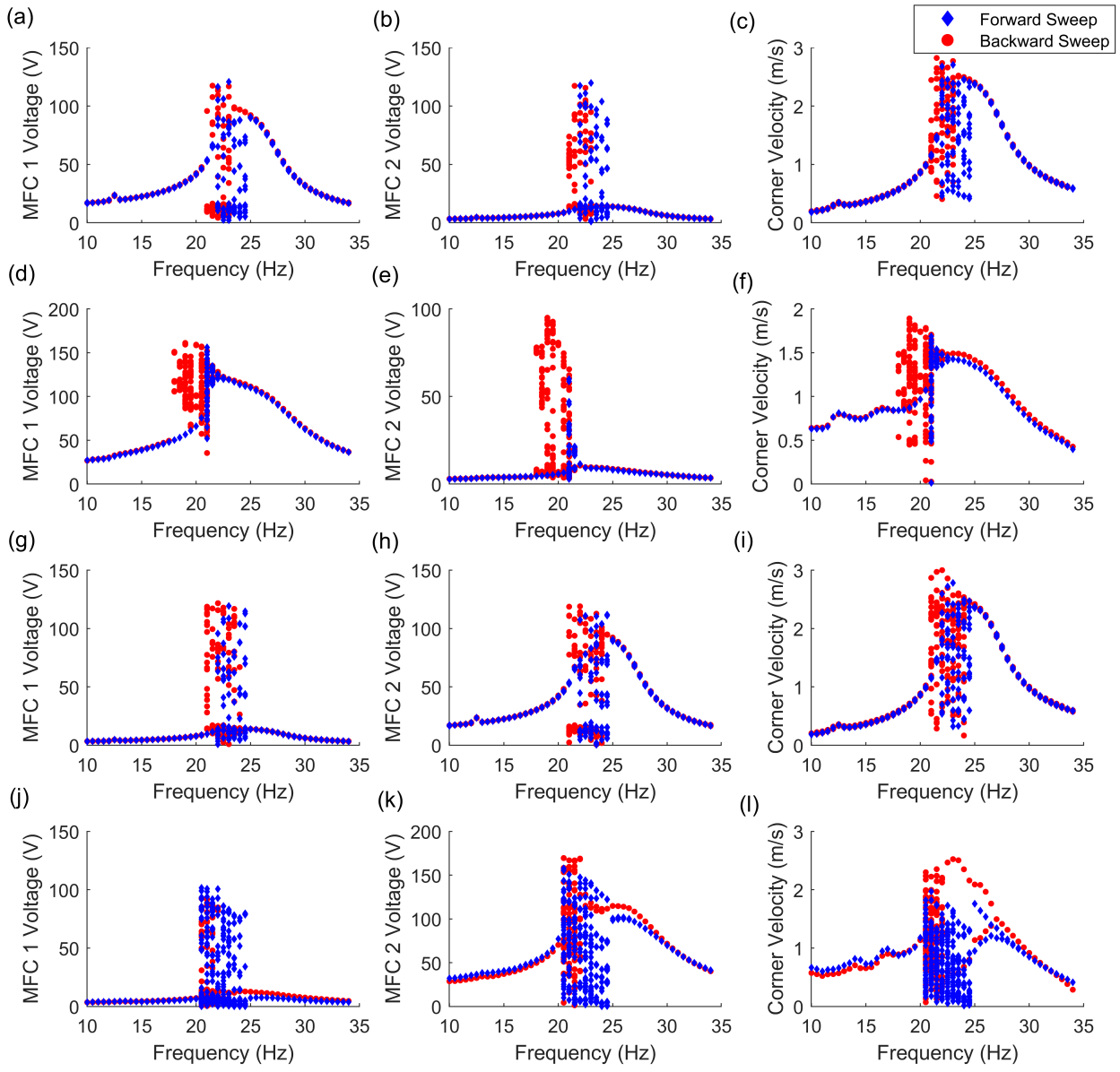

Figure 4.5: Peak to peak amplitudes from forward and backward frequency sweeps at 2 g. From initial state I, model predictions of (a) MFC 1 open circuit voltage, (b) MFC 2 open circuit voltage, (c) corner velocity, and experimental results for (d) MFC 1 open circuit voltage, (e) MFC 2 open circuit voltage, (f) corner velocity. From initial state II, model predictions of (g) MFC 1 open circuit voltage, (h) MFC 2 open circuit voltage, (i) corner velocity, and experimental results for (j) MFC 1 open circuit voltage, (k) MFC 2 open circuit voltage, (l) corner velocity.

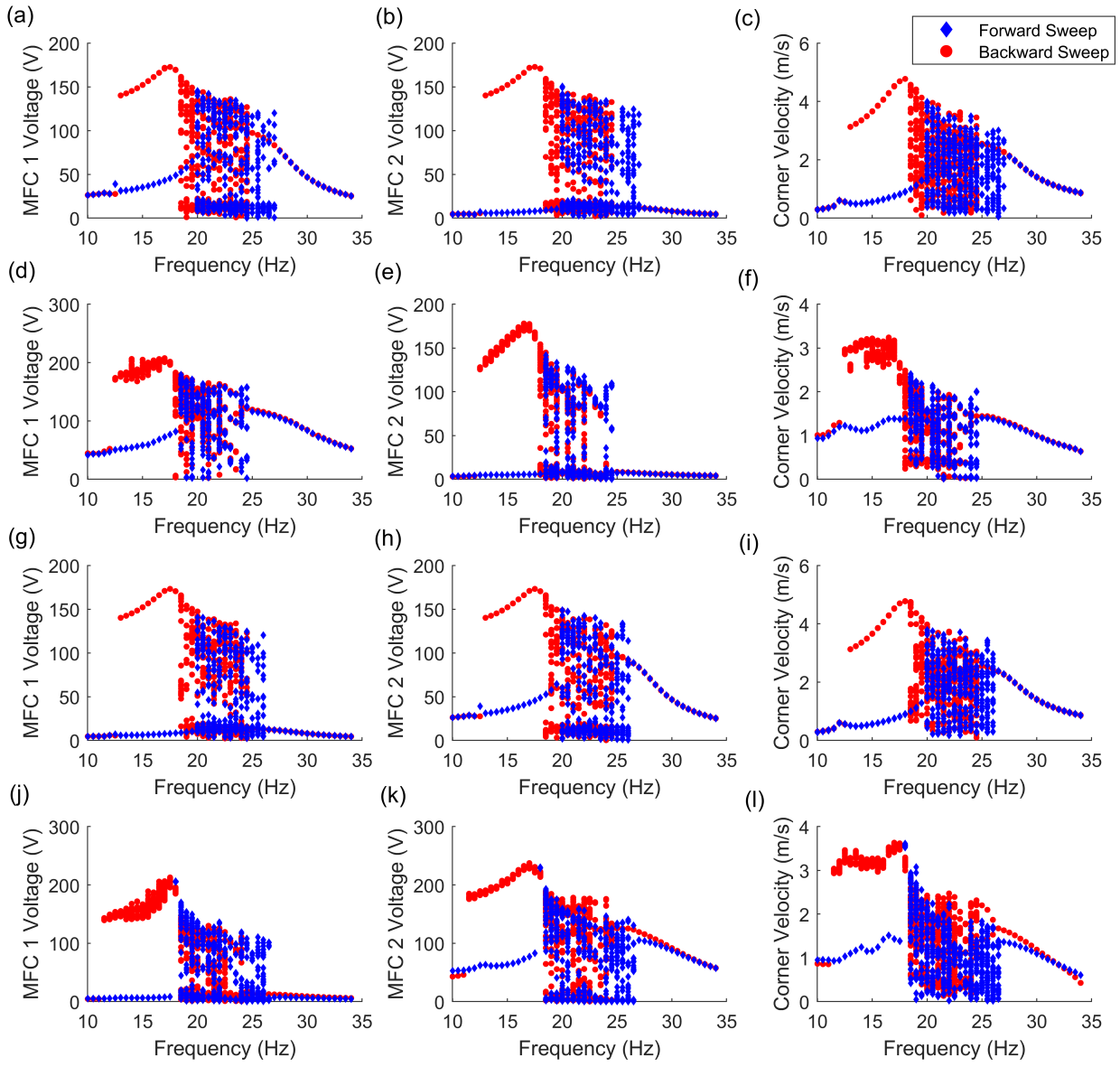

Figure 4.6: Peak to peak amplitudes from forward and backward frequency sweeps at 3 g. From initial state I, model predictions of (a) MFC 1 open circuit voltage, (b) MFC 2 open circuit voltage, (c) corner velocity, and experimental results for (d) MFC 1 open circuit voltage, (e) MFC 2 open circuit voltage, (f) corner velocity. From initial state II, model predictions of (g) MFC 1 open circuit voltage, (h) MFC 2 open circuit voltage, (i) corner velocity, and experimental results for (j) MFC 1 open circuit voltage, (k) MFC 2 open circuit voltage, (l) corner velocity.

fects increase with higher excitation levels. For both states and regardless of sweep direction, the softening effect pushes the resonant peak to peak amplitudes towards lower frequencies for the 1 g response, and for 2 g and 3 g the boundaries between single and cross-well regions are pushed below first plate bending mode even further. Hysteretic regions separating the jumps in amplitude also grow larger with increasing excitation levels. For example, this is experimentally observed in 3 g from 12.5 Hz to 18 Hz for state I and 11.5 Hz to 17.5 Hz for state II in Figure 4.6(d)-(f) and (j)-(l), respectively. At 3 g, the backward sweeps induce high amplitude limit cycle oscillations while the forward sweeps remain linear over the same bandwidths. In contrast, the forward sweeps extend the cross-well regions at their upper boundaries. These differences are a consequence of different solutions gaining and losing stability at various frequencies, and are not necessarily the only steady-state solutions in existence. The transition into limit cycle oscillations during backward sweeps may be due to the coalescence of vibrational energy carried by the cross-well motion at higher excitation frequencies. It does not exist in the forward sweep due to the laminate being in low energy orbit when approaching the requisite limit cycle frequencies.

The higher order analytical model is able to predict the electromechanical response and dynamic nonlinear effects observed in the experimental results. The stiffness softening effect is present in all simulations where the first resonant peak is pushed below its natural frequency, which translates to cross-well dynamics occurring mostly below the first bending mode. Hysteretic regions are present between forward and backward sweeps which separate the boundaries between single and cross-well regimes. In Figure 4.6(a)-(c) and (g)-(i), forward sweeps extend the cross-well boundary past the first mode while backward sweeps induce high amplitude limit cycle oscillations not seen in forward sweeps from 13 Hz to 18 Hz. The strength of these nonlinear effects increase with rising acceleration levels as experimentally observed. How the MFC voltage

and corner velocity peak to peak amplitudes vary across frequency ranges are well correlated between simulations and experimental data and the cross-well bandwidth extension observed with increasing acceleration levels is also captured by the model. In addition, there is good agreement for the dynamic regimes exhibited by the laminate as functions of the excitation frequency and acceleration levels. The voltage amplitudes show better agreement than the corner velocity amplitudes, which are generally over-predicted by the model. Following the model's lower stiffness trends in Figure 4.3, the simulations predict cross-well oscillations to occur at the lower acceleration level of 1 g while they were first observed at 1.5 g in the experimental data. There is a clear correlation between corner velocity and voltage magnitudes where cross-well oscillations induce higher amplitudes than linear responses. Single-well MFC 1 voltages are much greater than those of MFC 2 while the laminate is oscillating about state I. This is due to the dominant strain direction aligning with MFC 1's piezoceramic fiber direction associated with the primary d_{11} effect while MFC 2 is mostly strained in the electrode direction normal to the fibers. The ratio of voltages between the MFCs is flipped for single-well vibrations about state II. During cross-well oscillations, the difference in voltage output is greatly reduced since both MFCs are being strained in the primary fiber direction.

While the two initial states lead to minor differences in the simulated dynamic regimes, these are not as pronounced as the differences in the experimental results. In the latter, state II consistently yields higher peak to peak amplitudes for the MFC voltages and the corner velocity with larger cross-well bandwidths when compared to state I. This is due the bistable laminate's asymmetric potential wells where state II has lower static out-of-plane displacements and a shallower well depth when compared to state I. Thus the vibrational barrier for snap-through is lower for state II. The shape discrepancy may be caused by manufacturing imperfections in the layup align-

ment, a nonuniform epoxy bond line, or the variation of electromechanical properties between the two MFCs as explained in Chapter 3. These geometric and material imperfections are difficult to measure or control, and the model does not account for these factors. Therefore the simulated amplitudes and cross-well bandwidths between the two initial states are mostly consistent with each other. The model also does not predict the MFC 1 over MFC 2 cross-well voltage bias for state I and MFC 2 bias over MFC 1 for state II. These effects cause the simulations to largely under-predict MFC 1 and over-predict MFC 2 voltages for state I and vice versa for state II. In the experiments, the laminate has a tendency to favor the initial state and not fully penetrate the other potential well during cross-well oscillations, with varying degrees of penetration between dynamic regimes. This asymmetry of cross-well orbit is characterized by larger amplitudes about the initial state which causes the voltage bias between the MFCs.

4.4 Characterization of Dynamic Regimes

Although the sampled peak to peak amplitudes in Figures 4.4-4.6 from the frequency sweeps provide a broad overview of the data, various cross-well regimes cannot be distinguished from the collection of points at each step. Aside from limit cycle oscillations, other nonlinear regimes are associated with lower response amplitudes and include intermittencies, chaotic, and subharmonic oscillations. Several points for a given frequency indicate the presence of harmonics while a much denser cluster of points suggest chaotic behavior. However, the limited detail makes identification of dynamic regimes per frequency difficult, especially for intermittencies consisting of both periodic and aperiodic characteristics. Therefore, the steady state time histories and their corresponding Fourier spectra, phase portraits, and Poincaré maps for each type of nonlinear response

are analyzed for distinguishing characteristics and matched between simulation and experimental data. This section evaluates example cases for each type of response found in the 3 g frequency sweeps, which is the lowest excitation level where all dynamic regimes are present for both states, and therefore a suitable input parameter for laminate response and performance characterization. The frequency content is obtained with Fast Fourier Transform (FFT) of time histories obtained during the sweeps. If there is a mismatch in excitation frequency between the model and the test results for the same cross-well behavior, then the closest frequency that yields the desired behavior is chosen for the simulation.

4.4.1 Periodic Oscillations

The analysis for high amplitude limit cycle oscillations is presented in Figure 4.7 for excitation parameters of 14.5 Hz and 3 g during backward sweep with initial state I. The model is able to predict this form of periodic oscillation involving continuous snap-through motion between the laminate's two potential wells which allows a periodic high-energy orbit to be sustained. It is associated with the largest velocity and voltage amplitudes out of all dynamic regimes due to the periodic attractor motion having the most penetration into both potential wells. The simulated periodic attractor motion has full and equal potential well penetration which results in identical voltage output between the MFCs as shown in Figure 4.7(a). This is in contrast to the experiment where an asymmetry in the high-energy orbit is a result of the laminate's bias towards the initial state I, and this leads to a slight difference in open circuit voltage between the MFCs as seen in Figure 4.7(b). Specifically, MFC 1 exhibits higher output voltages than MFC 2 and this is correlated by the slightly larger corner velocities while the laminate is in state I. However, this bias

is observed to diminish with higher acceleration levels, and limit cycle oscillations show the lowest amount of trajectory asymmetry out of all cross-well regimes. Combined with the larger corner velocity and voltage amplitudes and the highest frequency of snap-through events within the same number of forcing periods, it is the most favorable regime for energy harvesting applications.

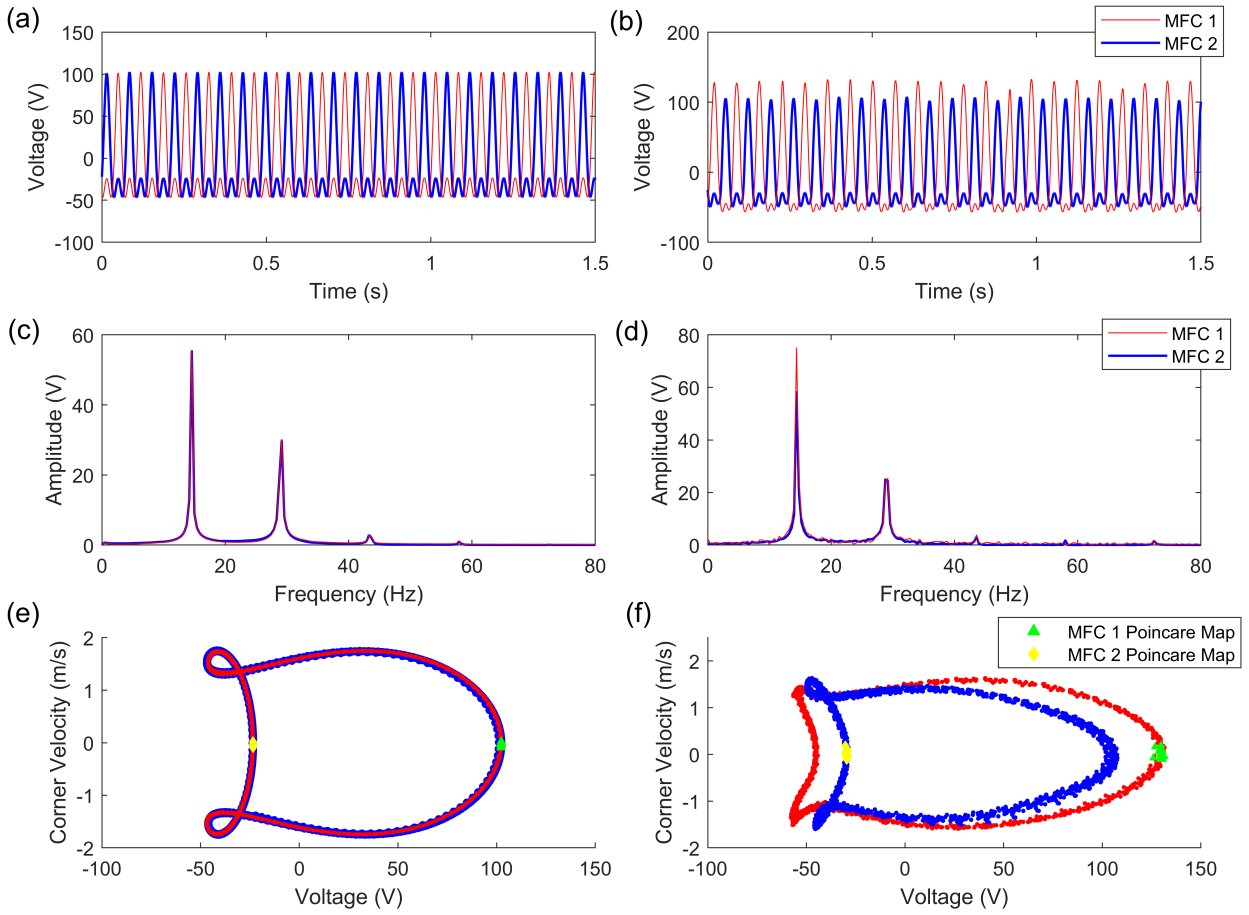

Figure 4.7: MFC 1 and MFC 2 open circuit voltage under limit cycle oscillations as time histories from the (a) model, (b) experiment, as FFTs from the (c) model, (d) experiment, and as phase portraits and Poincaré maps from the (e) model, and (f) experiment at 14.5 Hz during 3 g state I backward sweep.

Aside from the asymmetry, the model successfully simulates the defining characteristics seen in the experimental response of the laminate. As shown in Figure 4.7(e) and (f), the 90° phase difference between the voltage and corner velocity allow the electromechanical phase portrait to

be generated and shows an asymmetric orbit for both MFCs. The sharp decline in voltage occurs when the MFCs are not under the primary d_{11} effect and this behavior alternates between MFCs according to their 180° phase difference as seen in the single-periodic response of the Poincaré maps and voltage time histories. The Fourier spectra in Figure 4.7(c) and (d) also show good agreement where the main harmonic (i.e. ω) of 14.5 Hz is dominant over its 2ω and 3ω superharmonic components with the latter harmonics contributing much less vibrational energy.

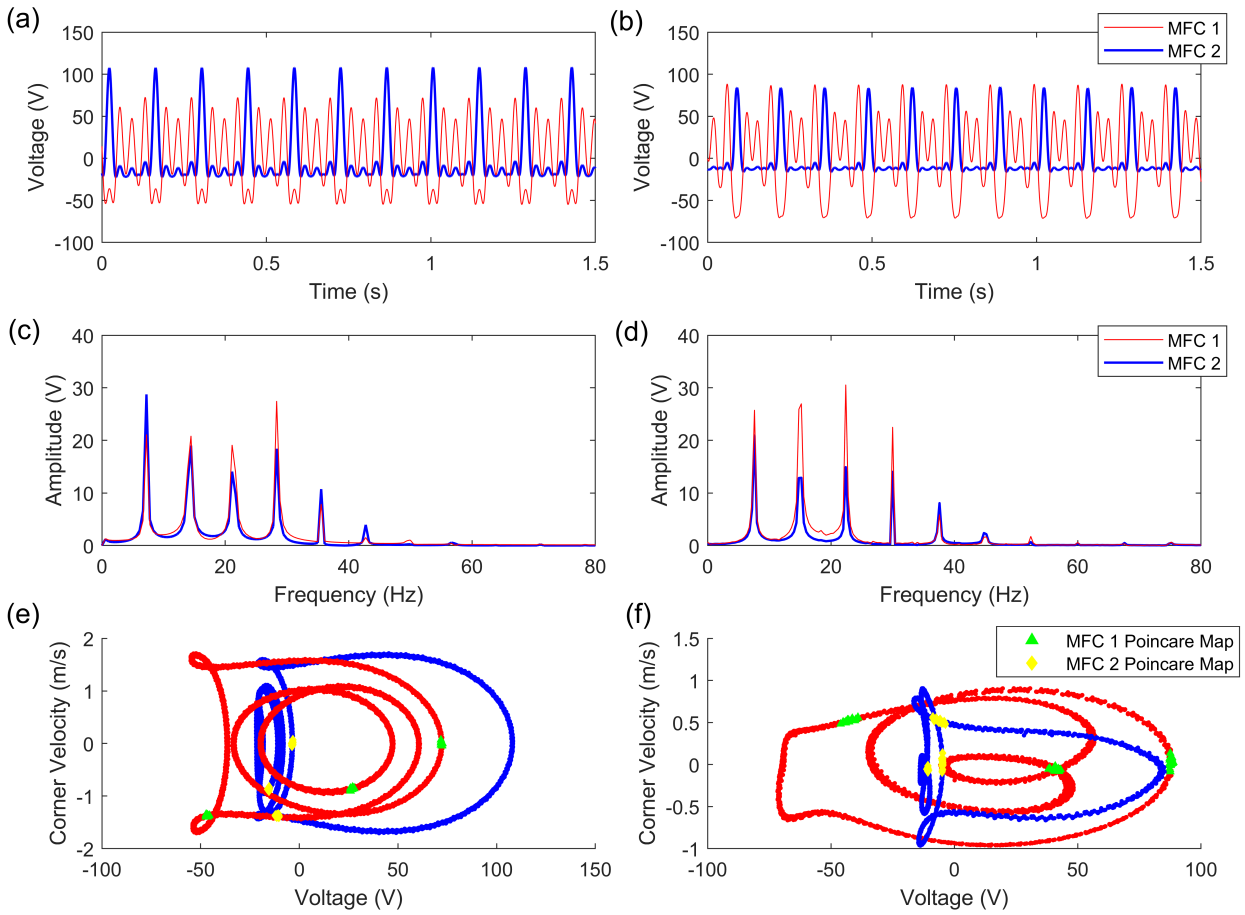

Figure 4.8: MFC 1 and MFC 2 open circuit voltage under subharmonic oscillations as time histories from the (a) model, (b) experiment, as FFTs from the (c) model, (d) experiment, and as phase portraits and Poincaré maps from the (e) model, and (f) experiment during 3 g state I backward sweep at 21.34 Hz and 22.5 Hz for the model and experiment, respectively.

Subharmonic oscillations are shown in Figure 4.8 with the excitation frequencies of 21.34 Hz

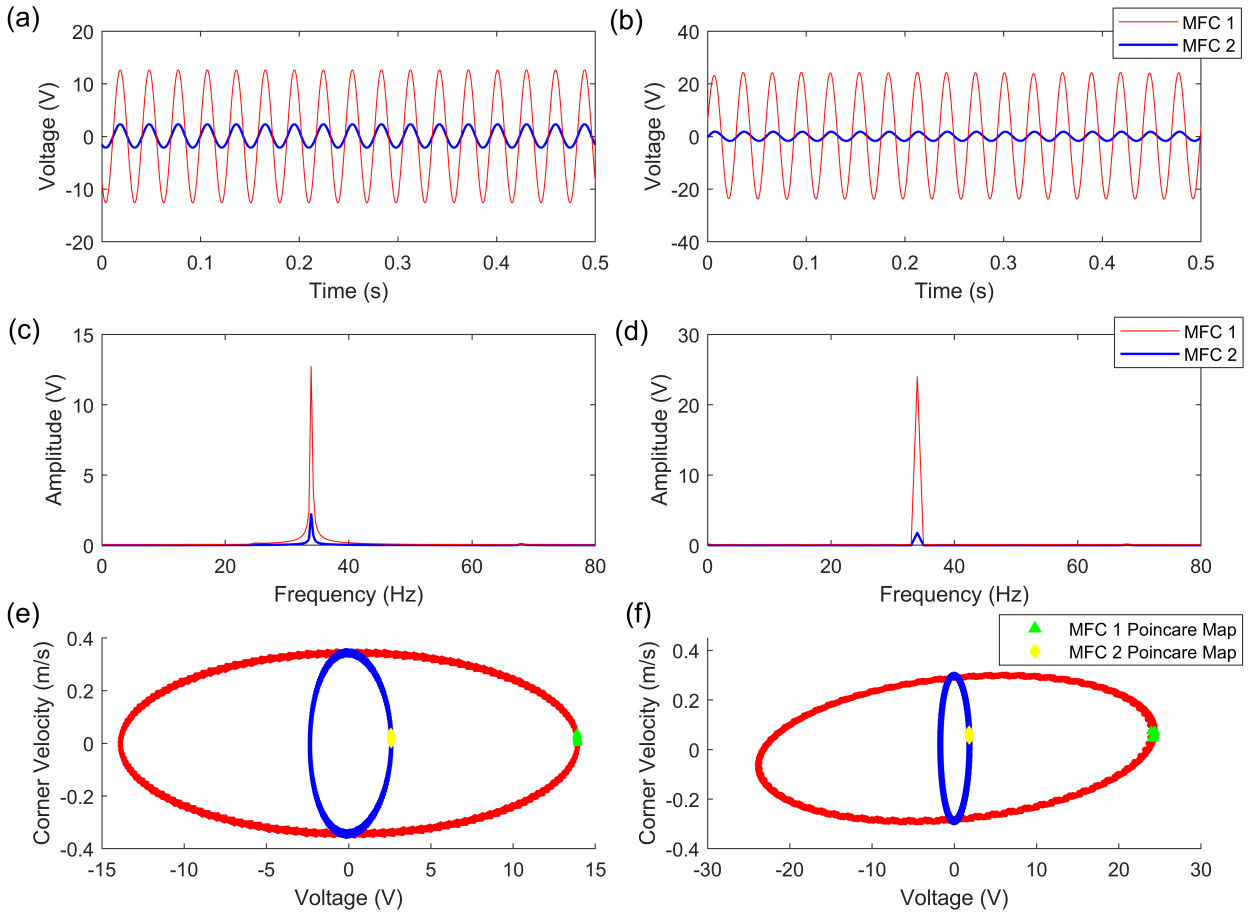

Figure 4.9: MFC 1 and MFC 2 open circuit voltage under linear oscillations as time histories from the (a) model, (b) experiment, as FFTs from the (c) model, (d) experiment, and as phase portraits and Poincaré maps from the (e) model, and (f) experiment at 34 Hz during 3 g state I backward sweep.

and 22.5 Hz respectively for the simulation and experiment while under the 3 g initial state I backward sweep. Specifically, period-3 oscillations that takes three forcing periods to complete a full cycle are shown [136]. It should be noted that throughout the simulated and experimental frequency sweeps across all excitation levels, a large range of subharmonic oscillations from period-2 to period-9 are exhibited by the laminate while under both single and cross-well vibrations. The simulated period-3 oscillations are obtained from separate backward sweeps with smaller frequency step sizes because the original increment of 0.5 Hz does not yield the desired periodicity.

The model successfully predicts the period-3 behavior that can be seen in the stroboscopically sampled Poincaré maps in as seen in Figure 4.8(e) and (f), where they show three distinct clusters within the electromechanical phase portraits for both MFCs. The FFTs in Figure 4.8(c) and (d) also shows this with the presence of order-1/3 harmonic components ($\omega/3$, $2\omega/3$, $3\omega/3$, etc) that share a fairly even distribution of the voltage amplitude. Out of all cross-well regimes, subharmonic oscillations retain the most asymmetric orbits with the vast majority of vibration centered around the initial state I. This leads to the largest discrepancy in output voltage between the two MFCs, but this phenomenon is not predicted by the model. The laminate's final periodic response is single-well linear oscillations as seen in Figure 4.9 at the non-resonant frequency of 34 Hz. As expected, the two MFC voltage signals are in phase with each other, MFC 1 outputs much larger voltages, the only frequency component is the excitation signal, and the Poincaré maps indicate a single-periodic response.

4.4.2 Aperiodic Oscillations

Shown in Figure 4.10, the next identified cross-well regime is chaotic oscillations from the 3 g initial state I backward sweep where the excitation frequency is 19 Hz for the simulation and 18.5 Hz for the experiment. To obtain enough data, the electromechanical phase portraits are generated from separately simulated and measured time histories of 15 minutes. Similar to periodic oscillations, the model is able to predict the unique properties of chaotic oscillations observed in the experimental results. The voltage time histories in Figure 4.10(a) and (c) reveal that the laminate motion involving snap-through events never quite repeats itself, though there are passages of nearly recurrent behavior, and therefore remains completely aperiodic [137]. The FFTs in Figure 4.10(b)

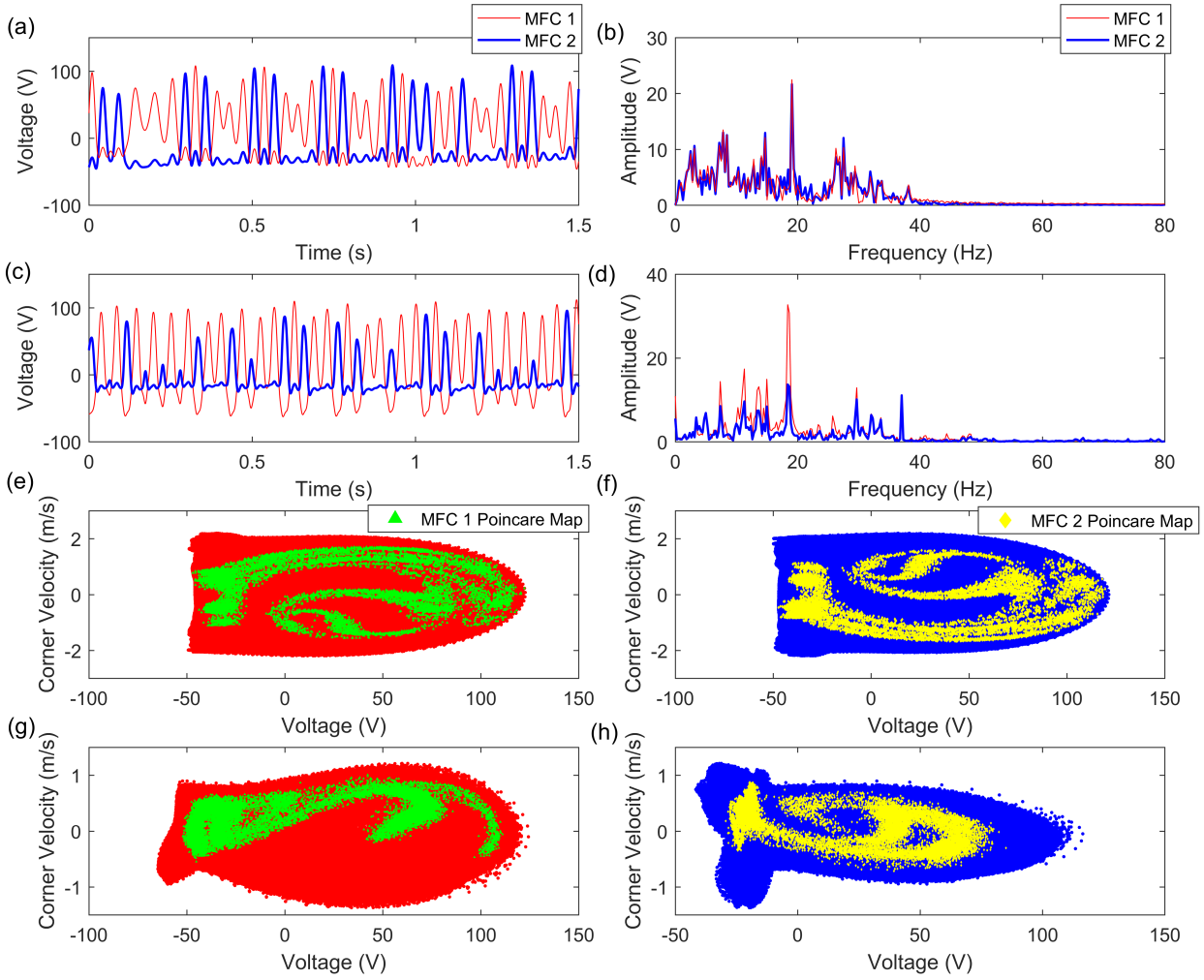

Figure 4.10: Model predictions of MFC 1 and MFC 2 open circuit voltages under chaotic oscillation with (a) time histories, (b) FFTs at 19 Hz during 3 g state I backward sweep, and experimental MFC 1 and MFC 2 open circuit voltages with (c) time histories and (d) FFTs at 18.5 Hz during 3 g state I backward sweep. Corresponding phase portraits and Poincaré maps for simulated open circuit voltages for (e) MFC 1, (f) MFC 2, and experimental open circuit voltages for (g) MFC 1, and (h) MFC 2.

and (d) show a much more broadband spectrum with the primary component being the excitation frequency, but energy is present over a wide range of frequencies. Its aperiodic nature prevent any distinct harmonics to exist within the laminate response.

The simulated Poincaré maps within the phase portraits in Figure 4.8(e)-(h) reveal an asymmetric strange attractor motion that qualitatively is in agreement with their experimental counterparts. However, the asymmetry in cross-well orbit still exists within the experimental results and is more severe than the periodic limit cycle oscillations as shown through the larger open circuit voltage difference between the MFCs. Although the phase portrait trajectories escape the potential well of state I and displays cross-well behavior, the majority of vibration is centered around state I with much less penetration into state II. The simulations still show full trajectory penetration into both potential wells and any difference in MFC voltages is a result of the sampled time history window and not the observed initial state bias. The infrequent snap-through events, lower velocities, and output voltages suggest the chaotic response to be less favorable for harvesting power than the high energy orbits of limit cycle oscillations.

The final cross-well response of the $[0^{MFC}/90^{MFC}]_T$ laminate is intermittency between chaotic and limit cycle oscillations from the 3 g initial state I backward sweep where the excitation frequencies are 18.5 Hz and 18 Hz for the simulation and experiment, respectively. This regime is shown in Figure 4.11. While the excitation parameters are kept constant, intermittency is defined as the sporadic switching between two qualitatively different responses, namely chaotic and limit cycle oscillations, and occurs only at the excitation frequency boundaries between these two regimes [138]. Both the simulated and experimental voltage time histories in Figure 4.11(a) and (b) display nearly periodic limit cycle motion irregularly interrupted by chaotic bursts. In the FFTs in Figure 4.11(c) and (d), the presence of chaos causes the spreading of vibrational energy into

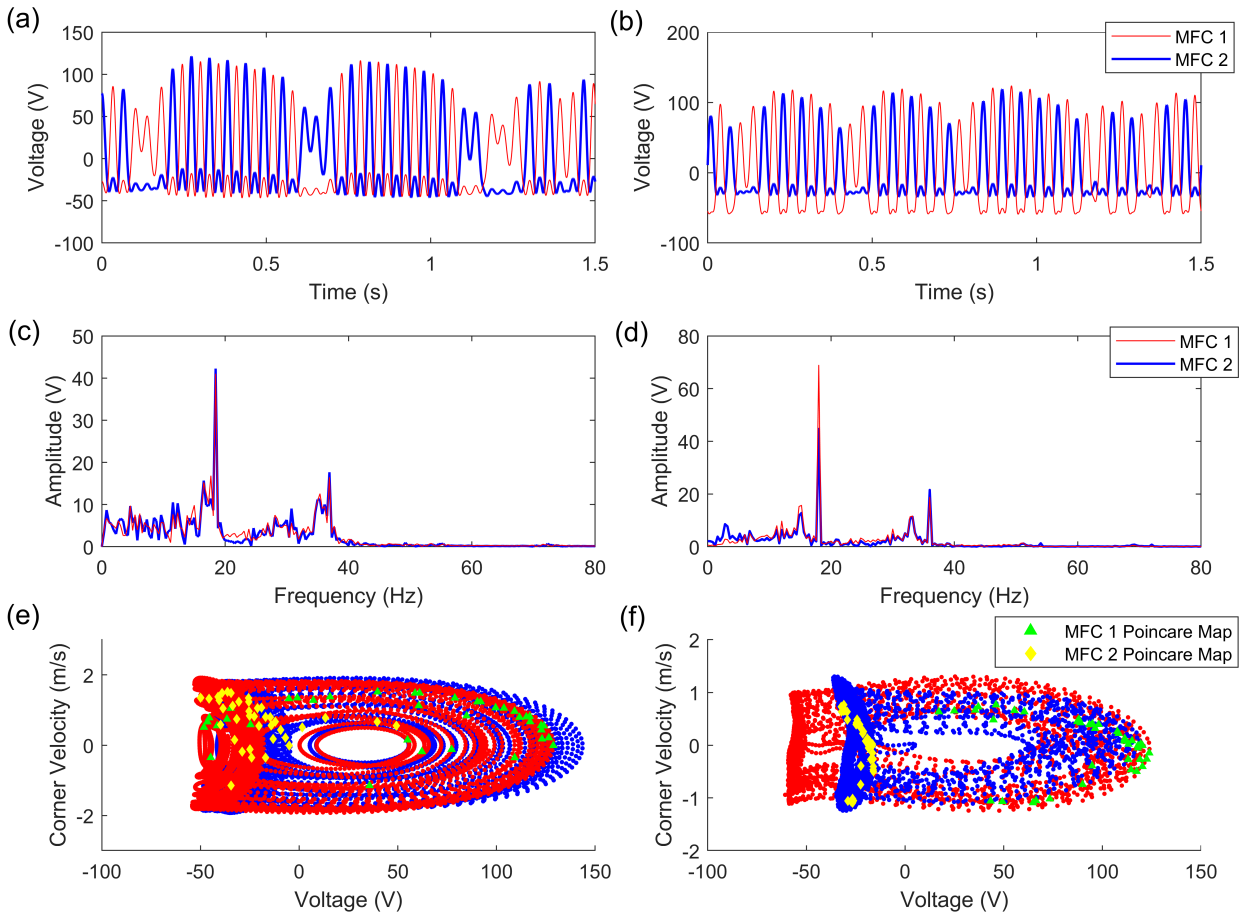

Figure 4.11: MFC 1 and MFC 2 open circuit voltage under intermittency between limit cycle and chaotic oscillations as time histories from the (a) model, (b) experiment, as FFTs from the (c) model, (d) experiment, and as phase portraits and Poincaré maps from the (e) model, and (f) experiment during 3 g state I backward sweep at 18.5 Hz and 18 Hz for the model and experiment, respectively.

frequencies other than the main harmonic and superharmonic components attributed to limit cycle oscillations. The behavior of this regime suggest that its energy harvesting capability is between those of limit cycle and chaotic oscillations. In the Poincaré maps in Figure 4.11(e) and (f) within the electromechanical phase portraits, the loss of periodicity is seen through spreading of sampled points when compared to the tight clusters of limit cycle oscillations in Figure 4.7(e) and (f). Although the asymmetric cross-well orbit and the resulting MFC 1 voltage bias over MFC 2 are

present in the experimental results, its severity is less than chaotic oscillations. Like the previous dynamic regimes, the simulations for intermittency show equal penetration into both potential wells. In the experiments, intermittency is also found between subharmonic and chaotic regimes although it is not presented here. At 20.5 Hz from initial state I for example, irregular alternation of period-2 and chaotic oscillations induces aperiodicity within the subharmonic response, where vibrational energy is distributed into the frequency spectrum between the order-1/2 harmonic components ($\omega/2$, $2\omega/2$, $3\omega/2$, etc).

4.5 Response Maps Across Excitation Parameters

A summary of the observed dynamic responses within the simulated and experimental frequency sweeps at all acceleration levels are shown in Figure 4.12. Nonlinearities involving stiffness softening and hysteresis are minimal at lower accelerations and resonance is still very close to the first bending mode for both states. As the excitation level rises, the regional hysteretic differences between forward and backward sweep directions grow while the resonant peaks are pushed to lower frequencies. Chaotic oscillations first appear at 1 g in the forward sweep simulations for both initial states in Figure 4.12(a) and (b) and at 1.5 g in the experimental initial state II forward sweep in Figure 4.8(d). From these locations, the cross-well bandwidth primarily expands in the sweep direction as the acceleration input increases. The overall growth trend of the cross-well bandwidth and general locations of nonlinear regimes are well correlated between the model and the experimental results. While the former yields consistent dynamic regimes between initial states with only minor differences, the contrast is much greater for the latter due to the previously discussed potential well asymmetry.

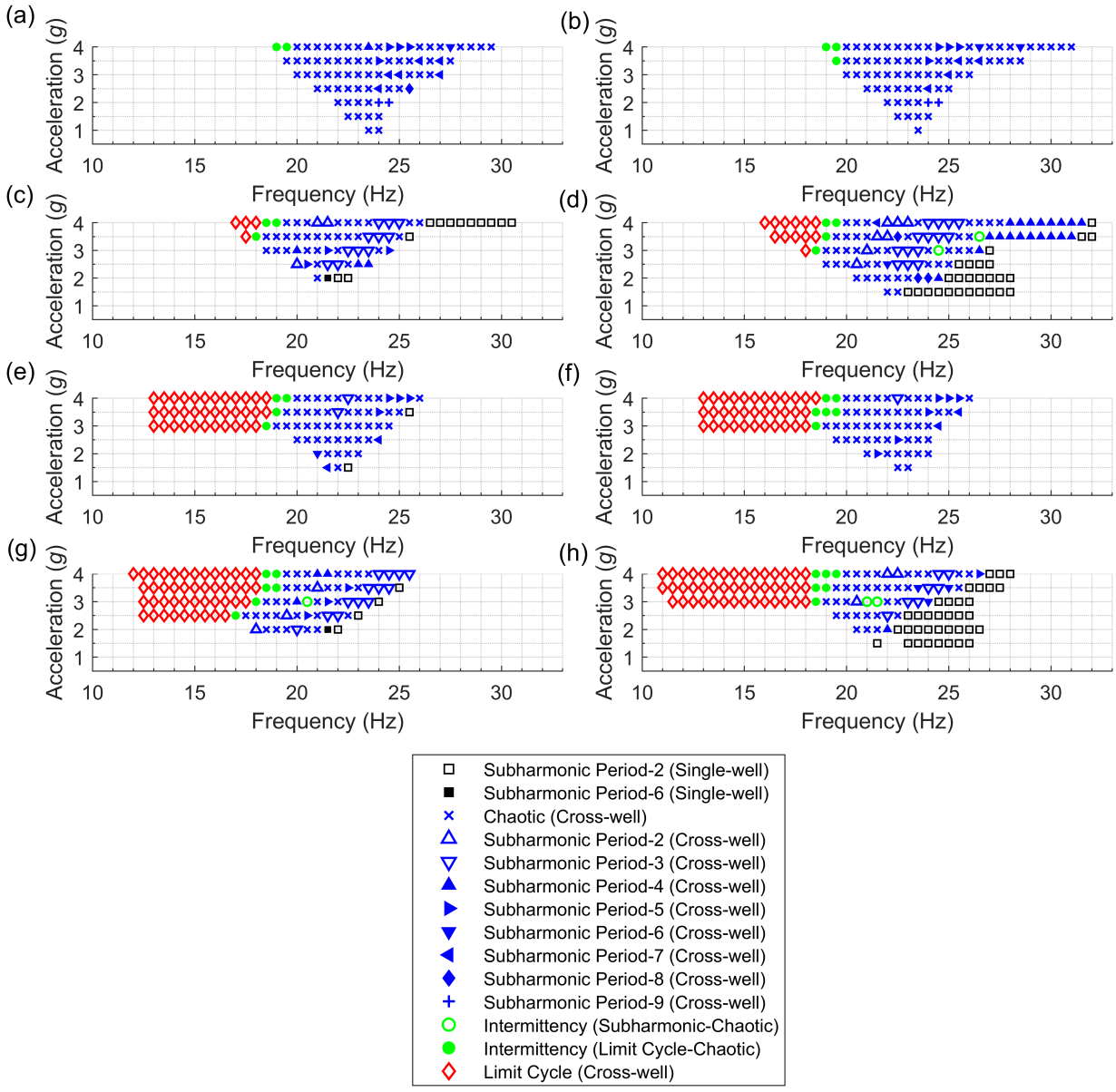

Figure 4.12: Observed dynamic behaviors within forward frequency sweeps from 0.5 g to 4 g for simulations with initial (a) state I and (b) state II, and for experiments with initial (c) state I and (d) state II. Observed dynamic behaviors within backward frequency sweeps from 0.5 g to 4 g for simulations with initial (e) state I and (f) state II, and for experiments with initial (g) state I and (h) state II.

From Figure 4.12, several nonlinear phenomena responsible for changes in dynamic behavior can be identified. Saddle node bifurcation is responsible for the large amplitude jump between single-well and cross-well oscillations as separated by hysteresis below the softened resonant frequency. At higher forcing amplitudes, the cross-well regime becomes limit cycle oscillations. As the excitation frequency is increased, chaotic bursts within the periodic motion become more frequent and longer through intermittency as shown in Figure 4.11. This continues until the cross-well motion becomes fully chaotic, and this phenomenon is consistently exhibited by both the model and experiment. The route to chaos from above the resonant frequency can be attributed to periodic doubling bifurcation. As the excitation frequency decreases, single-well period-1 oscillations branch into period-2 oscillations until quickly becoming chaotic. This is more consistently observed in the experiment and the model only shows this bifurcation in Figure 4.12(e) due to the combination of it occurring under a much smaller bandwidth and the large sweep step size.

A notable difference between the model and experiment is that the former does not predict any intermittencies between chaotic and subharmonic oscillations. In the simulations, the laminate is qualitatively observed to show near subharmonic behavior that is ultimately chaotic according to how they are characterized in Figures 4.8 and 4.10. Due to the varying degrees of chaos being entirely present within the nonlinear response, the laminate never sporadically switches between fully subharmonic and fully chaotic oscillations. Another distinction is that experimental cross-well regimes first appear at lower excitation frequencies than the model predictions even though its linear bending mode is at a higher frequency. This is due to experimental stiffness softening effect being stronger than the model's as acceleration levels increase. Differences in where cross-well subharmonic and chaotic oscillations occur near the softened resonant frequency and the periodicity of subharmonic oscillations can be attributed to variable initial conditions present in

frequency sweeps. The laminate may have multiple regimes coexist under the same input, but only one is physically realizable depending on the initial conditions to the excitation. In sweeps, the laminate's final state serve as initial conditions to the next frequency and these are inconsistent between the model and experiment.

4.6 Energy Harvesting Capability

4.6.1 Power Generation of Each Regime

Excluding limit cycle oscillations, Figure 4.6 shows that the open circuit voltage amplitudes of cross-well regimes are similarly ranged and this holds true for various acceleration levels. Even after accounting for the steady rise in maximum amplitudes towards the onset of limit cycle oscillations at 3 g, it is unclear how each regime's average power output will compare relative to each other due to their intermixing in this bandwidth, and warrants further investigation. To evaluate the energy harvesting capability of the $[0^{MFC}/90^{MFC}]_T$ bistable laminate, resistor sweeps are experimentally conducted across 1 kΩ, 1.78 kΩ, 3.16 kΩ, 5.62 kΩ, 10 kΩ, 15.8 kΩ, 25.1 kΩ, 39.8 kΩ, 63.1 kΩ, 100 kΩ, 178 kΩ, 316 kΩ, 562 kΩ, and 1 MΩ in order to match the impedance of each MFC to the load resistance, which maximizes their power output.

With each MFC, the sweeps are run at 3 g for the observed regimes outlined in the previous section, and the results are presented in Figures 4.13 and 4.14 for states I and II, respectively. A summary of the resistor sweep results and the power output of each dynamic regime are presented in Table 4.2. The excitation frequencies are where the maximum power is generated for each regime with the exception of cross-well subharmonic oscillations, which are chosen to be period-3

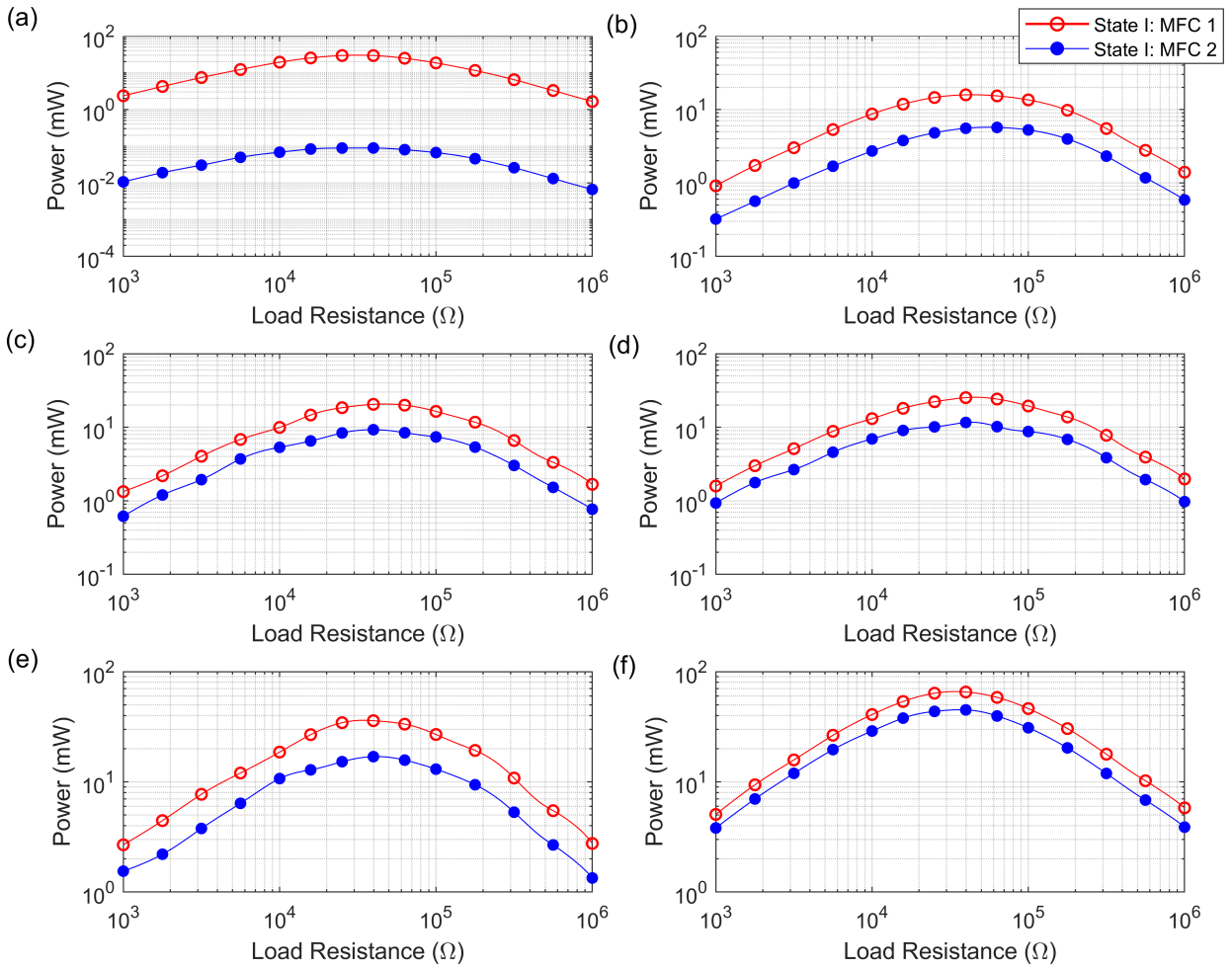

Figure 4.13: Power outputs of MFC 1 and MFC 2 for initial state I during resistor sweeps at 3 g for (a) linear at 24.5 Hz, (b) subharmonic period-3 at 22.5 Hz, (c) intermittency subharmonic-chaotic at 20.5 Hz, (d) chaotic at 18.5 Hz, (e) intermittency limit cycle-chaotic at 18 Hz, and (f) limit cycle oscillations at 17 Hz.

for both states to allow fair comparison. As observed in [69], the range of load resistances in the sweeps do not suppress any of the nonlinear phenomena (i.e. shunt damping effect) exhibited by the laminate, and so it is able to maintain the cross-well responses resulting from each excitation frequency. This is certainly favorable for examining the harvesting performance of each dynamic regime, and is likely due to the mechanical nonlinearity inherent to bistability being dominant over the piezoelectric coupling of the MFCs.

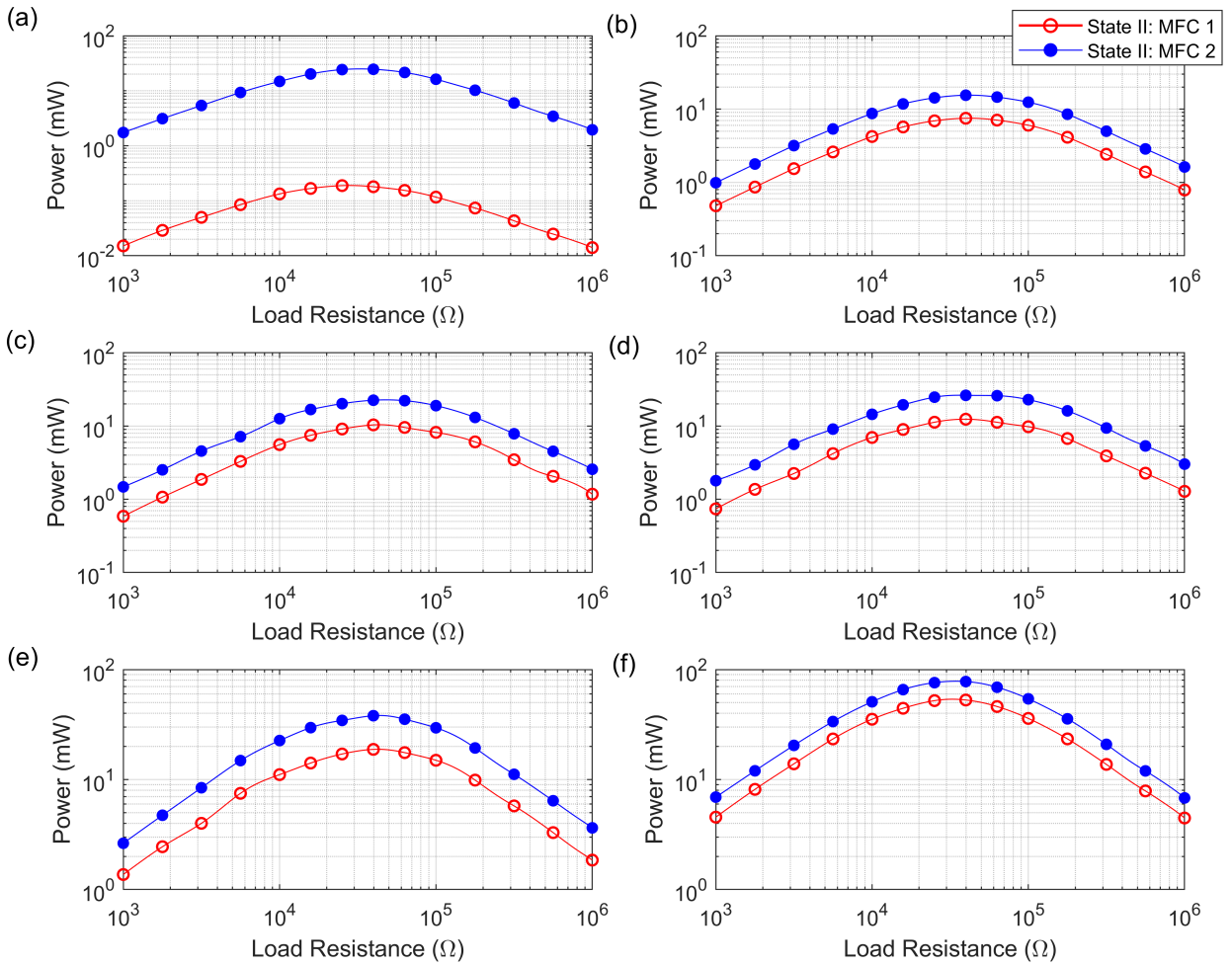

Figure 4.14: Power outputs of MFC 1 and MFC 2 for initial state II during resistor sweeps at 3 g for (a) linear at 26.5 Hz, (b) subharmonic period-3 at 23 Hz, (c) intermittency subharmonic-chaotic at 21 Hz, (d) chaotic at 19 Hz, (e) intermittency limit cycle-chaotic at 18.5 Hz, and (f) limit cycle oscillations at 17.5 Hz.

Figures 4.13 and 4.14 show that the optimal resistor load is 39.8 kΩ for every regime except for the linear response in state I, which is 25.1 kΩ. High amplitude limit cycle oscillations output the most power at 110.3 mW and 130.7 mW for states I and II, with the least amount of difference between the MFCs due to the minimal asymmetry that exists in the high energy orbit. This is the most favorable regime for energy harvesting as the single-periodic cross-well orbit allow snap-through events to most frequently and consistently occur, and the large associated velocities

Table 4.2: Resistor sweep results and peak power output of each dynamic regime at 3 g excitation.

Dynamic Regime	Initial State	Frequency (Hz)	Optimal Load Resistance (kΩ)	MFC 1 Power (mW)	MFC 2 Power (mW)	Total Power (mW)
Linear Single-well	I	24.5	25.1	29.41	0.09	29.50
	II	26.5	39.8	0.18	24.57	24.75
Subharmonic Cross-well	I	22.5	39.8	15.82	5.54	21.37
	II	23	39.8	7.50	15.45	22.95
Intermittency Subharmonic	I	20.5	39.8	20.49	9.26	29.76
	II	21	39.8	10.37	22.51	32.88
Chaos	I	18.5	39.8	25.26	11.61	36.87
	II	19	39.8	12.39	26.25	38.64
Intermittency Limit Cycle	I	18	39.8	35.90	16.93	52.83
	II	18.5	39.8	18.81	38.07	56.88
Limit Cycle	I	17	39.8	65.35	44.99	110.34
	II	17.5	39.8	52.87	77.79	130.66

translate to deeper well penetration. The other cross-well responses show larger power gaps between the MFCs as the orbital asymmetry grows, and this is the maximum for linear oscillations due to their orbit about a single state allowing just one MFC to be operating in the d_{11} mode.

After limit cycle oscillations, the power generation of the regimes in descending order are intermittency between limit cycle and chaotic oscillations, chaos, single-well linear oscillations, intermittency between subharmonic and chaotic oscillations, and cross-well subharmonic oscillations for state I. The peak linear response outperforms cross-well subharmonic behavior since it is at the boundary between single and cross-well regimes which is near the reduced resonant frequency. Although linear maximum amplitudes may be lower as seen in Figures 4.5 and 4.6, Figure 4.8(a) and (b) reveal that snap-through occurs more infrequently for subharmonic oscillations and signifies that their peak amplitudes are hit less often when compared to other cross-well responses. It is interesting to see that the resonant single-well response of one MFC can outperform the cross-well power output of both MFCs in some cases. For state II, the performance order is the same

as state I except for linear oscillations now being placed between intermittency and cross-well subharmonic oscillations due to the peak linear response being further away from the resonance. Periodic regimes retain smooth power vs. load resistance peaks due to their consistent output while those with aperiodic behavior are more disjointed even when the measurements are averaged over long durations. When comparing the initial states, state II consistently has better cross-well performance with less separation between MFCs because of its lower critical out-of-plane displacements for initiating snap-through.

4.6.2 Inducing Asymmetry with Imperfections

Since the optimal resistor load of 39.8 kΩ is found to be common between almost all dynamic regimes across various frequencies, backward frequency sweeps at 3 g with this load resistance is conducted to evaluate the laminate's optimal power output across its first bending mode. The results are shown in Figure 4.15(a) and (b) for the model simulations and (e) and (f) for the experiment from both initial states. The responses per forcing frequency follows the trend seen in the Figure 4.6 amplitudes, where peak power is generated during high amplitude limit cycle oscillations. Near the cross-well boundary from 24 Hz to 25 Hz, MFC 1 in initial state I and MFC 2 in state II have higher average power while under single-well rather than cross-well vibrations. Even with the large jump in contribution from the other MFC during cross-well motion, the single-well near-resonance still generates more total power, albeit over a smaller portion of the cross-well bandwidth. However as the excitation frequency decreases, the cross-well power output overtakes that of the single-well response, and these trends can be seen in both the simulations and the experiment.

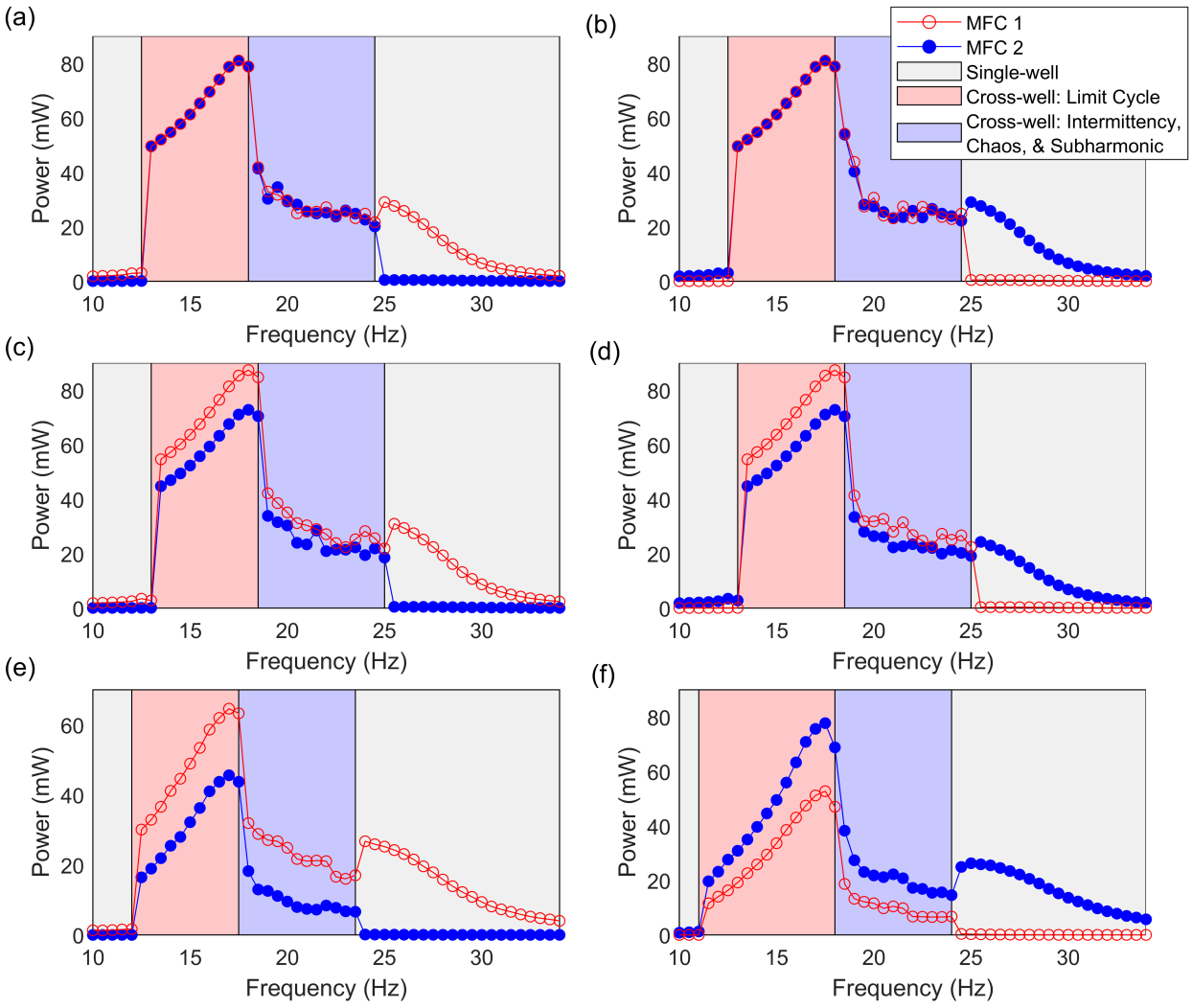

Figure 4.15: Average power output per MFC with 39.8 kΩ resistance load during 3 g backward frequency sweep. Ideal model results from initial (a) state I, (b) state II, imperfect model results from initial (c) state I, (d) state II, and experimental results from initial (d) state I, and (e) state II.

Even though the model and experiment show good agreement with regards to the variation of power output relative to the dynamic regime, the model shows nearly identical power generation between the MFCs and also between the initial states under periodic cross-well oscillations. Slightly more variation exists while the laminate is under aperiodic dynamics such as chaos or intermittency. In the experiment however, both MFCs generate more power during cross-well

oscillations from initial state II and exhibit lower power gaps across the spectrum due to the previously discussed potential well asymmetry. For the same reason, state II has larger bandwidth for both limit cycle oscillations and other cross-well regimes.

As previously discussed, imperfections within the laminate that arise from manufacturing errors are the cause of the mismatch in the experimental voltage and corner velocity responses between the $[0^{MFC}/90^{MFC}]_T$ laminate's two initial states. Although these factors cannot be easily controlled or quantified, their qualitative effects on the laminate response are evaluated to provide more insight into the experimental results. The idealized electromechanical model assumes a perfect layup, uniform thicknesses, and identical material properties between the two MFCs. If one of these assumptions are relaxed, then the asymmetric effects can be empirically predicted. Varying the ply thicknesses and piezoelectric constants between the MFCs in Chapter 3 created a discontinuity between the two stable branches through the elimination of the static pitchfork bifurcation behavior. This lead to geometric asymmetry between the two stable states observed in the experimental data. Similarly, imperfection is introduced in the dynamic model by raising the 0° MFC 2 ply thickness by 5% to induce larger static out-of-plane displacements for state I when compared to state II.

The average power output of each MFC connected to 39.8 kΩ resistor loads from the imperfect model is also presented in Figure 4.15(c) and (d) during 3 g backward frequency sweeps for both initial states. In addition to showing good agreement in the energy harvesting performance between the model and experiment, the effects of introducing imperfections can be assessed. With the ply thickness imperfection, power gaps are created between the MFCs during cross-well oscillations that more closely matches the experimental response for initial state I in Figure 4.15(c). This is due to the stable shape asymmetry causing larger strains within the laminate while vibrat-

ing about initial state I. This state has higher static out-of-plane displacements and so the laminate will reach larger amplitudes. For the initial state II in Figure 4.15(d), MFC 1 power still remains dominant over MFC 2 due to the aforementioned reason and the imperfect model not being able to replicate the laminate's tendency to favor the initial state during cross-well orbit. The empirically induced potential well asymmetry also does not yield the significant power output difference between the initial states that is observed in the experiment, with the only notable differences in the responses under single-well and aperiodic regimes. So while the effects of asymmetry can be partially predicted by empirically tuning geometric parameters from their idealized values, there are limitations to what can be accurately replicated. However, the experiment's deviation from the idealized electromechanical response of the laminate suggest that it does contain some forms of imperfection causing the asymmetric behavior.

4.6.3 Charging Durations and Snap-Through Actuation

With the peak power output and cross-well bandwidth of the laminate found to be sufficient at a reasonable excitation level, its energy harvesting capability is experimentally directed towards triggering snap-through motion between either stable states. To achieve this, the AC output of the MFCs must be rectified into a DC signal so that a storage component such as a battery or capacitor can be charged, then discharged as the voltage input for actuation. Although there are a wide range of piezoelectric energy harvesting circuits available in literature which focus on maximizing power transfer, a commercially available module is utilized for ease of implementation since the objective is to enable morphing. The self-powered ALD EH301A energy harvesting circuit rectifies the MFC output and charges its onboard capacitors until it reaches a high cutoff voltage of 5.2 V,

then discharges through an electrical load until the low cutoff voltage of 3.1 V is reached, at which point charging resumes and the cycle restarts.

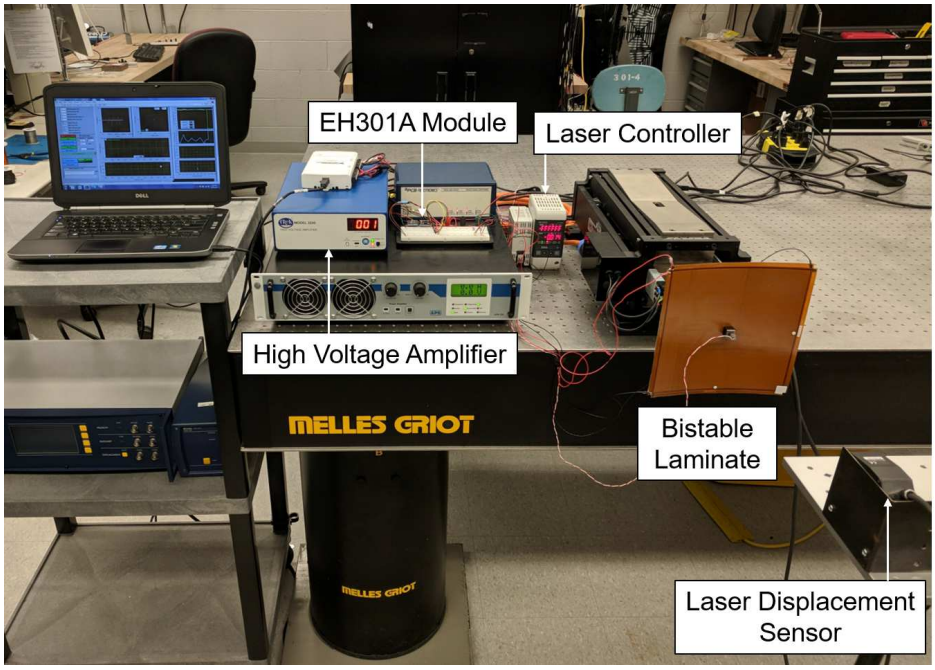

Figure 4.16: Experimental test setup for charging energy harvesting circuit and initiating snap-through morphing.

To initiate snap-through, only a single MFC needs to be actuated at a time. For the bistable $[0^{MFC}/90^{MFC}]_T$ laminate in state I, actuating MFC 1 past the limit voltage will cause snap-through to occur to the second stable branch, and the laminate will fully transition into state II when the voltage is removed. In state II, actuating MFC 2 will cause jump to the first stable branch in the same manner and state I is reached once the power is shut off. In Section 3.4.3, the limit voltages were experimentally found to be 860 V to MFC 1 for triggering snap-through from state I to II, and 630 V to MFC 2 for state II to I. It should be noted that any input that is larger than the limit voltage of each state will still cause snap-through.

Since the limit voltages are much greater than what the EH301A module or even the rectified

MFCs can supply, a high voltage amplifier is necessary for meeting the actuation requirements. Figure 4.16 presents the experimental setup used for charging the EH301A module which then discharges to a Trek 2220 high voltage amplifier that provides an amplification factor of 200 to the input signal. The amplified voltage is then supplied to either MFC for triggering snap-through and this event is measured with a Keyence LK-G402 laser sensor, which records the out-of-plane displacement time history at a laminate corner. The rest of the setup is similar to Figure 4.1 where LabVIEW records time history data and controls the shaker with the laminate attached. In morphing platforms where the Trek 2220 amplifier is impractical, the AVID Dual Channel High Voltage Driver could be used instead because it provides the lightweight and compact form needed for actuating MFCs in a small Unmanned Aerial Vehicle (UAV) [139].

Due to there being two MFCs outputting power under vibration, the connection scheme that yields the lowest charging duration must first be determined. Figure 4.17 shows the charging time history from 0 V to the high cutoff voltage of 5.2 V while the MFCs are connected to the EH301A module in series, parallel, and separately. The excitation input is 3 g at 17 Hz for state I and 17.5 Hz for state II, which correspond to the experimental high amplitude limit cycle oscillations with peak power outputs. For both states, the parallel connection outperforms other schemes due to the capacitance of MFCs being combined which raises the overall current output to the onboard capacitors of the module. This connection scheme compensates for the P1 type MFC's low capacitance and current output which are critical for minimizing charge durations.

In contrast, the series connection cuts the effective capacitance in half and reduces the overall current output which is correlated by its slowest charge times. Like the power measurements, the charging performance of each MFC is state dependent with MFC 1 having a lower time than MFC 2 for initial state I and vice versa for state II. In addition, the times to reach the high cutoff voltage

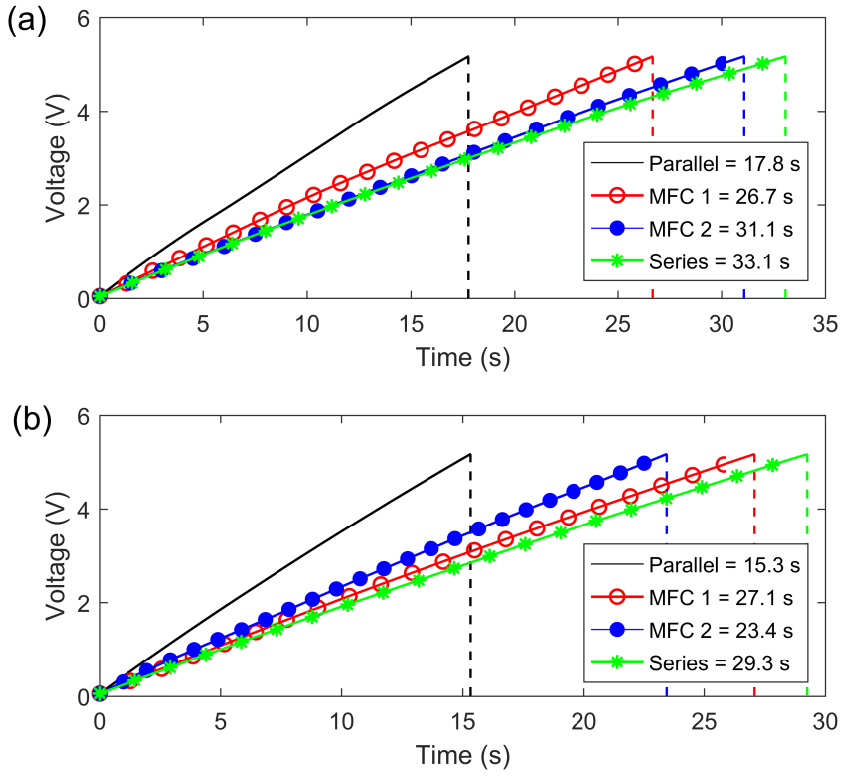

Figure 4.17: EH301A module charge durations at 3 g excitation with MFCs connected in parallel, series, and separately for initial (a) state I at 17 Hz and (b) state II at 17.5 Hz during limit cycle oscillations.

are consistently lower for state II when compared to state I. Although not shown here, the order of charge durations between the connection types are found to be consistent with the results in Figure 4.17 throughout all dynamic regimes for both states.

With the parallel connection between the MFCs confirmed to be the optimal scheme, the charging performance of the previously analyzed dynamic regimes listed in Table 4.2 are shown in Figure 4.18 at 3 g for both initial states while the MFCs are connected in parallel. Every type of response is able to successfully charge the EH301A module in under a minute, with limit cycle oscillations producing the fastest times at 17.8 s for initial state I and 15.3 s for state II. Periodic responses exhibit smooth charging curves due to their consistent output while any regimes

with chaotic behavior do not. For both states, the order of charge durations between the regimes match their order of power output with the exception of single-well linear oscillations retaining a faster time than chaotic oscillations for state I and intermittency between subharmonic and chaotic oscillations for state II.

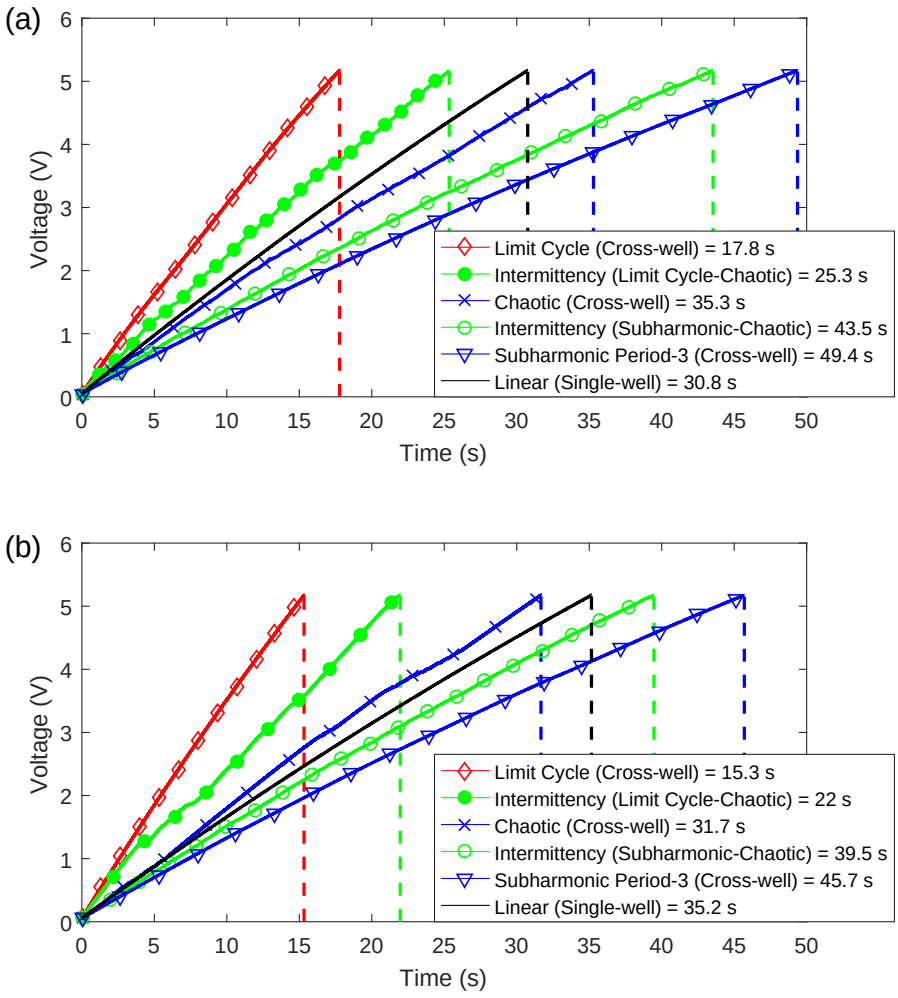

Figure 4.18: EH301A module charge durations at 3 g excitation with MFCs connected in parallel for initial (a) state I and (b) state II during all dynamic regimes and their frequencies listed in Table 4.2.

The discrepancies may be due to the MFCs being connected in parallel as opposed to the

separate measurements made for their power outputs, which results in constructive interference of the current output between the two MFCs. Regardless of regime, while one MFC is primarily strained in the piezoceramic fiber direction and has the dominant d_{11} response, the other MFC is simultaneously strained in the electrode direction and produces a much lower electromechanical response, and these responses are in phase. This can be seen in the time histories in Figures 4.7-4.11, where the phase difference between the two MFCs are identical for both the voltage and current. Under cross-well vibrations, the d_{11} responses alternate between the two MFCs whenever snap-through occurs, and MFC 1's d_{11} response is greater than MFC 2 for initial state I and vice versa for state II due to the previously discussed asymmetry of cross-well orbits. The parallel configuration favors the linear regime over chaos for state I and intermittency for state II since the primary MFC always operates in the d_{11} mode under linear oscillations while the cross-well regimes exhibit alternating d_{11} responses from both MFCs. However, other cross-well regimes such as limit cycle oscillations are still able to outperform linear vibrations due to the effective current output of the former being greater than that of the latter.

Once the EH301A module reaches the 5.2 V threshold from charging, the shaker is shut off and the module begins to supply the input voltage signal to connected amplifier. During this discharge phase, snap-through from state I to II and vice versa are achieved when the amplifier is connected to either MFC and turned on. This is evidenced by the corresponding discharge voltage and corner displacement time histories shown in Figure 4.19. snap-through occurs 1.3 s after the amplifier is turned on by supplying approximately 1000 V to either MFC, as seen in the large displacement jump followed by free vibration that settles into the opposing stable branch. Once the amplifier is shut off and the input voltage is released, the laminate fully settles into the other state and this is indicated by the much smaller change in displacement. Note that the discharge rate increases when

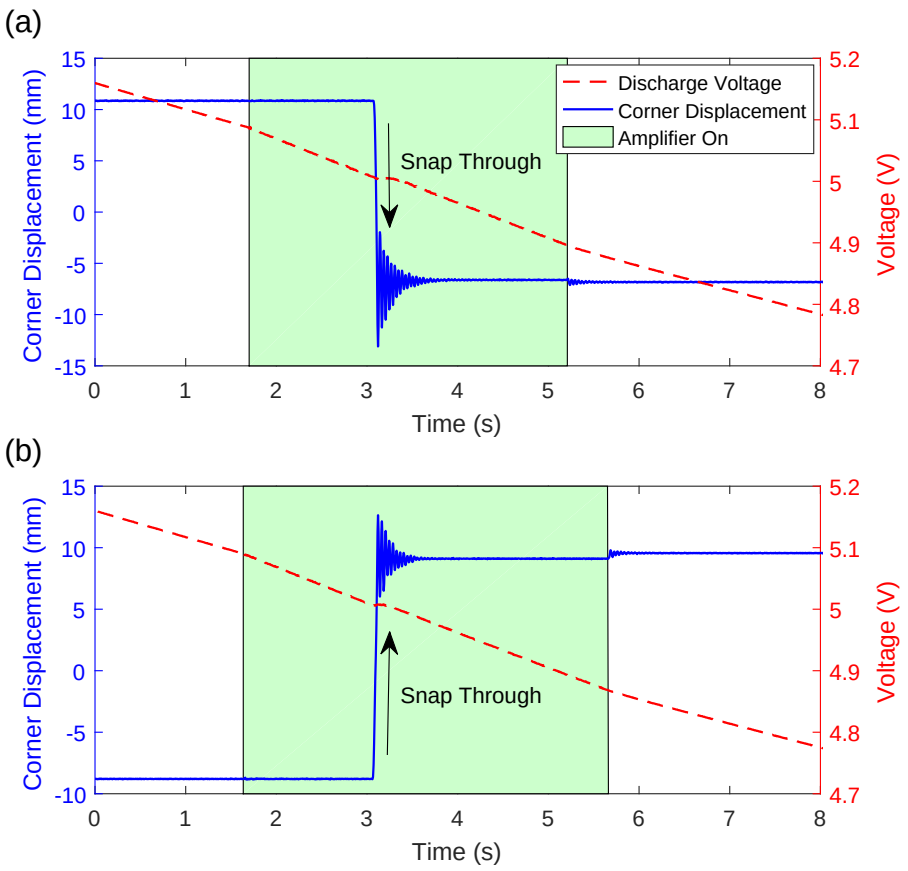

Figure 4.19: Laminate corner displacement and EH301A discharge time histories during snap-through morphing from (a) state I to II and (b) state II to I.

the amplifier is on which signifies that more power is being drawn from the module. Although a high voltage amplifier is required, the laminate demonstrates multi-role capabilities by achieving snap-through morphing with the energy collected from both single-well and cross-well vibrations over a wide bandwidth.

4.7 Chapter Summary

The electromechanical responses and energy harvesting performance of a $[0^{MFC}/90^{MFC}]_T$ piezoelectrically generated bistable laminate under base harmonic excitation are investigated with

analytical model simulations and experiments. Its inherent structural nonlinearities are exploited to induce high amplitude broadband cross-well vibrations to maximize power generation from the MFCs. The linearized modal analysis yields vibration modes and the corner velocity frequency response function about each stable configuration, which show good agreement with experimental results. Under high amplitude excitation, the nonlinear response of the laminate is predicted by numerically solving the electromechanically coupled equations of motion. Open circuit voltage and corner velocity amplitudes under frequency sweeps at various acceleration levels are adequately correlated with their experimental counterparts and exhibit dynamic nonlinearities such as sweep direction dependent hysteresis and stiffness softening. Various cross-well regimes such as intermittency, limit cycle, chaotic, and subharmonic oscillations observed in experiments are predicted by the model at either identical or similar excitation parameters. Characteristics of the observed regimes are found through time histories, spectrum analysis, phase portraits, and Poincaré maps of select data, which are then used to determine the response of all other sweep results.

The power output of each regime is then experimentally measured through resistor sweeps and high amplitude limit cycle oscillations are found to be the optimal dynamic response. When charging an energy harvesting module, the quickest times are measured when the MFCs are connected in parallel since the overall current output is maximized, and the collected energy is then discharged through a high voltage amplifier and back into either MFC to initiate snap-through. The laminate's viability for energy harvesting is demonstrated, allowing it to retain multiple roles when including its snap-through morphing capability. Due to the model idealizing material and geometric properties, initial state dependent asymmetric behavior caused by manufacturing imperfections and asymmetric cross-well orbits within the experimental results are not seen in the simulations. If an imperfection is empirically introduced into the model, these asymmetries are only partially

accounted for. Overall however, the electromechanical model is able to produce fairly accurate voltage and power outputs of a piezoelectric bistable laminate under nonlinear cross-well vibrations. Its viability for energy harvesting is both analytically and experimentally confirmed with favorable power output over a wide frequency range.

CHAPTER 5

Control of Cross-well Responses and Dynamics

The dynamics of bistable composites include various steady-state responses which can be single-well oscillations about either configuration, or cross-well oscillations involving periodic or aperiodic snap-through motion between either stable state. Bistable composites have attracted the most attention when being designed for energy harvesting due to their energetic responses, large displacements, and broadband characteristics associated with snap-through dynamics. Piezoelectric transducers are often bonded onto the laminate as the primary means of energy conversion. However, cross-well oscillations become undesirable if these composites are to be utilized as morphing structures, where their stable shapes must be held without any instabilities. For this purpose, the first half of this chapter proposes an active control strategy that directly suppresses the cross-well vibrations of a bistable composite laminate into a single potential well. This is numerically and experimentally demonstrated through the $[0^{MFC}/90^{MFC}]_T$ piezoelectrically generated bistable laminate, which had its nonlinear dynamical responses characterized in Chapter 4. With the generalized voltage coordinate v_k defined in Chapter 2, the 0° and 90° MFCs are labelled as v_1 and v_2, respectively. Its basic shapes can be seen in Figure 5.1.

The $[0^{MFC}/90^{MFC}]_T$ laminate is ideal for active control applications since the MFCs are simultaneously the actuator and host structure, which means it has much more actuation authority

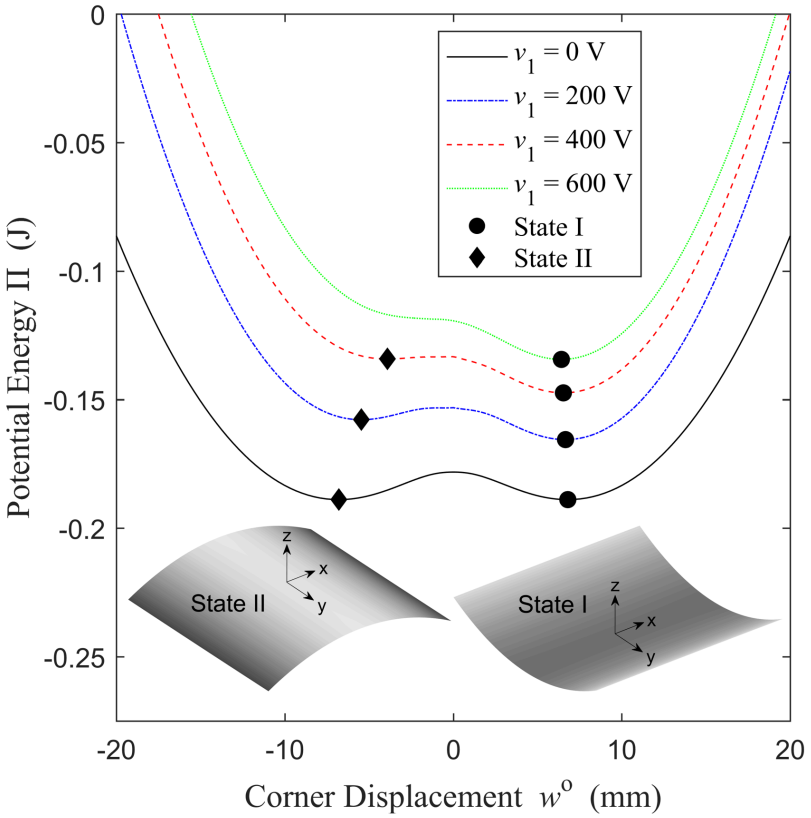

Figure 5.1: Double well diagram and corresponding stable shapes of a $[0^{MFC}/90^{MFC}]_T$ laminate. State II potential well eliminated with v_1 MFC static actuation while $v_2 = 0$ V.

compared to conventional bistable composites with piezoelectric transducers. While under cross-well oscillations, either MFC is actuated to the limit voltage to eliminate the initial stable branch and potential well. At the limit voltage, snap-through occurs to the other state and the laminate can only oscillate about the remaining well. This is illustrated in Figure 5.1, where incrementally increasing the applied voltage on the single MFC v_1 will force the state II initial well to become shallower until entirely losing its concavity at the limit voltage. Past this point at $v_1 = 600$ V, the initial well no longer exists and the laminate is forced to orbit about the remaining state I well. Note that the limit voltage is lower than what is reported in Chapter 3 because a $[0^{MFC}/90^{MFC}]_T$ bistable laminate with a bonding voltage of 1200 V is used here. The Positive Position Feedback

(PPF) controller [140, 141] is then simultaneously applied through the other MFC to achieve large amplitude reduction. State I can also be eliminated by actuating v_2 and the potential energy behavior is symmetric to what is shown in Figure 5.1. Suppression of cross-well dynamics is also attempted with just the single PPF controller and its performance is compared with the dual control strategy in terms of settling time and steady state amplitude within the MFC operating limits. Configuration control is demonstrated by placing the laminate in either state depending on which MFC is chosen to be the PPF controller.

The second half of this chapter conversely demonstrates how the global cross-well bandwidth of a bistable VEH can be widened by imparting perturbations whenever it is under single-well orbit. To enhance the performance in broadband energy harvesting applications, bistable VEHs seek to maximize the range of excitation parameters which triggers high amplitude cross-well vibrations necessary for large power output. Classical frequency sweep characterization does not reveal all co-existent solutions, among which may be high energy orbits that extend the desired cross-well response. Large voltage perturbations can be imparted on to the $[0^{MFC}/90^{MFC}]_T$ bistable laminate while under single-well oscillations, which are necessary to access and maintain high energy orbits in multi-solution regions. When an MFC is the actuator v_a, the other is assigned to be the energy harvester v_h, thus enabling both functions without the need for additional piezoelectric transducers. Through numerical simulations of the electromechanically coupled equations of motion for the $[0^{MFC}/90^{MFC}]_T$ laminate, a voltage disturbance strategy to initiate jumps from low to high energy solutions is presented. This strategy is then applied in frequency sweeps to demonstrate cross-well bandwidth extension.

5.1 Positive Position Feedback Controller

To achieve suppression of cross-well oscillations, the SDOF PPF controller actuating a single MFC is implemented in conjunction with the higher order analytical model from Chapter 2. The proposed PPF controller is a second order damped oscillator which uses position feedback measurements that are collocated with the actuator in positive feedback [140]. The feedback controller builds an internal model of the disturbance frequency that is known prior, and adds damping in the closed-loop at said frequency in a linear system. Goh et. al [140] shows that the closed-loop stability of the PPF controller is independent of the controller dynamics and less sensitive to high frequency spillover relative to velocity feedback methods since the PPF controller rolls off at high frequencies. Further, sufficient conditions on guaranteed stability of unmodeled dynamics and modes that are not targeted by the internal model are derived which can always be satisfied through choice of controller gain and damping ratio. The SDOF scalar PPF controller equation is given by

$$\ddot{v}_{\mathrm{c}} + 2\zeta_{\mathrm{c}}\omega_{\mathrm{c}}\dot{v}_{\mathrm{c}} + \omega_{\mathrm{c}}^2 v_{\mathrm{c}} = k_c\omega_{\mathrm{c}}^2 r \tag{5.1}$$

where v_{c} is the voltage control input, ζ_{c} is the controller damping ratio, ω_{c} is the controller natural frequency, k_c is the controller gain, and r is the position feedback. ω_{c} is set to match the excitation frequency ω_f since this is always the largest frequency component in single-well linear oscillations after potential well elimination. r is chosen to be the out-of-plane displacement at spatial

coordinates x and y as given by

$$r(x,y,t) = \frac{1}{2}\begin{Bmatrix} x^2 & y^2 & x^2y^2 & x^4 & y^4 \end{Bmatrix}\{q\} - w_0^o(x,y) \tag{5.2}$$

where $w_0^o(x,y)$ is the static out-of-plane displacement at x and y of the desired stable state. $w_0^o(x,y)$ is subtracted so that there is zero displacement bias associated with either stable state in the position feedback. Equation 5.2 shows that using the out-of-plane displacement as the feedback measurement can be viewed as an output feedback problem [142], where the output vector is given below.

$$\{O\} = \frac{1}{2}\begin{Bmatrix} x^2 & y^2 & x^2y^2 & x^4 & y^4 \end{Bmatrix} \tag{5.3}$$

Since the MFCs serve as actuators driven by a voltage source, the second electromechanical equation of motion in Equation 2.67 is dropped and the voltage terms in Equation 2.63 become the control input to the system, as seen below.

$$[M]\{\ddot{q}\} + [D(\dot{q})] + [K(q)] = \{F\} - [\theta]\{v\} \tag{5.4}$$

To more easily represent the feedback dynamics, the electromechanical coupling matrix $[\theta]$ and voltage input $\{v\}$ in Equation 5.4 are rewritten as

$$-[\theta]\{v\} = \begin{bmatrix} \{P_1\} & \{P_2\} & \{P_3\} & \{P_4\} & \{P_5\} \end{bmatrix} \begin{Bmatrix} v_1 \\ v_2 \\ 0 \\ 0 \\ 0 \end{Bmatrix}$$

$$= \{P_1\}v_1 + \{P_2\}v_2 \tag{5.5}$$

where v_{c} in Equation 5.1 is chosen to be either v_1 controlling oscillations about state II or v_2 controlling oscillations about state I. The remaining voltage input becomes v_{s}, or the static voltage input which provides the DC signal required to eliminate a potential well while the laminate is under cross-well oscillations. Alternatively, v_s can be zero if the PPF controller is the only desired control input to the closed-loop system. In a subsequent numerical and experimental examples, the effectiveness of both control strategies are compared, that is, the suppression of cross-well oscillations with and without a static voltage input. Let $\{P_{\mathrm{c}}\}$ and $\{P_{\mathrm{s}}\}$ be the input vectors given by $\{P_1\}$ or $\{P_2\}$ in Equation 5.5 associated with v_{c} and v_{s}, respectively. A block diagram of the feedback system is shown in Figure 5.2.

In order satisfy sensor-actuator collocation in an output feedback problem, the angle between the output vector $\{O\}$ and the transpose of the input vector $\{P_{\mathrm{c}}\}$ must approximately be zero as

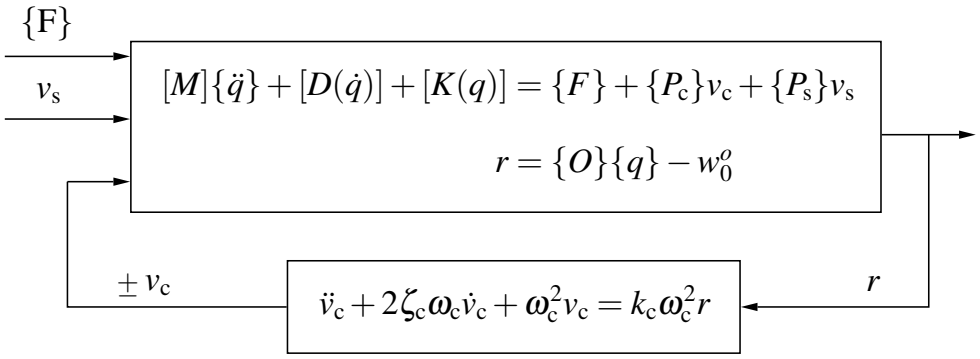

Figure 5.2: Block diagram of the feedback system. v_c is positive if $v_c = v_1$ and negative if $v_c = v_2$.

shown below.

$$\arccos\left(\frac{\{O\}\cdot\{P_c\}^T}{\|\{O\}\|\|\{P_c\}^T\|}\right) \approx 0 \tag{5.6}$$

This corresponds to a need to choose the spatial location x and y such that Equation 5.6 is satisfied. Fortunately for the $[0^{MFC}/90^{MFC}]_T$ laminate, the structure of the transposed input vector $\{P_c\}^T$ allows for a viable sensor placement which satisfies the condition. (x, y) is chosen to be the center edge location of the laminate along the major curvature axis of each stable state. For state I, $x = 0$ and $y = L_y/2$, which means the output vector becomes

$$\{O\} = \left\{0 \quad L_y^2/8 \quad 0 \quad 0 \quad L_y^4/32\right\} \tag{5.7}$$

and it has the same approximate direction as the transposed input vector

$$\{P_c\}^T = \left\{p_1 \quad p_2 \quad p_3 \quad p_4 \quad p_5\right\} \tag{5.8}$$

since $|p_2|$ is much greater than all other $\{P_c\}^T$ component magnitudes when $v_c = v_2$. Physi-

cally, this means that under voltage actuation, the major curvature is weakly coupled to the minor curvature in $\{P_{\mathrm{c}}\}^T$, but the former is affected to a much greater degree, which is approximately represented in $\{O\}$ at the edge location. The higher ordered curvature component $L_y^4/32$ in $\{O\}$ has a negligible effect on the collocation condition.

For state II, $x = L_x/2$ and $y = 0$, which means the output vector becomes

$$\{O\} = \begin{Bmatrix} L_x^2/8 & 0 & 0 & L_x^4/32 & 0 \end{Bmatrix} \tag{5.9}$$

and has the same approximate direction as $\{P_{\mathrm{c}}\}^T$ since $|p_1|$ is much greater than all other $\{P_{\mathrm{c}}\}^T$ component magnitudes when $v_c = v_1$. A caveat is that since $p_1 > 0$ and $p_2 < 0$, the sign of v_{c} must be made negative for state I when $v_{\mathrm{c}} = v_2$ so that the collocation condition in Equation 5.6 holds. In other words, the direction of the control voltage v_c must correspond to that of the position feedback given that the latter is opposite between states I and II due to how they are defined relative to the laminate coordinate system. This is reflected in the block diagram in Figure 5.2. Combining Equations 5.4 and 5.1 with the nonlinear damping matrix in Equations 2.65 and 5.2 yields the closed-loop system as shown below.

$$\begin{bmatrix} \{F\} + \{P_{\mathrm{s}}\}v_s \\ 0 \end{bmatrix} = \begin{bmatrix} [M] & \{0\} \\ \{0\} & 1 \end{bmatrix} \begin{bmatrix} \{\ddot{q}\} \\ \ddot{v_{\mathrm{c}}} \end{bmatrix} + \begin{bmatrix} \alpha[M] & \{0\} \\ \{0\} & 2\zeta_{\mathrm{c}}\omega_{\mathrm{c}} \end{bmatrix} \begin{bmatrix} \{\dot{q}\} \\ \dot{v_{\mathrm{c}}} \end{bmatrix}$$
$$+ \begin{bmatrix} [0] & -\{P_{\mathrm{c}}\} \\ -k_c\omega_{\mathrm{c}}^2\{O\} & \omega_{\mathrm{c}}^2 \end{bmatrix} \begin{bmatrix} \{q\} \\ v_{\mathrm{c}} \end{bmatrix} + \begin{bmatrix} [K(q)] + \beta[K(\dot{q})] \\ k_c\omega_{\mathrm{c}}^2 w_0^o(x,y) \end{bmatrix} \tag{5.10}$$

5.2 Experimental Methodology

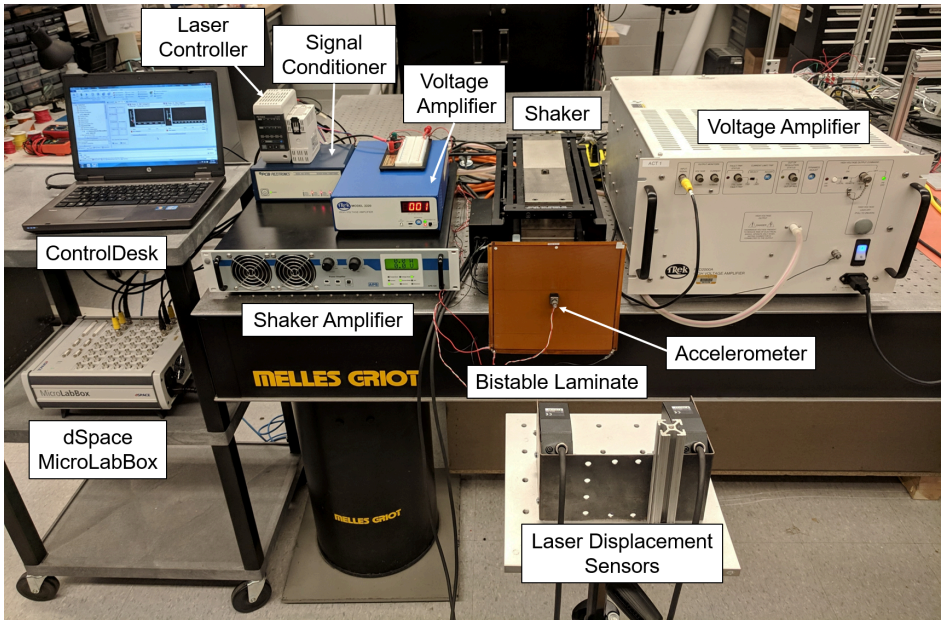

Figure 5.3: Experimental setup for implementing active control and measuring the dynamic response of a 200 x 200 mm^2 $[0^{MFC}/90^{MFC}]_T$ laminate.

The suppression of cross-well vibration for the $[0^{MFC}/90^{MFC}]_T$ laminate is achieved with the experimental setup shown in Figure 5.3, which is similar to what is presented in Section 4.1. The APS 113 seismic shaker powered by the APS 125 amplifier provides the harmonic excitation to the laminate that is held between two neodymium cube magnets at the geometric center. The base acceleration is measured with a PCB Piezoelectronics 352C67 accelerometer which is attached to the outer magnet and two Keyence LK-G402 laser sensors measure the edge and corner out-of-plane displacement time histories. The laser sensor measuring the edge location provides the position feedback to the PPF controller while corner location sensor records the laminate response. The dSPACE MicroLabBox is used to implement the algorithms and provide A/D and D/A conversion with all signals sampled and output at 1000 Hz. The algorithms are written in Simulink

and executed on MicroLabBox which is interfaced through ControlDesk. The subsequent PPF and static control signals are amplified through the Trek 2220 and the Trek PZD2000A high voltage amplifiers, respectively.

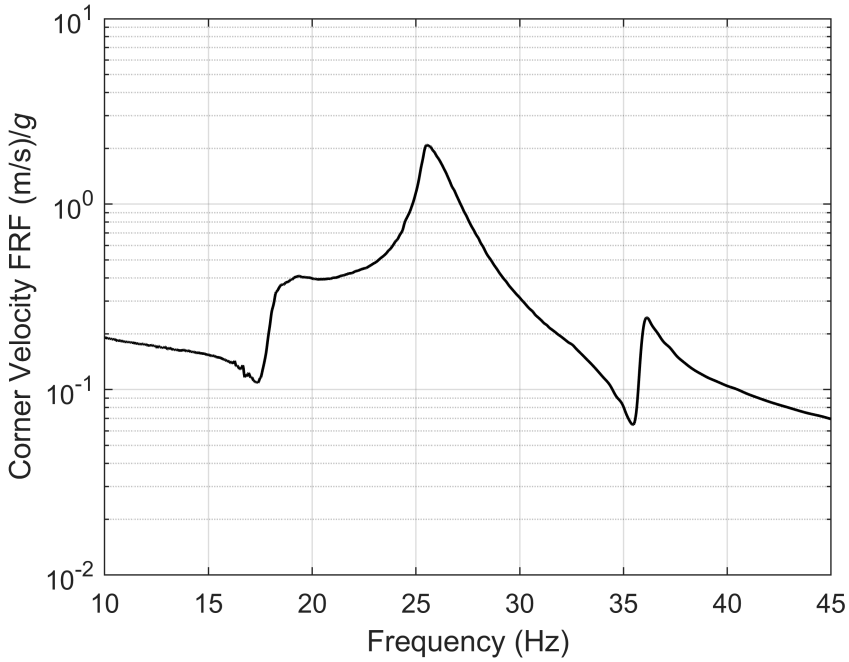

Figure 5.4: Experimental corner velocity to base acceleration frequency response function of the $[0^{MFC}/90^{MFC}]_T$ laminate for state I.

As previously mentioned, the $[0^{MFC}/90^{MFC}]_T$ bistable laminate with a bonding voltage of 1200 V for both MFCs are the subject of this active control section. For the experimental specimen, the average thickness of the DP-460 epoxy adhesive is measured to be 0.145 mm and the average density of the laminate is found to be 4195 kg/m^3. All other material properties remain the same and are shown in Table 3.1. The simulated stable states post bifurcation have static out-of-plane displacements of $\pm$6.80 mm at the corner locations and $\pm$7.48 mm at the center edge locations along the major curvature axis of each state. The latter values are used for $w_0^o(x, y)$ in Equation 5.2. The numerical limit voltage where a potential well disappears and the laminate snaps through to the remaining well is found to be 504 V from either state. Due to the differing bonding

voltages, the damping ratios and coefficients found in Section 4.2.3 do not apply here and must be reacquired. Again, the quadrature peak picking method [133] is used to obtain these parameters from an experimental corner velocity to base acceleration FRF in state I, as shown in Figure 5.4. This low amplitude FRF is measured during forward frequency sweeps from 10 Hz to 45 Hz at 0.05 g to minimize nonlinear effects while both MFCs are in open circuit. The first bending mode is at 25.52 Hz and the second twisting mode is at 36.12 Hz. With the natural frequencies for the bending and twisting modes, the corresponding damping ratios are found to be $\zeta_1 = 0.0245$ and $\zeta_2 = 0.0173$ for state I. Then the mass and stiffness damping coefficients are $\alpha = 7.867$ and $\beta = 2.443 \cdot 10^{-9}$ according to the first two elastic modes in Equation 2.66.

5.3 Suppression of Cross-well Oscillations

5.3.1 Numerical Simulations

With the inputs to the electromechanical model established, the resulting differential equations of motion are placed in state space form and numerically solved in MATLAB using the *ode15s* solver. The open-loop system is given by Equation 5.4 with v_1 and v_2 set to zero and the closed-loop system is given by Equation 5.10. In all simulations, the open-loop system is solved for $t = [0, 2]$ s, where the initial conditions for $\{q\}$ are always set to be the curvatures corresponding to state I and $\{\dot{q}\} = \{0\}$. Then the open-loop state at $t = 2$ and $v_c = \dot{v_c} = 0$ serve as the initial conditions to the closed-loop system, which is solved for $t \geq 2$ s. The controller damping ratio ζ_c is set to 0.1 and only the gain k_c is varied between the results. For the dual control strategy, $v_s = 504$ V to eliminate the initial potential well with the least amount of input voltage.

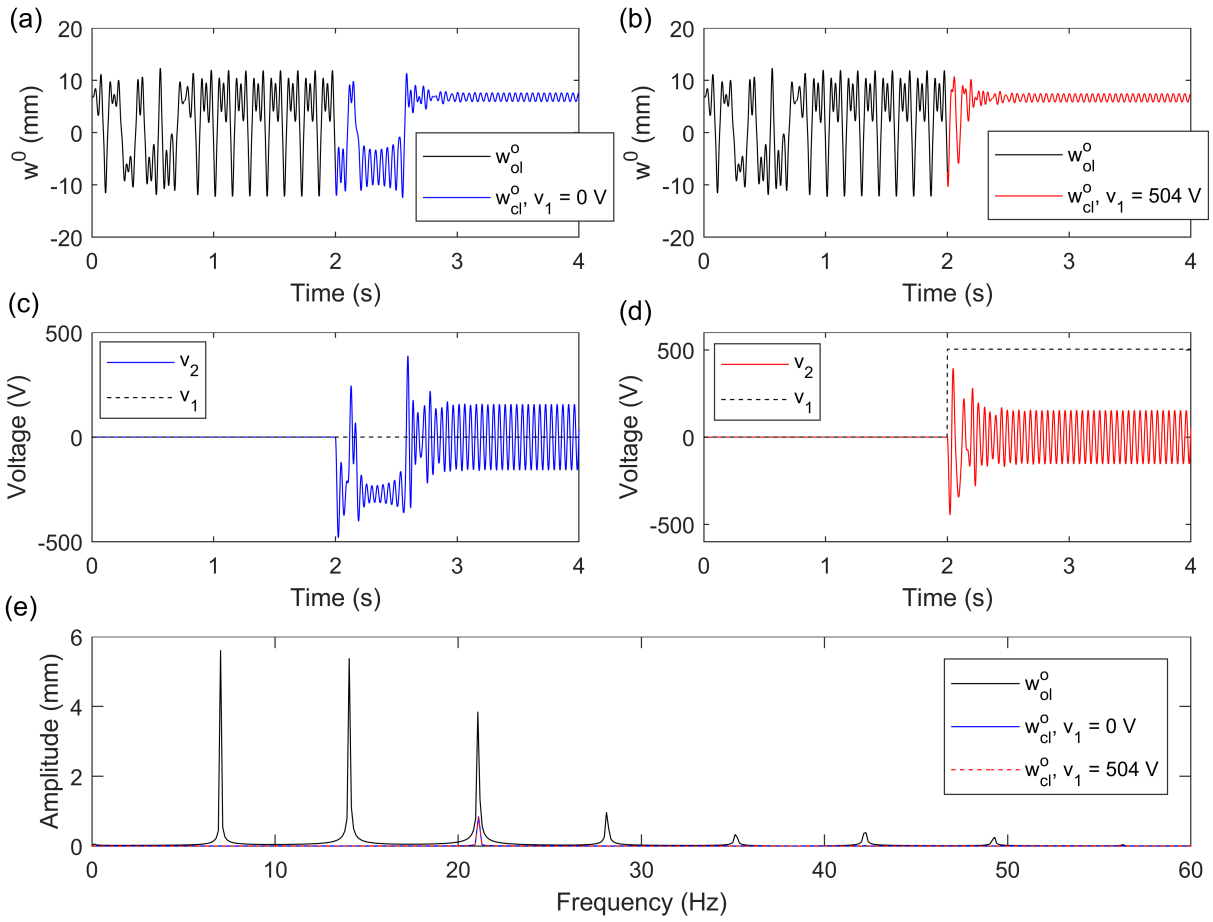

Figure 5.5: Simulated suppression of subharmonic oscillations through single PPF controller $v_c = v_2$ with time histories of (a) corner displacement w^o, (c) input voltages v_1 and v_2, through simultaneous static actuation $v_s = v_1 = 504$ V and PPF controller $v_c = v_2$ with time histories of (b) corner displacement w^o, (d) input voltages v_1 and v_2, and their (e) FFTs of steady state corner displacement w^o. Controller parameters are $\zeta_c = 0.1$ and $k_c = 37000$ and the base excitation is 21.1 Hz and 2 g from initial state I.

Although bistable oscillators exhibit a wide variety of cross-well behaviors, three prominent regimes are chosen specifically to demonstrate how they can be suppressed through active control techniques. Period-3 subharmonic oscillations require three forcing periods to complete a full cycle and are characterized by the presence of order-1/3 harmonic components. The model for the $[0^{MFC}/90^{MFC}]_T$ laminate predicts period-3 oscillations to be induced in open-loop steady state at a base excitation of 21.1 Hz and 2 g from the initial state I. Figure 5.5 shows their suppression into

state I through two separate control strategies. Figure 5.5(a) and (c) are the corner displacement w^o and input voltage $v_c = v_2$ and $v_s = v_1$ time histories when only the the single PPF controller with $k_c = 37000$ is implemented in the closed-loop system, respectively. Figure 5.5(b) and (d) plots are for the simultaneous implementation of the PPF controller $v_c = v_2$ with $k_c = 37000$ and static actuation $v_s = v_1 = 504$ V. Figure 5.5(e) shows the FFT of the steady state corner displacement time histories for the open and closed-loop systems. Although saturation is set within the closed-loop ODE function handle in MATLAB, the controller gains are chosen so that the control voltage v_c always stays within the MFC operating limit of ± 500 V assuming zero DC bias. In addition, even though the position feedback location is at the center edge of the laminate, the corner displacements are presented in the results. This is because only the corners have significant out-of-plane deflections in both stable states, so they alone are appropriate locations for evaluating cross-well motion.

Both strategies successfully push the laminate out of cross-well orbit and into single-well oscillations, but the dual static and PPF controller largely reduces the closed-loop transients seen with the single PPF controller before the laminate settles into steady state. The settling time is defined as the duration for the error $|w^o(t) - w^o_{ss}|$ between the laminate response $w^o(t)$ and the steady state amplitude w^o_{ss} to fall within 20% of w^o_{ss}. This results in the dual control method having a lower settling time of 0.44 s compared to the single PPF controller's settling time of 0.91 s, which is a 51.65% reduction. Given that both strategies have identical controller damping ratios and gains, their final steady state amplitudes are similar with single PPF controller and dual control yielding 0.85 mm and 0.82 mm, respectively. The FFT plot in Figure 5.5(e) shows that the subharmonic oscillation's primary frequency component ω_f retains an amplitude of 3.85 mm, which means the single and dual control reduce it by significant margins of 77.92% and 78.70%, respectively. In ad-

dition to the primary forcing frequency, all harmonic components are completely subdued, which enables the suppression of period-3 orbits. By forcefully eliminating a potential well through static actuation v_s, the dual control yields better control performance in terms of settling time when compared to the single PPF controller. This is not only observed with subharmonic oscillations, but with all other cross-well regimes and is correlated with experimental data. As shown in the next experimental section, there is a limit to what the single PPF controller can successfully suppress and potential well elimination becomes necessary to achieve single-well control.

Figure 5.6 shows the suppression of high amplitude limit cycle oscillations with dual control where (a) and (c) show the corner displacement and control voltage time histories for the simultaneous PPF controller $v_c = v_2$ and static actuation $v_s = v_1 = 504$ V into state I while (b) and (d) are for the simultaneous PPF controller $v_c = v_1$ and static actuation $v_s = v_2 = 504$ V into state II, and (e) shows their open and closed-loop w^o FFTs in steady state. For both cases, $\zeta_c = 0.1$ and $k_c = 28000$. With the base excitation of 18 Hz and 2 g from initial state I, limit cycle oscillations are induced in open-loop steady state and these are characterized by continuous snap-through events which allow a periodic high-energy orbit to be sustained between the two stable configurations. Due to the periodic attractor motion enabling large amounts of penetration into both potential wells, it is associated with the largest out-of-plane displacement amplitudes of all cross-well regimes. Figure 5.6 demonstrates complete configuration control through the suppression of cross-well oscillations into either state I or II depending on which MFCs are v_c and v_s in the $[0^{MFC}/90^{MFC}]_T$ laminate. Due to the electromechanical model retaining perfect symmetry of potential wells, the total amplitude reduction is identical whether the laminate is controlled into state I or II. With the open and closed-loop primary frequency components having steady state amplitudes of 14.22 mm and 0.89 mm, respectively, a total reduction of 93.74% is achieved.

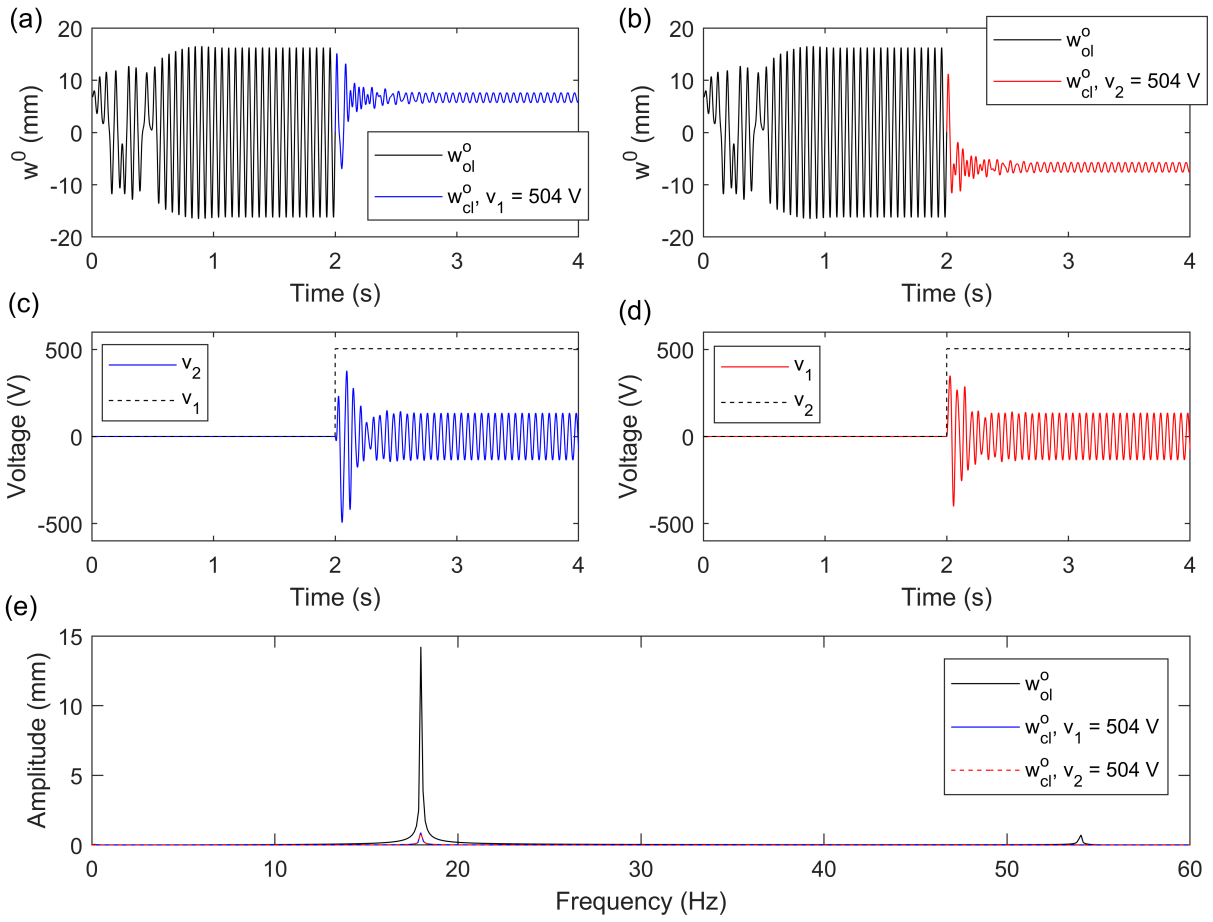

Figure 5.6: Simulated suppression of limit cycle oscillations through simultaneous static actuation $v_s = v_1 = 504$ V and PPF controller $v_c = v_2$ with time histories of (a) corner displacement w^o, (c) input voltages v_1 and v_2, through simultaneous static actuation $v_s = v_2 = 504$ V and PPF controller $v_c = v_1$ with time histories of (b) corner displacement w^o, (d) input voltages v_1 and v_2, and their (e) FFTs of steady state corner displacement w^o. Controller parameters are $\zeta_c = 0.1$ and $k_c = 28000$ and the base excitation is 18 Hz and 2 g from initial state I.

A disadvantage of potential well elimination and the dual control strategy is the large power consumption required by the static actuation, but this can be mitigated by removing v_s once the laminate is under single-well oscillations in either state. This is demonstrated through the suppression of chaotic oscillations as seen in Figure 5.7, where (a) and (b) show the corner displacement and control voltage for the simultaneous implementation of the PPF controller $v_c = v_2$ with $k_c = 33000$ and static actuation $v_s = v_1 = 504$ V in blue, then its removal $v_s = v_1 = 0$ V in red,

and (c) shows their steady state open and closed-loop w^o FFTs.

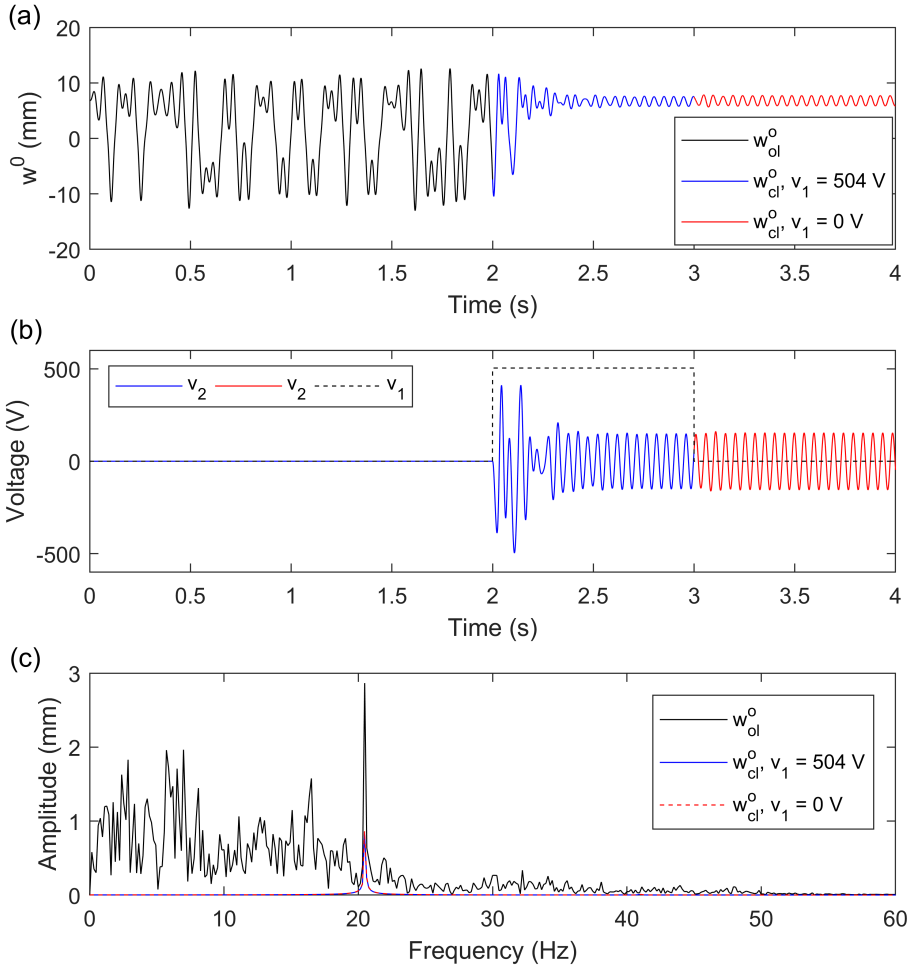

Figure 5.7: Simulated suppression of chaotic oscillations through simultaneous static actuation $v_s = v_1 = 504$ V and PPF controller $v_c = v_2$ from 2 to 3 s, then $v_s = v_1 = 0$ V from 3 to 4 s. Figure presents time histories of the (a) corner displacement w^o, (b) input voltages v_1 and v_2, and the (c) FFTs of steady state corner displacement w^o. Controller parameters are $\zeta_c = 0.1$ and $k_c = 33000$ and the base excitation is 20.5 Hz and 2 g from initial state I.

Chaotic oscillations are induced by the base excitation of 20.5 Hz and 2 g from initial state I, and are characterized by aperiodic snap-through events through the strange attractor motion. This is exhibited by the broadband spectrum retaining energy over a wide range of frequencies as seen in the FFTs in Figure 5.7(c). Once the laminate reaches steady state through dual control about state I, $v_s = v_1$ can be shut off to save power consumption without having the laminate

diverge back into cross-well vibrations. This change in v_s leads to a small shift in the out-of-plane displacement of state I due to transitioning to a different location on its stable branch. However, the total amplitude reduction is mostly maintained where the final steady state amplitudes for $v_s = 504$ V and $v_s = 0$ V are 0.83 mm and 0.86 mm which correspond to 71.04% and 69.99% decreases of the primary frequency component, respectively. Aside from the primary forcing frequency, the broadband frequency components of chaotic oscillations are completely negated.

5.3.2 Experimental Results

With the objective of verifying the numerical results for suppressing cross-well orbits, the active control strategies are experimentally implemented on the $[0^{MFC}/90^{MFC}]_T$ bistable laminate. The base excitation levels from initial state I are identical to those used in the simulations to demonstrate correlation in the laminate's dynamic response. For dual control with potential well elimination, the MFC input v_s is kept consistent with the simulations at 504 V while saturation of v_c is still within the MFC operating limit of ± 500 V. The only deviation are with the PPF controller parameters, which are tuned for each cross-well response to reach comparable performance in settling time to and amplitude of closed-loop steady state oscillations. The experimental damping ratio for all cases are $\zeta_c = 0.01$ while the gains are tuned for each run so that the PPF control voltage v_c is not saturated in closed-loop steady state. Suppression of cross-well oscillations are not guaranteed if the closed-loop transients are not allowed to saturate due to the MFCs' lower amounts of actuation authority over the laminate when compared to the model. To satisfy the PPF collocation condition in Equation 5.6 as explained in Section 5.1, the direction of v_c is opposite between $v_c = v_1$ and $v_c = v_2$ controlling vibrations about states II and I, respectively. This is

experimentally imposed through the sign of the gain k_c where it is negative for suppression into state I and positive for state II.

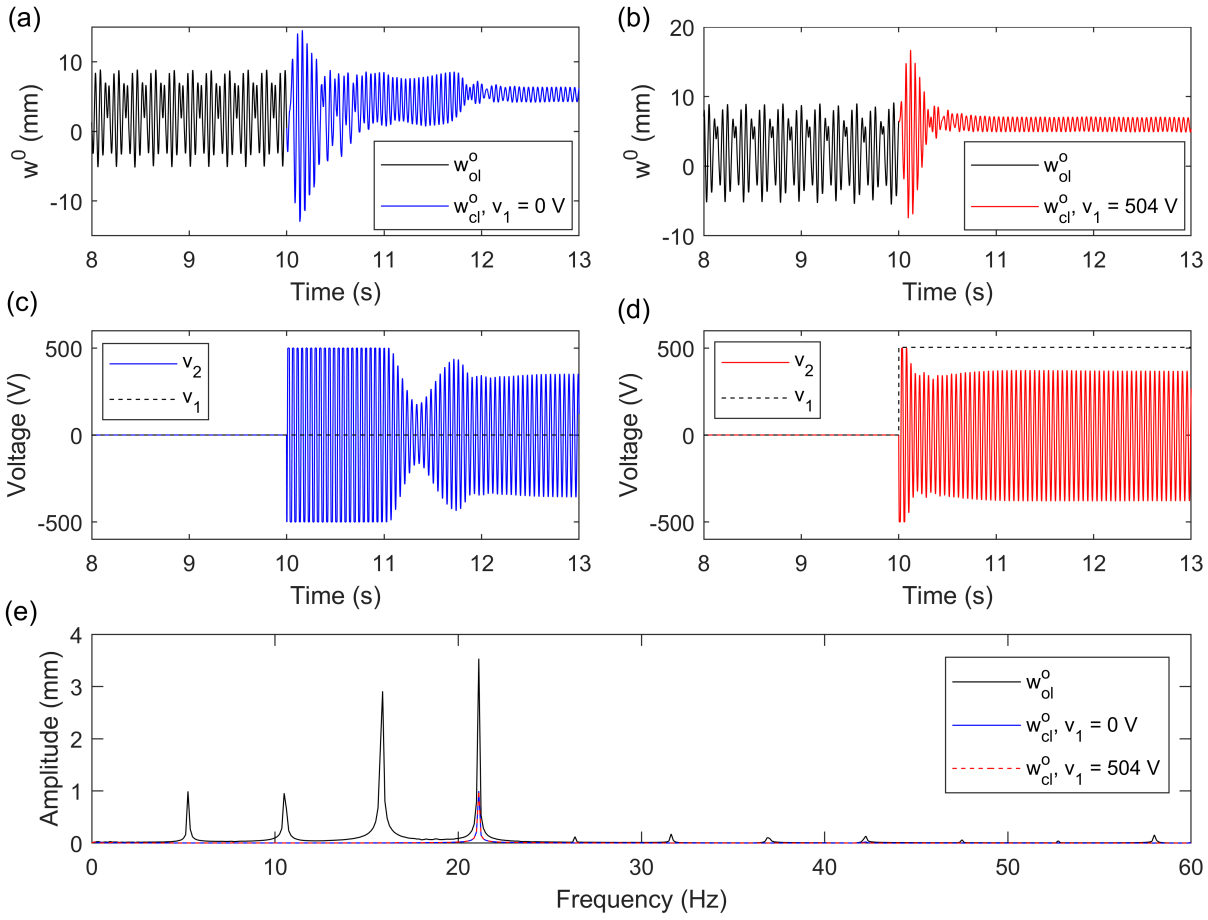

Figure 5.8: Experimental suppression of subharmonic oscillations through single PPF controller $v_c = v_2$ with time histories of (a) corner displacement w^o, (c) input voltages v_1 and v_2, through simultaneous static actuation $v_s = v_1 = 504$ V and PPF controller $v_c = v_2$ with time histories of (b) corner displacement w^o, (d) input voltages v_1 and v_2, and their (e) FFTs of steady state corner displacement w^o. Controller parameters are $\zeta_c = 0.01$ and $k_c = -0.40$ and the base excitation is 21.1 Hz and 2 g from initial state I.

At the base excitation of 21.1 Hz and 2 g, period-4 subharmonic oscillations are induced and their suppression into state I are presented in Figure 5.8 with the single PPF controller and the dual control strategy. The individual plots containing the time histories of the corner displacement w^o, input voltages $v_c = v_2$ and $v_s = v_1$, and FFTs of the steady state w^o within Figure 5.8 are presented

in identical order as their simulated counterparts in Figure 5.5 with $k_c = -0.40$ for both methods. Before the active control results are discussed, differences in the open-loop cross-well responses between the numerical and experimental results are explained. As investigated in Section 4.4.1, the subharmonic oscillations in the open-loop w^o time histories in Figure 5.8(a) and (b) are asymmetric and their amplitudes are over-predicted by the model. The laminate has a tendency to favor the initial state and not fully penetrate the other potential well under cross-well orbits, with varying degrees of penetration between dynamic regimes, and this effect is not predicted by the model. Subharmonic oscillations contain the least amount of vibrational energy out of all cross-well responses and will therefore retain the greatest amounts of asymmetry in their orbits. This effect also limits the w^o peak to peak amplitudes when compared to the simulations. Due to artificial stiffness imposed upon the laminate by the assumed shape functions, the electromechanical model over-predicts the out-of-plane displacements of each stable state as shown in Section 3.4.1. This also contributes to the larger w^o amplitudes in the simulations.

Although the periodicity of the experimental subharmonic orbit is slightly higher with the existence of order-1/4 harmonic components when compared to the numerical period-3 motion, cross-well suppression results are correlated between the two control strategies. Both are able to force the laminate out of subharmonic oscillations and into single-well oscillations, but the difference in duration of the closed-loop transients is greater in the experimental results. This is due to the dual control method's static $v_s = 504$ V being able to bring the control voltage v_c out of saturation much sooner than the single PPF controller. With the initial well eliminated, the laminate is able to settle into single-well oscillations about state I with much less difficulty. Given the same definition for settling time to closed-loop steady state oscillations as the numerical results, the dual control method with the eliminated initial well has a settling time of 0.89 s compared to the single

PPF controller's settling time of 2.34 s, which corresponds to a larger duration reduction of 61.97% when compared to the simulations. With the PPF controller damping ratios and gains having the same magnitudes between the two strategies, their closed-loop steady state amplitude are nearly identical at 1.00 mm and 1.01 mm for the single PPF and dual control methods, respectively. These correspond to reductions of 71.70% and 71.41% from the subharmonic primary frequency component amplitude of 3.53 mm as seen in the FFT plot in Figure 5.8(e). As predicted by the simulations in Figure 5.5, all harmonic components are also subdued.

The suppression of high amplitude limit cycle oscillations into either potential well is experimentally demonstrated in Figure 5.9 and verifies the corresponding simulation results in Figure 5.6 with the identical base excitation of 18 Hz and 2 g from initial state I. Figure 5.9(a) and (b) show the corner displacement and control voltage time histories for the dual control $v_c = v_2$ with $k_c = -0.21$ and $v_s = v_1 = 504$ V into state I while for (c) and (d) the dual control voltages are flipped so that $v_c = v_1$ with $k_c = 0.20$ and $v_s = v_2 = 504$ V, which forces the laminate into state II, and (g) shows their steady state w^o FFTs. Since the continuous snap-through motion in open-loop leads to the most energetic laminate response out of all cross-well regimes, limit cycle oscillations show the least amount of trajectory asymmetry associated with the largest amount of orbital penetration into both potential wells. This means the open-loop w^o amplitudes for this particular regime have the best agreement between the model and experiments, in contrast to the subharmonic oscillations in Figure 5.8. However for the same reason, limit cycle oscillations are the most difficult to control and the dual control strategy has the lowest suppression performance when compared to other cross-well regimes. Although the laminate escapes cross-well orbit with minimal transients in closed-loop, the PPF control voltage v_c stays saturated significantly longer at 1.98 s in Figure 5.9(a) and 1.65 s in Figure 5.9(c) than when suppressing subharmonic or chaotic oscillations. This

translates to a larger settling time to closed-loop steady state whether the laminate is placed into state I or II. In addition, the steady-state v_c amplitude is closest to saturation out of all presented cases.

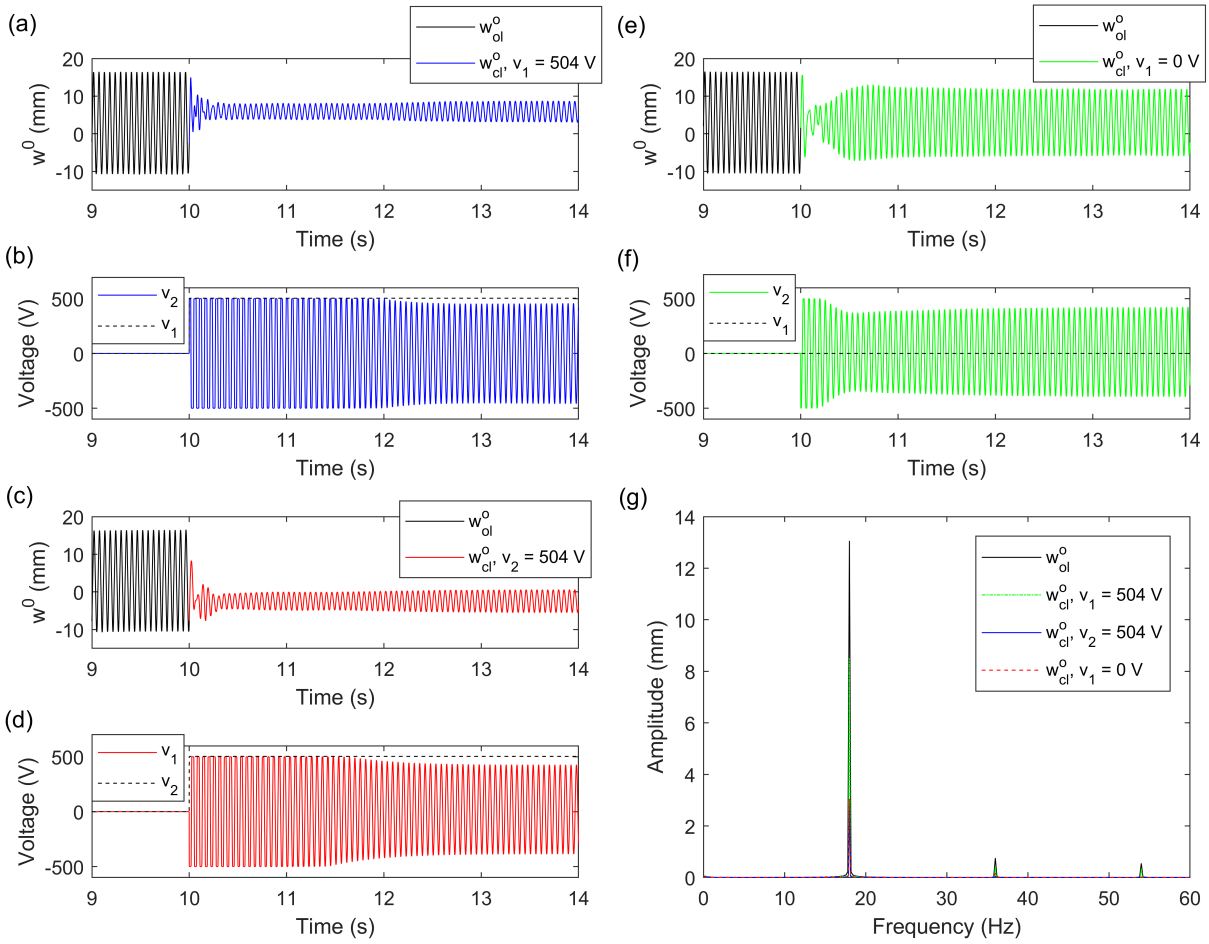

Figure 5.9: Experimental suppression of limit cycle oscillations through simultaneous static actuation $v_s = v_1 = 504$ V and PPF controller $v_c = v_2$ at $k_c = -0.21$ with time histories of (a) corner displacement w^o, (b) input voltages v_1 and v_2, through simultaneous static actuation $v_s = v_2 = 504$ V and PPF controller $v_c = v_1$ at $k_c = 0.20$ with time histories of (c) corner displacement w^o, (d) input voltages v_1 and v_2, through single PPF controller $v_c = v_2$ at $k_c = -0.07$ with time histories of (e) corner displacement w^o, (f) input voltages v_1 and v_2, and their (g) FFTs of steady state corner displacement w^o. Damping ratio is $\zeta_c = 0.01$ and the base excitation is 18 Hz and 2 g from initial state I.

In Figure 5.9(c), the out-of-plane displacement magnitude of state II in closed-loop is lower than that of state I due to asymmetric potential well locations exacerbated by the cross-well or-

bital asymmetry. This is caused by manufacturing imperfections of the $[0^{MFC}/90^{MFC}]_T$ laminate involving layup alignment, nonuniform epoxy bond line, and the variation of electromechanical properties between the two MFCs. Due to the slight difference in controller gain k_c and potential well asymmetry, the closed-loop primary frequency components have steady state amplitudes of 2.80 mm and 3.05 mm when suppressed into states I and II, respectively, and are found to be much greater than the simulations and other experimental cases. These correspond to reductions of 78.56% and 76.65% from the open-loop steady state amplitude of 13.06 mm. Aside from the amount of vibration attenuation being open-loop regime dependent, the difficulty in experimentally controlling limit cycle oscillations is also derived from the MFCs having less actuation authority over the entire laminate when compared to the idealized model.

To bolster the merits of dual control with potential well elimination over single PPF control, an experimental case is presented where the latter method fails to keep the laminate out of cross-well orbit. This is in contrast to Figure 5.8(a) where the single PPF controller is able to suppress subharmonic oscillations, albeit with longer closed-loop transients. Figure 5.9(e) and (f) presents the corner displacement and control voltage time histories in open-loop limit cycle oscillations and then under the application of just the single PPF controller $v_c = v_2$ with $k_c = -0.07$ in closed-loop. As with other cases, the gain is tuned so that the steady state v_c is closest to the MFC limits without actually saturating. Unlike the dual control strategy in Figure 5.9(a), the single PPF controller is unable to keep the laminate constrained in a potential well and it quickly diverges back into limit cycle oscillations in closed-loop. Although there is some amplitude mitigation with the steady state primary frequency component being 8.51 mm, the net suppression is less than what the dual control method can achieve with oscillations confined to a single well. The single PPF controlled response also retains the superharmonic components characteristic of the open-loop limit cycle oscillations,

which in comparison are subdued under dual control. In all, this comparison reveals that if the laminate's cross-well response retains enough amplitude and inertia, potential well elimination is required to keep it suppressed in single-well oscillations.

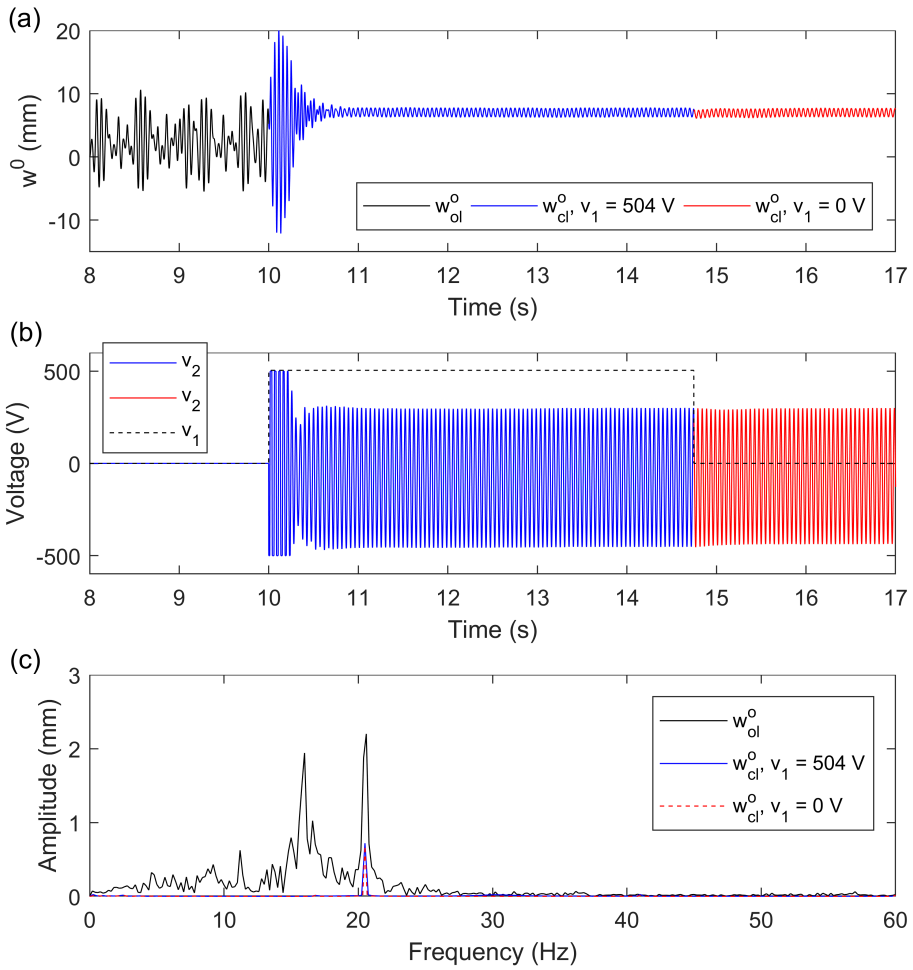

Figure 5.10: Experimental suppression of chaotic oscillations through simultaneous static actuation $v_s = v_1 = 504$ V and PPF controller $v_c = v_2$ from 10 to 14.8 s, then $v_s = v_1 = 0$ V beyond 14.8 s. Figure presents time histories of the (a) corner displacement w^o, (b) input voltages v_1 and v_2, and the (c) FFTs of steady state corner displacement w^o. Controller parameters are $\zeta_c = 0.01$ and $k_c = -0.80$ and the base excitation is 20.5 Hz and 2 g from initial state I.

The final experimental case is the suppression of chaotic oscillations into state I, where v_s is removed once the laminate is under closed-loop single-well oscillations to mitigate DC power consumption. Under the base excitation of 20.5 Hz and 2 g from initial state I, Figure 5.10(a) and (b)

show the corner displacement and control voltage time histories for the simultaneous implementation of the PPF controller $v_c = v_2$ with $k_c = -0.80$ and static actuation $v_s = v_1 = 504$ V in blue, then its removal $v_s = v_1 = 0$ V in red, and (c) presents their steady state w^o FFTs. As seen in simulations, the open-loop chaotic oscillations are characterized by a more broadband frequency spectrum when compared to periodic cross-well regimes, but still retain the previously discussed asymmetric effects exhibited by subharmonic and limit cycle oscillations. More importantly, Figure 5.10 experimentally verifies that the laminate will remain in single-well oscillations once the static voltage v_s is shut off. The total amplitude reduction is maintained where the final steady state amplitudes are 0.72 mm and 0.68 mm for $v_s = 504$ V and $v_s = 0$ V, respectively. These correspond to a reduction of 67.27% and 69.09% from the primary open-loop frequency component of 2.20 mm and the chaotic broadband frequency components are suppressed as predicted in Figure 5.7. It should be noted that the closed-loop control voltage v_c signal in Figure 5.10(b) shows negative DC bias caused by real-time drift in the position measurements taken by the laser displacement sensors. This v_c bias places the state I potential well location at a higher out-of-plane displacement than the other experimental cases, which do not show as significant of a bias.

5.4 Extension of Cross-well Bandwidths

5.4.1 Electromechanical System

This section numerically examines how the range of frequencies that trigger cross-well vibrations can be widened through voltage actuation of the MFCs in a $[0^{MFC}/90^{MFC}]_T$ bistable laminate. To allow simultaneous MFC actuation and energy harvesting, the electromechanical system

must be modified. Starting with the state space form of the laminate's equations of motion in Equations 4.19a-4.19c, v_1 is driven by a voltage source and serves as the actuation signal v_a and control input to the system if the laminate is under single-well oscillations about state II. The actuation signal v_a is v_2 if under single-well oscillations about state I. Note that v_1 and v_2 correspond to the 0° and 90° MFCs, respectively. These assignments allow the MFCs to have adequate authority for inducing snap-through due to their piezoceramic fiber alignment relative to the stable cylindrical shapes of the laminate. The remaining voltage degree of freedom becomes the harvesting signal v_h connected in parallel to the resistive load R. Since the system loses an unknown degree of freedom to v_a, the corresponding state space equation in Equation 4.19c is dropped, and the remainder is shown below.

$$\{\dot{p}_3\} = \dot{v}_h = \begin{cases} \begin{Bmatrix} [C_p]_{11}^{-1} & [C_p]_{12}^{-1} \end{Bmatrix} \left(\frac{1}{R} \{p_3\} - [\Theta]^T \{p_2\} \right) & \text{if } v_h = v_1,\, v_a = v_2 \text{ (5.11a)} \\ \begin{Bmatrix} [C_p]_{21}^{-1} & [C_p]_{22}^{-1} \end{Bmatrix} \left(\frac{1}{R} \{p_3\} - [\Theta]^T \{p_2\} \right) & \text{if } v_h = v_2,\, v_a = v_1 \text{ (5.11b)} \end{cases}$$

The resulting state space equations in Equations 4.19a, 4.19b, and either 5.11a or 5.11b are assembled in MATLAB and numerically evaluated with the *ode15s* solver. Under the inputs of the control signal v_a, load resistance R, base acceleration a_b, and excitation frequency ω_f, the time dependent $\{q\}$ and v_h responses are simulated for a given set of $\{q\}$, $\{\dot{q}\}$, and v_h initial conditions. The load resistance for v_h is set to $R = 10$ GΩ to simulate open circuit conditions in all numerical simulations. The out-of-plane displacement of the laminate can then be found with the admissible fourth order polynomial shape function as given below.

$$w^o(x, y, t) = \frac{1}{2} \left(q_1(t)\, x^2 + q_2(t)\, y^2 + q_3(t)\, x^2 y^2 + q_4(t)\, x^4 + q_5(t)\, y^4 \right) \tag{5.12}$$

5.4.2 Low to High Energy Orbits with Voltage Perturbations

Before cross-well bandwidths can be evaluated through frequency sweeps, the form of voltage perturbations for placing the bistable laminate into co-existing high energy attractors must be defined. Unlike SDOF Duffing oscillators where all stable co-existing attractors can be feasibly identified through either analytical or numerical methods, the MDOF system for the $[0^{MFC}/90^{MFC}]_T$ laminate contains six degrees of freedom and forces numerically integrated solutions to be computationally expensive. Since its basins of attraction cannot be efficiently characterized for a large range of system inputs, there are limitations to the solution searching strategies that can be effectively employed. Although more may exist, numerical forward and backward frequency sweeps reveal at most two co-existing steady state solutions for any given forcing level due to hysteresis, which is associated with amplitude jumps between single and cross-well orbits following either saddle node or period doubling bifurcation. It is possible that frequency bandwidths that exhibit single-well oscillations in both sweep directions also contain high energy solutions at the same excitation amplitude. Accessing the associated attractors are done in an exploratory manner through MFC voltage perturbations, which are necessary due to the disparity in the relative sizes of the basins of co-existing attractors at low forcing levels.

The form of voltage perturbation is chosen to be a rectangular pulse that is sequentially applied through the different phases of the forcing signal, or the laminate's out-of-plane displacement under single-well steady state vibrations. Since the basin of attraction that surrounds any generic attractor is highly sensitive to the response phase of the system [99, 106, 107], changing the basins through phase shifts in a systematic fashion can lead the laminate's orbital trajectory to the desired high energy attractor. This is achieved by varying when the pulse is applied and constraining where

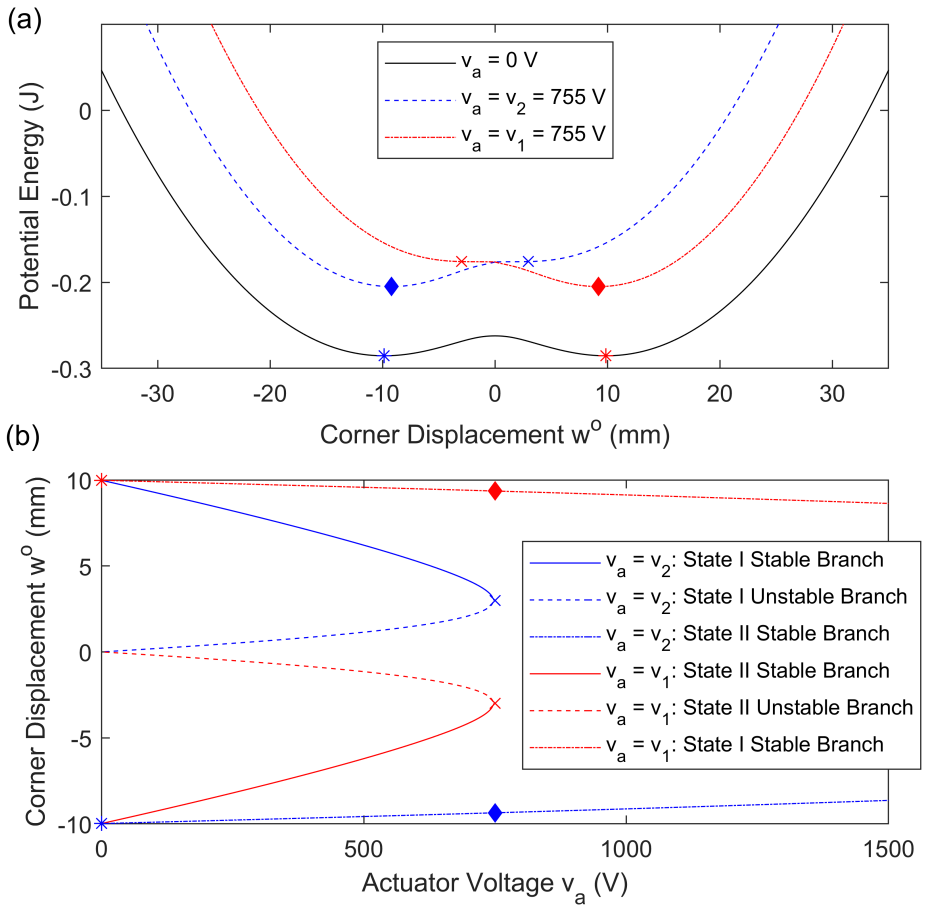

Figure 5.11: (a) Potential well elimination through static actuation of either v_1 or v_2 and (b) corresponding corner displacement w^o vs. v_1 or v_2 showing snap-through between either stable shapes of the $[0^{MFC}/90^{MFC}]_T$ laminate.

it ends, which results in the laminate's position in the phase space at the end of the pulse to be kept approximately identical while the basins of attraction are continuously altered. Since all co-existing stable solutions are not pre-identified, it is not guaranteed whether this strategy will yield the desired cross-well orbit and the required computation time is unknown. Even if the laminate successfully achieves the jump and maintains orbit, there may be additional stable attractors that could outperform the current solution in energy conversion.

The amplitude of the voltage pulse is v_a = 755 V, which is lowest value that induces quasi-static

snap-through between either stable states of the $[0^{MFC}/90^{MFC}]_T$ laminate with a bonding voltage of 1500 V. As seen in Figure 5.11(b), limit point behavior is exhibited at v_a = 755 V where the initial stable branch will lose stability and jump to the second stable branch where it will remain regardless of what the the actuation voltage v_a is. Figure 5.11(a) shows that the corresponding potential well of the initial stable state disappears when v_a = 755 V and forces the system into the remaining well. It will then remain monostable until v_a is either lowered or removed. The markers show the corresponding points between the two plots to illustrate the relationship between v_a and the potential energy of the system. Since the elimination of the initial potential well is not affected by harmonic excitation levels, the laminate will always snap-through to the other state at the limit voltage. This is advantageous in two ways, which are that the jump phenomenon associated with snap-through occurs very quickly, and thus the duration of actuation and power requirement is lower than sinusoidal voltage excitation, which also reduces the net simulation time. The second is that snap-through to the other state places the laminate on a location of the phase space that has a higher chance of being outside its initial attractor's basin of attraction. To ensure the consistency of this location, the voltage pulse ends when the corner out-of-plane displacement w^o reaches its first peak post snap-through which allows the corner velocity to be zero with every iteration. The corner is evaluated because it is the only location to have significant out-of-plane deflections in both stable states, so they alone are appropriate for evaluating cross-well orbits. It should be noted that this approach is a simplification of the higher-dimensional phase space representing the actual system and is used here for ease of implementation.

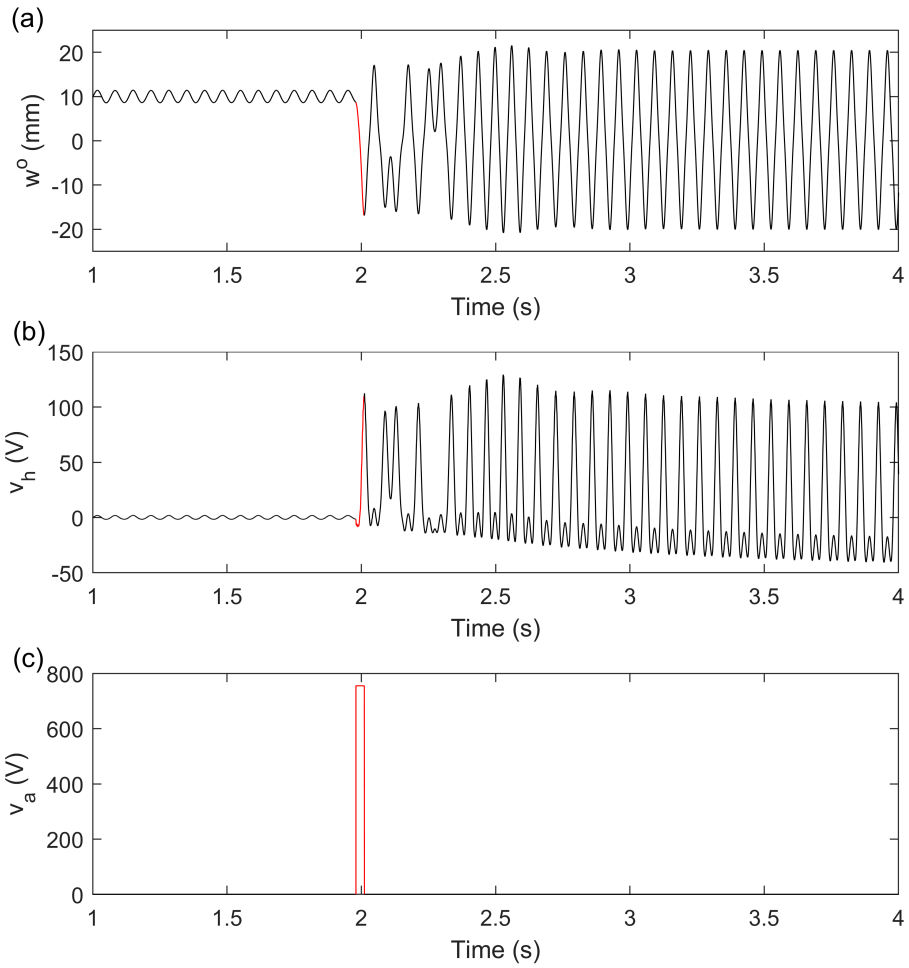

Figure 5.12: Jump from state I single-well to high amplitude limit cycle oscillations through a voltage pulse applied at $\phi = -0.6\pi$ rad w^o phase difference from t_a = 2 s under harmonic excitation of 1.5 g and 15.0 Hz showing time histories of (a) corner displacement w^o, (b) harvester voltage $v_h = v_1$, and (c) actuator voltage $v_s = v_2$. Red lines show time windows where where $v_a = 755$ V.

Two examples of switching from low to high energy orbits through a rectangular voltage pulse are presented in Figures 5.12 and 5.13 to illustrate the devised strategy. Figure 5.12(a), (b), and (c) show the corner displacement w^o, harvester voltage v_h, and actuator voltage v_a time histories of the jump from single-well orbit about state I to high amplitude limit cycle oscillations under the harmonic excitation of 15 Hz and 1.5 g. Since the system is initially oscillating about state I, $v_a = v_2$ and $v_h = v_1$. Figure 5.13(a), (b), and (c) show the switch from single-well orbit about

state II to chaotic oscillations at 20.7 Hz and 1.5 g, which is attributed by aperiodic snap-through events through the strange attractor motion. The solution switching method is effective regardless of which cross-well regime the laminate jumps into, which include intermittency, subharmonic, and superharmonic oscillations. Unlike limit cycle oscillations, the system is initially at state II, and so the voltage degree of freedom assignments are flipped so that $v_a = v_1$ and $v_h = v_2$. The large amplitude difference of the harvester voltage v_h between single-well and cross-well orbits in Figures 5.12(b) and 5.13(b) shows why the latter is preferred by VEHs, even at the upfront energy cost of voltage perturbations. Under a short duration, the net energy scavenged by nonlinear VEHs in high energy orbits post perturbation will far exceed what is harvested when they are in low energy orbits with no disturbances [99, 106, 107].

In the simulations of Figures 5.12 and 5.13, the initial conditions for $\{q\}$ are set to be the curvatures corresponding to either state I or II while $\{\dot{q}\} = 0$ and $v_h = 0$ V. Initially, the unactuated system $v_a = 0$ V is solved until $t = t_a = 2$ s to allow the laminate to settle into a steady state solution. Then the system state $\{q\}$, $\{\dot{q}\}$, and v_h at $t = t_a$ serve as the initial conditions to the actuated system $v_a = 755$ V, which is solved until w^o reaches its first peak after snap-through, or at $t = t_b$. The system is then reverted back to the unactuated $v_a = 0$ V at $t = t_b$ where the last state of actuated system is again carried over as initial conditions. If the jump into cross-well orbit is either not achieved or sustained for $t > t_b$, then the time history is re-simulated with the voltage pulse $v_a = 755$ V applied at a w^o phase difference ϕ from $t = t_a$. This procedure is repeated over one period of the single-well linear oscillations, where the phase difference is cycled through $\phi \in [-2\pi, 0]$ rad in -$n\pi$ increments until there is a successful switch into a co-existing high energy attractor. If the switch never occurs within this ϕ range, the step size n could be lowered and the solution search procedure repeated, but the desired attractor may also not exist. The number of

perturbation attempts could indicate the difficulty of reaching the high energy orbit based on the relative size of its basin of attraction compared to that of the low energy orbit. For jumps into limit cycle and chaotic oscillations in Figures 5.12 and 5.13, successful switches are made at $\phi = -0.6\pi$ and $\phi = -1.8\pi$ from $t_a = 2$ s, respectively.

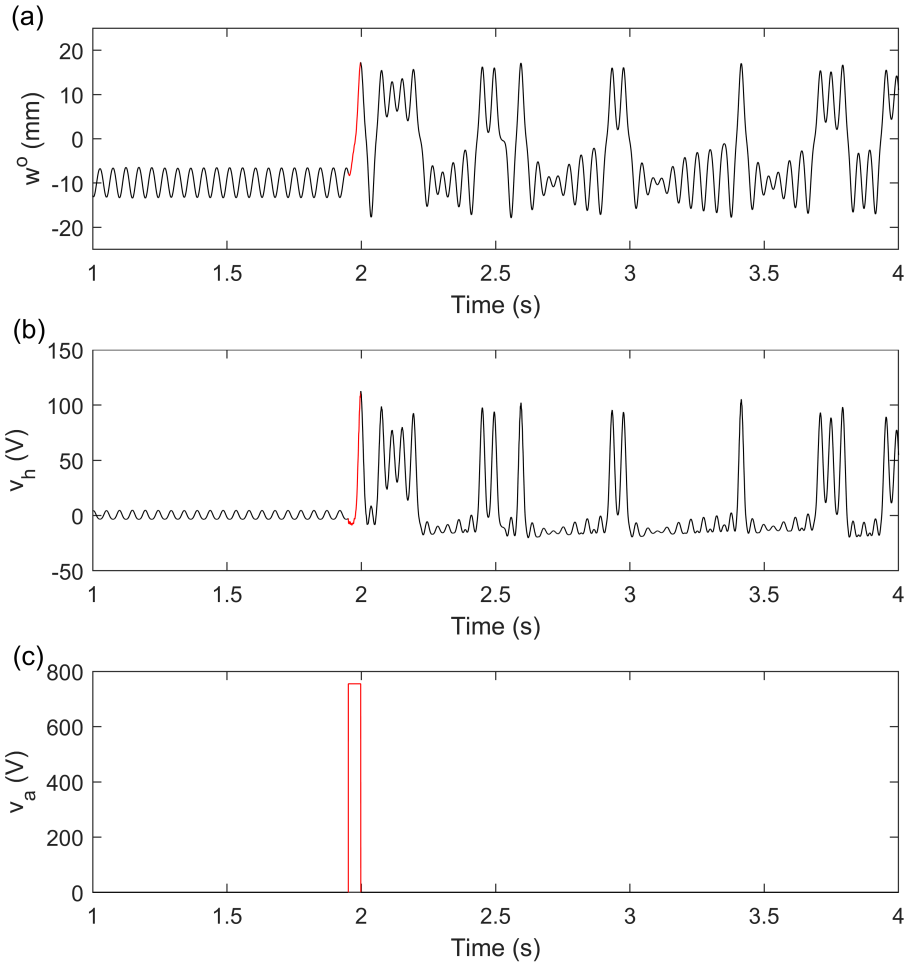

Figure 5.13: Jump from state 2 single-well to chaotic oscillations through a voltage pulse applied at $\phi = -1.8\pi$ rad w^o phase difference from t_a = 2 s under harmonic excitation of 1.5 g and 20.7 Hz showing time histories of (b) corner displacement w^o, (d) harvester voltage $v_h = v_2$, and (f) actuator voltage $v_s = v_1$. Red lines show time windows where where $v_a = 755$ V.

To better illustrate how the phase shifts are induced by varying where v_a is initiated, the system inputs from Figure 5.12 are taken to show all successful and unsuccessful switches from single-

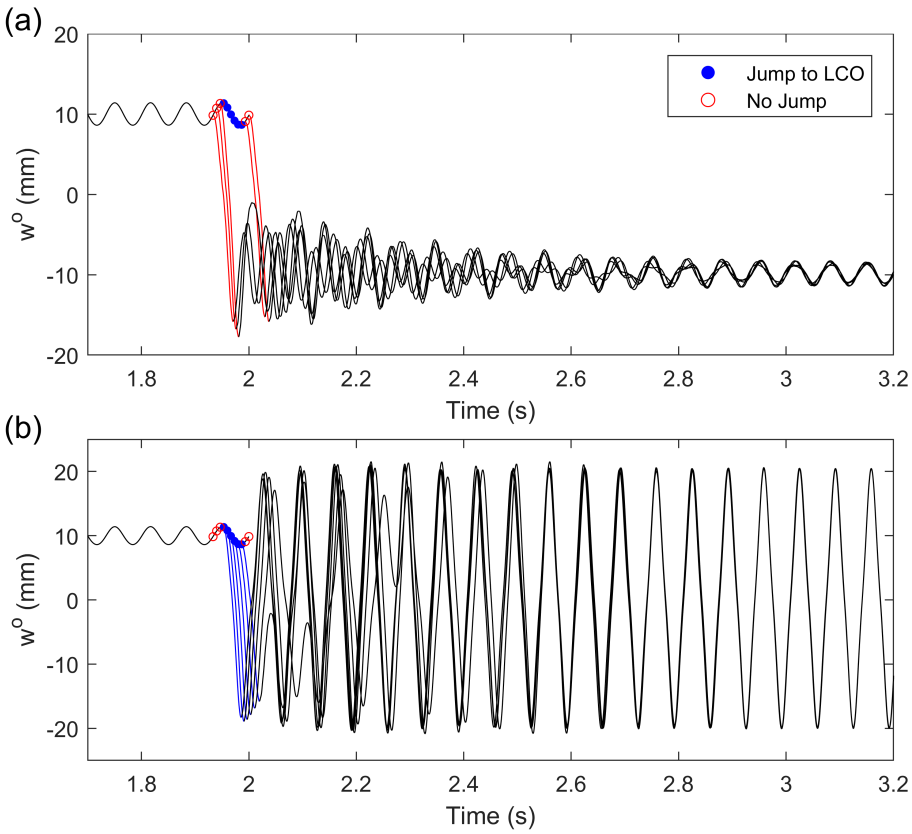

Figure 5.14: Under harmonic excitation of 1.5 g and 15.0 Hz, (a) unsuccessful and (b) successful jumps from state I single-well to high amplitude limit cycle oscillations through voltage pulses applied at $\phi \in [-2\pi, 0]$ rad w^o phase differences from t_a = 2 s in -0.2π steps. Blue and red markers show clusters of initial conditions where v_a is activated that do and do not allow switching from low to high energy orbits, respectively. Corresponding blue and red lines show time windows where $v_a = 755$ V.

well to limit cycle oscillations in Figure 5.14. The perturbation phase difference from $t_a = 2$ s is cycled through $\phi \in [-2\pi, 0]$ in -0.2π increments. For these particular inputs, the unsuccessful attempts are grouped into two clusters indicated by red markers, and range within $\phi \in [-0.2\pi, 0]$ and $\phi \in [-2\pi, -1.6\pi]$. The successful perturbations are grouped into a single cluster within $\phi \in [-1.4\pi, -0.4\pi]$ and are indicated by blue markers. The red and blue lines show time windows where the rectangular voltage pulse is activated. For each iteration at t_b, or where the pulse is removed, the resulting phase of the corner displacement w^o corresponds to where v_a is initiated. This

indicates that changing the perturbation phase difference ϕ relative to t_a will cause a controllable phase shift and alter the basins of attraction at t_b. If the laminate is placed in a co-existing high energy attractor's basin of attraction, the switch will be successful. All solutions following successful disturbances converge to the same limit cycle orbit in Figure 5.14(b) and those following unsuccessful disturbances converge to the same single-well orbit about state II in Figure 5.14(a). These behaviors suggest that the two solutions co-exist under the same input and no other attractors are present. Figure 5.15 present examples of unsuccessful and successful time dependent trajectories into high amplitude limit cycle oscillations from varying when the system is perturbed.

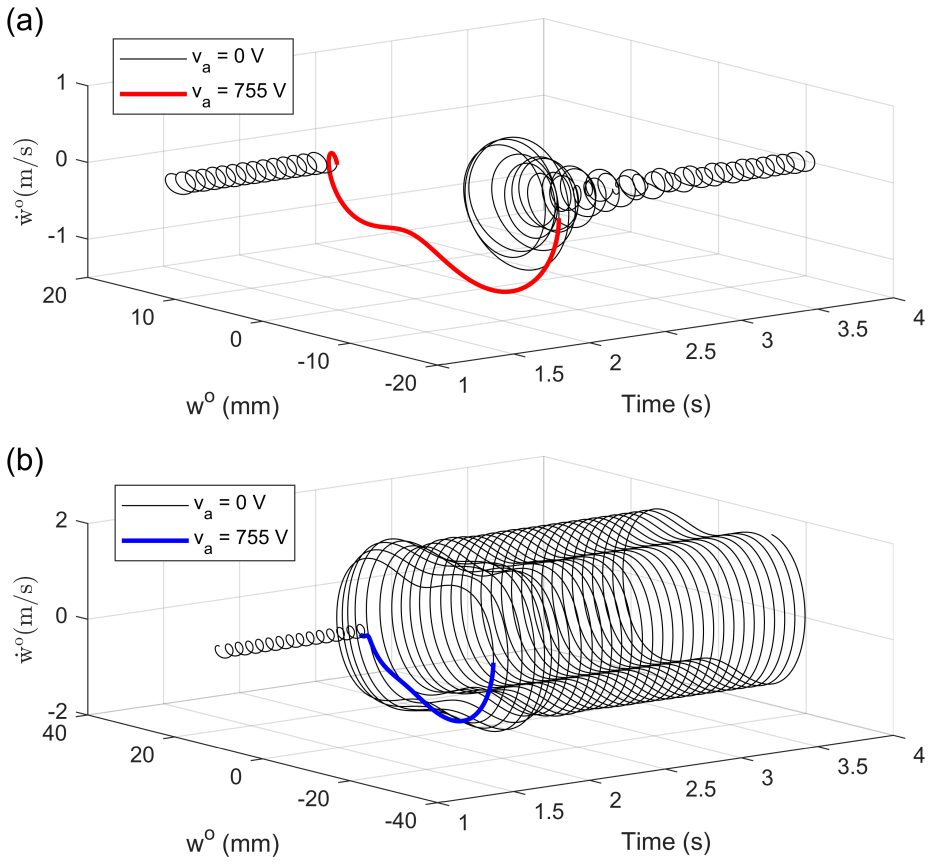

Figure 5.15: Numerically simulated orbital trajectories of an (a) unsuccessful and (b) successful jump from state I single-well into cross-well limit cycle oscillations. Harmonic excitation at 1.5 g and 15.0 Hz. Corresponding blue and red lines show time windows where $v_a = 755$ V.

5.4.3 Numerical Frequency Sweep Results

With the method established for perturbing the $[0^{MFC}/90^{MFC}]_T$ bistable laminate from low to high energy orbits, how this can be used to extend the cross-well bandwidth of the system is now investigated. For bistable VEHs to maintain effectiveness under a broadband environment at lower forcing levels, their narrowed nominal high energy bandwidths must be widened. This enables access to co-existent cross-well attractors at frequencies where the laminate cannot escape from single-well orbits without any external disturbances. For the unactuated system, Figure 5.16(a) and (b) present the numerical forward and backward frequency sweep results from 5 Hz to 30 Hz in 0.5 Hz increments at 2.5 g and 1.5 g, respectively. Peak to peak amplitudes of the harvester voltage v_h are obtained from simulated time histories with stroboscopic sampling at each excitation frequency over several forcing periods, as shown in Section 4.3.2. At each frequency, samples appear as a single point for linear single-well oscillations at low amplitudes and cross-well limit cycle or superharmonic oscillations at high amplitudes. Samples appear as multiple points for nonlinear responses including intermittency, subharmonic, and chaotic oscillations, and retain much larger v_h amplitudes than their single-well counterparts. Before the frequency sweeps are performed, the initial conditions for $\{q\}$ are set to be the curvatures corresponding to state I, and $\{\dot{q}\} = \{v\} = 0$. During the sweeps for each frequency, the $\{q\}$, $\{\dot{q}\}$, and v_h states of the final time step are used as the initial conditions for the next excitation frequency while $v_a = 0$. For both forcing levels, hysteretic regions between the sweep directions separate the boundaries between single and cross-well regimes as characterized by large amplitude jumps. The cross-well responses appear around the first plate bending mode which undergoes softening where its resonant peak is pushed below its natural frequency. At 2.5 g, the nominal cross-well bandwidths are 21 Hz to 25 Hz and 20 Hz

to 23.5 Hz in the forward and backward sweep directions, respectively. These bandwidths shrink at the lower forcing level of 1.5 g, where they are 22.5 Hz to 23.5 Hz and 21 Hz to 22 Hz in the forward and backward sweep directions, respectively. The peak v_h amplitudes also decrease with the lower excitation level.

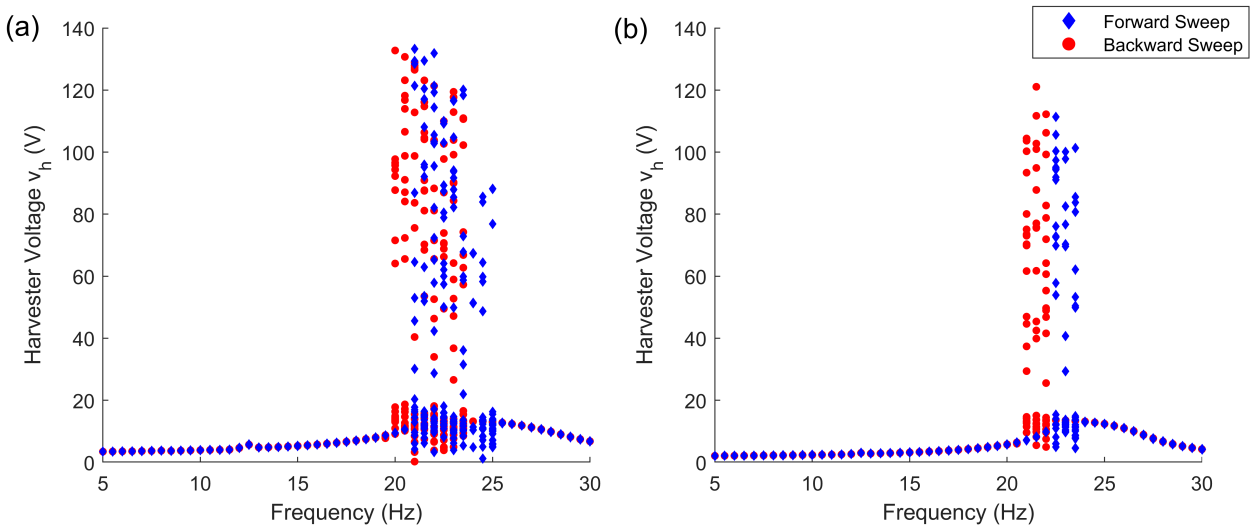

Figure 5.16: Stroboscopically sampled peak to peak harvester voltage v_h amplitudes during forward and backward frequency sweeps at (a) 2.5 g and (b) 1.5 g from initial state I for the unactuated $v_a = 0$ V system.

From these nominal sweeps, the results for how the laminate's high energy bandwidth changes when voltage perturbations are introduced into the system are shown in Figure 5.17(a) and (c) for forward and backward frequency sweeps at 2.5 g, respectively. As described in the previous section, the procedure of cycling the activation of the rectangular voltage pulse $v_a = 755$ V through $\phi \in [-2\pi, 0]$ rad w^o phase difference from $t = t_a$ is applied whenever the laminate is in single-well orbit at each frequency step. If it is already in cross-well orbit, then the system is left unperturbed and the sweep is continued. The ϕ sample step size is chosen to be -0.1π, and the solution search procedure is ended either when there is a successful jump into a co-existing high energy attractor, or the laminate fails to switch after cycling through the entire ϕ range. The latter case does not

necessarily mean that the desired co-existent attractor does not exist since an initial condition leading to the proper phase shift may have been missed. If it does exist, then the number of attempts describe the difficulty of accessing this solution. Although the ϕ step size could be lowered or v_a altered, this was not implemented to keep computation times manageable. Figure 5.17(b) and (d) reveal how many perturbation attempts were made while sampling through $\phi \in [-2\pi, 0]$ in the forward and backward sweep directions, respectively. None being made indicates that the system is already under cross-well oscillations. At any given frequency step, if $v_h = v_1$, $v_a = v_2$, and the laminate is under single-well orbit about state II, then the MFC harvester and actuator assignments are flipped ($v_h = v_2$, $v_a = v_1$) when the voltage pulse is activated so that snap-through can be initiated. If the single-well orbit is about state I, $v_h = v_2$, and $v_a = v_1$, then the assignments are also flipped when v_a is applied.

The application of voltage perturbations in both sweep directions reveal co-existing cross-well attractors at excitation frequencies well beyond the nominal high energy bandwidths and their hysteretic regions shown in Figure 5.16(a). The extended bandwidths show distinct regions of similar nonlinear responses with varying levels of accessibility. For the forward sweep, 7.5 Hz to 11 Hz exhibit a mix of subharmonic and superharmonic oscillations, then the response changes to limit cycle oscillations until 17 Hz. From this frequency, the laminate undergoes a mix of intermittency, chaotic, and subharmonic oscillations until 26.5 Hz, and the total resulting cross-well bandwidth is 19 Hz, which is a 375% increase from the nominal 4 Hz of the unperturbed system. The backward sweep shows identical responses with the exception of its bandwidth's upper boundary being 26 Hz. This results in a total bandwidth of 18.5 Hz, which is a 429% increase from the nominal size of 3.5 Hz. The near identical responses between sweep directions suggest that the solution searching procedure is thorough enough to not be influenced by hysteresis.

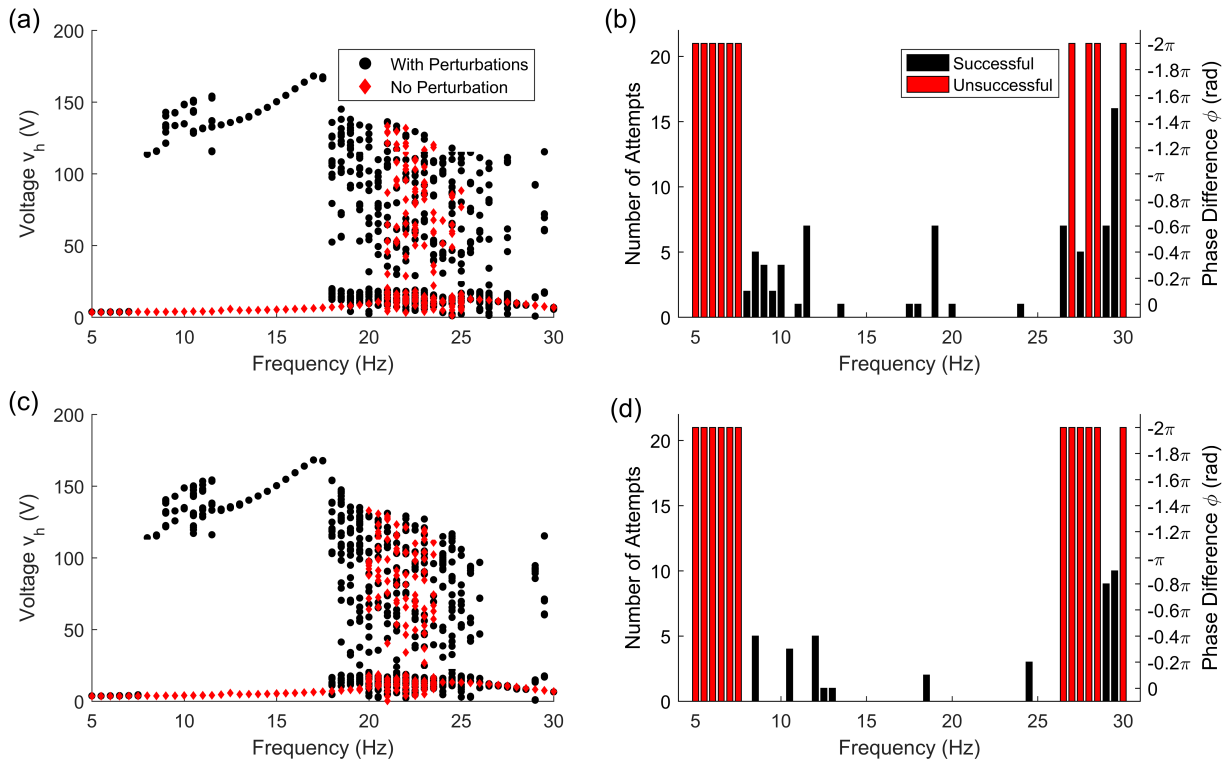

Figure 5.17: Stroboscopically sampled peak to peak harvester voltage v_h amplitudes with and without voltage perturbations during (a) forward and (c) backward frequency sweeps at 2.5 g from initial state I. Corresponding number of voltage perturbation attempts and w^o phase difference ϕ between when rectangular pulse is activated and t_a for (b) forward and (d) backward frequency sweeps.

However its effects can be observed in the number of perturbation attempts needed for jumping into the high energy attractor. Below 11 Hz, the backward sweep requires less trials to access the subharmonic and superharmonic orbits due to the initial conditions being carried from the frequencies above when the system undergoes high amplitude limit cycle oscillations. At isolated frequencies beyond the upper boundary of the extended bandwidth, the forward sweep is able to access more co-existing high energy attractors. For both directions, the regions corresponding to limit cycle oscillations and the nominal cross-well bandwidths require less attempts. This suggests that their basins of attraction are larger compared to those of the low energy attractors and more

accessible than the solutions in other regions. The significant bandwidth extensions demonstrate the perturbation strategy's effectiveness in enhancing the bistable laminate's energy harvesting performance.

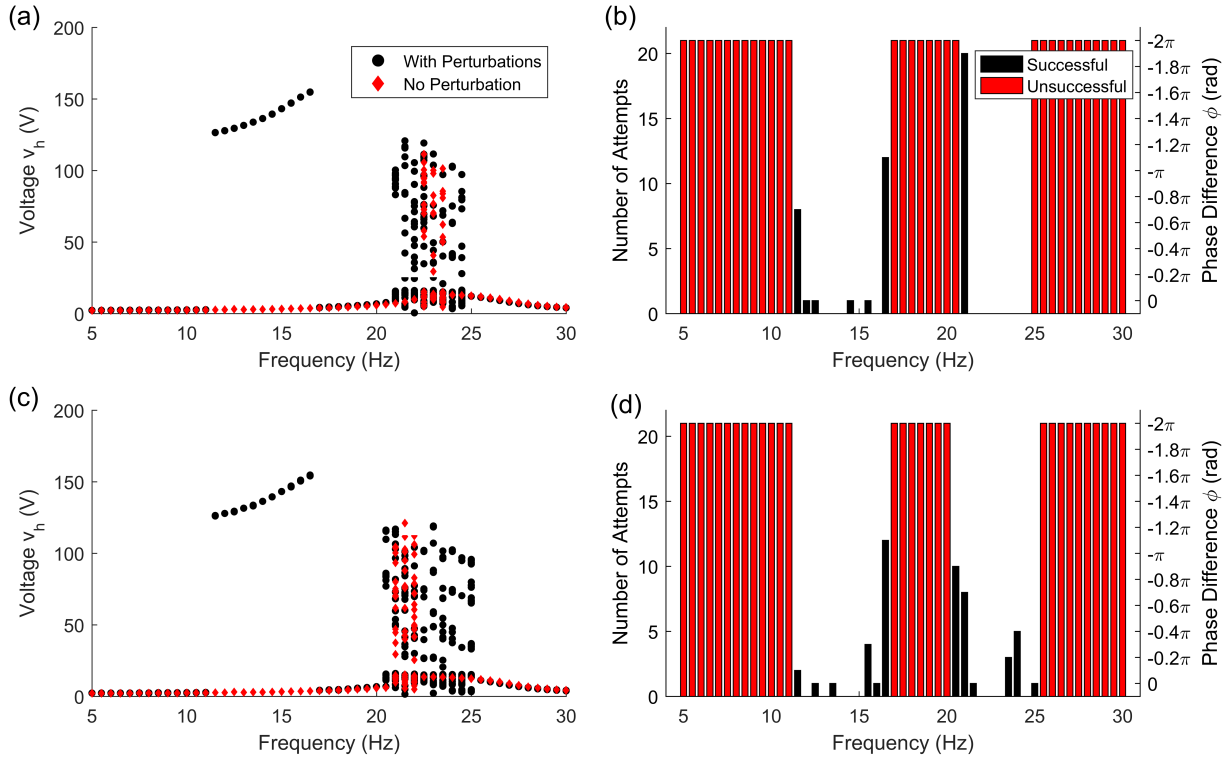

Figure 5.18: Stroboscopically sampled peak to peak harvester voltage v_h amplitudes with and without voltage perturbations during (a) forward and (c) backward frequency sweeps at 1.5 g from initial state I. Corresponding number of voltage perturbation attempts and w^o phase difference ϕ between when rectangular pulse is activated and t_a for (b) forward and (d) backward frequency sweeps.

To determine if the cross-well bandwidth extension from voltage perturbations can be maintained at a lower forcing level, frequency sweep results at 1.5 g are shown in Figure 5.18(a) and (b) in the forward direction and (c) and (d) in the backward direction. The large bandwidth enhancement achieved at 2.5 g becomes divided into two narrower regions, where the first is 11.5 Hz to 16.5 Hz containing limit cycle oscillations as the co-existing attractor, and the second is 21 Hz

to 24.5 Hz for the forward sweep and 20.5 Hz to 25 Hz for the backward sweep. Relative to their nominal bandwidths from Figure 5.16(b), the combined extended bandwidths are 750% and 850% increases for the forward and backward sweeps, respectively. The frequency ranges between the two regions and below the first limit cycle region remain under single-well oscillations due to the co-existing high energy attractor's basins of attraction either diminishing or entirely disappearing. At 2.5 g, the cross-well regions that on average took a higher number of attempts for successful perturbations now remain in low energy orbit through the 1.5 g sweeps. Although the range of frequencies where the bistable laminate can sustain high power output is still enhanced including access to the desirable limit cycle oscillations, the size of the extended bandwidth decreases with lower forcing levels.

5.5 Chapter Summary

Although there have been numerous efforts into harnessing the snap through dynamics of bistable composites with piezoelectric transducers to achieve large energy conversion, these same dynamics are undesirable under morphing applications where control of the structure's configuration is paramount. To suppress cross-well vibrations that primarily result from periodic excitation at low frequencies, the first half of the chapter proposes a novel control strategy and implements it with the $[0^{MFC}/90^{MFC}]_T$ piezoelectrically generated bistable laminate. While under cross-well regimes such as subharmonic, chaotic, or limit cycle oscillations, a single MFC is actuated to the laminate's limit voltage to eliminate one of its potential wells and force it into the remaining stable state. Simultaneously, a PPF controller suppresses the resulting single-well oscillations through the other MFC. This dual control strategy is numerically and experimentally demonstrated to be

effective at suppressing various cross-well regimes, and results in significant reduction of amplitude while staying within MFC operating limits. When compared to implementing a single PPF controller without any static actuation, dual control retains better performance in settling time to single-well steady state while being able to push limit cycle oscillations out of cross-well orbit. In addition, configuration control is possible where the choice of MFC dictates which state the laminate settles into in the closed-loop system. To mitigate the large power consumption caused by static actuation, it is removed once the laminate is in single-well steady state and the laminate is found to remain suppressed within the potential well. The active control capability of the laminate prevents snap through instability when under large enough external vibrations.

The latter half of the chapter presents a perturbation strategy of initiating jumps between single-well to cross-well orbits to widen the high energy bandwidths of the $[0^{MFC}/90^{MFC}]_T$ bistable laminate. The highly energetic response resulting from large amplitudes and broadband spectrum of cross-well oscillations result in greater power generation for bistable VEHs when compared to what linear vibrations can yield. By accessing their associated co-existing attractors through external disturbances, the laminate's energy harvesting performance can be enhanced through the extension of effective operational conditions. Phase shifts in the system response are induced by controlling when the voltage pulses are applied to alter the basins of attraction until the laminate lands on the desired attractor. The pulse magnitude is where the system exhibits limit point behavior and the resulting snap through actuation mechanism brings consistency between perturbation trials. Numerical simulations show significant increase to the bandwidths inducing cross-well oscillations when the perturbation strategy is employed. Cross-well bandwidths increase by 375% and 429% in forward and backward frequency sweeps at 2.5 g, respectively. These increases are enlarged to 750% and 850% when the forcing is lowered to 1.5 g for forward and backward sweeps,

respectively. With the perturbations, the favorable broadband cross-well response is maintained and the efficient conversion from vibrational to electrical energy is possible even at low forcing levels.

CHAPTER 6

Conclusions

6.1 Dissertation Summary

This dissertation focuses on how bistability in composite laminates can be induced with piezoelectric actuation through MFCs. Design efficiencies that arise out of having the MFCs act as both the transducers and primary structure allow for the bistable laminate to retain multiple functions in morphing, energy harvesting, and vibration control. The work in this dissertation addresses outstanding research challenges in each of these smart applications. The following section provides detailed summaries of each chapter.

6.1.1 Chapter 2

The electromechanically coupled analytical model of a piezoelectrically generated bistable laminate is derived for both static and dynamic analysis. By bonding two actuated MFCs in an unsymmetric layup and releasing the voltage post cure, piezoelectric strain anisotropy and the resulting in-plane residual stresses yield two statically stable states that are cylindrically shaped. To capture the large out-of-plane deformations associated with bistable composite laminates, CLT is extended to included nonlinear terms in the kinematic strain-displacement relationships according

to the von Karman plate theory, which allows for moderate rotations of the middle surface and large out-of-plane displacements. Within the CLT constitutive equations, the thermal analogy is used to replace thermal strains induced by temperature change to piezoelectric strains caused by an applied electric field due to MFC voltage actuation. The resulting piezoelectric forces and moments per unit length are responsible for generating the residual stresses necessary for bistability through the elastic potential energy.

To predict the cylindrical geometries, Rayleigh-Ritz approximations are made for the mid-plane strain and displacement functions which satisfy geometric boundary conditions. Second and third order polynomials proposed by Dano and Hyer [36] provide adequate accuracy for static profiles, but higher order shape functions are necessary to retain low errors for dynamic analysis. By allowing spatially variable curvatures through fourth and fifth order polynomials, the laminate stiffness is not artificially raised which allows for accurate forcing level input to laminate response output trends. The elastic potential energy carrying the laminate stiffness and the bonding voltage loading terms is minimized relative to the number of unknown coefficients associated with the Rayleigh-Ritz shape functions. The resulting nonlinear equilibrium equations can be numerically solved to obtain the static laminate shapes under a variety of specified geometrical parameters and piezoelectric loading. The stability of the solution is determined by evaluating if the Jacobian matrix of the equilibrium equations is positive definite.

The nonlinear electromechanical MDOF equations of motion are derived using Lagrange's equations, where the degrees of freedom are the generalized curvature and voltage coordinates. To allow for dynamic voltage control and response with the MFCs, the electromechanical coupling terms are separately obtained using the piezoelectric constitutive equations, internal electric energy, and piezoelectric potential energy, and they are combined with the elastic potential energy. The

total potential energy is then reformulated to be a function of just the generalized curvature and voltage coordinates to reduce computation times. The kinetic energy is also obtained to account for the inertial forces and base excitation at the laminate center. Once the equations of motion are found, Rayleigh damping is assumed to incorporate energy dissipation in the system.

6.1.2 Chapter 3

Utilizing the static analytical model of the $[0^{MFC}/90^{MFC}]_T$ bistable laminate from Chapter 2, the effects of the laminate side length, adhesives, and their cure cycles on the resulting shapes and their stability are characterized in order to design a viable morphing structure. For square laminates bonded at 1500 V with P1 type MFCs, the minimum side length to induce perfectly symmetric bistability is predicted to be 85 mm and lengths greater than this value yield stable geometries with greater out-of-plane deformations post bifurcation. To ensure enough margin for modelling and manufacturing errors, a 200 mm side length is chosen for fabrication. Adhesive thickness and high cure cycle temperatures are found to have an adverse effect on bistability, and so the room temperature cure of the DP-460 epoxy is chosen to avoid thermal loading on the MFCs while maintaining a thin bond line.

The $[0^{MFC}/90^{MFC}]_T$ laminate is then manufactured and its unactuated geometry, bifurcation behavior, and snap-through actuation are experimentally measured and compared against model predictions. FEA is also conducted to provide an additional modelling tool for static analysis. Overall, good agreement is found in the stable shapes with errors growing towards the edges and corners due to free edge effects and manufacturing errors. The higher order analytical model retains the greatest accuracy when compared to the FEA and the lower order model. When both

MFCs are simultaneously actuated, the laminate's bifurcation point disappears due to material and geometric imperfections. By actuating one MFC at a time within its operating limits, the laminate can snap-through unassisted between either stable states. This is analytically and experimentally demonstrated and the capability is critical for morphing where full configuration control is required.

Limitations may exist for structural applications due to the active laminate's lower stiffness when compared to conventional fiber-reinforced composites. However, it is envisioned that the concept of piezoelectrically induced bistability will be extended into more complex structures. Piezoelectric strain could be additive to thermal or elastic strain within bistable composites to generate larger motion, alleviate snap-through requirements, and minimize design restrictions. This has the potential of producing a fully load bearing bistable structure that maintains complete snap-through capability without any external assistance. Overall, this chapter has demonstrated the validity of the static model for the piezoelectrically generated bistable laminate by capturing complex nonlinear phenomena associated with its stable shapes, stability, and the snap-through behavior.

6.1.3 Chapter 4

The electromechanical responses and energy harvesting performance of a $[0^{MFC}/90^{MFC}]_T$ piezoelectrically generated bistable laminate under base harmonic excitation are investigated with analytical model simulations and experiments. Its inherent structural nonlinearities are exploited to induce high amplitude broadband cross-well vibrations to maximize power generation from the MFCs. The linearized modal analysis yields vibration modes and the corner velocity frequency response function about each stable configuration, which show good agreement with experimental

results. Under high amplitude excitation, the nonlinear response of the laminate is predicted by numerically solving the electromechanically coupled equations of motion. Open circuit voltage and corner velocity amplitudes under frequency sweeps at various acceleration levels are adequately correlated with their experimental counterparts and exhibit dynamic nonlinearities such as sweep direction dependent hysteresis and stiffness softening. Various cross-well regimes such as intermittency, limit cycle, chaotic, and subharmonic oscillations observed in experiments are predicted by the model at either identical or similar excitation parameters. Characteristics of the observed regimes are found through time histories, spectrum analysis, phase portraits, and Poincaré maps of select data, which are then used to determine the response of all other sweep results.

The power output of each regime is then experimentally measured through resistor sweeps and high amplitude limit cycle oscillations are found to be the optimal dynamic response. When charging an energy harvesting module, the quickest times are measured when the MFCs are connected in parallel since the overall current output is maximized, and the collected energy is then discharged through a high voltage amplifier and back into either MFC to initiate snap-through. The laminate's viability for energy harvesting is demonstrated, allowing it to retain multiple roles when including its snap-through morphing capability. Due to the model idealizing material and geometric properties, initial state dependent asymmetric behavior caused by manufacturing imperfections and asymmetric cross-well orbits within the experimental results are not seen in the simulations. If an imperfection is empirically introduced into the model, these asymmetries are only partially accounted for. Overall however, the electromechanical model is able to produce fairly accurate voltage and power outputs of a piezoelectric bistable laminate under nonlinear cross-well vibrations. Its viability for energy harvesting is both analytically and experimentally confirmed with favorable power output over a wide frequency range.

6.1.4 Chapter 5

Although there have been numerous efforts into harnessing the snap through dynamics of bistable composites with piezoelectric transducers to achieve large energy conversion, these same dynamics are undesirable under morphing applications where control of the structure's configuration is paramount. To suppress cross-well vibrations that primarily result from periodic excitation at low frequencies, the first half of the chapter proposes a novel control strategy and implements it with the $[0^{MFC}/90^{MFC}]_T$ piezoelectrically generated bistable laminate. While under cross-well regimes such as subharmonic, chaotic, or limit cycle oscillations, a single MFC is actuated to the laminate's limit voltage to eliminate one of its potential wells and force it into the remaining stable state. Simultaneously, a PPF controller suppresses the resulting single-well oscillations through the other MFC. This dual control strategy is numerically and experimentally demonstrated to be effective at suppressing various cross-well regimes, and results in significant reduction of amplitude while staying within MFC operating limits. When compared to implementing a single PPF controller without any static actuation, dual control retains better performance in settling time to single-well steady state while being able to push limit cycle oscillations out of cross-well orbit. In addition, configuration control is possible where the choice of MFC dictates which state the laminate settles into in the closed-loop system. To mitigate the large power consumption caused by static actuation, it is removed once the laminate is in single-well steady state and the laminate is found to remain suppressed within the potential well. The active control capability of the laminate prevents snap through instability when under large enough external vibrations.

The latter half of the chapter presents a perturbation strategy of initiating jumps between single-well to cross-well orbits to widen the high energy bandwidths of the $[0^{MFC}/90^{MFC}]_T$ bistable

laminate. The highly energetic response resulting from large amplitudes and broadband spectrum of cross-well oscillations result in greater power generation for bistable VEHs when compared to what linear vibrations can yield. By accessing their associated co-existing attractors through external disturbances, the laminate's energy harvesting performance can be enhanced through the extension of effective operational conditions. Phase shifts in the system response are induced by controlling when the voltage pulses are applied to alter the basins of attraction until the laminate lands on the desired attractor. The pulse magnitude is where the system exhibits limit point behavior and the resulting snap through actuation mechanism brings consistency between perturbation trials. Numerical simulations show significant increase to the bandwidths inducing cross-well oscillations when the perturbation strategy is employed. Cross-well bandwidths increase by 375% and 429% in forward and backward frequency sweeps at 2.5 g, respectively. These increases are enlarged to 750% and 850% when the forcing is lowered to 1.5 g for forward and backward sweeps, respectively. With the perturbations, the favorable broadband cross-well response is maintained and the efficient conversion from vibrational to electrical energy is possible even at low forcing levels.

6.2 Main Research Contributions

The following list summarizes the major contributions of this dissertation in the research area of multistable composite structures for morphing, broadband energy harvesting, and active vibration control.

- A novel method for generating bistability in composite laminate plates is proposed and successfully achieved. This involves bonding two MFCs while they are actuated in a unsymmet-

ric layup and removing the voltage post cure to yield two cylindrically stable shapes. Having an entirely active structure where the piezoelectric transducers are both the actuator and primary structure allows for it to have multiple applications in morphing, energy harvesting, and vibration control.

- An electromechanical model of the piezoelectrically generated bistable laminate is derived to predict its nonlinear static and dynamic behavior under various operating conditions. The primary contributions of the analytical model are accounting for MFC actuation as the mechanism for inducing bistability and predicting the electromechanically coupled nonlinear dynamic response of the laminate. Thermal analogy is utilized to model the strain effects of MFC actuation and higher order shape functions are used to raise the accuracy of predicted geometries and stability characteristics by allowing spatially variable curvatures. The static model is then extended to include electromechanical coupling from the piezoelectric constitutive equations and nonlinear dynamics with Lagrange's equations. The resulting MDOF equations of motion allows for the MFC voltage input and output to the system to be predicted under nonlinear vibrations, which has not been implemented before.

- The piezoelectrically generated bistable laminate is successfully manufactured using the $[0^{MFC}/90^{MFC}]_T$ layup. Its static profiles, bifurcation behavior, and stability are accurately captured by the analytical model across the voltage range of the MFCs. Due to the increased actuation authority of the MFCs and lowered laminate stiffness, unassisted reversible snap-through morphing is demonstrated within their operating limits. This work shows that using piezoelectric straining as a design tool for generating multistability could overcome performance restrictions in morphing.

- The broadband energy harvesting performance is shown to be favorable while the laminate is under snap-through dynamics which include intermittency, limit cycle, chaotic, and sub-harmonic oscillations. By having an entirely piezoelectric laminate where the MFCs are directly responsible for bistability, the design conflict between the passive composite and active transducer can be avoided. This allows the desirable cross-well oscillations to be more easily triggered while still maintaining large out-of-plane displacement amplitudes. The model simulations capture the MFC voltage magnitudes, dynamic regime per excitation parameter, and nonlinearities including hysteresis and stiffness softening observed in the experimental results with fair accuracy. This work also shows that the laminate's energy harvesting and morphing capabilities can be bridged by utilizing the harvested power in a charged module to initiate snap-through actuation.

- A novel control strategy for suppressing cross-well oscillations is proposed and implemented to prevent snap-through instabilities under dynamic loading. While under any of the cross-well regimes, a single MFC is actuated to the limit voltage to eliminate a potential well and force the oscillations into the remaining well. A PPF controller is simultaneously applied through the other MFC to suppress the resulting single-well vibrations. Experimental results provide model validation for placing the laminate into either of the two stable states depending on the MFC assignments as the PPF controller and static actuator.

- Extension of cross-well bandwidths is demonstrated with voltage perturbations from the MFCs to cause solution switching from single-well to cross-well oscillations. The main contribution is in controlling when the voltage pulses are applied to induce systematic phase shifts to continuously alter the basins of attraction until the laminate lands on the desired

high energy attractor. This perturbation strategy is numerically shown to widen the range of excitation conditions where cross-well oscillations can be initiated, which enhances the broadband energy harvesting capability of the bistable laminate.

6.3 Recommendations for Future Work

With the concept of piezoelectrically induced bistability in composite structures, there are several different research directions that future work can take. Piezoelectric actuation could be combined with thermal or elastic residual stresses as the mechanism for yielding multistable composites. This has the potential to address the disadvantages of both conventional and piezoelectrically generated bistable laminates by allowing them to be load bearing morphing structures through stiffness retention and have enough actuation authority to quasi-statically trigger reversible snap-through between stable configurations. With the analytical model, parametric analysis would have to be conducted to yield composite designs which can satisfy both requirements. Another challenge would be establishing a manufacturing procedure which allows the actuated MFCs to survive while being bonded onto the host structure. MFCs cannot withstand the cure temperatures for conventional CFRP composite laminates, so they would have to be bonded post cure as the outer plies. Mechanically prestressed composites present more design freedom where the actuators can be incorporated as the inner plies during the curing process. For more complex structures, multi-physics FEA could be developed to accurately model the thermalelastic and electromechanical coupling effects presented by the proposed combination of active and passive materials.

With the experimentally validated analytical model, gradient-based design optimization could be conducted for piezoelectrically generated bistable laminates with broadband energy harvesting

metrics as the objectives. Multi-frequency power and energy metrics which are normalized against the laminate's physical properties and forcing level could be optimized against its dimensions, layup, and bonding voltage as design variables. The size of cross-well bandwidths would also need to be accounted for in the metrics since it provides a measure of operational effectiveness. With the lack of any optimized multistable VEHs in the current literature, this work could yield design trends and guidelines which aid in maximizing performance. The challenge is in managing computation times since the current model requires numerical integration to obtain the desired metrics, and so more efficient solutions using techniques such as the harmonic balance method may be required.

Experimental work could be conducted on extending the bistable laminate's cross-well bandwidths to provide validation for the corresponding numerical analysis in this dissertation. A more sophisticated experimental setup is required to enable control of when the voltage pulses are applied and removed. Measurements from a laser vibrometer or a displacement sensor would be used to track the motion of the laminate and this data would provide the timing for when the perturbations are applied in real time. The energy output from the harvester MFC could be measured over time to determine the duration needed to recover the energy spent on the perturbations. On the modelling side, the perturbation strategy could be improved by identifying all basins of attraction for a given set of initial conditions. This would greatly lower the number of trials required to trigger the jump from low to high energy orbits since the possible solutions are identified beforehand. The difficulty is in managing the large number of degrees of freedom of the electromechanical system and their derivatives during numerical integration.

6.4 List of Publications

Journal Publications

1. Lee, A.J., Xie, A., and Inman, D.J., "Suppression of Cross-well Oscillations for Bistable Composites through Potential Well Elimination", *Journal of Vibration and Acoustics*, 2019. (Under Review)

2. Lee, A.J. and Fernandez, J.M., "Inducing Bistability in Collapsible Tubular Mast Booms with Thin-Ply Composite Shells", *Composite Structures*, 2019. (Under Review)

3. Lee, A.J. and Inman, D.J., "Electromechanical Modelling of a Bistable Plate with Macro Fiber Composites under Nonlinear Vibrations", *Journal of Sound and Vibration*, Vol. 446, No. 28, 2019, pp. 326-342.

4. Lee, A.J. and Inman, D.J., "Multifunctional Bistable Laminate: Snap Through Morphing Enabled by Broadband Energy Harvesting", *Journal of Intelligent Material Systems and Structures*, Vol. 29, No. 11, 2018, pp. 2528-2543.

5. Lee, A.J., Moosavian, A. and Inman, D.J., "Control and Characterization of a Bistable Laminate Generated with Piezoelectricity", *Smart Materials and Structures*, Vol. 26, No. 8, 2017, pp. 085007.

6. Lee, A.J., Moosavian, A. and Inman, D.J., "A Piezoelectrically Generated Bistable Laminate for Morphing", *Materials Letters*, Vol. 190, 2017, pp. 123-126.

7. Lee, A.J., Wang, Y., and Inman, D.J., "Energy Harvesting of Piezoelectric Stack Actuator from a Shock Event", *Journal of Vibration and Acoustics*, Vol. 136, No. 1, 2014, pp.

011016-1-011016-7.

Conference Proceedings

1. Lee, A.J. and Inman, D.J., "Extension of Cross-well Bandwidths for a Bistable Oscillator", *SPIE Active and Passive Smart Structures and Integrated System*, 3-7 March 2019, Denver, CO.

2. Fernandez, J.M. and Lee, A.J., "Bistability in Collapsible Tubular Mast Booms", *AIAA Spacecraft Structures Conference, AIAA SciTech Forum*, 7-11 January 2019, San Diego, CA.

3. Lee, A.J. and Inman, D.J., "Electromechanical Response of a Bistable Laminate with Macro Fiber Composites from Nonlinear Vibrations", *29th International Conference on Adaptive Structures and Technologies*, 30 September - 4 October 2018, Seoul, South Korea.

4. Lee, A.J., Xie, A., and Inman, D.J., "Suppression of Cross-well Oscillations with Active Control of a Bistable Laminate", *ASME Smart Materials, Adaptive Structures and Intelligent Systems*, 10-12 September 2018, San Antonio, TX.

5. Lee, A.J. and Inman, D.J., "Broadband Energy Harvesting Performance of a Piezoelectrically Generated Bistable Laminate", *36th International Modal Analysis Conference*, 12-15 February 2018, Orlando, FL.

6. Lee, A.J. and Fernandez, J.M., "Mechanics of Bistable Two-Shelled Composite Booms", *AIAA Spacecraft Structures Conference, AIAA SciTech Forum*, 8-12 January 2018, Kissimmee, FL.

7. Lee, A.J., Moosavian, A., and Inman, D.J., "Piezoelectrically Strained Bistable Laminates with Macro Fiber Composites", *SPIE Active and Passive Smart Structures and Integrated System*, 25-29 March 2017, Portland, OR.

8. Moosavian, A., Chae, E.J., Pankonien, A.M., Lee, A.J., and Inman, D.J., "A Parametric Study on a Bio-inspired Continuously Morphing Trailing Edge", *SPIE Bioinspiration, Biomimetics, and Bioreplication*, 25-29 March 2017, Portland, OR.

9. Lee, A.J., Moosavian, A., and Inman, D.J., "An Investigation into Piezoelectrically Induced Bistability", *27th International Conference on Adaptive Structures and Technologies*, 3-5 October 2016, Lake George, NY.

10. Lee, A.J., Wang, Y., and Inman, D.J., "Power Harvesting Prediction of Piezoelectric Stack Actuator from a Shock Event", *ASME International Design Engineering Technical Conferences & Computers and Information in Engineering Conference*, 4-7 August 2013, Portland, OR.

APPENDICES

APPENDIX A

Miscellaneous Design Factors and Curvature Errors

A.1 Effects of Modelling Constituent MFC Plies

The analytical results in Chapter 3 are obtained by modelling each MFC in the $[0^{MFC}/90^{MFC}]_T$ bistable laminate as a single orthotropic lamina with effective material properties shown in Table 3.1. In reality, the MFC consists of rectangular piezoceramic fibers encased in epoxy, layers of interdigitated electrodes, Kapton, and acrylic as shown in Figure 1.6 and in [52, 122]. To determine how accounting for each constituent layer will affect the stable shapes and stability results, each material is modelled through CLT by modifying the laminate layup from $[0^{MFC}/90^{MFC}]_T$ to $[Ka/Ac/90^{CE}/0^{PZT}/90^{CE}/Ac/Ka_2/Ac/0^{CE}/90^{PZT}/0^{CE}/Ac/Ka]_T$. This is equivalent to the original cross-ply layup where each MFC now consists of seven plies instead of one. Note that only the copper electrode and piezoceramic fiber layers are orthotropic and retain ply angles while the Kapton and acrylic are isotropic. The resulting laminate consists of fourteen total plies and the material properties of each ply is given in Table A.1 [122].

Table A.1: Material properties of MFC constituent layers.

Layer	E_1 (GPa)	E_2 (GPa)	ν_{12}	G_{12} (GPa)	Thickness (mm)
Kapton	2.5	2.5	0.34	0.93	0.0254
Acrylic	2.7	2.7	0.35	1.0	0.0127
Copper Electrodes	30.48	4.39	0.28	1.73	0.0178
Piezoceramic Fibers	47.16	20.29	0.37	7.66	0.1905

The properties of the orthotropic layers were reported to be found using a rule of mixtures approach. The piezoelectric constants remain unchanged from Table 3.1, but these only apply for the piezoceramic fiber layers. This means a voltage application will directly induce piezoelectric strain in the fiber layer while all other layers remain inactive.

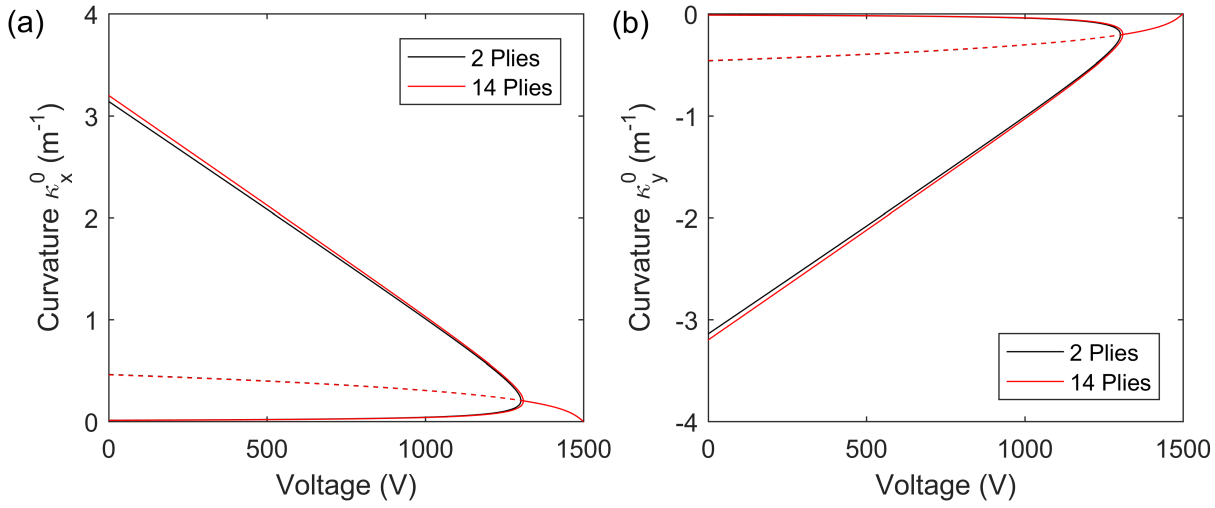

Figure A.1: Curvatures (a) κ_x^0 and (b) κ_y^0 vs. voltage of the 200 x 200 mm^2 piezoelectrically generated bistable laminate modelled with the 2 ply layup $[0^{MFC}/90^{MFC}]_T$ and the 14 ply layup $[Ka/Ac/90^{CE}/0^{PZT}/90^{CE}/Ac/Ka_2/Ac/0^{CE}/90^{PZT}/0^{CE}/Ac/Ka]_T$. Solid lines are stable and striped lines are unstable.

The curvatures vs. voltage plots of the $[0^{MFC}/90^{MFC}]_T$ laminate represented as two plies and fourteen plies are given in Figure A.1, where solid lines are stable and striped lines are unstable. The lower order analytical model is numerically evaluated to obtain the curvature results. Note that the epoxy adhesive bonding the two MFCs are neglected in this analysis. At the bonding

voltage of 1500 V, the laminate remains flat with zero curvature and displacement. Once the voltage is removed, the resulting delta voltage generates curvature due to the mismatch of effective piezoelectric constants. The laminate retains a monostable saddle shape until bifurcation, where the branch splits into two cylindrically stable paths and a single unstable saddle path. The two layups show close agreement in their curvatures and the bifurcation delta voltages are -197 V for the two ply and -190 V for the fourteen ply configurations. The two ply layup predicts lower major curvatures and a more delayed bifurcation point, and so the resulting stable shapes are slightly more accurate when compared to experimental fits in Figure 3.9. Since there are only minor differences between the two, the original $[0^{MFC}/90^{MFC}]_T$ layup is used in all static and dynamic analysis in this dissertation for ease of modelling.

A.2 Ply Angles and Layup

This appendix section examines how the stable geometries of the piezoelectrically generated bistable laminate varies when its MFC ply angles are varied away from the $[0^{MFC}/90^{MFC}]_T$ layup analyzed in Chapter 3. Through parametric analysis with the lower order analytical model, Figure A.2 and A.3 respectively present the maximum magnitude of the major curvature and twist curvature between stable configurations at every combination of MFC ply angles θ_1^{MFC} and θ_2^{MFC}. The ply angles in the 200 x 200 mm^2 $[\theta_1^{MFC}/\theta_2^{MFC}]_T$ laminate range from -90 ° to 90° to cover the possible design space. Since the curvatures are assumed to be constant across the domain, they provide a more succinct description of the laminate shape when compared to the out-of-plane displacements, which can largely vary depending on the position. Note that the DP-460 epoxy adhesive is accounted for in this analysis and the bonding voltage is assumed to be 1500 V.

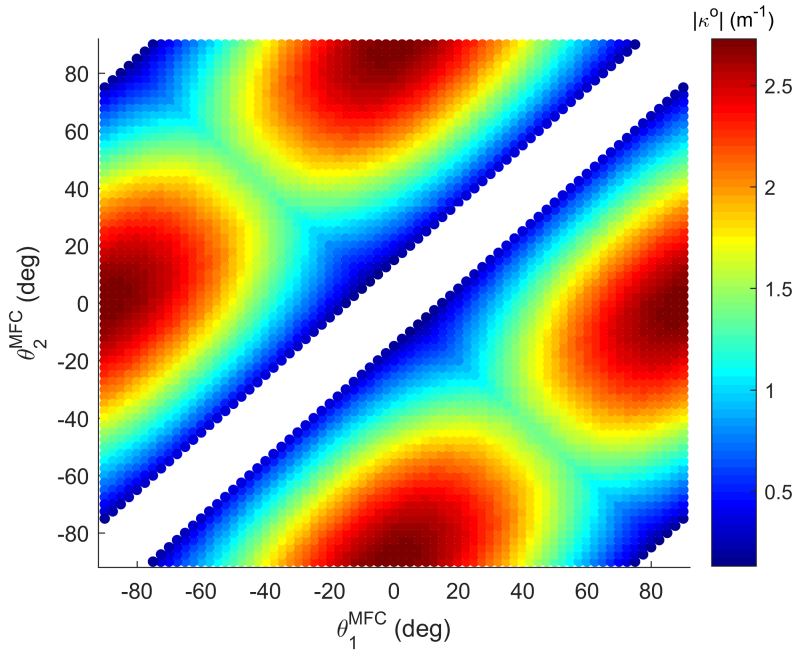

Figure A.2: Maximum major curvature magnitude of a 200 x 200 mm^2 $[\theta_1^{MFC}/\theta_2^{MFC}]_T$ bistable laminate between either stable state vs. θ_1^{MFC} and θ_2^{MFC}. Only layups yielding bistable configurations are plotted.

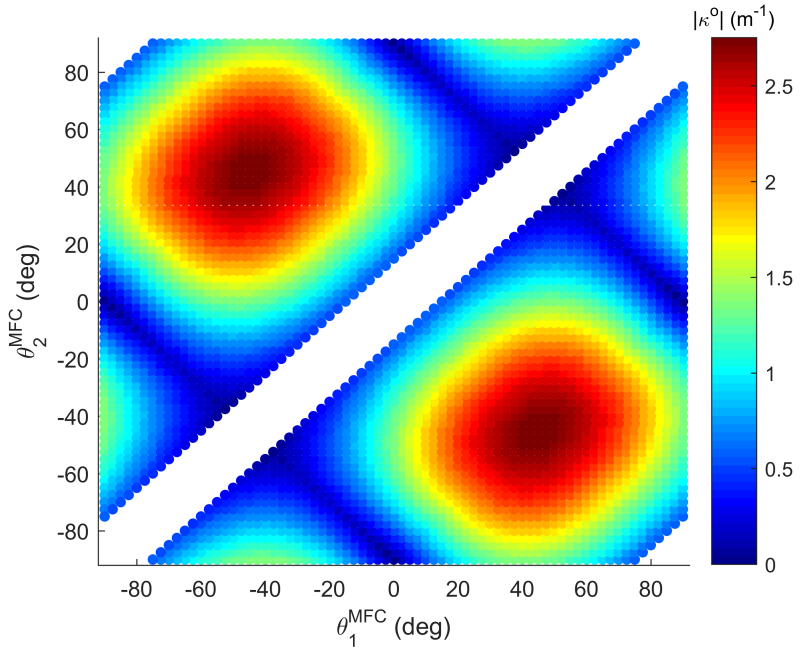

Figure A.3: Maximum twist curvature magnitude of a 200 x 200 mm^2 $[\theta_1^{MFC}/\theta_2^{MFC}]_T$ bistable laminate between either stable state vs. θ_1^{MFC} and θ_2^{MFC}. Only layups yielding bistable configurations are plotted.

Both Figures A.2 and A.3 only plot bistable points and the diagonal and corner gaps are the result of the corresponding layups yielding monostable configurations. The $[\theta_1^{MFC}/\theta_2^{MFC}]_T$ laminate loses bistability when the two ply angles are either identical or close together. Figure A.2 reveals that the major curvature κ_x^o or κ_y^o is at a maximum when θ_1^{MFC} and θ_2^{MFC} are any combination of 0° and ±90° while these layups correspond to zero twist curvature κ_{xy}^o. In contrast, Figure A.3 shows that maximum twist curvature occurs when the layup is either $[-45^{MFC}/45^{MFC}]_T$ or $[45^{MFC}/-45^{MFC}]_T$ while their corresponding major curvatures are zero. Both figures show that a cross-ply layup is the most favorable for yielding large deflections where the two ply angles have the most separation. As the difference between these angles lessen, the magnitude of all curvatures decrease.

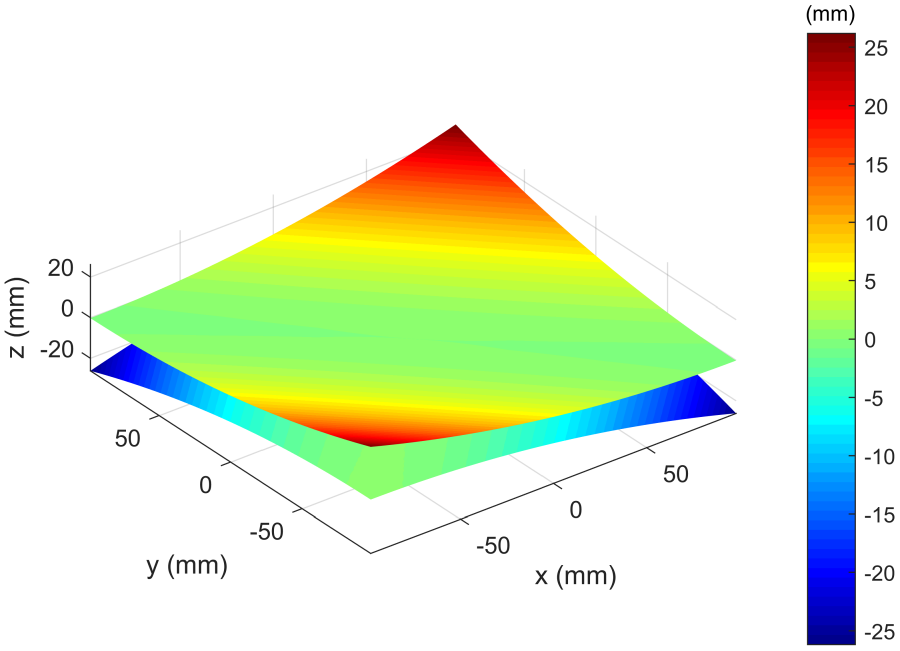

Figure A.4: Out-of-plane displacements of a 200 x 200 mm^2 $[-45^{MFC}/45^{MFC}]_T$ bistable laminate in its two stable states.

Figure A.4 shows the stable shapes of a 200 x 200 mm^2 $[-45^{MFC}/45^{MFC}]_T$ bistable laminate to examine how twist curvature influences the resulting deformations. Compared to the $[0^{MFC}/90^{MFC}]_T$ laminate in Figure 3.3, the presence of twist curvature causes the out-of-plane displacements to increase at two corners and decrease at the other two corners. This effect is taken to the extreme with the $[-45^{MFC}/45^{MFC}]_T$ layup, where the maximum corner displacements increase by a factor of two while the other two corners retain zero deflection. While its maximum displacement may be larger, its shapes are less useful than those of the $[0^{MFC}/90^{MFC}]_T$ laminate as a morphing structure where symmetric cylindrical geometries are preferred. Aircraft structures such as trailing edges of an airfoil require a consistent amount of deflection across its entire edge, which cannot be achieved with twist curvature alone.

A.3 Absolute Errors of Curvatures

To better visualize the curvature differences, this appendix section presents the curvature absolute error $\kappa^o_{model} - \kappa^o_{experiment}$ between the model predictions and experimentally measured profiles given in Figures 3.12 and 3.11. Specifically, Figures A.5-A.7 show the κ^o_x, κ^o_y, and κ^o_{xy} errors of the lower order, higher order, and finite element models, respectively, for both stable states. The errors in all three models increase towards the laminate edges and corners. The higher order model in Figure A.6 retain the greatest accuracy for the major and minor curvatures κ^o_x and κ^o_y while the FEA in Figure A.7 is able to capture the twist curvature κ^o_{xy} profiles with the least amount of error.

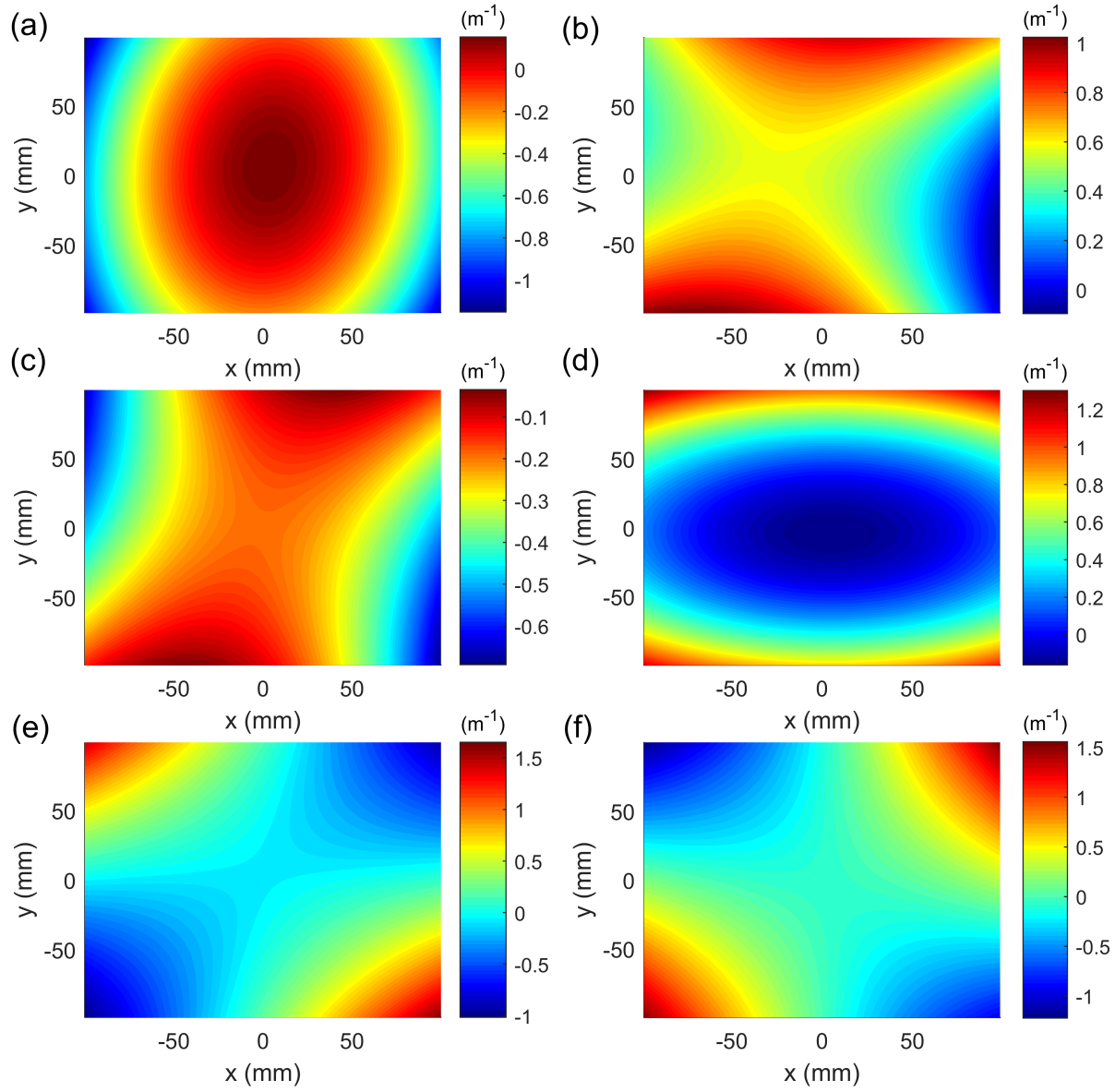

Figure A.5: 200 x 200 mm^2 $[0^{MFC}/90^{MFC}]_T$ lower order model absolute errors against experimental measurements for κ_x^o in (a) state I, (b) state II, for κ_y^o in (c) state I, (d) state II, and for κ_{xy}^o in (e) state I and (f) state II.

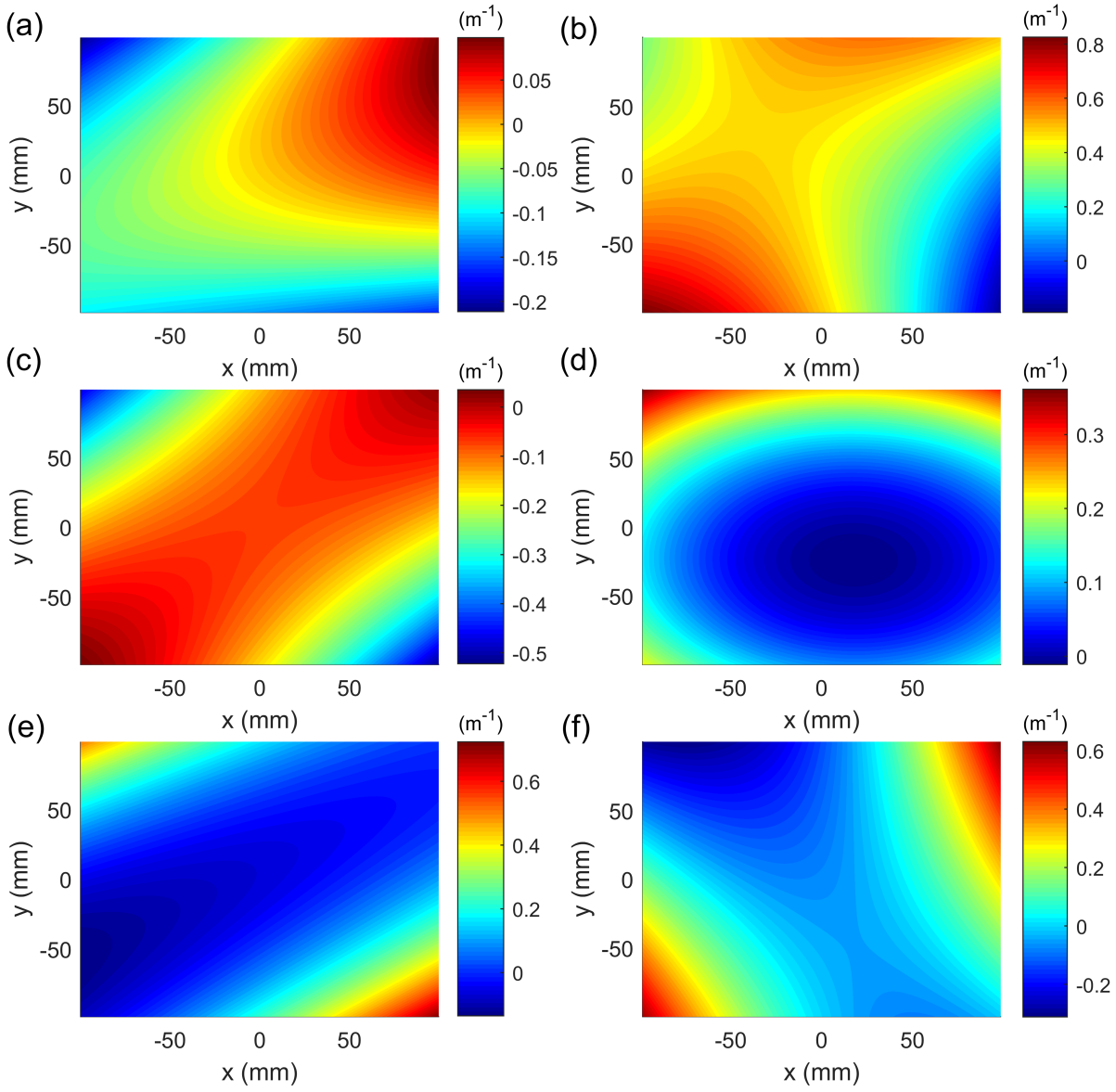

Figure A.6: 200 x 200 mm^2 $[0^{MFC}/90^{MFC}]_T$ higher order model absolute errors against experimental measurements for κ_x^o in (a) state I, (b) state II, for κ_y^o in (c) state I, (d) state II, and for κ_{xy}^o in (e) state I and (f) state II.

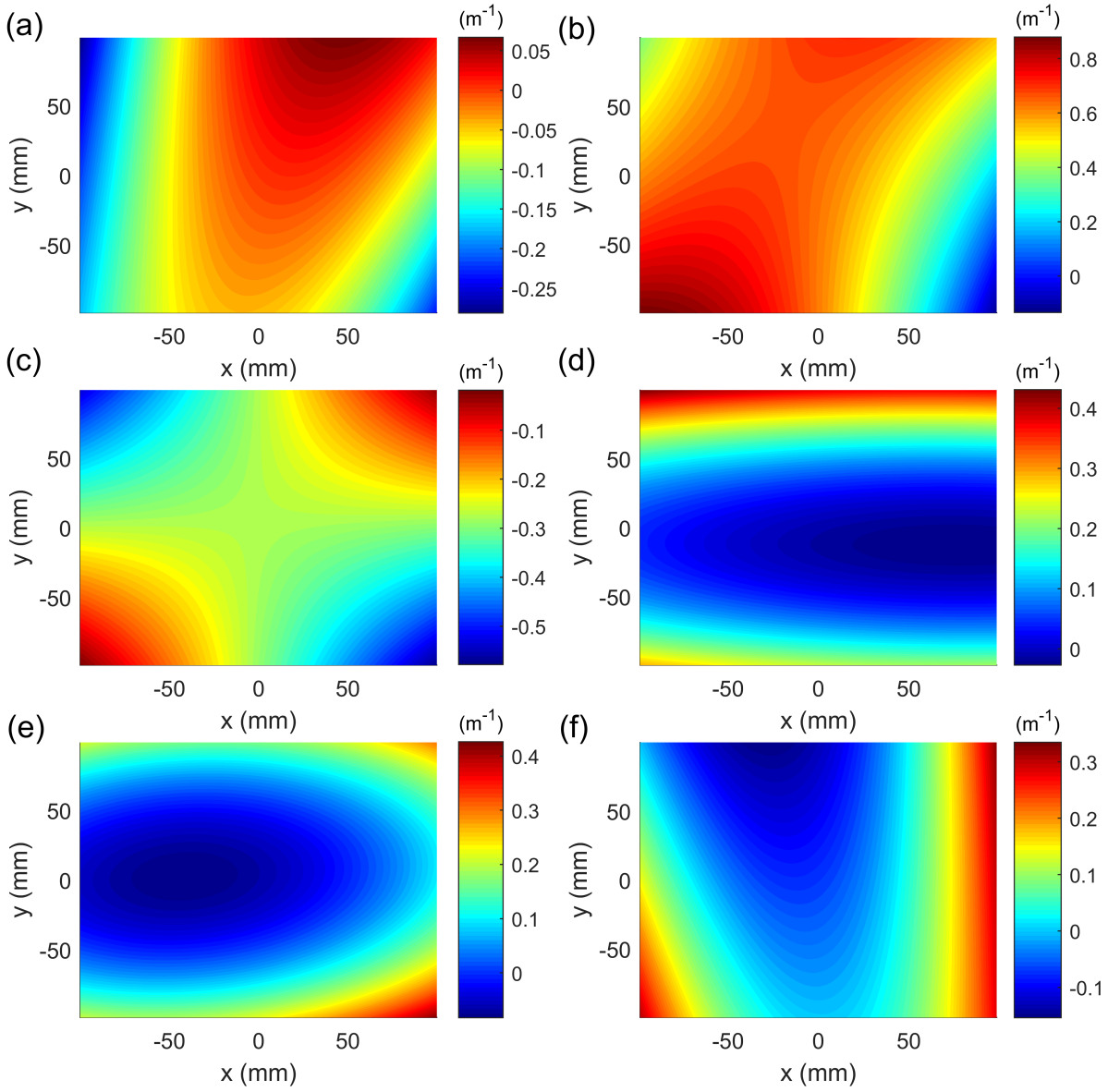

Figure A.7: 200 x 200 mm^2 $[0^{MFC}/90^{MFC}]_T$ finite element analysis absolute errors against experimental measurements for κ_x^o in (a) state I, (b) state II, for κ_y^o in (c) state I, (d) state II, and for κ_{xy}^o in (e) state I and (f) state II.

APPENDIX B

Additional Frequency Sweep Results

This appendix presents the electromechanical response of the $[0^{MFC}/90^{MFC}]_T$ bistable laminate during forward and backward frequency sweeps which were not covered in Chapter 4. Specifically, the responses are peak to peak MFC voltage and corner velocity amplitudes obtained with stroboscopic sampling of the time histories at each excitation step from both initial states. The results under the forcing level of 0.5 g, 1.5 g, 2.5 g, 3.5 g, and 4 g are given in Figures B.1, B.2, B.3, B.4, and B.5, respectively. In each figure, the first and third rows are the model results obtained from simulations of the state space form for the electromechanically coupled equations of motion in Equations 4.19a-4.19c. The second and fourth rows are the corresponding experimental results. The exact dynamic regime per frequency step in these figures are listed in Figure 4.12.

Overall, the theoretical and experimental findings presented in Section 4.3.2 still apply here. As observed in the frequency sweep results under 1 g, 2 g, and 3 g in Figures 4.4-4.6, nonlinear behaviors that strengthen with rising forcing input are seen in Figures B.1-B.5 for both the simulations and experiments. These include softening of the primary resonant peak, sweep direction dependent hysteresis, cross-well orbital asymmetries between MFC voltages, and initial state dependent asymmetries in response amplitudes and cross-well bandwidths.

Some notable differences between the model and experiments primarily arise out of potential

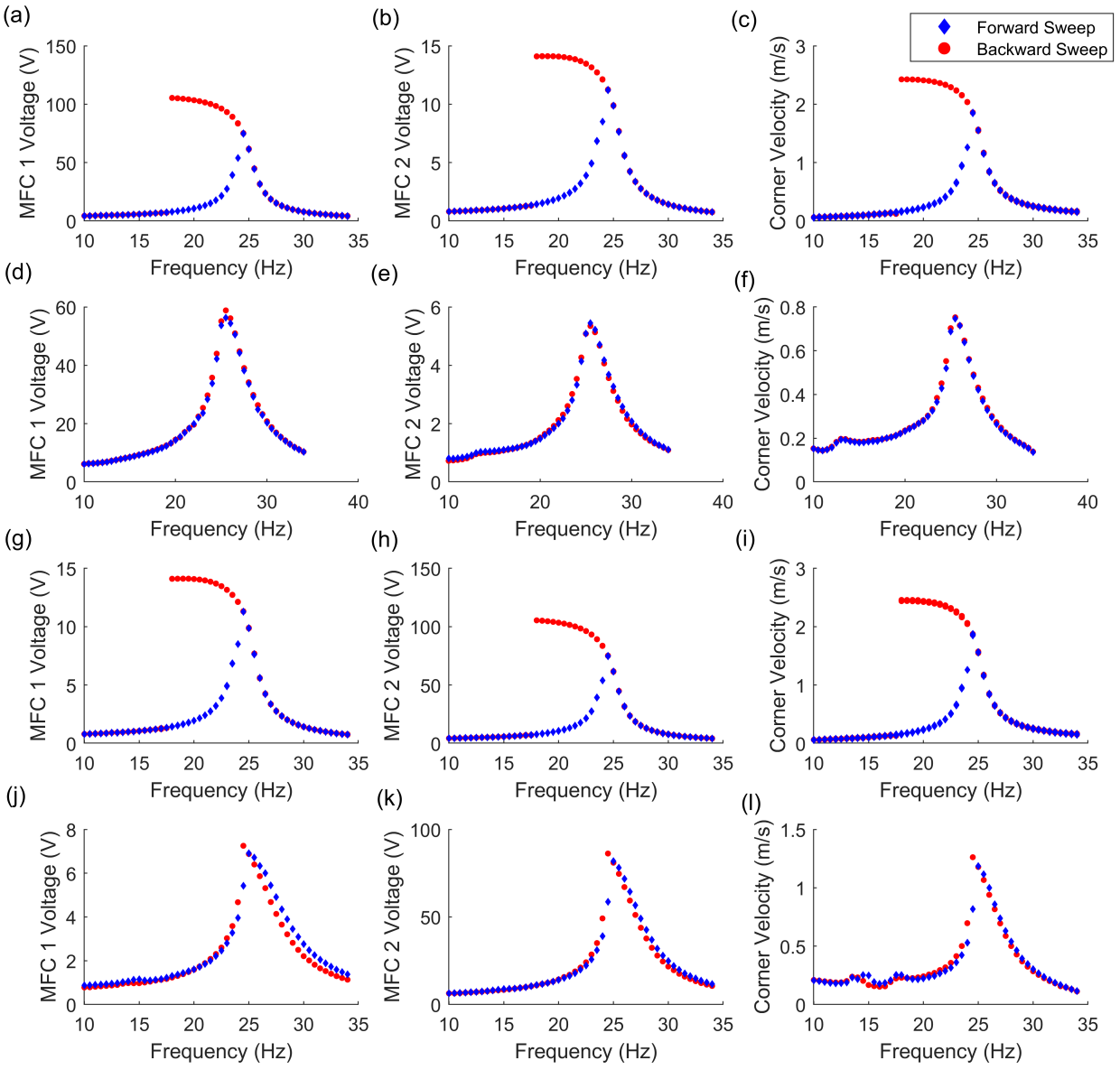

Figure B.1: Peak to peak amplitudes from forward and backward frequency sweeps at 0.5 g. From initial state I, model predictions of (a) MFC 1 open circuit voltage, (b) MFC 2 open circuit voltage, (c) corner velocity, and experimental results for (d) MFC 1 open circuit voltage, (e) MFC 2 open circuit voltage, (f) corner velocity. From initial state II, model predictions of (g) MFC 1 open circuit voltage, (h) MFC 2 open circuit voltage, (i) corner velocity, and experimental results for (j) MFC 1 open circuit voltage, (k) MFC 2 open circuit voltage, (l) corner velocity.

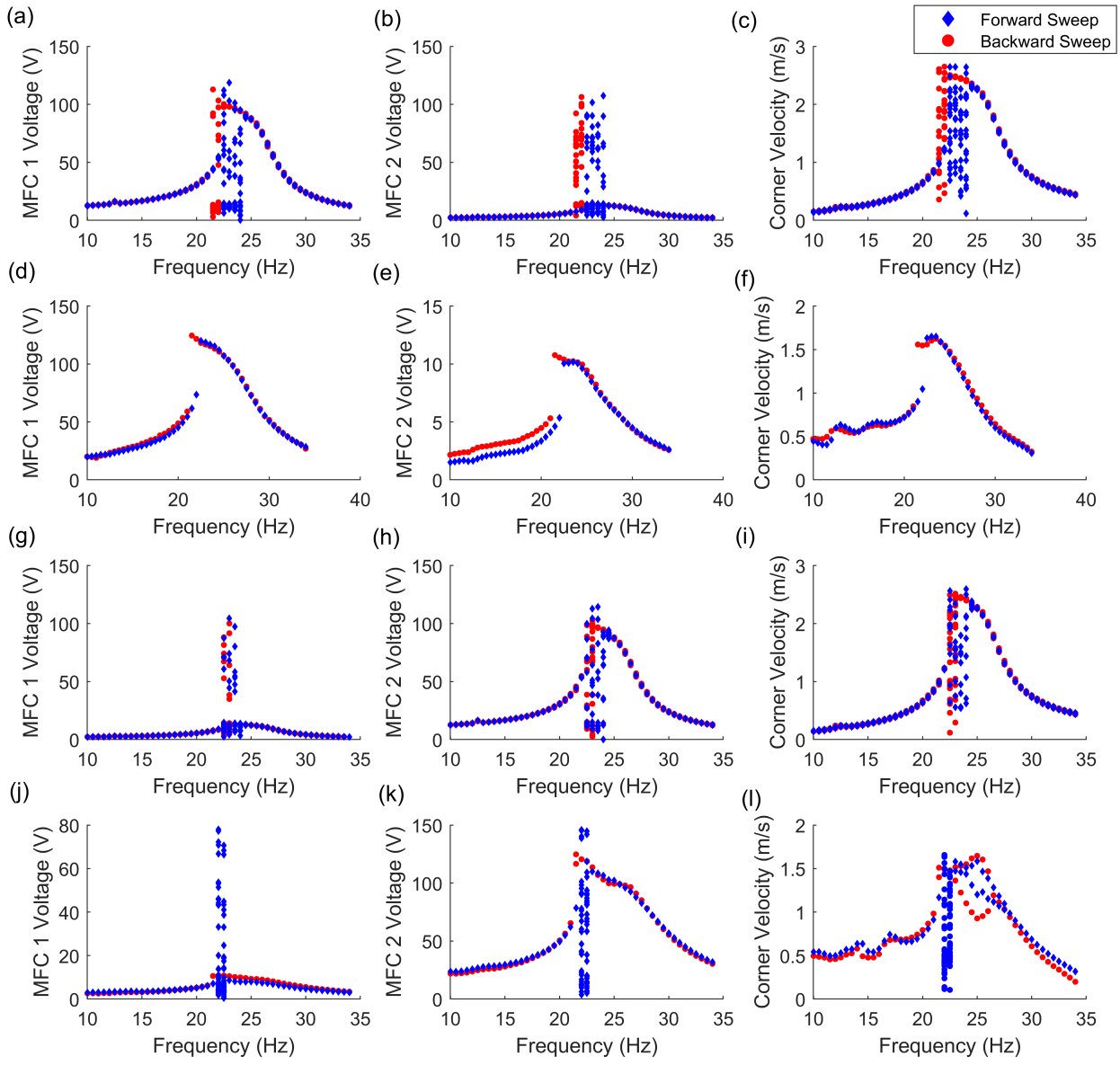

Figure B.2: Peak to peak amplitudes from forward and backward frequency sweeps at 1.5 g. From initial state I, model predictions of (a) MFC 1 open circuit voltage, (b) MFC 2 open circuit voltage, (c) corner velocity, and experimental results for (d) MFC 1 open circuit voltage, (e) MFC 2 open circuit voltage, (f) corner velocity. From initial state II, model predictions of (g) MFC 1 open circuit voltage, (h) MFC 2 open circuit voltage, (i) corner velocity, and experimental results for (j) MFC 1 open circuit voltage, (k) MFC 2 open circuit voltage, (l) corner velocity.

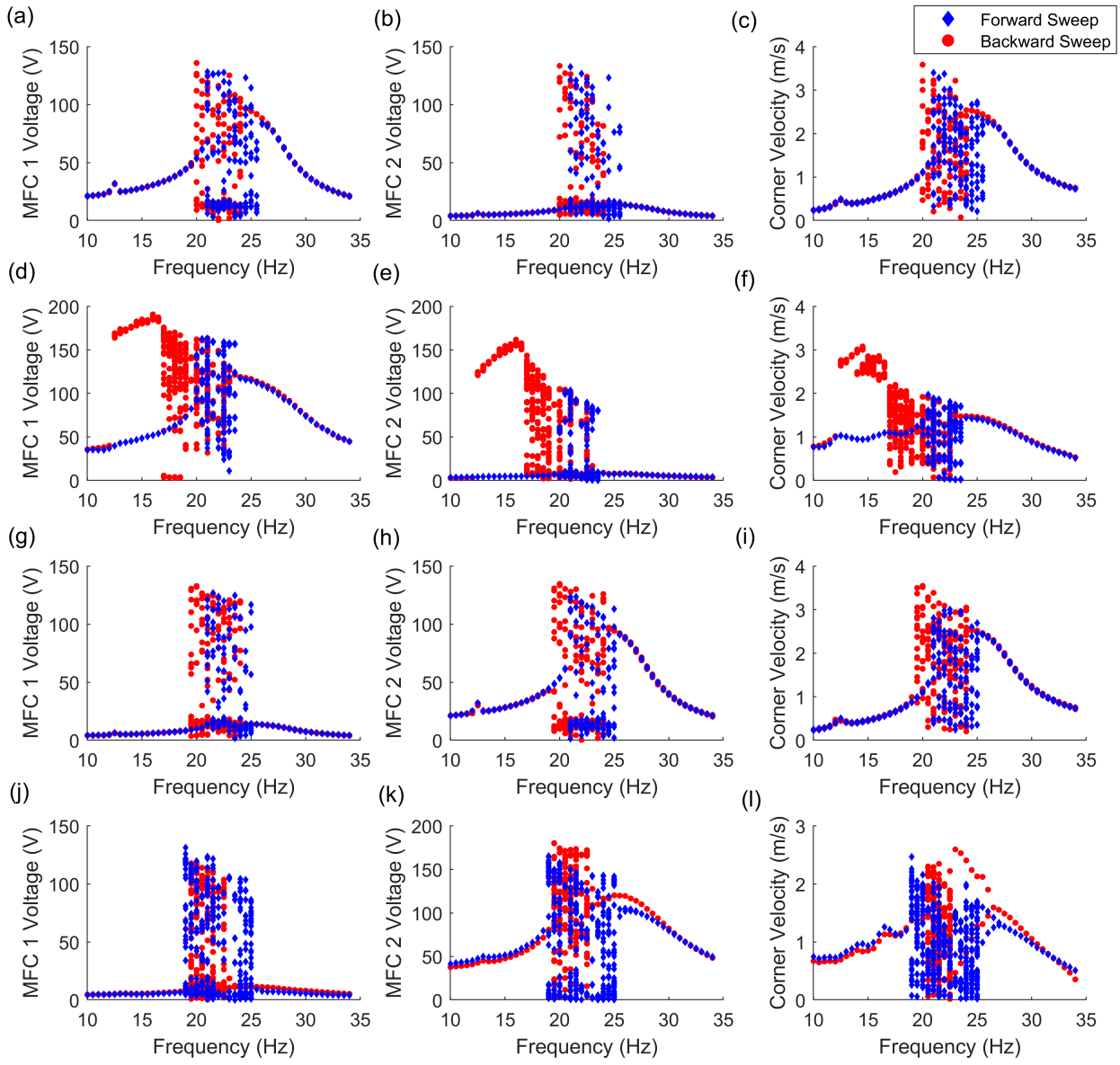

Figure B.3: Peak to peak amplitudes from forward and backward frequency sweeps at 2.5 g. From initial state I, model predictions of (a) MFC 1 open circuit voltage, (b) MFC 2 open circuit voltage, (c) corner velocity, and experimental results for (d) MFC 1 open circuit voltage, (e) MFC 2 open circuit voltage, (f) corner velocity. From initial state II, model predictions of (g) MFC 1 open circuit voltage, (h) MFC 2 open circuit voltage, (i) corner velocity, and experimental results for (j) MFC 1 open circuit voltage, (k) MFC 2 open circuit voltage, (l) corner velocity.

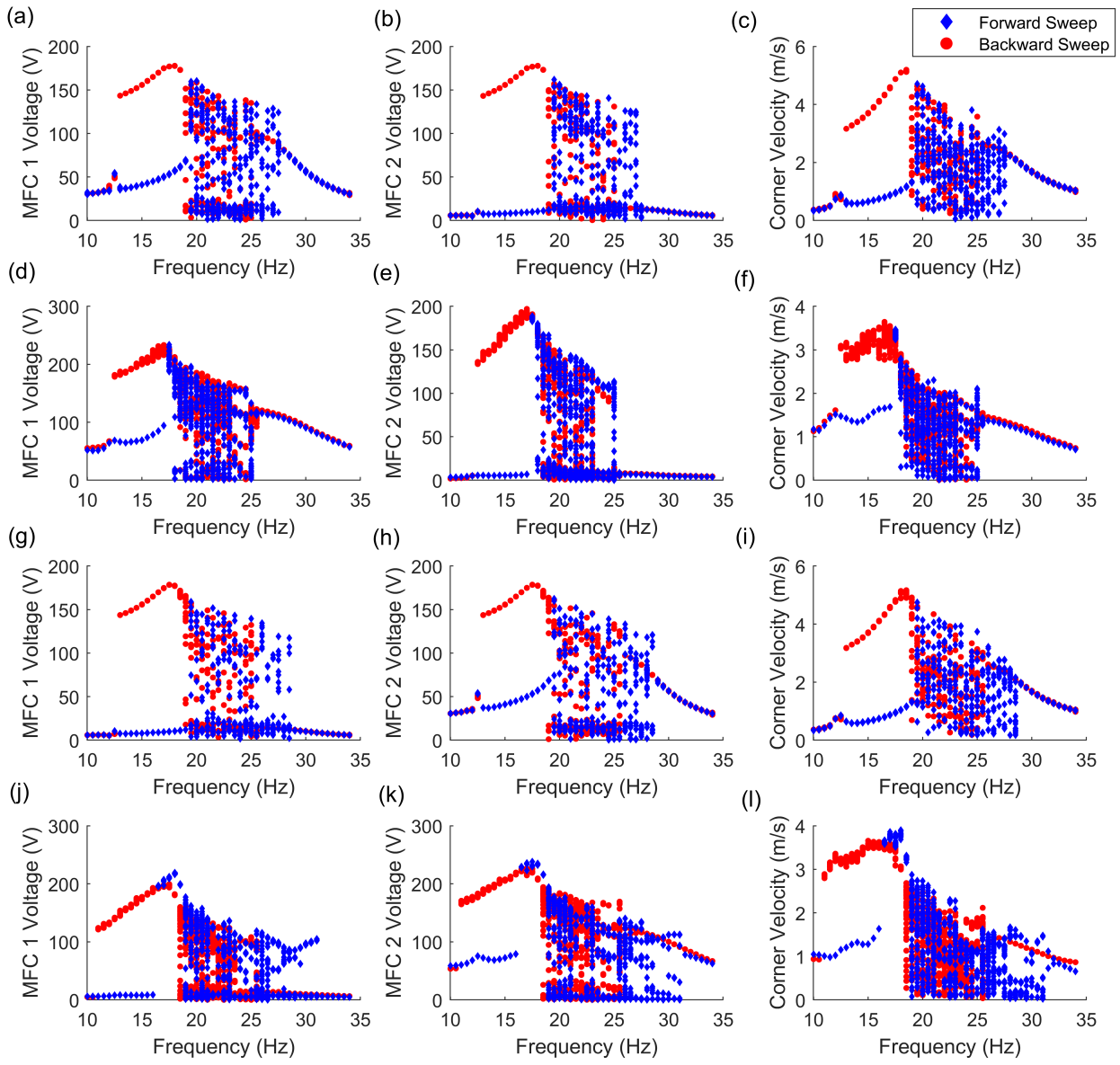

Figure B.4: Peak to peak amplitudes from forward and backward frequency sweeps at 3.5 g. From initial state I, model predictions of (a) MFC 1 open circuit voltage, (b) MFC 2 open circuit voltage, (c) corner velocity, and experimental results for (d) MFC 1 open circuit voltage, (e) MFC 2 open circuit voltage, (f) corner velocity. From initial state II, model predictions of (g) MFC 1 open circuit voltage, (h) MFC 2 open circuit voltage, (i) corner velocity, and experimental results for (j) MFC 1 open circuit voltage, (k) MFC 2 open circuit voltage, (l) corner velocity.

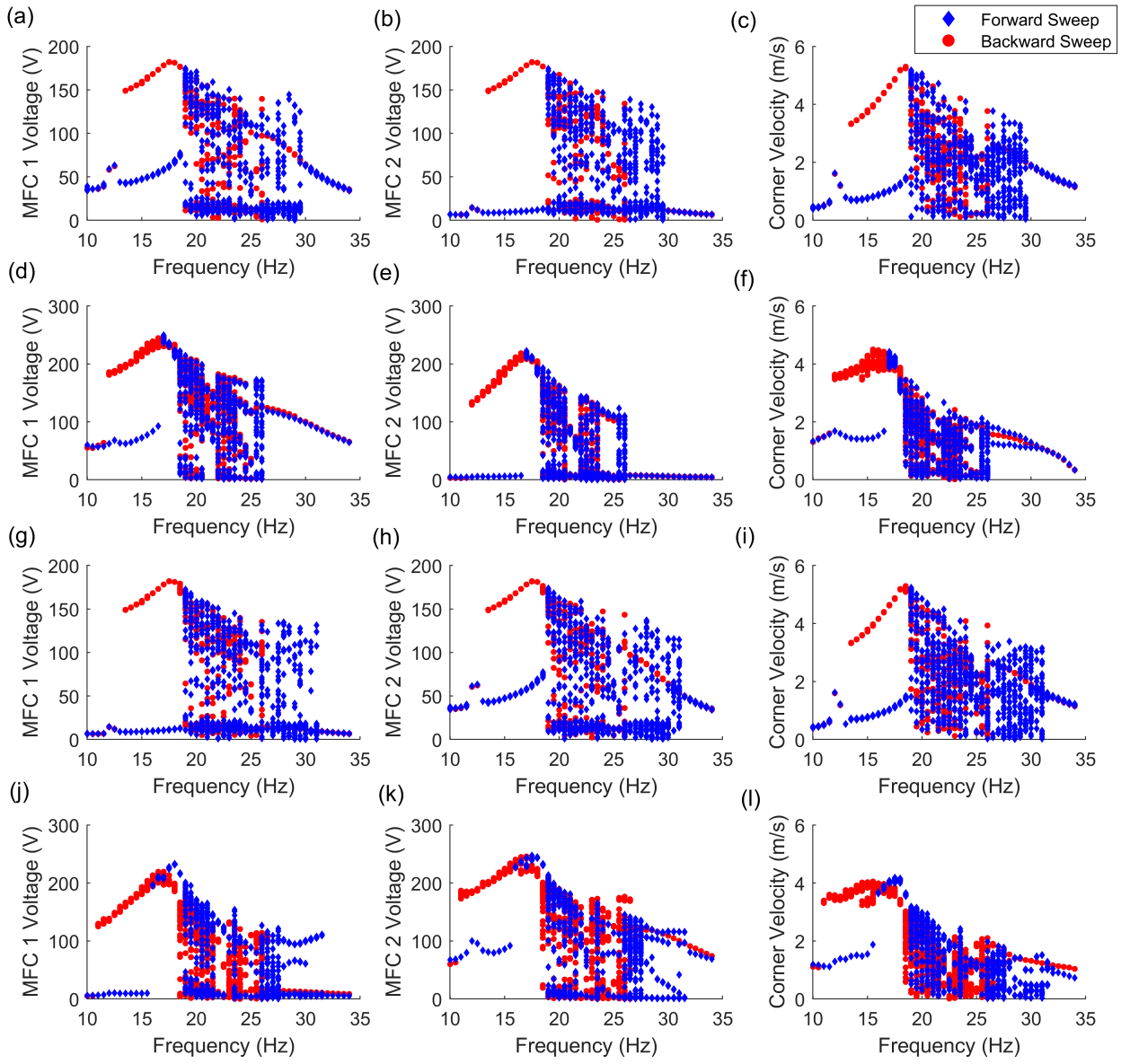

Figure B.5: Peak to peak amplitudes from forward and backward frequency sweeps at 4 g. From initial state I, model predictions of (a) MFC 1 open circuit voltage, (b) MFC 2 open circuit voltage, (c) corner velocity, and experimental results for (d) MFC 1 open circuit voltage, (e) MFC 2 open circuit voltage, (f) corner velocity. From initial state II, model predictions of (g) MFC 1 open circuit voltage, (h) MFC 2 open circuit voltage, (i) corner velocity, and experimental results for (j) MFC 1 open circuit voltage, (k) MFC 2 open circuit voltage, (l) corner velocity.

well asymmetries which cause different cross-well responses between initial states. In Figure B.2, the experimental sweeps from initial state I in (d)-(f) only exhibit single-well oscillations while the corresponding sweeps from initial state II in (j)-(l) show cross-well oscillations at the softened mode. In contrast, the model assumes perfect symmetry between the laminate's two potential wells and therefore exhibits much more similar response between initial states. Another example of this is in Figure B.3, where the experimental backward sweep from initial state I in (d)-(f) is where limit cycle oscillations are first seen while the corresponding sweep from initial state II in (j)-(l) does not show this cross-well regime. The simulations also do not exhibit limit cycle oscillations until the forcing level increases to 3 g. At 0.5 g in Figure B.1, all responses remain under single-well oscillations and the simulations show a larger hysteretic region where the location of the amplitude jumps between forward and backward frequency sweeps are much more separated than the experimental results. For 3.5 g and 4 g in Figures B.4 and B.5, both the model and experiment exhibit all dynamic regimes characterized in Section 4.4.

BIBLIOGRAPHY

[1] Hu, N. and Burgueño, R., "Buckling-induced smart applications: recent advances and trends," *Smart Materials and Structures*, Vol. 24, No. 6, 2015, pp. 063001.

[2] Emam, S. A. and Inman, D. J., "A review on bistable composite laminates for morphing and energy harvesting," *Applied Mechanics Reviews*, Vol. 67, No. 6, 2015, pp. 060803.

[3] Pellegrini, S. P., Tolou, N., Schenk, M., and Herder, J. L., "Bistable vibration energy harvesters: A review," *Journal of Intelligent Material Systems and Structures*, Vol. 24, No. 11, 2012, pp. 1303–1312.

[4] Harne, R. L. and Wang, K. W., "A review of the recent research on vibration energy harvesting via bistable systems," *Smart Materials and Structures*, Vol. 22, No. 2, 2013, pp. 023001.

[5] Johnson, D. R., Thota, M., Semperlotti, F., and Wang, K. W., "On achieving high and adaptable damping via a bistable oscillator," *Smart Materials and Structures*, Vol. 22, No. 11, 2013, pp. 115027.

[6] Johnson, D. R., Harne, R. L., and Wang, K. W., "A Disturbance Cancellation Perspective on Vibration Control Using a Bistable Snap-Through Attachment," *Journal of Vibration and Acoustics*, Vol. 136, No. 3, 2014, pp. 031006.

[7] Hyer, M. W., "Some Observations on the Cured Shape of Thin Unsymmetric Laminates," *Journal of Composite Materials*, Vol. 15, No. 2, 1981, pp. 175–194.

[8] Hyer, M. W., "Calculations of the Room-Temperature Shapes of Unsymmetric Laminates," *Journal of Composite Materials*, Vol. 15, No. 6, 1981, pp. 492–501.

[9] Gibson, R. F., *Principles of Composite Material Mechanics*, CRC press, 2011.

[10] Akira, H. and Hyer, M. W., "Non-linear temperature-curvature relationships for unsymmetric graphite-epoxy laminates," *International Journal of Solids and Structures*, Vol. 23, No. 7, 1987, pp. 919–935.

[11] Hyer, M. W., "The room-temperature shapes of four-layer unsymmetric cross-ply laminates," *Journal of Composite Materials*, Vol. 16, No. 4, 1982, pp. 318–340.

[12] Jun, W. and Hong, C. S., "Effect of residual shear strain on the cured shape of unsymmetric cross-ply thin laminates," *Composites Science and Technology*, Vol. 38, No. 1, 1990, pp. 55–67.

[13] Dang, J. and Tang, Y., "Calculation of the room-temperature shapes of unsymmetric laminates," *Proceedings of the International Symposium on Composite Materials and Structures*, The Chinese Society of Theoretical and Applied Mechanics, American , 1986, pp. 201–206.

[14] Jun, W. and Hong, C. S., "Cured shape of unsymmetric laminates with arbitrary lay-up angles," *Journal of Reinforced Plastics and Composites*, Vol. 11, No. 12, 1992, pp. 1352–1366.

[15] Peeters, L., Powell, P., and Warnet, L., "Thermally-induced shapes of unsymmetric laminates," *Journal of Composite Materials*, Vol. 30, No. 5, 1996, pp. 603–626.

[16] Dano, M. L. and Hyer, M. W., "Thermally-induced deformation behavior of unsymmetric laminates," *International Journal of Solids and Structures*, Vol. 35, No. 17, 1998, pp. 2101–2120.

[17] Daynes, S., Potter, K., and Weaver, P., "Bistable prestressed buckled laminates," *Composites Science and Technology*, Vol. 68, No. 15-16, 2008, pp. 3431–3437.

[18] Daynes, S., Diaconu, C. G., Potter, K. D., and Weaver, P. M., "Bistable Prestressed Symmetric Laminates," *Journal of Composite Materials*, Vol. 44, No. 9, 2010, pp. 1119–1137.

[19] Chillara, V. and Dapino, M., "Mechanically-prestressed bistable composite laminates with weakly coupled equilibrium shapes," *Composites Part B: Engineering*, Vol. 111, 2017, pp. 251–260.

[20] Daynes, S. and Weaver, P., "Analysis of unsymmetric CFRP–metal hybrid laminates for use in adaptive structures," *Composites Part A: Applied Science and Manufacturing*, Vol. 41, No. 11, 2010, pp. 1712–1718.

[21] Li, H., Dai, F., Weaver, P., and Du, S., "Bistable hybrid symmetric laminates," *Composite Structures*, Vol. 116, 2014, pp. 782–792.

[22] Guest, S. and Pellegrino, S., "Analytical models for bistable cylindrical shells," *Proceedings of the Royal Society A: Mathematical, Physical and Engineering Sciences*, Vol. 462, No. 2067, 2006, pp. 839–854.

[23] Coburn, B. H., Pirrera, A., Weaver, P. M., and Vidoli, S., "Tristability of an orthotropic doubly curved shell," *Composite Structures*, Vol. 96, 2013, pp. 446–454.

[24] Eckstein, E., Pirrera, A., and Weaver, P. M., "Multi-mode morphing using initially curved composite plates," *Composite Structures*, Vol. 109, No. 1, 2014, pp. 240–245.

[25] Brinkmeyer, A., Santer, M., Pirrera, A., and Weaver, P. M., "Pseudo-bistable self-actuated domes for morphing applications," *International Journal of Solids and Structures*, Vol. 49, No. 9, 2012, pp. 1077–1087.

[26] Wang, B. and Fancey, K. S., "A bistable morphing composite using viscoelastically generated prestress," *Materials Letters*, Vol. 158, 2015, pp. 108–110.

[27] Kebadze, E., Guest, S. D., and Pellegrino, S., "Bistable prestressed shell structures," *International Journal of Solids and Structures*, Vol. 41, No. 11-12, 2004, pp. 2801–2820.

[28] Dai, F., Li, H., and Du, S., "Design and analysis of a tri-stable structure based on bi-stable laminates," *Composites Part A: Applied Science and Manufacturing*, Vol. 43, No. 9, 2012, pp. 1497–1504.

[29] Dai, F., Li, H., and Du, S., "A multi-stable lattice structure and its snap-through behavior among multiple states," *Composite Structures*, Vol. 97, 2013, pp. 56–63.

[30] Mattioni, F., Weaver, P., Potter, K., and Friswell, M., "Analysis of thermally induced multistable composites," *International Journal of Solids and Structures*, Vol. 45, No. 2, 2008, pp. 657–675.

[31] Mattioni, F., Weaver, P., and Friswell, M., "Multistable composite plates with piecewise variation of lay-up in the planform," *International Journal of Solids and Structures*, Vol. 46, No. 1, 2009, pp. 151–164.

[32] Arrieta, A. F., Kuder, I. K., Waeber, T., and Ermanni, P., "Variable stiffness characteristics of embeddable multi-stable composites," *Composites Science and Technology*, Vol. 97, 2014, pp. 12–18.

[33] Kuder, I. K., Arrieta, A. F., and Ermanni, P., "Design space of embeddable variable stiffness bi-stable elements for morphing applications," *Composite Structures*, Vol. 122, 2015, pp. 445–455.

[34] Cui, Y. and Santer, M., "Highly multistable composite surfaces," *Composite Structures*, Vol. 124, 2015, pp. 44–54.

[35] Cui, Y. and Santer, M., "Characterisation of tessellated bistable composite laminates," *Composite Structures*, Vol. 137, 2016, pp. 93–104.

[36] Dano, M. L. and Hyer, M. W., "Snap-through of unsymmetric fiber-reinforced composite laminates," *International Journal of Solids and Structures*, Vol. 39, No. 1, 2001, pp. 175–198.

[37] Lachenal, X., Weaver, P. M., and Daynes, S., "Multi-stable composite twisting structure for morphing applications," *Proceedings of the Royal Society A: Mathematical, Physical and Engineering Sciences*, Vol. 468, No. 2141, 2012, pp. 1230–1251.

[38] Mattioni, F., Weaver, P. M., Potter, K. D., and Friswell, M. I., "The application of thermally induced multistable composites to morphing aircraft structures," *Industrial and Commercial Applications of Smart Structures Technologies 2008*, Vol. 6930, International Society for Optics and Photonics, 2008, p. 693012.

[39] Daynes, S., Weaver, P., and Potter, K., "Aeroelastic study of bistable composite airfoils," *Journal of Aircraft*, Vol. 46, No. 6, 2009, pp. 2169–2174.

[40] Daynes, S., Nall, S., Weaver, P., Potter, K., Margaris, P., and Mellor, P., "Bistable composite flap for an airfoil," *Journal of Aircraft*, Vol. 47, No. 1, 2010, pp. 334–338.

[41] Diaconu, C. G., Weaver, P. M., and Mattioni, F., "Concepts for morphing airfoil sections using bi-stable laminated composite structures," *Thin-Walled Structures*, Vol. 46, No. 6, 2008, pp. 689–701.

[42] Daynes, S., Weaver, P., and Trevarthen, J., "A morphing composite air inlet with multiple stable shapes," *Journal of Intelligent Material Systems and Structures*, Vol. 22, No. 9, 2011, pp. 961–973.

[43] Kuder, I. K., Fasel, U., Ermanni, P., and Arrieta, A. F., "Concurrent design of a morphing aerofoil with variable stiffness bi-stable laminates," *Smart materials and structures*, Vol. 25, No. 11, 2016, pp. 115001.

[44] Kuder, I. K., Arrieta, A. F., Rist, M., and Ermanni, P., "Aeroelastic response of a selectively compliant morphing aerofoil featuring integrated variable stiffness bi-stable laminates," *Journal of Intelligent Material Systems and Structures*, Vol. 27, No. 14, 2016, pp. 1949–1966.

[45] Dano, M. L. and Hyer, M. W., "The response of unsymmetric laminates to simple applied forces," *Mechanics of Composite Materials and Structures*, Vol. 3, No. 1, 1996, pp. 65–80.

[46] Schlecht, M. and Schulte, K., "Advanced calculation of the room-temperature shapes of unsymmetric laminates," *Journal of Composite Materials*, Vol. 33, No. 16, 1999, pp. 1472–1490.

[47] Chopra, I., "Review of state of art of smart structures and integrated systems," *AIAA Journal*, Vol. 40, No. 11, 2002, pp. 2145–2187.

[48] Aimmanee, S. and Hyer, M. W., "Analysis of the manufactured shape of rectangular THUNDER-type actuators," *Smart Materials and Structures*, Vol. 13, No. 6, 2004, pp. 1389.

[49] Hyer, M. W. and Jilani, A. B., "Deformation characteristics of circular RAINBOW actuators," *Smart Materials and Structures*, Vol. 11, No. 2, 2002, pp. 175.

[50] Bent, A. A. and Hagood, N. W., "Piezoelectric fiber composites with interdigitated electrodes," *Journal of intelligent material systems and structures*, Vol. 8, No. 11, 1997, pp. 903–919.

[51] Williams, R. B., Inman, D. J., Schultz, M. R., Hyer, M. W., and Wilkie, W. K., "Nonlinear tensile and shear behavior of macro fiber composite actuators," *Journal of Composite Materials*, Vol. 38, No. 10, 2004, pp. 855–869.

[52] "Macro Fiber Composite - MFC," https://www.smart-material.com/media/Datasheets/MFC_V2.3-Web-full-brochure.pdf.

[53] Giddings, P., Bowen, C., Butler, R., and Kim, H., "Characterisation of actuation properties of piezoelectric bi-stable carbon-fibre laminates," *Composites Part A: Applied Science and Manufacturing*, Vol. 39, No. 4, 2008, pp. 697–703.

[54] Bowen, C. R., Butler, R., Jervis, R., Kim, H. A., and Salo, A. I. T., "Morphing and shape control using unsymmetrical composites," *Journal of Intelligent Material Systems and Structures*, Vol. 18, No. 1, 2007, pp. 89–98.

[55] Portela, P., Camanho, P., Weaver, P., and Bond, I., "Analysis of morphing, multi stable structures actuated by piezoelectric patches," *Computers and Structures*, Vol. 86, No. 3-5, 2008, pp. 347–356.

[56] Schultz, M. R. and Hyer, M. W., "Snap-Through of Unsymmetric Cross-Ply Laminates Using Piezoceramic Actuators," *Journal of Intelligent Materials Systems and Structures*, Vol. 14, No. 12, 2003, pp. 795–814.

[57] Ren, L., "A theoretical study on shape control of arbitrary lay-up laminates using piezoelectric actuators," *Composite Structures*, Vol. 83, No. 1, 2008, pp. 110–118.

[58] Gude, M., Hufenbach, W., and Kirvel, C., "Piezoelectrically driven morphing structures based on bistable unsymmetric laminates," *Composite Structures*, Vol. 93, No. 2, 2011, pp. 377–382.

[59] Bowen, C. R. and Kim, H. A., "Mechanics and Design of Smart Composites: Modeling and Characterization of Piezoelectrically Actuated Bistable Composites," *IEEE Transactions on Ultrasonics, Ferroelectrics and Frequency Control*, Vol. 58, No. 9, 2011, pp. 131–168.

[60] Giddings, P. F., Kim, H. A., Salo, A. I., and Bowen, C. R., "Modelling of piezoelectrically actuated bistable composites," *Materials Letters*, Vol. 65, No. 9, 2011, pp. 1261–1263.

[61] Schultz, M. R., Wilkie, W. K., and Bryant, R. G., "Investigation of Self-Resetting Active Multistable Laminates," *Journal of Aircraft*, Vol. 44, No. 4, 2007, pp. 1069–1076.

[62] Kim, H. A., Betts, D. N., Salo, A. I. T., and Bowen, C. R., "Shape Memory Alloy-Piezoelectric Active Structures for Reversible Actuation of Bistable Composites," *AIAA Journal*, Vol. 48, No. 6, 2010, pp. 1265–1268.

[63] Huber, J., Fleck, N., and Ashby, M., "The selection of mechanical actuators based on performance indices," *Proceedings of the Royal Society of London. Series A: Mathematical, physical and engineering sciences*, Vol. 453, No. 1965, 1997, pp. 2185–2205.

[64] Bilgen, O., "Dynamic control of a bistable wing under aerodynamic loading," *Smart Materials and Structures*, Vol. 22, No. 2, 2013, pp. 025020.

[65] Arrieta, A. F., Bilgen, O., Friswell, M. I., and Hagedorn, P., "Dynamic control for morphing of bi-stable composites," *Journal of Intelligent Material Systems and Structures*, Vol. 24, No. 3, 2013, pp. 266–273.

[66] Simsek, M. R. and Bilgen, O., "Hybrid Position Feedback Controller for Inducing Cross-Well Motion of Bistable Structures," *AIAA Journal*, Vol. 54, No. 12, 2016, pp. 4011–4021.

[67] Tang, L., Yang, Y., and Soh, C. K., "Toward Broadband Vibration-based Energy Harvesting," *Journal of Intelligent Material Systems and Structures*, Vol. 21, No. 18, 2010, pp. 1867–1897.

[68] Erturk, A., Hoffmann, J., and Inman, D. J., "A piezomagnetoelastic structure for broadband vibration energy harvesting," *Applied Physics Letters*, Vol. 941, No. 10, 2009, pp. 254102–174103.

[69] Erturk, A. and Inman, D., "Broadband piezoelectric power generation on high-energy orbits of the bistable Duffing oscillator with electromechanical coupling," *Journal of Sound and Vibration*, Vol. 330, No. 10, 2011, pp. 2339–2353.

[70] Lin, J. T. and Alphenaar, B., "Enhancement of Energy Harvested from a Random Vibration Source by Magnetic Coupling of a Piezoelectric Cantilever," *Journal of Intelligent Material Systems and Structures*, Vol. 21, No. 13, 2010, pp. 1337–1341.

[71] Tang, L., Yang, Y., and Soh, C. K., "Improving functionality of vibration energy harvesters using magnets," *Journal of Intelligent Material Systems and Structures*, Vol. 23, No. 13, 2012, pp. 1433–1449.

[72] Masana, R. and Daqaq, M. F., "Relative performance of a vibratory energy harvester in mono- and bi-stable potentials," *Journal of Sound and Vibration*, Vol. 330, No. 24, 2011, pp. 6036–6052.

[73] Cottone, F., Gammaitoni, L., Vocca, H., Ferrari, M., and Ferrari, V., "Piezoelectric buckled beams for random vibration energy harvesting," *Smart Materials and Structures*, Vol. 21, No. 3, 2012, pp. 035021.

[74] Arrieta, A. F., Hagedorn, P., Erturk, A., and Inman, D. J., "A piezoelectric bistable plate for nonlinear broadband energy harvesting," *Applied Physics Letters*, Vol. 97, No. 10, 2010.

[75] Arrieta, A. F., Delpero, T., Bergamini, A. E., and Ermanni, P., "Broadband vibration energy harvesting based on cantilevered piezoelectric bi-stable composites," *Applied Physics Letters*, Vol. 102, No. 17, 2013, pp. 173904.

[76] Betts, D. N., Bowen, C. R., Kim, H. A., Gathercole, N., Clarke, C. T., and Inman, D. J., "Nonlinear dynamics of a bistable piezoelectric-composite energy harvester for broadband application," *The European Physical Journal Special Topics*, Vol. 222, No. 7, 2013, pp. 1553–1562.

[77] Li, H., Dai, F., and Du, S., "Broadband energy harvesting by exploiting nonlinear oscillations around the second vibration mode of a rectangular piezoelectric bistable laminate," *Smart Materials and Structures*, Vol. 24, No. 4, 2015, pp. 045024.

[78] Harris, P., Skinner, W., Bowen, C. R., and Kim, H. A., "Manufacture and Characterisation of Piezoelectric Broadband Energy Harvesters Based on Asymmetric Bistable Cantilever Laminates," *Ferroelectrics*, Vol. 480, 2015, pp. 67–76.

[79] Syta, A., Bowen, C. R., Kim, H. A., Rysak, A., and Litak, G., "Experimental analysis of the dynamical response of energy harvesting devices based on bistable laminated plates," *Meccanica*, Vol. 50, No. 8, 2015, pp. 1961–1970.

[80] Scarselli, G., Nicassio, F., Pinto, F., Ciampa, F., Iervolino, O., and Meo, M., "A novel bistable energy harvesting concept," *Smart Materials and Structures*, Vol. 25, No. 5, 2016, pp. 055001.

[81] Syta, A., Bowen, C. R., Kim, H. A., Rysak, A., and Litak, G., "Responses of bistable piezoelectric-composite energy harvester by means of recurrences," *Mechanical Systems and Signal Processing*, Vol. 76, 2016, pp. 823–832.

[82] Harris, P., Arafa, M., Litak, G., Bowen, C. R., and Iwaniec, J., "Output response identification in a multistable system for piezoelectric energy harvesting," *European Physical Journal B*, Vol. 90, 2017.

[83] Pan, D., Ma, B., and Dai, F., "Experimental investigation of broadband energy harvesting of a bi-stable composite piezoelectric plate," *Smart Materials and Structures*, Vol. 26, No. 3, 2017, pp. 035045.

[84] Pan, D., Li, Y., and Dai, F., "The influence of lay-up design on the performance of bi-stable piezoelectric energy harvester," *Composite Structures*, Vol. 161, 2017, pp. 227–236.

[85] Udani, J. P., Wrigley, C., and Arrieta, A. F., "Performance metric comparison study for non-magnetic bi-stable energy harvesters," *Active and Passive Smart Structures and Integrated Systems 2017*, Vol. 10164, International Society for Optics and Photonics, 2017, p. 101641B.

[86] Diaconu, C. G., Weaver, P. M., and Arrieta, A. F., "Dynamic analysis of bi-stable composite plates," *Journal of Sound and Vibration*, Vol. 322, No. 4, 2009, pp. 987–1004.

[87] Arrieta, A. F., Neild, S. A., and Wagg, D. J., "Nonlinear dynamic response and modeling of a bi-stable composite plate for applications to adaptive structures," *Nonlinear Dynamics*, Vol. 58, No. 1-2, 2009, pp. 259–272.

[88] Arrieta, A. F., Spelsberg-Korspeter, G., Hagedorn, P., Neild, S. A., and Wagg, D. J., "Low order model for the dynamics of bi-stable composite plates," *Journal of Intelligent Material Systems and Structures*, Vol. 22, No. 17, 2011, pp. 2025–2043.

[89] Arrieta, A. F., Neild, S. A., and Wagg, D. J., "On the cross-well dynamics of a bi-stable composite plate," *Journal of Sound and Vibration*, Vol. 330, No. 14, 2011, pp. 3424–3441.

[90] Vogl, G. A. and Hyer, M. W., "Natural vibration of unsymmetric cross-ply laminates," *Journal of Sound and Vibration*, Vol. 330, No. 20, 2011, pp. 4764–4779.

[91] Firouzian-Nejad, A., Ziaei-Rad, S., and Moore, M., "Vibration analysis of bi-stable composite cross-ply laminates using refined shape functions," *Journal of Composite Materials*, 2016.

[92] Wu, Z., Li, H., and Friswell, M. I., "Advanced nonlinear dynamic modelling of bi-stable composite plates," *Composite Structures*, Vol. 201, No. March, 2018, pp. 582–596.

[93] Betts, D. N., Kim, H. A., Bowen, C. R., and Inman, D. J., "Optimal configurations of bistable piezo-composites for energy harvesting," *Applied Physics Letters*, Vol. 100, No. 95, 2012, pp. 114104–17.

[94] Arrieta, A. F., Bilgen, O., Friswell, M. I., and Ermanni, P., "Modelling and configuration control of wing-shaped bi-stable piezoelectric composites under aerodynamic loads," *Aerospace Science and Technology*, Vol. 29, No. 1, 2013, pp. 453–461.

[95] Arrieta, A. F., Delpero, T., and Ermanni, P., "Analytical Electromechanical Model of Cantilevered Bi-Stable Composites for Broadband Energy Harvesting," *Volume 2: Mechanics and Behavior of Active Materials; Structural Health Monitoring; Bioinspired Smart Materials and Systems; Energy Harvesting*, ASME, 2013, p. V002T07A014.

[96] Taki, M. S., Tikani, R., Ziaei-Rad, S., and Firouzian-Nejad, A., "Dynamic responses of cross-ply bi-stable composite laminates with piezoelectric layers," *Archive of Applied Mechanics*, Vol. 86, No. 6, 2016, pp. 1003–1018.

[97] Daqaq, M. F., Masana, R., Erturk, A., and Dane Quinn, D., "On the Role of Nonlinearities in Vibratory Energy Harvesting: A Critical Review and Discussion," *Applied Mechanics Reviews*, Vol. 66, No. 4, 2014, pp. 040801.

[98] Daqaq, M. F., "Response of uni-modal duffing-type harvesters to random forced excitations," *Journal of Sound and Vibration*, Vol. 329, No. 18, 2010, pp. 3621–3631.

[99] Mallick, D., Amann, A., and Roy, S., "Surfing the High Energy Output Branch of Nonlinear Energy Harvesters," *Physical Review Letters*, Vol. 117, 2016, pp. 197701.

[100] Friswell, M. I., Faruque Ali, S., Bilgen, O., Adhikari, S., Lees, A. W., and Litak, G., "Non-linear piezoelectric vibration energy harvesting from a vertical cantilever beam with tip mass," *Journal of Intelligent Material Systems and Structures*, Vol. 23, No. 13, 2012, pp. 1505–1521.

[101] Cao, J., Zhou, S., Wang, W., and Lin, J., "Influence of potential well depth on nonlinear tristable energy harvesting," *Applied Physics Letters*, Vol. 106, No. 17, 2015.

[102] Zhou, S., Cao, J., Inman, D. J., Lin, J., and Li, D., "Harmonic balance analysis of nonlinear tristable energy harvesters for performance enhancement," *Journal of Sound and Vibration*, Vol. 373, 2016, pp. 223–235.

[103] Daqaq, M. F., "On intentional introduction of stiffness nonlinearities for energy harvesting under white Gaussian excitations," *Nonlinear Dynamics*, Vol. 69, No. 3, 2012, pp. 1063–1079.

[104] Zhou, S., Cao, J., Inman, D. J., Liu, S., Wang, W., and Lin, J., "Impact-induced high-energy orbits of nonlinear energy harvesters," *Applied Physics Letters*, Vol. 106, 2015, pp. 93901.

[105] Sebald, G., Kuwano, H., Guyomar, D., and Ducharne, B., "Experimental Duffing oscillator for broadband piezoelectric energy harvesting," *Smart Materials and Structures*, Vol. 20, No. 10, 2011.

[106] Lan, C., Tang, L., and Qin, W., "Obtaining high-energy responses of nonlinear piezoelectric energy harvester by voltage impulse perturbations," *European Physical Journal Applied Physics*, Vol. 79, 2017, pp. 20902.

[107] Udani, J. P. and Arrieta, A. F., "Sustaining high-energy orbits of bi-stable energy harvesters by attractor selection," *Applied Physics Letters*, Vol. 111, No. 17, 2017, pp. 213901–173905.

[108] Masuda, A. and Sato, T., "Global stabilization of high-energy resonance for a nonlinear wideband electromagnetic vibration energy harvester," *Active and Passive Smart Structures and Integrated Systems 2016*, Vol. 9799, International Society for Optics and Photonics, 2016, p. 97990K.

[109] Cammarano, A., Neild, S. A., Burrow, S. G., and Inman, D. J., "The bandwidth of optimized nonlinear vibration-based energy harvesters," *Smart Materials and Structures*, Vol. 23, No. 5, 2014.

[110] Huguet, T., Badel, A., Druet, O., and Lallart, M., "Drastic bandwidth enhancement of bistable energy harvesters: Study of subharmonic behaviors and their stability robustness," *Applied Energy*, Vol. 226, 2018, pp. 607–617.

[111] Lakes, R. S., "Extreme Damping in Composite Materials with a Negative Stiffness Phase," *Physical Review Letters*, Vol. 86, 2001, pp. 2897–2900.

[112] Udani, J. P. and Arrieta, A. F., "Efficient potential well escape for bi-stable Duffing oscillators," *Nonlinear Dynamics*, 2018, pp. 1–15.

[113] Lee, A. J., Moosavian, A., and Inman, D. J., "A piezoelectrically generated bistable laminate for morphing," *Materials Letters*, Vol. 190, 2017, pp. 123–126.

[114] Lee, A. J., Moosavian, A., and Inman, D. J., "Control and characterization of a bistable laminate generated with piezoelectricity," *Smart Materials and Structures*, Vol. 26, 2017, pp. 085007.

[115] Lee, A. J. and Inman, D. J., "A multifunctional bistable laminate: Snap-through morphing enabled by broadband energy harvesting," *Journal of Intelligent Material Systems and Structures*, Vol. 29, No. 11, 2018, pp. 2528–2543.

[116] Amabili, M., *Nonlinear vibrations and stability of shells and plates*, Cambridge University Press, 2008.

[117] Whitney, J. M., *Structural analysis of laminated anisotropic plates*, CRC Press, 1987.

[118] Udani, J. P. and Arrieta, A. F., "Analytical Modeling of Multi-sectioned Bi-stable Composites: Stiffness Variability and Embeddability," *Composite Structures*, 2019.

[119] Erturk, A. and Inman, D. J., *Piezoelectric energy harvesting*, John Wiley & Sons, 2011.

[120] Gigliotti, M., Wisnom, M. R., and Potter, K. D., "Loss of bifurcation and multiple shapes of thin [0/90] unsymmetric composite plates subject to thermal stress," *Composites Science and Technology*, Vol. 64, No. 1, 2004, pp. 109–128.

[121] Pirrera, A., Avitabile, D., and Weaver, P. M., "Bistable plates for morphing structures: A refined analytical approach with high-order polynomials," *International Journal of Solids and Structures*, Vol. 47, No. 25-26, 2010, pp. 3412–3425.

[122] Williams, R. B., *Nonlinear Mechanical and Actuation Characterization of Piezoceramic Fiber Composites*, Ph.D. thesis, Virginia Polytechnic Institute and State University, 2004.

[123] Kim, J., Kim, H., and Lee, D., "Adhesion characteristics of carbon / epoxy composites treated with low- and atmospheric pressure plasmas," *Journal of Adhesion Science and Technology*, Vol. 17, No. 13, 2003, pp. 1751– 1771.

[124] Jumbo, F. S., Ashcroft, I. A., Crocombe, A. D., and Abdel Wahab, M. M., "Thermal residual stress analysis of epoxy bi-material laminates and bonded joints," *International Journal of Adhesion and Adhesives*, Vol. 30, No. 7, 2010, pp. 523–538.

[125] Côté, F., Masson, P., Mrad, N., and Cotoni, V., "Dynamic and static modelling of piezoelectric composite structures using a thermal analogy with MSC/NASTRAN," *Composite Structures*, Vol. 65, No. 3-4, 2004, pp. 471–484.

[126] Schlecht, M., Schulte, K., and Hyer, M., "A comparative study for the calculation of the temperature dependent shapes of unsymmetric laminates based on finite element analysis and extended classical lamination theory," *Mechanics of Composite Materials*, Vol. 31, No. 3, 1995, pp. 247–254.

[127] Betts, D. N., Salo, A. I. T., Bowen, C. R., and Kim, H. A., "Characterisation and modelling of the cured shapes of arbitrary layup bistable composite laminates," *Composite Structures*, Vol. 92, 2009, pp. 1694–1700.

[128] Kant, T. and Swaminathan, K., "Estimation of transverse/interlaminar stresses in laminated composites a selective review and survey of current developments," *Composite Structures*, Vol. 49, 2000, pp. 65–75.

[129] Mittelstedt, C. and Becker, W., "Interlaminar Stress Concentrations in Layered Structures: Part I A Selective Literature Survey on the Free-Edge Effect since 1967," *Journal of Composite Materials*, Vol. 38, No. 12, 2004, pp. 1037–1062.

[130] Nosier, A. and Maleki, M., "Free-edge stresses in general composite laminates," *International Journal of Mechanical Sciences*, Vol. 50, 2008, pp. 1435–1447.

[131] Sodano, H. A., "An experimental comparison between several active composite actuators for power generation," *Smart Materials and Structures*, Vol. 15, 2006, pp. 1211–1216.

[132] Choi, Y. T., Wereley, N. M., and Purekar, A. S., "Energy Harvesting Devices Using Macrofiber Composite Materials," *Journal of Intelligent Material Systems and Structures*, Vol. 21, No. 6, 2010, pp. 647–658.

[133] Inman, D. J., *Engineering Vibration*, Pearson, 4th edition, Upper Saddle River, NJ, 2013.

[134] Kyriazoglou, C. and Guild, F. J., "Finite element prediction of damping of composite GFRP and CFRP laminates a hybrid formulation vibration damping experiments and Rayleigh damping," *Composites Science and Technology*, Vol. 66, No. 3, 2006, pp. 487 – 498.

[135] Moon, F. C., *Chaotic and fractal dynamics: introduction for applied scientists and engineers*, John Wiley & Sons, 2008.

[136] Virgin, L. N., *Introduction to experimental nonlinear dynamics: a case study in mechanical vibration*, Cambridge University Press, 2000.

[137] Strogatz, S. H., *Nonlinear Dynamics and Chaos with Student Solutions Manual: With Applications to Physics, Biology, Chemistry, and Engineering*, CRC Press, 2018.

[138] Pomeau, Y. and Manneville, P., "Intermittent Transition to Turbulence in Dissipative Dynamical Systems," *Communications in Mathematical Physics*, Vol. 74, 1980, pp. 189–197.

[139] Pankonien, A. M. and Inman, D. J., "Aeroelastic performance evaluation of a flexure box morphing airfoil concept," *Active and Passive Smart Structures and Integrated Systems 2014*, Vol. 9057, International Society for Optics and Photonics, 2014, p. 905716.

[140] Goh, C. J. and Caughey, T. K., "On the stability problem caused by finite actuator dynamics in the collocated control of large space structures," *International Journal of Control*, Vol. 41, No. 3, 1985, pp. 787–802.

[141] Fanson, J. L. and Caughey, T. K., "Positive position feedback control for large space structures," *AIAA Journal*, Vol. 28, No. 4, 1990, pp. 717–724.

[142] Friswell, M. I. and Inman, D. J., "The relationship between positive position feedback and output feedback controllers," *Smart Materials and Structures*, Vol. 8, No. 3, 1999, pp. 285–291.